

Alfred-Wegener-Institut
Helmholtz Zentrum für Polar- und Meeresforschung
Forschungsstelle Potsdam, Sektion Permafrostforschung

Subsea permafrost in the Laptev Sea: Influences on degradation, state and distribution

Dissertation
zur Erlangung des akademischen Grades
“doctor rerum naturalium”
(Dr. rer. nat.)
in der Wissenschaftsdisziplin “Angewandte Geophysik”

eingereicht an der
Mathematisch-Naturwissenschaftlichen Fakultät
der Universität Potsdam

von
Fabian Kneier

Ort und Tag der Disputation: Potsdam, 8. November 2019

Hauptbetreuer*in: Prof. Hans-Wolfgang Hubberten
Betreuer*innen: Dr. Paul Overduin, Dr. Trond Ryberg
Gutachter*innen: Prof. Hans-Wolfgang Hubberten, Dr. Paul Overduin,
Prof. Michael Krautblatter

Abstract

During lower sea levels in glacial periods, deep permafrost formed on large continental shelf areas of the Arctic Ocean. Subsequent sea level rise and coastal erosion created subsea permafrost, which generally degrades after inundation under the influence of a complex suite of marine, near-shore processes. Global warming is especially pronounced in the Arctic, and will increase the transition to and the degradation of subsea permafrost, with implications for atmospheric climate forcing, offshore infrastructure, and aquatic ecosystems.

This thesis combines new geophysical, borehole observational and modelling approaches to enhance our understanding of subsea permafrost dynamics. Three specific areas for advancement were identified: (I) sparsity of observational data, (II) lacking implementation of salt infiltration mechanisms in models, and (III) poor understanding of the regional differences in key driving parameters. This study tested the combination of spectral ratios of the ambient vibration seismic wavefield, together with estimated shear wave velocity from seismic interferometry analysis, for estimating the thickness of the unfrozen sediment overlying the ice-bonded permafrost offshore. Mesoscale numerical calculations (10^1 to 10^2 m, thousands of years) were employed to develop and solve the coupled heat diffusion and salt transport equations including phase change effects. Model soil parameters were constrained by borehole data, and the impact of a variety of influences during the transgression was tested in modelling studies. In addition, two inversion schemes (particle swarm optimization and a least-square method) were used to reconstruct temperature histories for the past 200–300 years in the Laptev Sea region in Siberia from two permafrost borehole temperature records. These data were evaluated against larger scale reconstructions from the region.

It was found (I) that peaks in spectral ratios modelled for three-layer, one-dimensional systems corresponded with thaw depths. Around Muostakh Island in the central Laptev Sea seismic receivers were deployed on the seabed. Derived depths of the ice-bonded permafrost table were between 3.7–20.7 m \pm 15 %, increasing with distance from the coast. (II) Temperatures modelled during the transition to subsea

permafrost resembled isothermal conditions after about 2000 years of inundation at Cape Mamontov Klyk, consistent with observations from offshore boreholes. Stratigraphic scenarios showed that salt distribution and infiltration had a large impact on the ice saturation in the sediments. Three key factors were identified that, when changed, shifted the modelled permafrost thaw depth most strongly: bottom water temperatures, shoreline retreat rate and initial temperature before inundation. Salt transport based on diffusion and contribution from arbitrary density-driven mechanisms only accounted for about 50% of observed thaw depths at offshore sites hundreds to thousands of years after inundation. This bias was found consistently at all three sites in the Laptev Sea region. (III) In the temperature reconstructions, distinct differences in the local temperature histories between the western Laptev Sea and the Lena Delta sites were recognized, such as a transition to warmer temperatures a century later in the western Laptev Sea as well as a peak in warming three decades later. The local permafrost surface temperature history at Sardakh Island in the Lena Delta was reminiscent of the circum-Arctic regional average trends. However, Mamontov Klyk in the western Laptev Sea was consistent to Arctic trends only in the most recent decade and was more similar to northern hemispheric mean trends. Both sites were consistent with a rapid synoptic recent warming.

In conclusion, the consistency between modelled response, expected permafrost distribution, and observational data suggests that the passive seismic method is promising for the determination of the thickness of unfrozen sediment on the continental Arctic shelf. The quantified gap between currently modelled and observed thaw depths means that the impact of degradation on climate forcing, ecosystems, and infrastructure is larger than current models predict. This discrepancy suggests the importance of further mechanisms of salt penetration and thaw that have not been considered – either pre-inundation or post-inundation, or both. In addition, any meaningful modelling of subsea permafrost would have to constrain the identified key factors and their regional differences well. The shallow permafrost boreholes provide missing well-resolved short-scale temperature information in the coastal permafrost tundra of the Arctic. As local differences from circum-Arctic reconstructions, such as later warming and higher warming magnitude, were shown to exist in this region, these results provide a basis for local surface temperature record parameterization of climate and, in particular, permafrost models. The results of this work bring us one step further to understanding the full picture of the transition from terrestrial to subsea permafrost.

Zusammenfassung

Als zu glazialen Zeiten der Meeresspiegel niedriger lag, konnte sich tiefer Permafrost (Dauerfrostboden) in weiten Teilen der Kontinentalschelfgebiete des arktischen Ozeans bilden. Durch den darauf folgenden Meeresspiegelanstieg und Küstenerosion wurde dieser überflutet und es entstand submariner Permafrost. Seit der Überflutung wird dieser durch eine Reihe komplexer mariner Prozesse in der küstennahen Zone degradiert. Die Klimaerwärmung ist in der Arktis besonders ausgeprägt, wodurch sich die Überflutung durch Küstenerosion sowie diese Degradationsprozesse in Zukunft weiter intensivieren werden. Dies wird weitreichende Konsequenzen für das Klimasystem (Freisetzung von Treibhausgasen), Offshore-Infrastruktur als auch aquatische Ökosysteme haben.

Diese Dissertation kombiniert neue geophysikalische, Bohrlochbeobachtungs-basierte und Modellierungsansätze, um unser Verständnis der speziellen Dynamik des submarinen Permafrosts zu verbessern. Drei spezifische Bereiche wurden identifiziert, welche das derzeitige Verständnis zum submarinen Permafrost maßgeblich einschränken, und in dieser Arbeit gezielt weiterentwickelt wurden: (I) Die spärliche Verfügbarkeit von Beobachtungsdaten, (II) die fehlende Implementation von Salzinfiltrationsmechanismen in Modelbeschreibungen und (III) das mangelnde Verständnis der regionalen Unterschiede von treibenden Einflußparametern. Hierfür wurde die Kombination spektraler Amplitudenverhältnisse der Umgebungsschwingungen im seismischen Wellenfeld (seismisches Hintergrundrauschen) mit der aus seismischer Interferometrie abgeschätzten Scherwellengeschwindigkeit zur Bestimmung der Mächtigkeit der aufgetauten Sedimentschicht oberhalb des eisgebundenen Permafrosts im Meeresboden getestet. Numerische Simulationen (auf der Skala von 10^1 bis 10^2 m, tausende Jahre) wurden zur Entwicklung und Lösung der gekoppelten Wärmeleitungs- und Salztransportgleichungen unter Berücksichtigung von Phasenübergängen angewandt. Hierbei wurden die Modelparameter zur Untergrundbeschaffenheit aus Bohrlochdaten bestimmt und die Auswirkungen verschiedener Parameter während der Meeresüberflutung untersucht. Zusätzlich wurden zwei Inversionsalgorithmen (Partikelschwarmoptimierung und ein Verfahren der kleinsten Quadrate) verwendet,

um die Temperaturen der letzten 200–300 Jahre in der Laptewsee-Region in Sibirien anhand zweier Temperaturdatensätze aus Permafrostbohrlöchern zu rekonstruieren. Diese Daten wurden im Vergleich zu größerskaligen Rekonstruktionen aus der Region ausgewertet.

Es konnte gezeigt werden, (I) dass die Höchstwerte im spektralen Amplitudenverhältnis, die für den eindimensionalen Fall eines 3-Schicht-Systems modelliert wurden, mit der Auftautiefe zusammenhingen. Seismische Instrumente wurden auf dem Meeresboden um die Insel Muostakh, in der zentralen Laptewsee gelegen, ausgebracht. Die gefundenen Tiefen der eisgebundenen Permafrosttafel lagen zwischen $3.7\text{--}20.7\text{ m} \pm 15\%$, und nahmen mit zunehmender Entfernung zur Küste zu. (II) Die modellierten Temperaturen während des Übergangs zum submarinen Permafrost entsprachen ab etwa 2000 Jahren nach der Überflutung isothermischen Bedingungen bei Cape Mamontov Klyk, in Übereinstimmung zu den Beobachtungen in den Bohrlöchern. Stratigrafische Szenarien zeigten, dass die Salzverteilung und -infiltration großen Einfluß auf den Sättigungszustand des Poreneises im Sediment hatte. Drei Schlüsselfaktoren wurden identifiziert, welche, wenn diese verändert wurden, die modellierte Auftautiefe des Permafrosts am stärksten beeinflussten: Die Temperaturen am Meeresboden, die Küstenerosionsrate und die Anfangstemperatur zum Zeitpunkt der Überflutung. Salztransport unter Berücksichtigung von Diffusion und beliebigen dichte-getriebenen Mechanismen unterschätzte die beobachteten Auftautiefen um circa 50% über hunderte bis tausende von Jahren nach der Überflutung. Diese Abweichung wurde konsistent an allen drei Untersuchungsstandorten in der Laptewsee-Region gefunden. (III) In den Temperaturrekonstruktionen wurden deutliche Unterschiede im lokalen Temperaturverlauf zwischen den Standorten in der westlichen Laptewsee und im Lena Delta festgestellt. Dazu gehörte ein Übergang zu wärmeren Temperaturen ein Jahrhundert später in der westlichen Laptewsee, sowie ein Maximum der Erwärmung drei Jahrzehnte später als im Lena Delta. Die lokale Permafrost-Oberflächentemperaturhistorie auf der Insel Sardakh im Lena Delta glich den zirkumarktischen mittleren Trends. Im Gegensatz dazu stimmte Mamontov Klyk in der westlichen Laptewsee nur im jüngsten Jahrzehnt mit den arktischen Trends überein und glich vielmehr dem mittleren Trend der Nordhemisphäre. Beide Standorte stimmten mit einer schnellen, synoptischen und kürzlichen Erwärmung überein.

Abschließend lässt sich festhalten, dass auf Grund der Übereinstimmung zwischen modelliertem Verhalten, erwarteter Permafrostverteilung und Beobachtungsdaten die passiv-seismische Methode vielversprechend für die Dickebestimmung der ungefrorenen Sedimente im arktischen Meeresboden ist. Durch die hier quantifizierte Diskrepanz zwischen aktuell modellierter und beobachteter Auftautiefen wird klar,

dass die Auswirkung der Degradation auf Klimaantrieb, Ökosysteme und Infrastruktur größer ist als dies von aktuellen Modellen vorhergesagt wird. Um diese Diskrepanz zu eliminieren, müssen weitere bisher unberücksichtigte Mechanismen der Salzeindringung und des Auftauens vor oder nach der Überflutung in zukünftigen Modellen mit einbezogen werden. Des Weiteren folgt aus dieser Arbeit, dass Modellierungen des submarinen Permafrosts die hier identifizierten Schlüsselfaktoren und ihre regionalen Unterschiede berücksichtigen müssen, um ihre Aussagekraft sicher zu stellen. Die Permafrostbohrlöcher liefern bisher fehlende, auf kurzer Zeitskala gut-aufgelöste Temperaturinformationen in der arktischen Küstentundra. Da lokale Abweichungen von zirkumarktischen Rekonstruktionen in dieser Region nachgewiesen werden konnten, stellen die Ergebnisse eine Grundlage für lokale Temperaturverlaufs-Parametrisierungen in Klima- und insbesondere Permafrostmodellen zur Verfügung. Die Ergebnisse dieser Arbeit weisen die Richtung für zukünftige Forschungs- und Modellierungsvorhaben und stellen einen wichtigen Schritt dar, um den Übergang von terrestrischem zu submarinem Permafrost zu verstehen.

Table of Contents

Abstract	i
Zusammenfassung	iii
1 Introduction	1
1.1 Scientific background	1
1.1.1 Permafrost - terrestrial and subsea	1
1.1.2 Subsea permafrost distribution	5
1.1.3 Relevance in the context of a changing Arctic	7
1.1.4 Influences on subsea permafrost	11
1.2 Hypotheses and objectives	14
1.3 Thesis organization	17
2 Detection of subsea permafrost degradation rates	19
2.1 An overview of geophysical methods and studies in subsea permafrost	20
2.2 Geophysical objectives	27
2.3 Passive seismic techniques	27
2.3.1 H/V passive seismics	30
2.3.2 Passive seismic interferometry	33
2.4 Instrument design & marine tests on Sylt	41
2.5 Arctic feasibility test site around Muostakh Island	43
2.6 Arctic deployment for wide area detection around Muostakh Island .	57
3 Modelling of subsea permafrost degradation processes	61
3.1 An overview on subsea permafrost modelling	62
3.2 Salt distribution - mechanisms beyond diffusional transport	64
3.3 Open questions in salt transport and permafrost degradation	65
3.4 Modelling objectives	67
3.5 Study sites	68
3.5.1 Primary study site: Cape Mamontov Klyk	68
3.5.2 Secondary study sites: Buor Khaya & Muostakh Island	70
3.6 Developing a model for subsea permafrost	72
3.6.1 Thermal regime of the subsurface: governing equations of conductive heat transfer	72
3.6.2 Model definitions: concentration and thaw depth	79
3.6.3 Saline effect on the state of permafrost	80
3.6.4 Salt transport: governing equation & parameterizations	83

3.6.5	Modelling approach	90
3.6.6	Model testing	94
3.7	Results: Influence of model parameters on subsea permafrost degradation	96
3.8	Discussion and implications	115
3.8.1	Modelled inundation parameters	115
3.8.2	Further factors affecting subsea permafrost degradation	124
3.8.3	Implications	128
4	From local to regional scale: Amending sparsely distributed temperature records	131
4.1	An overview of borehole temperature reconstruction	136
4.2	On the transferability of ground to air temperatures	142
4.3	Reconstruction objectives	143
4.4	Borehole sites and climate	143
4.5	Borehole temperatures	145
4.6	Inversion method	147
4.6.1	Forward model	147
4.6.2	Optimization	150
4.6.3	Sensitivity analysis	154
4.7	Results and discussion of the reconstruction from the permafrost boreholes	157
4.7.1	Recoverable period	157
4.7.2	Optimization	158
4.7.3	Surface temperature reconstructions and fit	159
4.7.4	Inversion method's impact on character of solution & sensitivity to temperature history parameterization	162
4.8	Discussion of spatial differences and implications	164
4.8.1	Comparison to other temperature data	164
4.8.2	Site differences	167
4.8.3	Methodological considerations	169
4.8.4	Implications	171
5	Conclusion and outlook	175
5.1	Outlook	179
	Appendices	183
	A Modelling tests for H/V method configuration	183
	Bibliography	185
	Acknowledgements	219

CHAPTER 1

Introduction

1.1 Scientific background

1.1.1 Permafrost - terrestrial and subsea

Permafrost is ground of perennially subzero temperature. The formal definition is a temperature of below 0°C for at least two consecutive years [Subcommittee Permafrost, 1988].

Permafrost formed widely under the influence of the cold climates of the polar regions on exposed ground (in soil as well as in rock), but can also be found in mountain regions, notably widespread on the Tibetan plateau, and generally wherever the microclimate is cold enough and the ground is not insulated, e.g. with thick snow or ice glaciers. Today permafrost affects 24% of the northern hemispheric landmass [Zhang et al., 1999] (see Fig. 1.1), but it also exists offshore on the continental shelves of the Arctic ocean as subsea permafrost.

Broad and shallow continental shelves that extend up to 800 km offshore compose the boundary between the deep Arctic basin and the surrounding land masses in Eurasia and North America. During the glacial maxima of the late Pliocene and Pleistocene sea levels were up to 120 m lower than they are today, due to the amount of water bound in the immense ice sheets. This exposed large shelf areas to the cold subaerial conditions of the Arctic climate. Atmospheric circulation and a more continental climate than today [Hubberten et al., 2004] led to dry and therefore unglaciated conditions on large territories from the Taimyr Peninsula at the eastern margin of the Eurasian ice sheet to the Yukon Territory at the western margin of the Laurentide Ice Sheet in North America [Ehlers and Gibbard, 2003, Schirmer et al., 2013]. Subjected to cold subaerial conditions deep permafrost formed both on

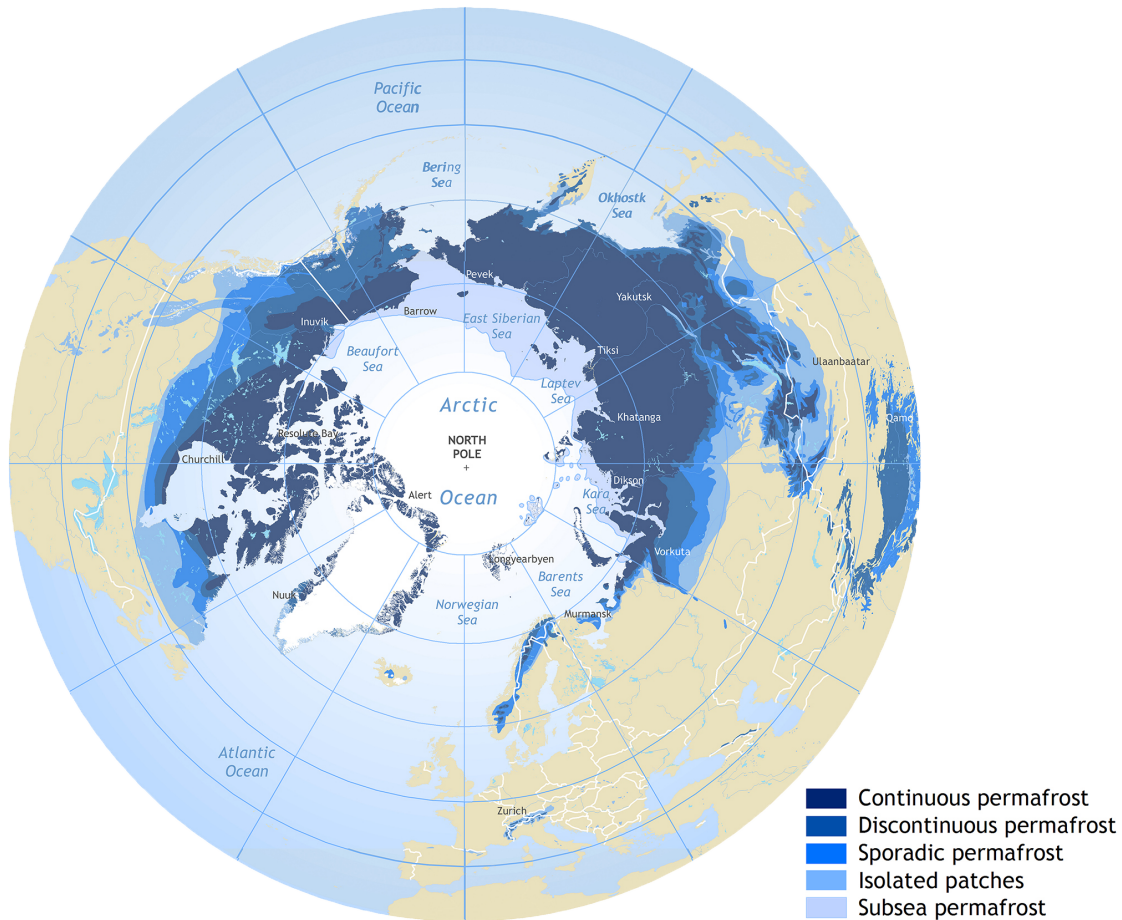


Figure 1.1: Distribution of permafrost in the northern hemisphere on a circum-Arctic scale, according to [Brown et al., 1997].

the modern terrestrial as well as on the exposed shelf territories. In central Siberia, permafrost depth today reaches several hundreds of meters with a maximum of over 1500 m.

In the Laptev Sea, large accumulation plains are thought to have stretched from the modern coastal lowlands over 200 km offshore on the shelf during sea level low stands. Sedimentation and syngenetic freezing (when the fine-grained sediments are deposited and frozen at the same time) under the cold, dry climate conditions created up to 50 m thick Ice Complex (Yedoma) deposits [Schirrmeister et al., 2011a, 2013]. Yedoma is composed of ice-rich silts and silty sands with characteristically high organic content (remains of the late Pleistocene mammoth fauna and tundra-steppe flora conserved well in permafrost conditions) and large penetrating ice wedges. The subsequent Holocene marine transgression flooded the Laptev Sea shelf again. Rates of sea level rise in this region reached 13.3 mm a^{-1} and 7.9 mm a^{-1} over time scales of centuries [Bauch et al., 2001]. The Holocene sea level highstand was approached near c. 5 ka before present (BP) [Bauch et al., 2001] and modern relative sea

level was reached no later than 3 ka BP [Whitehouse et al., 2007] (see also Fig. 1.2). Inundation of terrestrial permafrost continued by coastal erosion and retreat of the volatile permafrost-dominated coastline. Mean long-term (c. 40 a) retreat rates in the Laptev Sea are 2.2 m a^{-1} but with high temporal variability and higher mean rates in recent years (5.3 m a^{-1}) [Günther et al., 2013a]. Inundation from sea level rise and coastal erosion thus occurred so rapidly that permafrost did not have the time to thaw completely, and was preserved as subsea permafrost. Fig. 1.2 illustrates a site of currently ongoing subsea transition through coastal erosion. While terrestrial permafrost can be either aggrading or degrading depending on the subaerial boundary conditions, subsea permafrost is relic terrestrial permafrost, and generally degrading under the relatively warm and salty boundary conditions of the shallow shelf oceans.

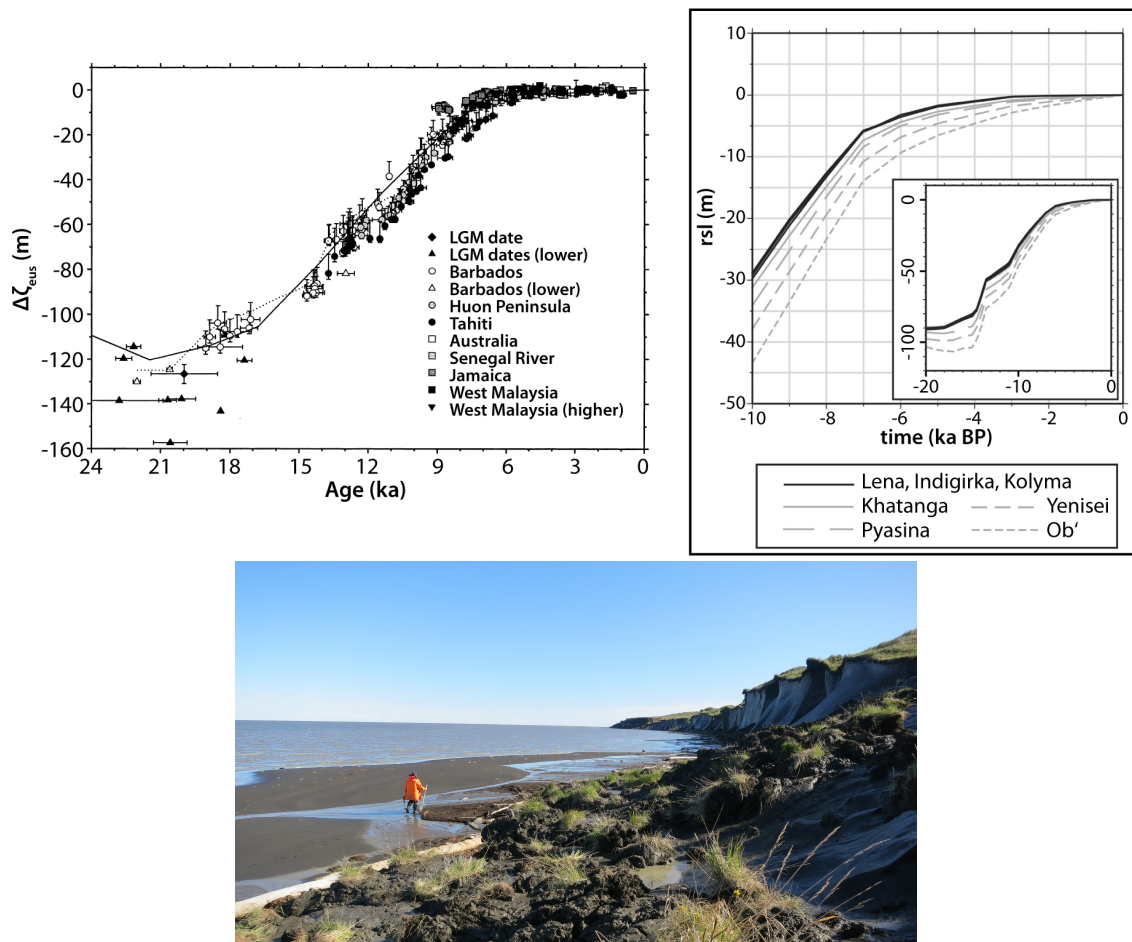


Figure 1.2: Sea level. **(left)** Global sea level curve: Combined eustatic sea level changes from the Last Glacial Maximum (LGM) to the present, after [Fleming et al., 1998]. **(right)** Relative sea level for the last 10 ka (inset shows the last 20 ka) at the mouth of major Siberian rivers including the Lena river in the Laptev Sea region (taken from Whitehouse et al. [2007]). **(bottom)** A site of ongoing coastal erosion and inundation of terrestrial permafrost by advancing sea water in the central Laptev Sea.

fluvial sand and marine mud deposits. These are interpreted to be connected to eight transgression/regression cycles. The ice-bearing permafrost body is believed to have been preserved through the transgressive phases. Modelling also suggests that subsea permafrost persistently existed landwards of the 60 m water depth mark on large parts of the Laptev Sea shelf throughout interglacial cycles for at least the last 400 ka [Romanovskii and Hubberten, 2001, Romanovskii et al., 2004].

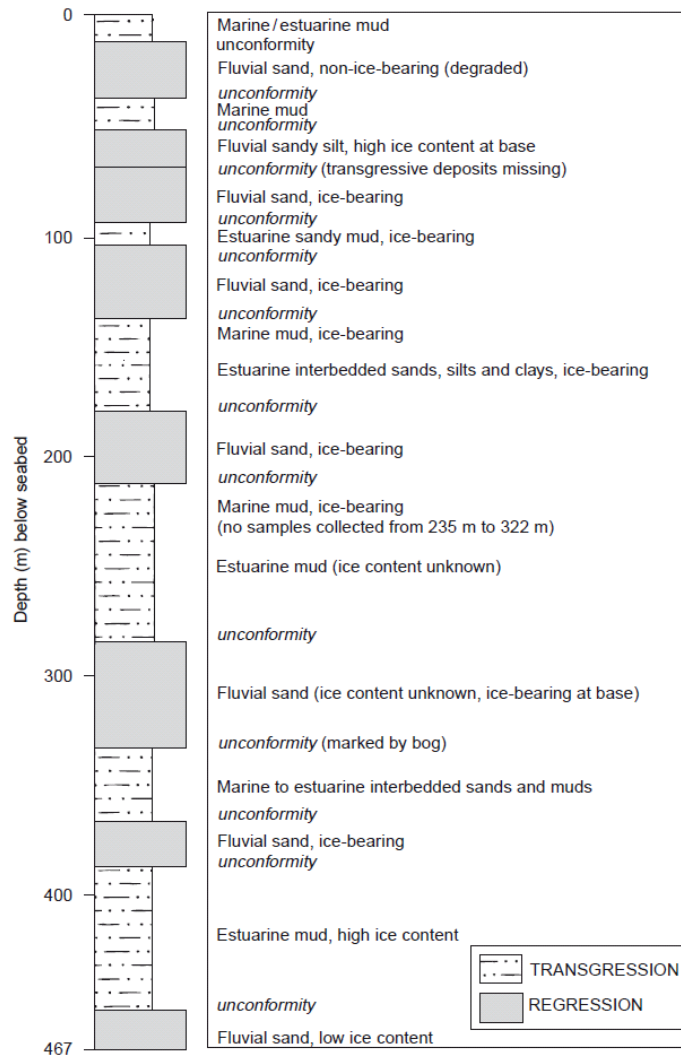


Figure 1.4: Stratigraphy in the shallow (32 m water depth) Canadian Beaufort Shelf. Eight repetitions of transgression and regression are recognized. (Graph taken from Osterkamp [2001], original data by Blasco [1995].)

1.1.2 Subsea permafrost distribution

Subsea permafrost extent remains hidden below sea water, in contrast to terrestrial permafrost extent and the erosion dynamics of permafrost-dominated coasts, which can even often be studied by remote sensing and satellite imagery. While extent

and the controlling processes are relatively well known for terrestrial permafrost, the extent and state of subsea permafrost and especially the controlling processes on its degradation are poorly understood. Direct observations are challenging due to the limited access and high operational expense involved in probing the sea bottom in the remote shelf regions of the Arctic Ocean. Given the sparsity of observations, subsea permafrost distribution has often been assumed to extend to the 120 m isobath, which delineates the approximate coastline in the late Pleistocene and was based on limited offshore boreholes [Brothers et al., 2012, 2016] (see for example in the map in Fig. 1.1 which placed the permafrost margin at the shelf break [Ruppel and Kessler, 2017]). Knowledge on distribution is based on good quality systematic observational data only in very few regions. This includes most notably the U.S. Beaufort Sea shelf (the relatively narrow shelf area of northern Alaska), where seismic-refraction-velocity [Brothers et al., 2012] and multichannel seismic reflection data [Brothers et al., 2016] spanning the entire shelf provides the most spatially extensive and dense data set on subsea permafrost extent, corroborated by borehole constraints [Ruppel et al., 2016]. The systematic mapping shows that subsea ice-bearing permafrost does not extend beyond the 20-30 m isobath and is within 37 km of the modern shoreline, revising older assumptions of larger extent and implying considerable thawing since the Late Pleistocene. On the Canadian Beaufort shelf, contrastingly, it underlies much of the shelf and could reach the 100 m isobath [Hu et al., 2013, Blasco et al., 2011, MacAulay and Hunter, 1982, Hunter et al., 1978]. Different extents in these regions most likely reflect different inundation histories, environmental influences or initial conditions. On the South Kara Sea shelf, a similar extent to the U.S. Beaufort Sea prevails [Portnov et al., 2013]. Recent interpretation of hydroacoustic anomalies infer a limit of the offshore extent to water depths of around 20 m, vs. previous estimates out to the 60 m isobath [Rekant and Vasiliev, 2011]. By far the largest area of Arctic shelf potentially underlain by subsea permafrost is the Laptev and East Siberian Sea shelves (see Fig. 1.1). The current understanding of the extent, thermal state and stability of subsea permafrost in this region is primarily based on modelling results [Soloviev et al., 1987, Kim et al., 1999, Delisle, 2000, Romanovskii and Hubberten, 2001, Romanovskii et al., 2005, Nicolsky and Shakhova, 2010, Nicolsky et al., 2012, Frederick and Buffett, 2014] and rather scattered information from shallow borehole or seismic surveys [Hinz et al., 1998, Kim et al., 1999, Rachold et al., 2007, Overduin et al., 2007b, Shakhova et al., 2010, Rekant et al., 2015]. From these, subsea permafrost in the Laptev Sea is estimated to be widespread on the whole shelf (continuous landward of the 60 m isobath), with an imprint of taliks – bodies of unfrozen ground in otherwise permafrost-affected ground – inherited from the inundated thermokarst landscape. Open taliks (i.e. connecting sub- and supra-permafrost waters) are expected only

in the area of active tectonic faults or below submerged taliks of large water bodies [Romanovskii et al., 2005, Nicolsky et al., 2012]. Observed methane supersaturated ocean water in the Laptev Sea possibly also reflects at least patchy thawing of subsea permafrost [Shakhova et al., 2010]. Near-shore boreholes reveal direct evidence of subsea permafrost [Rachold et al., 2007, Overduin et al., 2015b], and offshore drilling discovered evidence on the outer shelf [Kassens et al., 2001], but borehole observations as important ground truth on the Arctic shelf remain sparse. This is especially true outside of the near-shore zone. An overview illustrating the sparsity of scientific boreholes on the Arctic shelf is shown in Fig. 1.5.

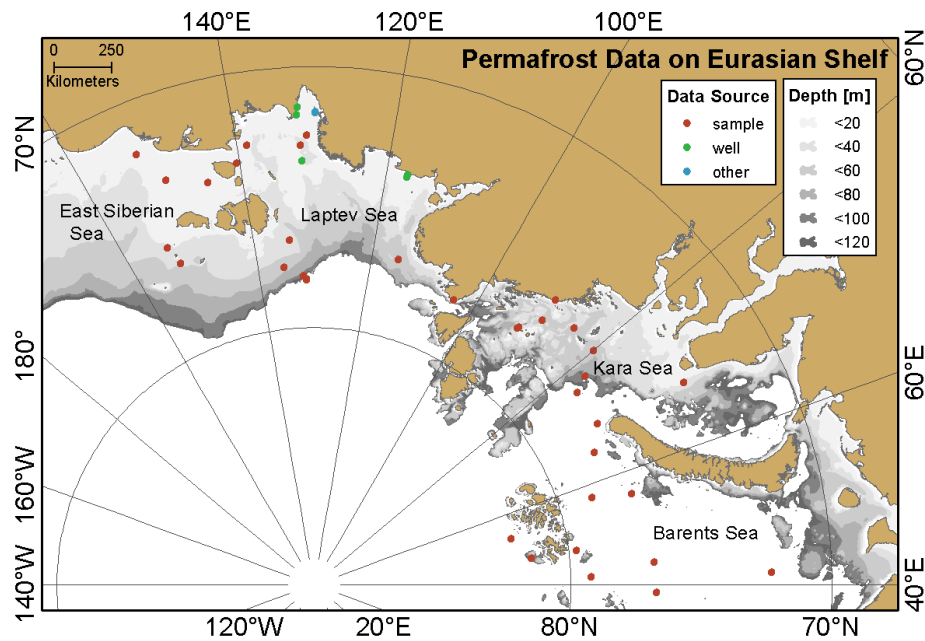


Figure 1.5: Permafrost data on the Eurasian continental shelf (Data sources in the East Siberian and Laptev Sea: [Günther et al., 2013b, Overduin et al., 2007a, Drachev et al., 2003, Are et al., 2000, Kunitsky, 1989, Slagoda, 1993, Zhigarev, 1997]).

1.1.3 Relevance in the context of a changing Arctic

Global climate change is projected to show the largest effects in high latitude regions, an effect termed ‘Arctic Amplification’ [Intergovernmental Panel on Climate Change (IPCC), 2013, Hansen et al., 2010]. This is connected with a suite of factors, including amplifying feedbacks of sea ice and snow cover decline associated with albedo decrease and increased energy absorption by land and sea. Results include air temperature increases that are 3–4 times higher than the global mean and predict warming oceans. This warming will amplify current warming of bottom waters [James et al., 2016]. Recently, a warming rate higher than the circum-Arctic average and 10 times above the global mean was reported in central Yakutia [Boike et al., 2016]. Sea ice extent

and thickness are decreasing rapidly. A longer open water season is resulting in longer periods of coastal erosion. Current shoreline retreat rates of ice-rich coasts are twice as high as the long-term mean in the Laptev Sea [Günther et al., 2013a]. Transition of terrestrial to subsea permafrost will thus increase and more permafrost volume will be subjected to the more strongly degradational, submarine conditions.

Permafrost degradation encompasses the warming of the permafrost body, the decrease in ice content (both of which can be accompanied by a change in the other at submarine conditions), the decrease in thickness of the permanently frozen zone in the soil up to its complete disappearance as well as partial thawing, such as the development of through-going taliks, creating unfrozen pathways through the frozen body that allow fluid and gas migration between the sub- and supra-permafrost zones. Subsea permafrost is a factor in marine infrastructure, such as harbour construction and oil producing industry. This includes construction of coastal facilities, structures on the sea floor or subsea pipelines, and is thus economically relevant. Degradation of ice-bearing permafrost in sea floor sediments may destabilize gas hydrates and may release greenhouse gases to the atmosphere. It is therefore a component of the global climate system [O'Connor et al., 2010]. Permafrost is associated with the gas hydrate stability zone on the shelf. Warming and degradation simultaneously influence gas hydrate stability and can create pathways through the formerly closed ice-cap in the sediments for gas migration from the destabilized zone to the sea floor. Further emission into the water column and atmosphere has the potential to contribute to atmospheric climate forcing. Thawing permafrost and subsea permafrost also release nutrients, carbon and major ions into the water, which can affect the aquatic chemistry in the Arctic seas. The resilience to such perturbation is currently unknown [International Ocean Discovery Program (2013–2023)]. Changes to the chemistry of the Arctic Ocean impact aquatic ecosystems and could lead to changes in currents and weather patterns [Toohey et al., 2016]. Mid-latitude weather is probably more susceptible to Arctic changes than to tropical influences with progressing climate change [Cohen, 2016]. For example, Arctic weather patterns are related to mid-latitude winter cooling and increased intraseasonal variability, i.e. more extreme weather events, across the continental northern hemisphere.

The Arctic shelves contain large gas hydrate deposits within and below the permafrost layer [O'Connor et al., 2010, McGuire et al., 2009]. Methane gas hydrates are the most abundant type. Methane hydrates are a frozen, highly-concentrated form of methane (CH_4) (Fig. 1.6). They are ice-like, crystalline solids that form when water and methane combine in a clathrate structure, essentially trapping gas molecules in a cage of ice. The gas in hydrate form is concentrated 180-fold (in a volume sense). Methane constitutes a very potent greenhouse gas. Per unit mass, it is 84 times

more potent than carbon dioxide (CO_2) over a 20 a time frame and remains 25 times more potent over a century [Intergovernmental Panel on Climate Change (IPCC), 2013]. Although its concentration in the atmosphere amounts to only 0.5 % that of carbon dioxide (1.83 ppm vs. ~ 400 ppm), its radiative forcing is approximately 25 % that of CO_2 [Ruppel and Kessler, 2017]. Gas hydrates form and are stable in intermediate-pressure and low-temperature conditions, and encountered in the near-seafloor sediments of continental slopes in water depths below 300–600 m and also within and beneath the permafrost both on land and on the Arctic shelves [Ruppel and Kessler, 2017]. The latter likely formed from thermogenic gas from conventional gas reservoirs underlying the permafrost, which migrated to shallower depth and was frozen in place at the base of permafrost [Collett et al., 2011]. The total amount of hydrate deposits in the Arctic shelves remains unclear. Rough estimates assume 2–65 Gt of CH_4 hydrate [McGuire et al., 2009]. Some research infers large amounts of 540 Gt carbon in hydrates beneath the East Siberian Arctic shelf, with the estimation of additional 360 Gt as free gas trapped below and 500 Gt in the first 25 m within the subsea permafrost (inferred from the terrestrial counterpart there) [Shakhova et al., 2010]. A plausible origin and proof of existence of such deposits anomalous in the current understanding of hydrate formation in the region remain unresolved [Ruppel and Kessler, 2017]. Although permafrost-associated gas hydrates likely make up only a very small fraction (approx. 1 %) of the total hydrate deposits, the subsea permafrost associated hydrates on the shelves are considered among the most susceptible to destabilization (and dissociation) under the time-scale of processes in current climate change [Ruppel, 2011, Hunter et al., 2013].

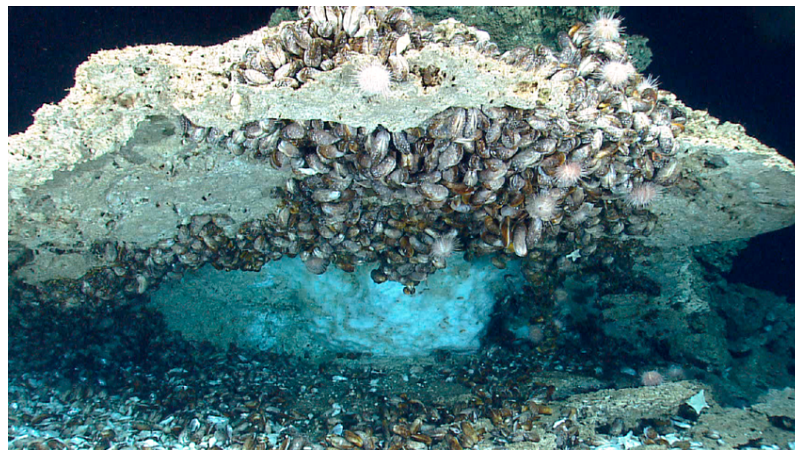


Figure 1.6: Gas hydrate (the white ice-like substance) on the sea floor of the Gulf of Mexico. In this instance, the hydrate formed in the deeper ocean in shallow sediments and is visible, unlike the permafrost-associated gas hydrates. Photograph taken by NOAA's Deep Discovery remotely operated vehicle. Photo credit: NOAA.

Once hydrates are destabilized and pathways through the permafrost barrier created, physical and biochemical mechanisms (including anaerobic oxidation of methane

(AOM) in the sediment column, and aerobic microbial oxidation with oxygen and bubble dissolution in the water column [James et al., 2016, Ruppel and Kessler, 2017]) can remove the methane from the soil and water column during gas migration. Investigation of potential methane sinks in the soil and water column during gas migration is of complementary importance to the physical permafrost state. These would mitigate the impact on atmospheric greenhouse gas concentrations by keeping hydrate-released methane from reaching the water-air interface. However, studies in the thawed Arctic shelf sediments are sparse [Overduin et al., 2015b], a fact directly related to the sparsity of borehole drilling. Only recently, first studies on the microbial communities in subsea permafrost sediments were conducted [Mitzscherling et al., 2017]. Moreover, the environmental conditions associated with subsea permafrost on the shelf probably moderate methane sinks following mobilization of gas from hydrates compared to hydrate deposits in deeper, temperate waters: The shallow depth and cold water temperatures decrease the time length of action and the magnitude of mitigating processes (such as bubble stripping, CH₄ dissolution, microbial oxidation), and gas emitted at the sea bottom is more likely to reach the surface. Marine sedimentary AOM sink processes may also be hampered, as these require sulfate, which may not have intruded sediments fully, after only being inundated for maximally 15 ka [Ruppel and Kessler, 2017]. In the Laptev Sea observed patches of ocean water supersaturated with methane have been proposed to be connected to actively degrading methane hydrates and open taliks allowing gas migration into the water column and as bubbles into the atmosphere. The findings of smaller extent of subsea permafrost in the U.S. Beaufort and South Kara Seas, on the other hand, implies that most hydrates - if present - would have already been released. Differentiating the source of observed methane remains a challenge. Instead of hydrate-derived, other possible sources are deep thermogenic gas or biogenic origin (microbial activity on thawed organic matter released from permafrost within the shelf sediments), and have been reported in terrestrial permafrost settings [Walter Anthony et al., 2012]. This makes it difficult to infer the extent of hydrate dissociation and subsea permafrost degradation from observed methane concentrations. Even if the connection remains controversial, however, it has been recognized that improved understanding of the mechanisms and rates of subsea permafrost degradation are prerequisites to meaningful future assessment of subsea permafrost impacts [Shakhova et al., 2017].

The evolution of permafrost in the marine realm is not solely controlled by temperature. This contrasts to the terrestrial environment, where temperature mediated by factors such as microclimate, aspect, vegetation or snow cover is the main controlling influence on permafrost. Offshore permafrost-affected sediments differ from their terrestrial counterparts through the infiltration of salt into the sediment. Saline pore

water affects the state of permafrost mainly by depressing the freezing temperature. Since most shelf sediment has slightly negative temperatures, it is the amount of salt that determines the thawed or frozen state of the permafrost soil (instead of temperature as in the terrestrial environment); therefore, it is the salt infiltration into freshwater, frozen sediments which degrades subsea permafrost at these negative temperatures [Osterkamp et al., 1989]. In addition, salt water infiltration can thaw pore space ice, potentially leading to convective or density-driven flow within the sediment and complicating a simple diffusive salt transport regime. Thus, salinity constitutes a second governing factor next to temperature in the evolution of subsea permafrost. The salt in the marine environment introduces unfrozen liquid pore water even under cryotic (below 0 °C) conditions. To determine the role of permafrost in stabilizing the ground and as a mitigation for fluid and gas flow, we need to be able to measure or predict its ice content. In order to distinguish the changes in the frozen state of the interstitial pore waters, an extension of the terrestrial permafrost terminology is necessary in the context of subsea permafrost. For clarification the following nomenclature is adopted throughout this manuscript (cf. [Osterkamp, 2001, Rachold et al., 2007]).

Terminology:

‘ice-bearing’	permafrost containing some ice
‘ice-bonded’	ice-bearing sediments where the sediment particles are cemented together by ice
‘frozen’	synonymous to ice-bearing or ice-bonded
‘thawed’ or ‘unfrozen’	refers to the absence of ice
‘state of permafrost’	given by its thermal state as well as the liquid water/ice content

1.1.4 Influences on subsea permafrost

Observations of subsea permafrost are required as ground-truth for its distribution and to constrain and validate model predictions [Osterkamp, 2001]. Factors that influence the evolution and degradation of subsea permafrost, both marine and terrestrial, can be categorized in two groups: (1) processes acting on the permafrost once it is submerged or beginning to be submerged by sea water, i.e after the onset of inundation, and (2) factors with regard to the initial conditions of permafrost before the onset of inundation.

The latter comprise the history of the coastal landscape such as thaw lake and talik

formation before the actual transgression [Overduin et al., 2007b] and are strongly associated with the air temperature history. This also determines the condition in which permafrost begins its transition to submarine influences.

A suite of marine, near-shore processes act upon the permafrost after the inundation by sea water. These include sea water temperature, seasonal sea-ice, storm surges and wave action. Inundation is often accompanied by erosion of the upper portion of the profile. In the near-shore coastal zone of the shelf (< 10 m depth) the degradation is further complicated by factors such as sedimentation, advective heat transport in the water column and bottom-fast sea ice. Salt water infiltration can thaw pore space ice, potentially leading to convective or density-driven flow within the sediment. Coastal erosion affects subsea permafrost, and in turn is affected by its degradation. A feedback mechanism exists by subsidence of near-shore ocean bottom due to ice-rich sediment thaw, possibly increasing erosion rates. However, the degree of this effect remains conjectural [Arctic Climate Impact Assessment (ACIA), 2004]. Due to the interaction of these processes, the transition of terrestrial to subsea permafrost remains poorly understood and with it its implications for degradation rates on the Arctic shelves.

After inundation, the state of permafrost is primarily controlled by the diffusive heat transport in the sediment under the influence of the sea-bottom temperature. In general, degradation occurs due to the large shift in surface temperature. While terrestrial surface temperatures have warmed only by 6–7 °C since the Last Glacial Maximum, inundation by sea water is up to 17 °C warmer than mean annual air/ground temperatures at that time [Frenzel et al., 1992, Nicolsky and Shakhova, 2010]. As the surface temperature is shifted from the old position, geothermal heat flux into the permafrost at the bottom is no longer balanced by the heat flux out of the permafrost surface with its changed temperature gradient. Consequently, a shift to the new mean equilibrium condition is set in motion, and warming of the permafrost throughout its depth profile as well as slow upward movement of the bottom permafrost table will occur. Thus degradation (decrease of permafrost thickness) from the bottom up commences after inundation. Degraded through-going taliks can form at places with thin initial thickness, rather by upward degradation in areas of higher geothermal flux taking advantage of the already raised base of permafrost [Romanovskii and Hubberten, 2001], or more by downward degradation taking advantage of pre-formed taliks below thaw lakes in the pre-inundated landscape [Overduin et al., 2007b, Nicolsky and Shakhova, 2010]. Permafrost may actively re-form in a narrow zone where the sea is shallow enough to permit bottom-fast sea ice formation, where sediment refreezing by cold winter air temperatures is possible [Arctic Climate Impact Assessment (ACIA), 2004]. The other major degradation

mechanism is downward degradation of the ice-bearing permafrost from saline pore waters. The marine processes directly affect the mechanisms of salt transport, and complicate a simple diffusional regime. Potential transport processes include density-driven convection by thawed lighter freshwater pore ice at the permafrost table, near-bottom currents or reciprocating wave movement in the water column that hydraulically initiates pore water movement, injected saline brines during bottom-fast sea ice adfreezing, and wave or storm perturbation of the fine-grained upper portion of the sea bottom sediments that leads to thorough mixing with sea water in the pore space. Their implementation in numerical models is particularly difficult as these processes are not necessarily quantitatively studied and – with the exception of convection – no mathematical development exists [Are, 2003]. Accounting for salt transport processes beyond diffusion in modelling efforts has been primarily limited to gravity-driven convection (see Sect. 3.1). However, this has been shown not to account for all observations [Swift and Harrison, 1984], emphasizing the relevance of the other processes potentially influencing pore water velocity and solute distribution in the sediments.

During the transition from terrestrial to subsea, five zones can be classified based on the dominating marine influence [Osterkamp, 2001]. These are depicted in Fig. 1.7. Zone 1 represents the initial terrestrial onshore permafrost. Zone 2 consists of the beach with its intertidal environment. Here, infiltration of sea water leads to

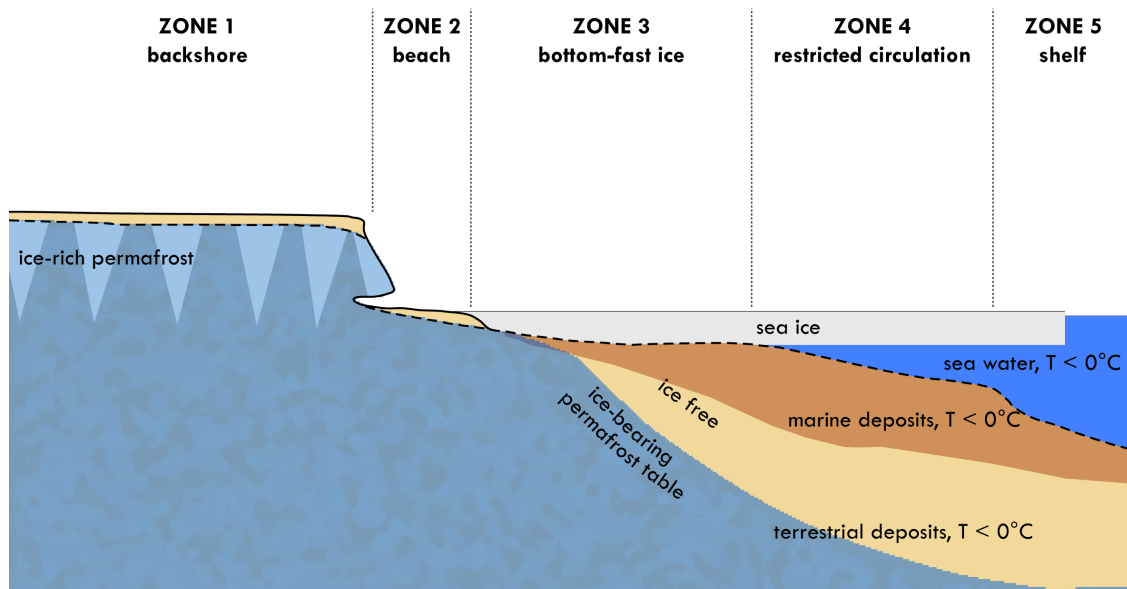


Figure 1.7: Schematic representation of the transition from onshore to subsea permafrost. Five different regions are illustrated with potential differences in the dominance of active marine processes. Graph adapted from [Osterkamp, 2001].

significant salt concentrations e.g. in the active layer. Zone 3 is characterized by the occurrence of seasonal bottom-fast sea ice cover. This allows conductive coupling of cold aerial winter temperatures to the seabed, while salt rejection during sea ice formation and restricted circulation lead to high salt concentrations, and brines can infiltrate the sediment during bottom-adfreezing. In summer, the shallow water temperatures remain relatively warm. Thus seasonality prevails. This zone extends to water depths of approximately 1.5–2 m. Seaward, zone 4 constitutes the area of water depths deep enough to prevent bottom-fast sea ice, but shallow enough to restrict circulation. Higher salinities and lower water temperatures occur in winter. Finally, zone 5 comprises ‘normal’ sea water with unaltered salinity and sea-bottom temperatures. This results in a practically constant regime in the upper forcing boundary for the subsea sediments. On the Arctic shelves, salinities of 30 – 34 and sea-bottom temperatures of -1.5 – -1.8 °C prevail [Arctic Climate Impact Assessment (ACIA), 2004].

1.2 Hypotheses and objectives

The overarching goal of this thesis is to advance our understanding of the processes driving the degradation of permafrost in the marine environment. This includes new observations, which are key to constraining modelling of subsea permafrost. A detailed assessment of the controlling processes through improved observational methods and modelling advances will shed light onto the degradation dynamics, which determine the spatial distribution and state of permafrost. This information is fundamental to our ability to predict the impact of subsea permafrost in the course of currently observed Arctic and global climate change.

Three key areas are defined for this thesis:

I Sparsity of observational data on the Arctic shelves. Observational data are limited by the remote character of the study region, and difficulty in obtaining permissions for geophysical exploration. Proposals for large scale and deep drilling projects are complicated by the shallow and intermediate character of the area: Shallow water prevents the use of large research vessels, especially in the near-shore zone. Sea ice formation, movement and breakup prevent year-round installation of instruments and make work impossible for key periods. Thus, it is recognized that a lack of areas with sufficient information and observational measurements to fully test model predictions exists [Osterkamp, 2001].

II Mechanisms of salt infiltration in the interstitial pore water. A multitude of processes act upon the permafrost once it is submerged or beginning to be submerged. Infiltrating saline pore water is the main mechanism for downward degradation of ice-bearing permafrost. Salt transport within the sediment is driven by a complex suite of potential processes, as discussed in Sect. 1.1.4, but quantitative mathematical development is lacking [Are, 2003]. Capturing the infiltration mechanisms of salt in mathematical models of mass transfer coupled with subsea permafrost dynamics is therefore missing beyond the diffusive transport mechanism and some gravity-driven convection studies. Realistic salt transport must be incorporated in model calculations to assess the relative impact of the various individual processes from these complex environmental interactions.

III Poor understanding of permafrost state and its spatial variability prior to inundation. Pre-inundation conditions range from cold deep to warm shallow terrestrial permafrost. Sediment composition varies from ice-rich fine and coarse grained sediments to hard rock. The local surface air temperature history of the site or of the region primarily determines the initial temperature profile, the initial permafrost thickness, and the development of surface degradation features on the coastal plain such as thermokarst, thaw lakes and taliks. All of these would affect the subsequent degradation of subsea

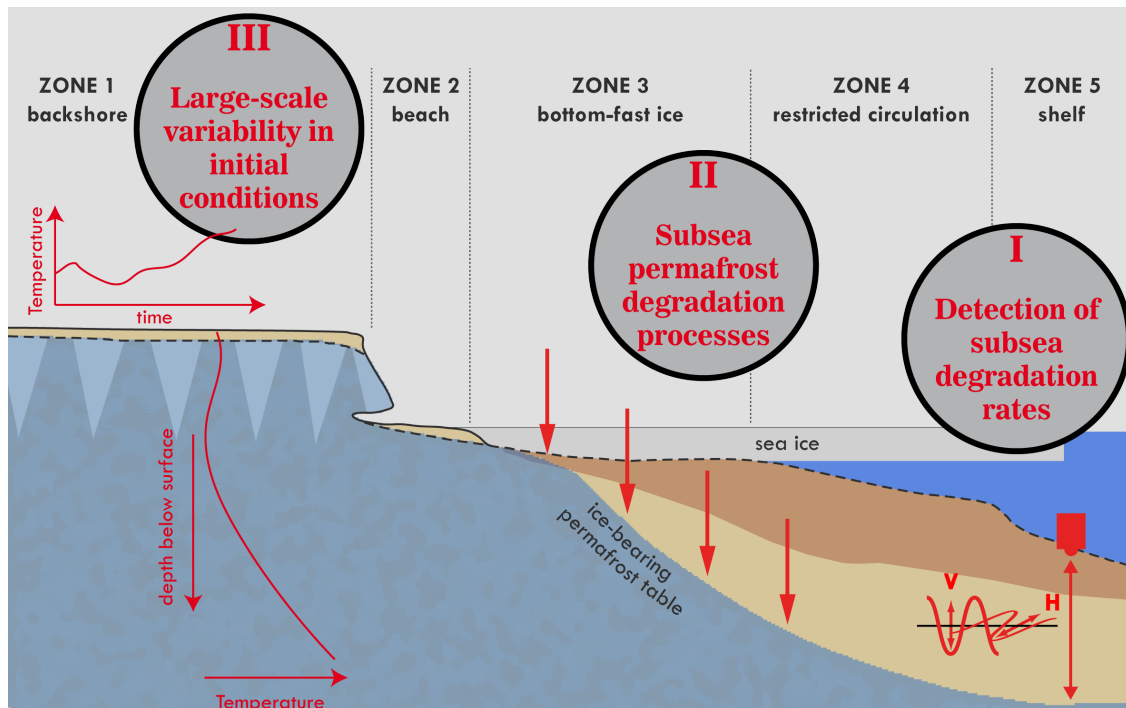


Figure 1.8: Diagram highlighting the defined key areas in this thesis in the context of the schematic transition from onshore to subsea permafrost.

permafrost [Overduin et al., 2007b]. The local climate history also directly influences subsea permafrost in zones 2–3. For assessment of processes on the local scale, knowledge of the local temperature history is a prerequisite, and provides the correct local parameterization of temperature forcing input. At a larger scale (regional and circum-Arctic), information on the spatial variability in temperature history will provide the basis for inference of subsea permafrost distribution. In the Arctic, however, temperature observations are sparse. Although strong regional and local scale variability in the climate system have been found to exist in Siberia [Pollack et al., 2003, Opel et al., 2013], local temperature histories in the ice-rich permafrost areas of the remote Russian Arctic are sparse or based on proxy data with potential seasonal biases and underrepresented in circum-Arctic reconstructions [McKay and Kaufman, 2014].

This thesis aims to combine new geophysical, borehole observational and modelling approaches to enhance our understanding of subsea permafrost dynamics. More specifically, this thesis is based on the following hypotheses and objectives, related to the current limitations in each area:

H 1 Ambient noise beneath the seabed contains information on thaw depths.

To test this hypothesis, the following objectives are performed:

- Development and feasibility test of a new geophysical technique to infer the thaw depth in Arctic shelf sediments from the ambient noise wavefield by combining two passive seismic methods, H/V spectra and seismic interferometry techniques.
- Inference of the depth of degraded, unfrozen sediments beneath the seabed around Muostakh Island, an actively eroding island in the central Laptev Sea, with point validation to the available observational data at this site.

H 2 Coupling heat and mass transport in a model of subsea permafrost improves representation of permafrost degradation compared to a model of conductive heat flow only.

The objectives to test this hypothesis are:

- Development of a numerical model for subsea permafrost evolution coupling heat transport and salt effects.

- Numerical assessment of the relative impact of the inundation processes on degradation depths, rates and salt distribution in a model of reduced complexity. Tested parameters include initial temperatures, sea bottom temperatures, cliff erosion, and coastline retreat rates. Modelling is constrained by borehole data from the COAST drilling transect and geophysical data. A focus is set on four processes potentially affecting the salt transport in the offshore sediments. The processes include (i) purely diffusive regime, (ii) advective component (as posed by e.g. buoyancy-driven convection), (iii) sediment porosity, and (iv) the presence of prior saline layers.

H 3 Past temperature histories recoverable from the subsurface temperature field reflect regional differences.

This hypothesis is tested by:

- Reconstruction of well-resolved local temperature histories for the past few hundred years in our Laptev Sea study region using shallow terrestrial (100 and 65 m deep) permafrost borehole temperature records.
- Evaluation of the spatial variability in temperature history in the Laptev Sea by comparing the temperature reconstructions to larger-scale reconstructions from the region.

1.3 Thesis organization

This thesis consists of five chapters. The introductory part (Chapter 1) provides the scientific background, relevance and definitions concerning the distribution of subsea permafrost and its degradation.

Chapters 2–4 address the three hypotheses and include material that has been published elsewhere. The results of Chapter 2 are published in *Geophysical Research Letters* (Overduin et al., 2015). The results of Chapter 4 are published in *Arktos* (Kneier et al., 2018). Chapter 5 summarizes the main conclusions and implications and identifies further research needs.

CHAPTER 2

Detection of subsea permafrost degradation rates

While boreholes are the most direct means to observe permafrost in the subsurface, and can yield the most complete data set on underground sediment properties, they are time-consuming and costly. Thus, they are sparsely available on the scale of the pan-Arctic shelves. Furthermore, they are destructive and only provide point samples, which make inference to lateral distribution presumptuous, and especially unreliable in areas of high variability.

Geophysical detection techniques provide a valuable, alternative data acquisition method to densely spaced borehole observations every few meters or centimeters. In geophysical surveys, observations can be extended to gain a spatially much wider set of observational data on a subsurface feature such as permafrost. Optimally, this is done from ground-truth-validated points for best mapping of the feature, depending on the specific method. Typically, a much larger area can then be studied with none or only few necessary ground truth boreholes, thus rendering it a highly efficient way of gaining observations on large spatial scales of the otherwise not easily-accessible subsurface.

In order for geophysical detection to work, a contrast in a physically measurable quantity must exist that distinguishes the phenomenon of interest and a geophysical technique must be available that is sensitive to this parameter. In the context of subsea permafrost, pore space ice and the contrast given by the change from liquid pore water to frozen interstitial ice in the permafrost sediments provides such a parameter. Ice and water have very different physical properties, such as greatly differing heat capacity, thermal conductivity, seismic wave velocity, electrical resistivity and dielectric constant (Table 2.1), which can subsequently be exploited by geophysical observation techniques. Typical threshold values indicative of permafrost in porous sediments are given in the description of the specific methods (Sect. 2.1). This detection definition is formally at odds with the definition of permafrost by

temperature alone. However, this practical application (distinction by ice content) is in fact very well suited to the needs in subsea permafrost studies (see Sect. 1.1.3). Lastly, the geophysical method should not be negatively impacted by the specific environmental conditions. For subsea permafrost studies, this means it may not be hindered by either the overlying salty sea water and saline sediments with associated electrical conductivity or other features simultaneously present in the ground such as wave reflecting gas bubble interfaces. This puts an additional limitation on employable methods and reduces the number from those that may be generally suitable for terrestrial permafrost detection. Ground-penetrating radar (GPR) is the most prominent of such techniques, as the high conductivity of salt water attenuates the GPR signal, strongly reduces the penetration depth, and the probing waves are not able to penetrate the saline sea bottom and much less the water when applied from the sea surface.

Table 2.1: Physical properties of liquid water and ice [Hauck and Kneisel, 2008].

property	liquid water	ice
heat capacity	4180 J kg ⁻¹ K ⁻¹	2100 J kg ⁻¹ K ⁻¹
thermal conductivity	0.56 W m ⁻¹ K ⁻¹	2.24 W m ⁻¹ K ⁻¹
electric resistivity	10 ¹ –10 ² Ω m	10 ⁴ –10 ⁸ Ω m
dielectric constant	81	3
P-wave velocity	1.5 km s ⁻¹	3–4 km s ⁻¹

In this chapter, after a short overview of geophysical detection methods used in subsea permafrost studies and their limitations (Sect. 2.1), the ambient noise field and passive seismic methods are introduced (Sect. 2.3). Testing the instrument design in marine underwater conditions on Sylt (Sect. 2.4) provides the basis for the following feasibility test at the Arctic site of Muostakh Island (Sect. 2.5) and the final wider array geometry of data acquisition (Sect. 2.6).

2.1 An overview of geophysical methods and studies in subsea permafrost

Several geophysical methods are sensitive to a contrast in unfrozen to ice-bearing sediment, and have been employed in subsea permafrost detection studies. These include direct current resistivity tomography (geoelectric method), active — reflective and refractive — seismic methods (active seismics), and electromagnetic sounding (EM method).

Overduin et al. [2012] demonstrate the suitability of direct current electrical resistivity for the detection of ice-bearing subsea permafrost in a lagoon in the Alaskan Beaufort Sea. This allows them to estimate vertical permafrost degradation rates of 1–4 cm yr⁻¹. The principle of the geoelectrical method (Fig. 2.1) is to inject a direct electrical current I into the ground via two current electrodes, measuring the resulting voltage difference ΔV at two potential electrodes, and obtaining the apparent resistivity by $\rho_a = K \cdot \frac{\Delta V}{I}$, where K is a geometric factor depending on the arrangement of the four electrodes [Hauck and Kneisel, 2008]. The injected current in the ground penetrates to deeper depth with increasing distance of the current electrodes A and B. Varying electrode spacings thus yields more information about the deeper part of the subsurface, while the maximum penetration depth is consequently limited by the maximum electrode spacing. The obtained resistivity is only the true resistivity of the subsurface for a homogeneous underground. In heterogeneous conditions it is the resulting quantity from the true resistivity distribution which is effectively penetrated in the associated electrode geometry. Using inversion methods the true resistivity distribution can be derived, yielding a 2-D model along a profile line (electrical resistivity tomography). In the Alaskan study, a floating electrode streamer was towed behind a small boat, and contained the electrical current injection dipole and an electrode array to measure the voltages for different electrode pairings. Consequently, the apparent resistivity was determined from each of the measured electrode pair potentials. Inversion of the apparent resistivity data at the surface to a sub-ocean bottom distribution of resistivity was performed for transects perpendicular and parallel to the shoreline. Laboratory experiments on retrieved sediment samples yielded electrical resistivities between 0.8–1.7 Ω m for unfrozen samples, and increasing resistivity with decreasing temperature (increasingly higher ice content), to values between 8–30 Ω m at -15 °C [Overduin et al., 2012]. A threshold of 10–20 Ω m was used to delineate the position of the ice-bearing permafrost table (Fig. 2.1). An advantage of the geoelectrical method is a good electrode-subsurface electrical contact in the marine environment that is not always given in its terrestrial usage. The inversion is however not unique, but intersecting profiles can be used to test independent data inversions. Water waves can further introduce noise into the resistivity data. Additionally, the depth range of detection is limited for small boats and streamers. Permafrost depths could only be captured to approximately 12 m below sea level with the 60 m array, limiting the employability to the very near-shore zone within the approximately 2 m isobath at the Alaskan site.

Seismic detection methods are based on the sharp increase of seismic wave velocities from unfrozen to frozen material. Typical P-wave velocities in the onshore unfrozen active layer (400–1500 m s⁻¹) contrast well those in the permafrost body (2000–

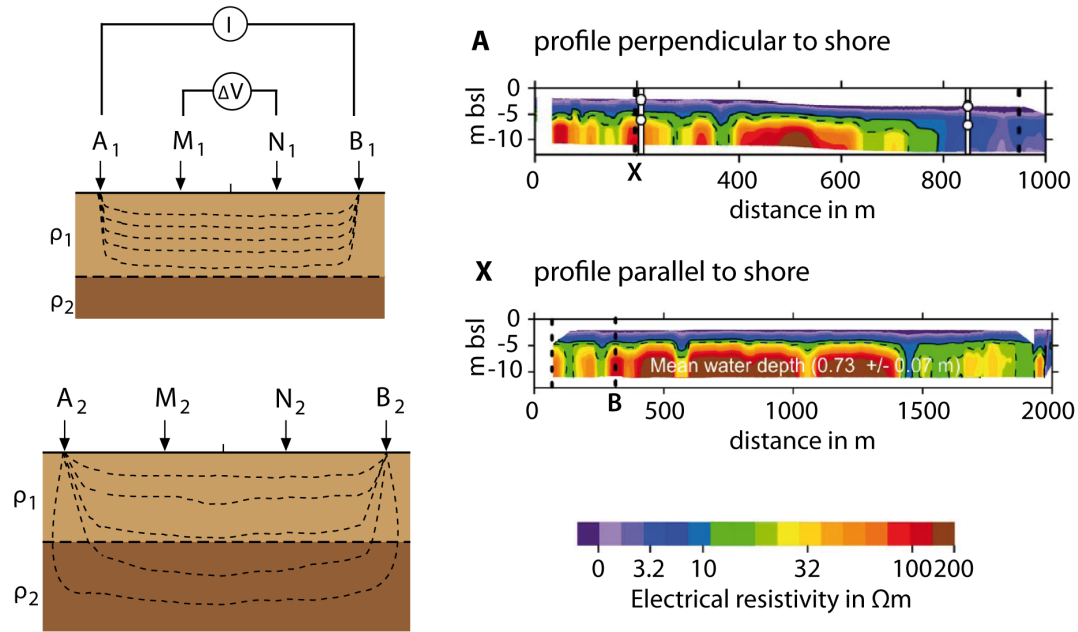


Figure 2.1: Geoelectrical resistivity tomography: **(left)** Schematic four-electrode configuration in resistivity measurements, with narrower (top) and wider (bottom) injection electrode spacing [Hauck and Kneisel, 2008]. **(right)** Inverse models of subbottom electrical resistivity for two transects at Elson Lagoon, Alaska. Dashed lines indicate intersections between transects [Overduin et al., 2012]).

4000 m s^{-1}) [Kneisel et al., 2008]. The wave propagation and velocities of seismic phases in the layered subsurface is determined by the detection of reflected and refracted waves at the interfaces. At such an interface, part of the seismic wave energy is reflected back to the surface while some energy is refracted into the underlying medium/layer. The seismic reflection method is based on the reflected waves recorded at geophones at the surface – spatially relatively close to the seismic source. They are suitable for great investigation depths, such as for detection of the permafrost base beneath the sea or lakes [Schwamborn et al., 2002]. The seismic refraction method is based on critically refracted waves. According to Snell's law ($\sin \theta_{\text{incident}} / \sin \theta_{\text{refracted}} = v_1 / v_2$), where the angles of incidence and refraction depend on the ratio of the seismic velocities of the upper (v_1) and lower (v_2) layers, critical refraction describes a certain angle $\theta_{\text{incident}} = \theta_{\text{crit}}$ that results in $\theta_{\text{refracted}} = 90^\circ$ (see Fig. 2.2). As rays are refracted away from a perpendicular to the interface only for $v_2 > v_1$, an increasing seismic velocity with depth is a prerequisite for the refraction seismic method, and typically given in subsea permafrost environments with a degraded/thawed layer on top of a relict frozen permafrost body. Then, the refracted wave travels parallel to or at the interface with the faster velocity of the lower layer. It produces oscillation stresses which in turn generate upward-travelling, so-called head waves, which are recorded by geophone arrays at the surface

— typically at larger spatial distances [Hauck and Kneisel, 2008]. The travel times of reflected and refracted waves result in recordings of specific time-distance plots which allow analysis of velocities and layer depths. The vertical resolution of seismic waves depends on the wavelength λ in the different media $\lambda = v/f$, where v is the propagation velocity of the wavelet and f the transmitted frequency. The theoretical vertical resolution is about one-quarter of the wavelength in the different media [Sheriff and Geldart, 1995].

Brothers et al. [2012] use a seismic-refraction-velocity-based method to map the conservative minimal distribution of subsea permafrost along intersecting profiles along the US Beaufort Sea shelf and employ seismic reflection analysis across the inferred seaward permafrost boundary as further constraint. In their study area, unfrozen coarse-grained sediments have velocities of 1700–1900 m s⁻¹ while ice-bonded coarse grained sediments range between 2300–5000 m s⁻¹ [Hunter et al., 1978, Morack and Rogers, 1984, Neave and Sellman, 1982, Rogers and Morack, 1980, Timur, 1968, Zimmerman and King, 1986]. They consequently interpret P-wave velocities ≥ 2.3 km s⁻¹ as permafrost layer refractions (Fig. 2.2). They can detect coarse-grained ice-bonded layers larger than 10 m thick (based on the quarter wavelength criteria). A disadvantage of refraction seismics is that it typically only resolves layers of increasing velocity with depth and may miss interbeddings with decreased seismic velocity or interbedded thin layers. Furthermore, fine-grained frozen sediments are undetectable due to lower seismic velocities, that are ambiguous to some unfrozen sediments [King and Hunter, 1982, Morack and Rogers, 1984]. This makes it impossible to definitely resolve the top of ice-bearing permafrost, if such complex deposits are present, but instead infers the minimum extent on the shelf. Also, data collected in the shallow water depths of the near-shore zone have poorer signal-to-noise ratios.

Brothers et al. [2016] employ the most spatially extensive and dense set of seismic reflection data on any Arctic shelf to date to determine the average velocities in an upper portion of the sediment column of approximately 600 m. This captures the full depth range over which onshore permafrost exists. From the velocity contours they map the minimal distribution of subsea permafrost on the entire US Beaufort Sea shelf in a 2 km grid resolution. They assume an average velocity of 2000 m s⁻¹ to represent the threshold from a sediment column containing continuous ice-bonded permafrost to unfrozen conditions. Again, ice-bonded permafrost may occur seaward of this line in discontinuous lenses below the resolution of either refraction or seismic velocity methods and in fine-grained lithologies.

Sub-bottom profilers (or sediment echo sounders) are another technique, also part of the field of high-resolution reflection seismics. Here, the superposition of two higher-

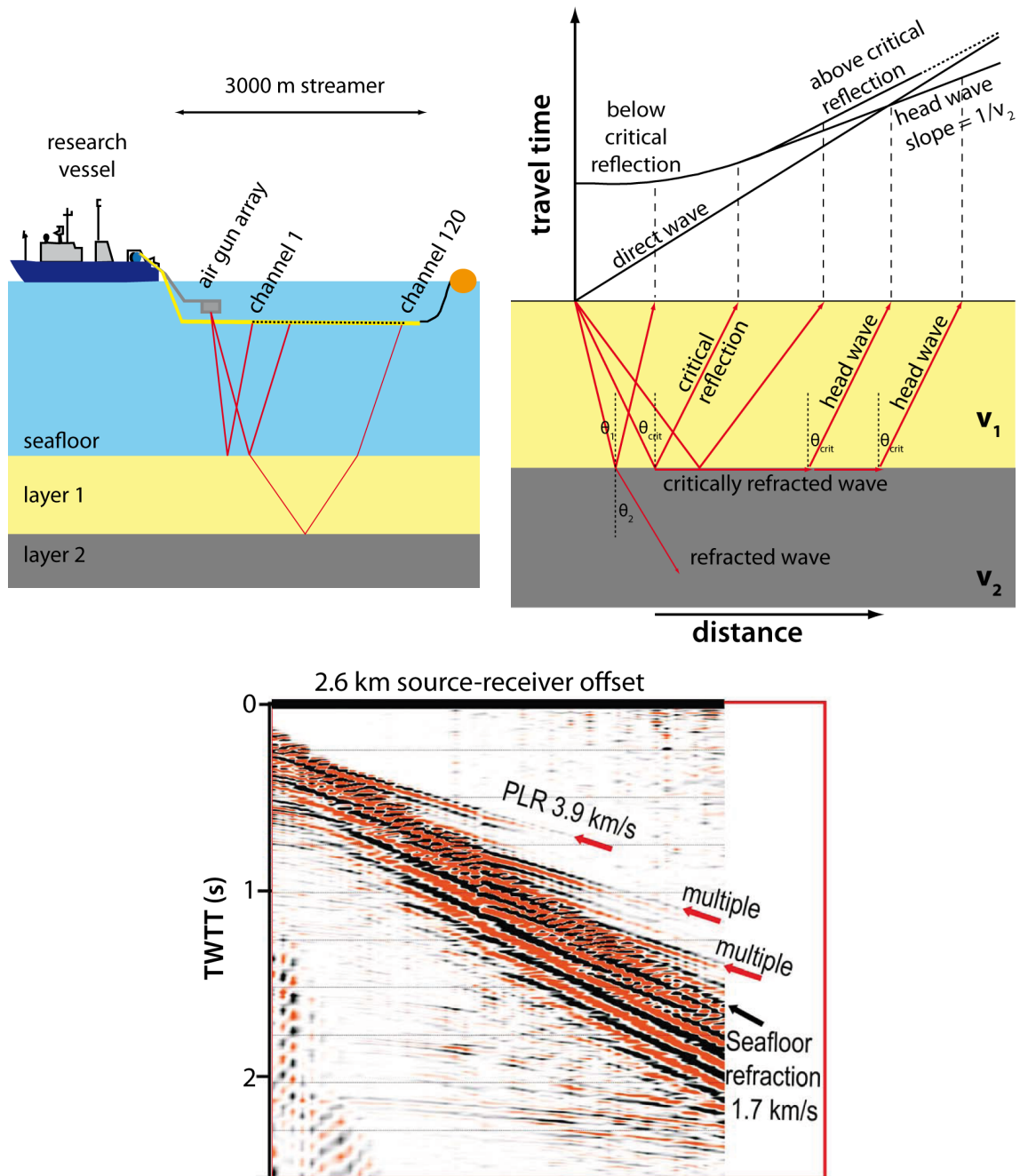


Figure 2.2: Seismic method: **(left)** Schematic standard configuration for reflection-seismic data acquisition: A research vessel tows an air gun array as the active source. Hydrophones in the streamer record the reflected seismic waves. **(right)** Raypath geometries and time-distance plot for the horizontal two-layer case (after Gebrande and Miller [1985]). **(bottom)** Seismic record plotted with hydrophone traces of two-way-travel-time (TWTT) as a function of distance along the streamer. The slope of the first arrivals gives the velocity and a permafrost layer refraction (PLR) and its two multiples are visible above the background seafloor refraction [Brothers et al., 2012].

frequency acoustic waves achieves a lower frequency beam with larger penetration depth and narrower irradiation aperture to probe the upper section of the sub-sea floor sediments. The PARASOUND system on the RV 'Polarstern' has been employed to observe subsea permafrost on the offshore shelf of the Laptev Sea [Fütterer and Niessen, 2004, Niessen, 2004, Rachor, 1997]. Their system consists of two 18 and 22 kHz sources with a superposition difference signal of 4 kHz. Lateral and vertical resolution is high, with a beam aperture of 4° . This yields a beam area on the sea floor of about 7% of the water depth, over which the echo signal is integrated. The 22 kHz beam can be used to determine water depth, while the lower frequency, 4 kHz beam has a penetration depth of up to 100 m into the sea-bottom depending on sediment composition [Bergmann, 1996]. An advantage of this method is the vertical resolution on the cm-scale, but high sea states frequently decrease this to just about sub-1m resolution [Portnov et al., 2013]. A disadvantage is that such systems are usually installed on larger research vessels, which are difficult to impossible to operate in more shallow shelf waters. The system also requires higher water depths because of the mechanism of beam generation by the interference technique and the involved non-linear effects after emission of the primary frequency beams. It is thus not especially suited to the very shallow near-shore transition zone.

Other shallow seismic and echo sounder studies include the observation of a strong reflective sequence indicative for permafrost in a study area on the mid- and outer Laptev Sea shelf [Hinz et al., 1998]. Rekant et al. [2015] use the high resolution seismic data collected from several previous expeditions to verify and extrapolate subsea permafrost over a larger area of the eastern Laptev Sea shelf. A prominent basal reflector is interpreted as a top of acoustically identified permafrost and the reflector is found to bear resemblance to present-day onshore thermokarst terrain.

Both reflection techniques are very sensitive to gas or air bubbles as these absorb acoustic energy and have large acoustic impedance. In subsea permafrost areas, the presence of gas bubbles in the ground and above is a factor in impeding seismic reflective and echosounder activities. For circumstances of massive sea bed methane escape into the water column, this effect itself has even been used to infer permafrost decay [Portnov et al., 2013]. In general, however, zones of acoustic transparency, i.e. where seismic energy is not coherently reflected back to the receiver, are of ambiguous nature and may be produced by the presence of gas and its absorption of acoustic energy, by an uneven distribution of gas accumulations and associated scattering, by ice-bearing sediments, calcium carbonate, or stratal disruptions from intense fluid flux [Portnov et al., 2013, Wood et al., 2002]. Thus, direct observations in a study area are required to verify the combination of these phenomena that is in fact present in the ground.

There is also a noteworthy, fundamental difference between conductivity- and seismic velocity-based methods with respect to the sensitivity to the underlying physical mechanisms. While electrical conduction occurs in the unfrozen fraction of the ground volume, seismic wave energy is transmitted mainly through the solid matrix. Therefore seismic velocity reaches a plateau at some point during freezing at which point velocity is nearly insensitive to a change in the already small unfrozen water content. Conversely, electrical resistivity continues to increase even when pore spaces are almost filled with ice [Kneisel et al., 2008].

Lastly, electromagnetic (EM) methods represent a variation of electrical conductivity/ resistivity methods. Instead of direct injection of current through electrodes as in the geoelectric method, EM techniques utilize electromagnetic fields from a transmitter loop which induce currents in the subsurface. These currents depend on the distribution of conductivity underground and generate associated secondary EM fields in turn. Sensing of these secondary fields with a second receiver loop antenna at the surface allows inference to the distribution of subsurface resistivities. Analysis can be performed in the time or frequency domain by either decay (time) curves or discrete frequency spectra. Different depths can be sampled by varying the sender-receiver properties, i.e. signal wave form, frequency spectrum and relative antenna geometries. In time-domain EM, the depth of the input electromagnetic field distribution depends on frequency, and electrical resistivities at different depth can be estimated using measurements at several frequencies. For a single frequency, the decay curve as a function of time after transmitter current shut-off is a measure of the response of the subsurface as a function of depths, too, as later responses originate from greater depths. Again, ambiguity in the interpretation due to overlapping electrical conductivity ranges for different rock, sediment types and water saturation levels must be carefully taken into account. Koshurnikov et al. [2016] apply and confirm the usability of a time-domain EM sounding technique for mapping subsea permafrost from the sea ice surface during winter/spring. They use two loop geometries sensitive to the upper 100 m and, approximately, 1 km, respectively. Analysis of the curves document apparent resistivities of a broadly 3-layer system of low, high and low values. Observation and numerical simulation yield a geoelectric model of true resistivities in a simple horizontally bedded medium model with $3.8 \Omega \text{ m}$ in the thawed upper 25 m and $300 \Omega \text{ m}$ in a 600 m thick permafrost layer below. Due to ambiguous effective resistivities, the high resistivity in the middle layer could be due to permafrost, but may also be controlled by gas hydrates, gases, bedrock or a combination thereof. Therefore, validation from drilling was required to confirm the high resistivity value below 25 m in laboratory measurements on the core samples and that it originated from ice-bonded conditions. Also, measurements are limited

to winter and spring sea ice conditions, which might differ from summer thaw depths in zones 3 and 4 (see Sect. 1.1.4) during the transition.

2.2 Geophysical objectives

Observations of ice-bearing permafrost in Arctic shelf sediments are necessary to determine its spatial distribution, to quantify its degradation rates [Overduin et al., 2012] and to help constrain modelling of the system-driving processes. The combination of detected thaw depths with coastal retreat rates can yield mean vertical permafrost degradation rates. Furthermore, larger-scale mapping of the ice-bearing permafrost can give insight about past impacts of warming since the Late Pleistocene and provide a baseline for quantifying the future effect of thawing during projected 21st century climate warming [Brothers et al., 2012]. Seismic methods have proven as a most suitable method for large-scale surveys. However, the use of active seismic sources in the Arctic Seas territories is often prohibited because these may disrupt marine fauna or are related to resource exploration. Access to the shallow near-shore zone is also restricted for the large research vessels. For this situation, ambient seismic noise as source and related passive seismic analysis techniques could form a suitable alternative approach.

The objectives of this chapter are to

- (i) develop and test the feasibility of a passive seismic approach to detect the thickness of unfrozen sediment overlying ice-bonded permafrost. For this, observations of the ambient noise wavefield at the seabed are analyzed by combining the spectral ratio of the average horizontal and vertical ground motion (H/V method) with seismic interferometry techniques.
- (ii) infer the depth of degraded, unfrozen sediments, i.e. the depth of the transition from ice-free to ice-bonded permafrost, beneath the seabed around Muostakh Island. This actively eroding island in the central Laptev Sea allows for point validation with other available observational data at this site.

2.3 Passive seismic techniques

Ambient vibration techniques are very cost-effective and environmentally friendly observation methods compared to classical (active) geophysical site investigations [Bard and SESAME participants, 2004]. A set of stations is set out and deployed

to record the ambient noise wave field over a period of time, and given certain conditions, subsequent analysis allows the retrieval of geophysical information on the ground similar to active seismic exploration.

Seismic ambient noise denotes ambient vibrations of the ground that are always present in measurements and typically form the noise background in active seismic signal processing. Its sources include tides, ocean waves breaking at the coast, wind and its effect on structures connected with the ground such as trees and buildings, industrial operations, modern infrastructure such as cars and trains, and even movement of wildlife or humans or multiply scattered remnants of earthquakes or volcanic tremors, to name only a few. Studies on the nature of the wavefield are few and in stark contrast to the number of those concerned with its application [Bonney-Claudet et al., 2006b]. The origin of the noise can be classified in two categories, natural and cultural sources, which differ in their frequency content. They are generally denoted with microseism and microtremors, respectively, though this terminology is not strictly adhered to in the literature and both often mean the same thing in recent works. Microseism energy is consistently correlated with oceanic and generally large-scale meteorological activities, while shorter-period microtremor noise is clearly correlated to cultural activities. The frequency characteristics are related to the respective origin, with low frequency microseism and higher frequency microtremors, and a roughly estimated boundary of 1 Hz between them. Investigation of the composition of the ambient wavefield, however, remains inconclusive concerning generally applicable results due to a scarcity of data, which is surprising considering the wide application based upon it [Bonney-Claudet et al., 2006b]. Thus, no general assumption can be made for the relative contributions of body and surface waves, the proportion between Rayleigh and Love waves within the surface waves, nor the contribution of fundamental and higher modes. Microseism is reported to consist mainly of fundamental mode Rayleigh waves [Li et al., 1984, Horike, 1985, Yamanaka et al., 1994], but at higher frequencies (> 1 Hz) a mix of body and surface waves of different modes may occur, and may strongly depend on soil and source properties and geometries. Bonney-Claudet et al. [2006a] conclude for a simple two-layer medium that if all source types and positions are considered, near-surface sources are dominant and that the vertical noise wavefield is composed predominantly of fundamental mode Rayleigh surface waves. The Love wave contribution to the noise is an area of ongoing research [Endrun, 2011], and is likely also high with at least 50% in both cultural and natural noise. In summary, the composition results seem to depend to a high degree on site geology and geometry (sediment thickness, slope, layer interfaces). Higher modes of Rayleigh waves and more complex subsurface heterogeneities as well as certain source geometries can contribute at

higher frequencies and therefore must be taken into account if interpreting, for example, the frequency range above the fundamental peak (e.g. second and third peaks) in the H/V method (Sect. 2.3.1).

Surface waves are therefore still widely expected to dominate the ambient noise wavefield (although that assumption cannot always be asserted). Another factor why surface waves dominate results from their geometrical spreading. While the amplitude of a body wave decreases with $1/r$ (the energy spreads over the surface of a sphere), the amplitude of surface waves decreases only with $1/\sqrt{r}$ (spreads over the circumference of a circle). Body waves have associated seismic velocities of v_p for the P-wave (the pressure wave with particle motion parallel to the direction of the wave propagation) and v_s for the shear waves SH and SV (particle displacement in a plane perpendicular to the wave direction, with either horizontal or vertical polarization). Surface waves exist on the 2-dimensional interface of the ground surface. Their amplitude decreases with increasing distance to this interface. The penetration depth depends on the frequency and they typically show dispersive behaviour, i.e. the phase velocity depends on their frequency as they are affected by the propagation velocity at different depths in layered media. Rayleigh waves are a surface wave type with particle motion in an elliptic rolling shape (ground roll, polarization of P and SV). Love waves on the other hand exhibit the transverse particle motion of SH waves parallel to the surface (as they are the interference of SH waves confined to a low-velocity surface layer). A third type are Scholte waves, which occur at an interface between a fluid and an elastic medium, thus they are the interface waves occurring along the sea bottom. The seismic velocity of these surface waves in a non-homogeneous medium is dispersive. For Rayleigh waves at the interface of air and an infinite halfspace and their counterpart of Scholte interface waves, their group and phase velocities are typically slightly smaller than the shear wave velocity v_s of the material., but the exact relationship depends upon factors such as frequency, the finite water depth, densities, and material seismic velocities. For high frequencies or large water depths, the relationship between both group and phase velocity of the interface wave to the shear wave velocity of the material can be described by a constant factor [Dong and Hovem, 2011].

Here, two passive seismic methods (H/V method and seismic interferometry) are combined to infer the thickness of the thawed Arctic shelf sediment above the relict permafrost from the ambient noise wavefield. Seismic interferometry techniques are used to obtain the shear wave velocity of the unfrozen layer, which is necessary to estimate the thickness from the peak frequency of the H/V spectra analysis. The respective techniques are detailed in the following two sections.

2.3.1 H/V passive seismics

The H/V method, which yields an estimation of the Fourier amplitude spectra of the horizontal to vertical components of the ambient noise vibrations recorded at one single station, has become a common observational tool in the context of shallow site assessment. The first work was introduced by Nogoshi and Igarashi [1971] and the technique was widely spread by Nakamura [1989]’s English publication, as typical measurement times at one single location in common terrestrial application are only on the order of 10 minutes [Endrun, 2011]. Since then, hundreds of scientific papers have been dedicated to the analysis, application, interpretation and theoretical background of this technique. It has been widely used from microzonation, i.e. the site-specific analysis of earthquake risks, to the planned operation in Mars landers for site exploration [Knapmeyer-Endrun et al., 2017, Panning et al., 2017].

H/V ratio as a function of frequency often show a clear maximum and this peak frequency f_0 is empirically found to correlate with the fundamental resonance frequency at the measurement site [Lachet and Bard, 1994, Lermo and Chavez-Garcia, 1994, Dravinski and G. Ding, 1996]. Theoretical considerations for a single lower-velocity layer on top of a halfspace [Malischewsky and Scherbaum, 2004] show that this correlation depends on the impedance contrast and is better for higher contrasts. Other applications, which aim to extract more information beyond peak frequencies from the H/V spectra (i.e. amplitudes and curve shapes), require a more rigorous understanding of the underlying origin of the H/V peak and the particular composition of the wavefield in each case. While Nakamura [2000] maintains that SH-wave resonance in the soft surface layer (multiple reflections in this surface layer) is the cause for the peak, interpretation has shifted in recent years and a growing number of authors agree that the curves correspond to the frequency-dependent ellipticity of Rayleigh waves [Lachet and Bard, 1994, Lermo and Chavez-Garcia, 1994, Yamanaka et al., 1994, Konno and Ohmachi, 1998, Fäh et al., 2001, Malischewsky and Scherbaum, 2004, Bonnefoy-Claudet et al., 2006a], and argue that the ambient wavefield is dominated by surface waves at least for frequencies above the fundamental resonance frequency of the sedimentary surface layer [Lunedei and Albarello, 2009]. For sources within the bedrock resonant S-waves in models have caused comparable H/V peaks, but have been reasoned to form only a negligible fraction of the ambient vibration wavefield [Bonnefoy-Claudet et al., 2006a]. Another contribution may come from Love waves, as the frequency of the Love wave Airy phase for sites with a moderate to strong impedance contrast in the 2-layer scenario is comparable to the peak frequency of the fundamental Rayleigh wave mode [Konno and Ohmachi, 1998, Bonnefoy-Claudet et al., 2008]. This would imply peak amplitude to greatly depend

on the relative content of Rayleigh and Love waves in the ambient wavefield [Endrun, 2011], but could also explain the observed temporal variations in measurements of H/V amplitudes [Panou et al., 2005, Endrun, 2011]. The SESAME (Site EffectS assessment using AMbient Excitations) project, a major undertaking to characterize local site effects based on ambient vibrations, also adopted this view of the multiple origin for the H/V peak: Rayleigh wave ellipticity, Airy phase of fundamental Love wave mode, and partly fundamental resonance of S body waves [Bard and SESAME participants, 2004]. Although it is widely accepted among authors that the microtremor H/V curves contain significant information about the subsurface site structure around the station, there is much debate on how to invert such data quantitatively for geophysical properties and site parameters based on the unknown composition of the ambient wavefield at each particular study site [Fäh et al., 2003, Scherbaum et al., 2003, Arai and Tokimatsu, 2004, Parolai et al., 2005, Picozzi et al., 2005, Köhler et al., 2007, Duceillier et al., 2013, Hobiger et al., 2013]. Based on theoretical considerations [Tuan et al., 2011] and numerical simulations [Lunedei and Albarello, 2010] the pattern of spectral H/V curves presents a complex relationship with subsoil features. With respect to simple stratigraphic configurations, however, the peak frequency yields a fair estimate of the fundamental resonance frequency of a site, which is directly linked to the thickness of the lower-velocity surface layer [Foti et al., 2011].

Best understood are simple one-dimensional, two-layer configurations with a dominant and sharp acoustic impedance contrast below a shallow surface layer at depth d [Malischewsky and Scherbaum, 2004, Bonnefoy-Claudet et al., 2006a, Tuan et al., 2008, Endrun, 2011, Sanchez-Sesma et al., 2011]. The degrading subsea permafrost, to a very good approximation, represents just such an environment with a low-velocity thawed thin surface layer above a relatively thick high-velocity frozen body. In such a setting and with the additional assumption that near-field source contributions are avoided [Chatelain et al., 2008, Lunedei and Albarello, 2010], the frequency f_0 of the fundamental peak in the H/V Fourier spectrum, i.e. the lowest dominant peak frequency, can be associated with the depth of the interface of impedance contrast and the average shear wave velocity of the overlying thawed sedimentary deposit. The correlation of f_0 to the fundamental seismic resonance frequency allows for this relationship. In this configuration, the peak frequency position is a stable feature regardless of the physical explanation of the peak origin (Rayleigh waves for high impedance contrast, S-wave resonance and/or Love waves for moderate to low contrast) or predominant wave types in the noise field [Bonnefoy-Claudet et al., 2006b], and deviations of the position to the resonance frequency are less than 15 % for impedance contrasts of 3.5 and higher [Malischewsky and Scherbaum, 2004,

Bonnefoy-Claudet et al., 2008]. The seismic resonance frequency (Fig. 2.3) of the n^{th} mode is related to the shear velocity v_s and thickness of the overlying layer d by

$$f_{\text{resonance},n} = (2n + 1) \cdot \frac{v_s}{4 \cdot d} \quad (2.1)$$

where f is given in Hz, the average shear wave velocity in m s^{-1} , and d in m [Lane et al., 2008, Ibs-von Seht and Wohlenberg, 1999]. The fundamental resonance frequency is given for $n = 0$, and estimated by the H/V peak frequency. If the average shear wave velocity for the upper layer is known, the depth of the impedance contrast, i.e. the transition to frozen permafrost conditions, can thus be calculated from Eq. 2.1. This method is therefore well suited to the subsea permafrost application despite the ongoing debate about origin and implications for more complicated conditions.

Beyond peak frequency retrieval, the spectral shapes in general may vary significantly in appearance based on the given composition of the observed wavefield as discussed above. Several studies have attempted a full inversion of H/V spectral curves by incorporating either different prior assumptions on wavefield composition or estimates of surface wave dispersion simultaneously recorded in small aperture arrays [Fäh et al., 2003, Arai and Tokimatsu, 2005, Parolai et al., 2005, Picozzi et al., 2005]. Sanchez-Sesma et al. [2011] recently considered all wavefield constituents without prior assumptions in the context of diffuse wavefield theory. First steps to employing this scheme to obtain inversions of subsurface velocity structures have been published

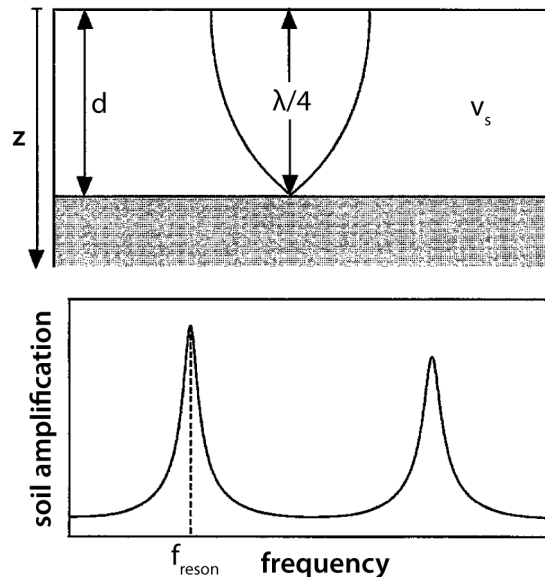


Figure 2.3: The site effect is given by a frequency response function. Resonant frequencies of a simple two-layer system occur for uneven multiples of $\lambda/4$. The frequency response function has maxima at these n^{th} mode resonance frequencies (Eq. 2.1). Graph taken from [Ibs-von Seht and Wohlenberg, 1999].

[Ducellier et al., 2013, Kawase et al., 2011] and may provide further options for analysis in the future.

2.3.2 Passive seismic interferometry

Seismic interferometry refers to the principle that by crosscorrelation (or convolution¹) of different seismic receiver observations, the Green's function, or impulse response, between these receivers can be obtained. The response retrieved by crosscorrelating two such receiver recordings and summing over different sources can therefore be interpreted as the response that would be observed at one of the receiver locations if the other one had been a source, and the method thus introduces so-called virtual sources. The technique is also called Green's function retrieval, synonymously, because such a response to a point source is described by the convolution of a Green's function — the impulse response of the ground — and a wavelet — the specific source signature. The term interferometry refers to its use in radio astronomy where it alludes to crosscorrelation methods. Seismic interferometry can be divided into two categories: passive and controlled-source seismic interferometry. The latter involves classic active exploration but with new processing methods, and was pioneered by Schuster [2001] and Bakulin and Calvert [2004]. Passive seismic interferometry uses the ambient noise wavefield. One advantage is that while the controlled-source method requires summation over various source positions, passive interferometry already yields a response based on a superposition of simultaneously acting uncorrelated sources in the ambient wavefield. This field is subdivided into retrieving surface wave transmission responses [Campillo and Paul, 2003, Shapiro and Campillo, 2004, Shapiro et al., 2005, Sabra et al., 2005a] and reflection responses [Claerbout, 1968, Scherbaum, 1987, Draganov et al., 2007, 2009], called direct-wave and reflected-wave interferometry respectively. Most of the research and application focus on the retrieval of surface waves. In this section, the idea behind passive seismic interferometry is presented, loosely following [Wapenaar et al., 2010a,b, Curtis et al., 2006]. The focus is put on the underlying principle which allows us to retrieve the shear wave velocity without the additional acquisition of independent data but rather from the same noise vibrations as the H/V ratio itself. More overviews of the seismic interferometry technique are provided by Wapenaar [2003], Schuster [2009, 2016], and Shapiro et al. [2005].

In a first step, it is instructive to consider a 1-dimensional configuration of an

¹ Because crosscorrelation is simply a convolution with the reverse of one of the signals, both operations could be equivalently used.

impulsive source's plane wave travelling from left to right (Fig. 2.4 a) in a lossless medium with constant propagation velocity c . Two receivers x_A and x_B record a response shown in Fig. 2.4 b&c. The Green's function $G(x_A, x_S, t)$, where the first argument denotes the receiver coordinate, the second denotes the source coordinate, and the last the time t , consists of an impulse at $t_A = \frac{(x_A - x_S)}{c}$. With the Dirac delta function, therefore

$$\begin{aligned} G(x_A, x_S, t) &= \delta(t - t_A) \\ G(x_B, x_S, t) &= \delta(t - t_B) \end{aligned}$$

Crosscorrelation of both responses is shown in Fig. 2.4 d. It yields only the traveltime from A to B , eliminating the common path from the source before A , hence an impulse at $t_B - t_A$. This impulse can be interpreted as the response observed at x_B to a source at x_A , i.e the Green's function $G(x_B, x_A, t)$. By dividing the receiver distance by the traveltime estimated from the Green's function, an estimate of the propagation velocity can be obtained. The position of the actual source or absolute time t_S need not be known.

Mathematically, the crosscorrelation of the impulse responses is denoted by $G(x_B, x_S, t) * G(x_A, x_S, -t) := \int G(x_B, x_S, t + t') G(x_A, x_S, t') dt'$, where asterisk denotes temporal convolution and the time reversal of one function yields a correlation. Substitution of the delta functions and integration does indeed yield $\delta(t - (t_B - t_A)) = \delta\left(t - \frac{x_B - x_A}{c}\right)$. This is the Green's function $G(x_B, x_A, t)$, for propagation from A to B . Thus we obtain for an impulse source:

$$G(x_B, x_A, t) = G(x_B, x_S, t) * G(x_A, x_S, -t) \quad (2.2)$$

The principle holds true if the source is not an impulse but an arbitrary wavelet $s(t)$. In this case, the responses at x_A and x_B are

$$\begin{aligned} u(x_A, x_S, t) &= G(x_A, x_S, t) * s(t) \\ u(x_B, x_S, t) &= G(x_B, x_S, t) * s(t) \end{aligned}$$

Crosscorrelation of both responses then gives the right-hand side of Eq. 2.2, convolved with $s(t) * s(-t) = S_S(t)$, the autocorrelation of the wavelet. Thus,

$$G(x_B, x_A, t) * S_S(t) = u(x_B, x_S, t) * u(x_A, x_S, -t) \quad (2.3)$$

In the case of an arbitrary wavelet as source function, the crosscorrelation of two receiver responses yields the Green's function between these receiver, convolved with

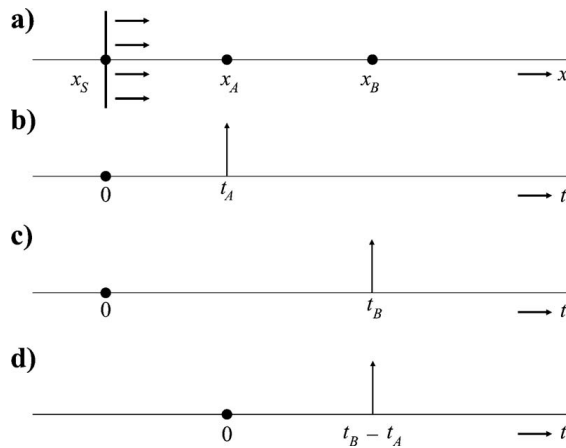


Figure 2.4: 1-dimensional schematic of direct-wave interferometry: (a) The plane wave of an impulsive source at x_S emitted rightward at $t = 0$. (b) The response recorded by receiver A at x_A (the Green's function $G(x_A, x_S, t)$). (c) The response for the receiver B at x_B . (d) The crosscorrelation of the two responses.

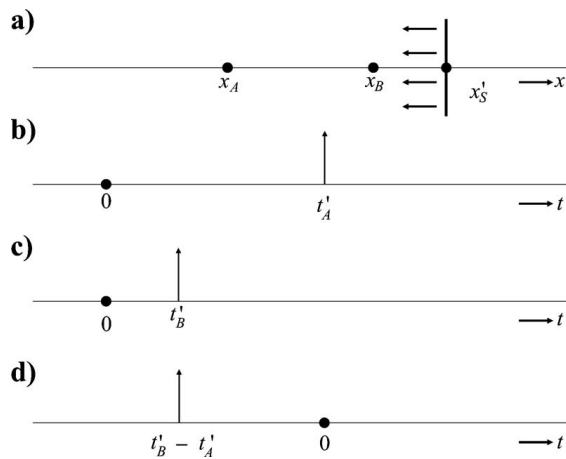


Figure 2.6: Configuration as in Fig. 2.4 but for a leftward-propagating impulsive plane wave. (b) and (c) are the respective responses for receivers at x_A and x_B again. The crosscorrelation (d) is interpreted as the time-reversed Green's function $G(x_B, x_A, -t)$.

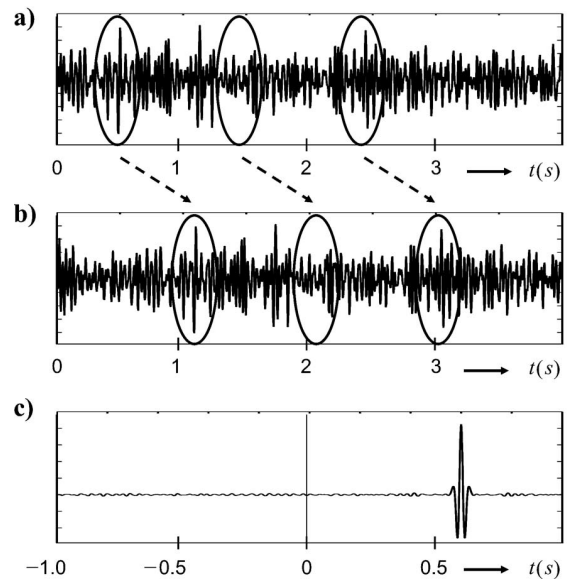


Figure 2.5: Configuration as in Fig. 2.4 but for a noise source situated at x_S : (a) The response recorded at receiver A ($u(x_A, x_S, t) = G(x_A, x_S, t) * N(t)$). (b) The response for receiver B . (c) The crosscorrelation of the two responses.

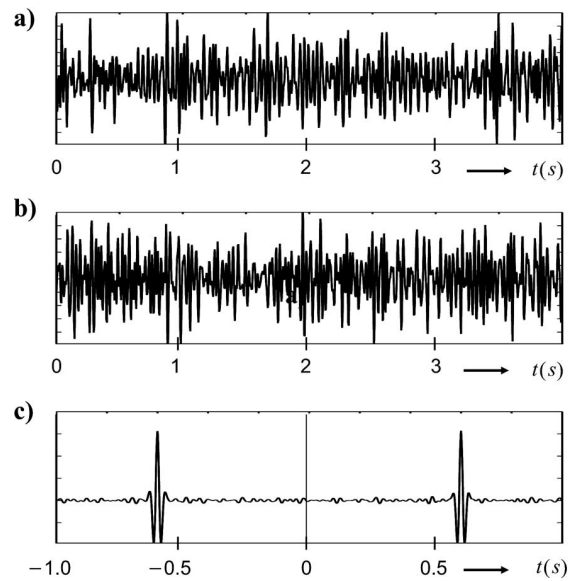


Figure 2.7: Configuration with two simultaneously acting noise sources at x_S and x'_S , emitting rightward- and leftward-propagating, uncorrelated noise fields respectively. The response recorded at x_A and x_B is given in (a) and (b). (c) shows the crosscorrelation which does not contain cross-terms.

the autocorrelation of the source wavelet. As the wavelet is arbitrary, this includes noise. Figure 2.5 shows the crosscorrelation of two responses to a bandlimited noise source $N(t)$. The result is, again, the impulse response between A and B , convolved with $S_N(t)$ and revealing a bandlimited impulse centered at the traveltime from A to B . The noise source itself need not be known to obtain a bandlimited version of the Green's function and estimate the propagation velocity.

In a second step, the source configuration is switched to x'_S to the right-hand side of the receivers and with a plane wave travelling from right to left (Fig. 2.6). Substitution of the delta functions in the crosscorrelation yields $G(x_B, x'_S, t) * G(x_A, x'_S, -t) = \delta(t - (t'_B - t'_A))$. With $t'_A = \frac{x'_S - x_A}{c}$ and t'_B analogously, this yields $\delta(t + \frac{x_B - x_A}{c})$, which is equal to the time-reversed Green's function $G(x_B, x_A, -t)$ with a response at the negative time axis. $G(x_B, x_A, t)$ is called the causal response of an impulse at $t = 0$, and since the causal and anticausal part are nonzero for $t > 0$ and $t < 0$ respectively, there is no overlap. Analog to above, the same derivation can be made if the source function is a wavelet $s(t)$. Then, depending on the length of the autocorrelation function, there may be some overlap for small $|t|$. Therefore, in a sum over the responses to all sources,

$$\{G(x_B, x_A, t) + G(x_B, x_A, -t)\} * S_S(t) = \sum_{i=1}^2 u(x_B, x_S^i, t) * u(x_A, x_S^i, -t) \quad (2.4)$$

the causal part $G(x_B, x_A, t) * S_S(t)$ can be extracted from the crosscorrelation response except for small distances $|x_B - x_A|$.

In controlled-source interferometry, the order of crosscorrelation and summation matters as cross-terms contribute to the crosscorrelation after summation, but for noise sources the situation is different. Two simultaneously acting noise sources $N_1(t)$ at x_S and $N_2(t)$ at x'_S yield responses at the receivers $u(x_A, t) = \sum_{i=1}^2 G(x_A, x_S^i, t) * N_i(t)$ and $u(x_B, t) = \sum_{j=1}^2 G(x_B, x_S^j, t) * N_j(t)$ (Fig. 2.7). In the case of a single source, the response in Fig. 2.5 b was just a shifted version of the response in Fig 2.5 a. Now both responses are superpositions of a leftward and rightward travelling wave. The noise sources are assumed uncorrelated

$$\langle N_j(t) * N_i(-t) \rangle = \delta_{ij} S_N(t) \quad (2.5)$$

where $\langle \cdot \rangle$ denotes the ensemble average, δ_{ij} is the Kronecker delta function. An ensemble averaging in practise is performed by integrating over sufficiently long time. The example noise in Fig. 2.7 is recorded over 160s for the crosscorrelation in panel

c, which shows no cross-terms. Mathematically, using Eq. 2.5,

$$\langle u(x_B, t) * u(x_A, -t) \rangle = \left\langle \sum_{j=1}^2 \sum_{i=1}^2 G(x_B, x_S^j, t) * N_j(t) * G(x_A, x_S^i, -t) * N_i(-t) \right\rangle \quad (2.6)$$

$$= \sum_{i=1}^2 G(x_B, x_S^i, t) * G(x_A, x_S^i, -t) * S_N(t) \quad (2.7)$$

Combination of Eq. 2.4 and Eq. 2.7, finally gives:

$$\{G(x_B, x_A, t) + G(x_B, x_A, -t)\} * S_N(t) = \langle u(x_B, t) * u(x_A, -t) \rangle \quad (2.8)$$

This means that two observed wavefield recordings by receivers at x_A and x_B — each recording being a superposition of noise field propagating leftwards and rightwards —, crosscorrelated, give the Green's function between x_A and x_B (retrievable as the time-positive branch of the resulting crosscorrelogram) plus its time-reversed version (the time-negative branch), convolved with the autocorrelation of the noise. Cross-terms do not contribute for uncorrelated noise sources.

The third step extends the direct-wave interferometry to higher dimensions. A 2-dimensional configuration is shown in Fig. 2.8. Instead of planar waves, two receivers are surrounded by many point sources that emit transient signals. The angular distribution (along Φ_S) is equidistant, but the distance to the center is random. The responses at the two respective receivers are seen in Fig. 2.8 b&c as a function of polar angle Φ_S . These are crosscorrelated for each source separately, which yields only the difference in traveltime from a source at a specific angle to each of the two receiver locations. This difference diminishes for increasing Φ_S until the traveltimes to both locations are equal at 90° and -90° (Fig. 2.8 d). The sources at $\Phi_S = 0^\circ$ and 180° are the same as in the 1-dimensional case. They yield the maximum traveltime difference of 0.6s in the example. Summation of all crosscorrelations in Fig. 2.8 e shows the familiar time-symmetric causal and anticausal Green's function, convolved with the autocorrelation of the bandwidth-limited wavelet of the transient source $\{G(\mathbf{x}_B, \mathbf{x}_A, t) + G(\mathbf{x}_B, \mathbf{x}_A, -t)\} * S_S(t)$. All traces away from the x-axis interfere destructively and do not contribute coherently. A precise derivation based on stationary-phase analysis is given by Snieder [2004]. According to his results, observable arrivals occur when the signal phase is stationary, i.e. that it approximately does not change with respect to perturbations of the raypaths. Due to the finite frequency content, it is not only the sources exactly on the x-axis that contribute to the events but all sources within Fresnel zones around the angles $\Phi_S = 0^\circ$ and 180° . These are depicted in Fig. 2.8 a with thick

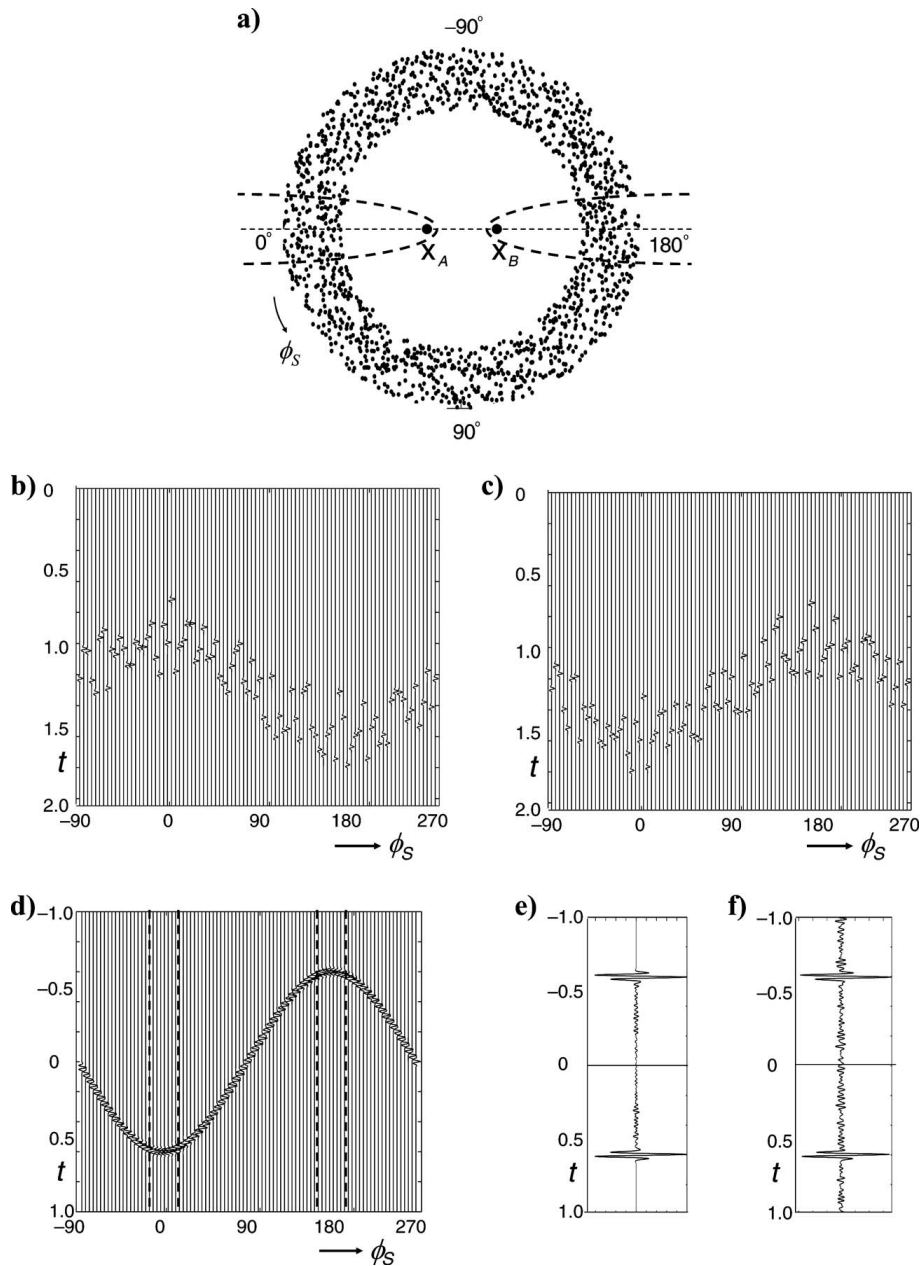


Figure 2.8: 2-dimensional schematic of direct-wave interferometry: (a) Point sources are distributed surrounding two receivers at x_A and x_B . The distribution illuminates the receivers isotropically. The thick, dashed lines denote the Fresnel zones. (b) The impulse responses at receiver A as a function of polar coordinate Φ_S . (c) Dito for receiver B . (d) The crosscorrelation of the two responses as a function of Φ_S . The Fresnel zones are denoted by dashed lines. (e) The sum of the correlations in (d), i.e. the sum over all sources. (f) This shows the single crosscorrelation of two responses to simultaneously acting, uncorrelated noise sources at all source coordinates. Graphs taken from [Wapenaar et al., 2010a]

dashed lines. Sources in these zones (or cones in three dimensions) contribute dominantly to the constructed inter-receiver impulse response. Analogous to the previous argumentation, simultaneously acting noise sources can take the place of the transient sources. When the noise is uncorrelated, the cross-terms disappear and the analogous equation to Eq. 2.8 is obtained for vector quantities \mathbf{x}_A and \mathbf{x}_B

$$\{G(\mathbf{x}_B, \mathbf{x}_A, t) + G(\mathbf{x}_A, \mathbf{x}_B, t)\} * S_N(t) = \langle u(\mathbf{x}_B, t) * u(\mathbf{x}_A, -t) \rangle \quad (2.9)$$

The symmetry of the response relies on the isotropic illumination of the receivers. Wapenaar [2004] proved a generalization for 3-dimensional media (acoustic or elastodynamic) for any inhomogeneous, lossless (not attenuating), anisotropic medium without assumptions about noise sources or diffusivity of the wavefield, based on reciprocity theory.

The most widely used application is the retrieval of seismic surface waves between receiver stations and the subsequent derivation of surface-wave velocity distribution [Campillo and Paul, 2003, Shapiro and Campillo, 2004, Sabra et al., 2005a,b, Shapiro et al., 2005, Lin et al., 2009]. The above 2-dimensional derivation holds for surface waves, as they can be interpreted as an approximate solution to a 2-dimensional wave equation with a frequency-dependent wave velocity – at least for the fundamental mode. Then the Green's function of the fundamental mode of the direct surface wave can be retrieved from crosscorrelograms of ambient noise recordings. In practise, the reconstruction is often only effective for the surface wave and direct arrival part of the Greens function, likely due to the near-surface distribution character of typically occurring noise sources [Curtis et al., 2006]. Ocean noise has been successfully employed [Lin et al., 2009], although it is not isotropic. This hampers the retrieval of time-symmetric results, but as long as at least one of the Fresnel zones is sufficiently covered with sources, either the causal or anticausal term can be retrieved. Bensen et al. [2007] demonstrate the retrieval of Rayleigh-wave velocities as a function of frequency and propose best practises of processing. A long list of studies has since employed this method (the interested reader is referred to the overview reviews mentioned above).

All of this in principle also hold true for reflected-wave interferometry using body waves. However, in passive interferometry, the ambient noise wavefield is the limiting factor and here, surface waves are by far the strongest events [Wapenaar et al., 2010a]. Retrieval of reflected waves from ambient noise is an order more difficult to achieve and requires a lot of effort to suppress surface wave signals (employing geophone arrays as receivers and/or filtering during processing). Forghani and Snieder [2010] identify further reasons why reflected-wave, i.e. body wave, Green's function response

is underestimated compared to surface waves in the methodology of ambient noise interferometry. These include less-favorable prerequisites on behalf of the ambient wavefield characteristics to be able to reconstruct body waves than to reconstruct surface waves. Also, correlation terms of body waves with themselves are much smaller even than the cross-terms between the body and surface waves. Although the latter would integrate to zero if sources were uniformly distributed, this is generally not fulfilled in practical applications using ambient noise instead of controlled sources. Nonetheless, the principle has been demonstrated in helioseismology [Rickett and Claerbout, 1999] and by employing elaborate recording and processing methods [Draganov et al., 2009]. The wide range of application of seismic interferometry also includes areas such as the estimation of building responses to seismic waves [Snieder and Safak, 2006], temporal monitoring of subsurface changes such as during earthquake [Brennguier et al., 2008a] or volcanic events [Nishimura et al., 2005, Sens-Schönfelder and Wegler, 2006, Brennguier et al., 2008b, 2011, Obermann et al., 2013], its potential for time-lapse reservoir monitoring [Mehta et al., 2008], waveform modelling, which exploits that only responses to sources on the boundary need to be stored to be able to obtain all responses between points within the volume [van Manen et al., 2006], underwater acoustics [Roux and Fink, 2003, Brooks and Gerstoft, 2007] and removal of ground roll from seismic exploration data, which is based on the fact that most practical passive studies mainly construct surface and direct waves rather than reflected waves [Curtis et al., 2006], thus these can be predicted and subsequently subtracted from active measurements [Halliday et al., 2010].

In summary, by crosscorrelation of diffuse wavefields, i.e. assuming that the noise sources are randomly distributed, the Green's function or seismic impulse response can be recovered. Most of the research and application is focused on the retrieval of surface waves because these form by far the most energetic part of the ambient noise wavefield and do not require impractical efforts of surface wave filtering. The retrieval of body waves by passive seismic interferometry could theoretically yield thaw depths more directly. However, the Arctic application sought for subsea permafrost from small boats on the shallow shelf is an easy-to-operate and -to-move system, in order to cover larger spatial areas. Thus, a combination of surface wave retrieval and H/V ratio peak frequency matches these criteria best. By analyzing the frequency-dependent dispersion relation of the surface wave crosscorrelogram, the shear wave velocity of the surface unfrozen layer can be determined. It is particularly noteworthy that the combined method is self-contained, i.e. almost entirely data-driven and based on the same set of observational noise data without the need to collect or assume additional subsurface information.

Feasibility study

In the context of this study it must be noted that the wavefield composition knowledge reviewed previously is based on studies in regions that always include man-made, cultural noise sources. No characterization specifically of the remote Arctic study sites is known to this author. As the wavefield composition cannot be easily estimated on the Arctic shelf, but may impact the suitability of the proposed methods (both H/V ratio peak interpretation and the seismic interferometry technique), this study conducts a feasibility test. The instrument design is first tested in a marine environment prior to the Arctic operation. To validate if the acquired depths can be related to the thaw depth, the method is tested at a known study site around Muostakh Island, where previous observations of thaw depth exist. Furthermore, although our subsea permafrost configuration resembles the simple 1-dimensional two-layer configuration with high impedance contrast ideal for H/V analysis, the presence of the water layer instead of a free surface may have a deviating impact. In a cooperation within the project with the University of Potsdam (Dr. Matthias Ohrnberger) forward modelling is performed to test the influence of the overlying water layer and is included in the interpretation. Lastly, a second expedition applies the successful method design to collect data over a wider area around Muostakh Island.

2.4 Instrument design & marine tests on Sylt

The underwater recording equipment was specifically designed and the set up consists of a low-power digital recorder, a standard short-period (4.5 Hz), three-component geophone, and a battery pack of 8x 1.5V D-cell batteries. These components were enclosed in a water-tight cylindrical aluminum container (dimensions: height 35 cm, diameter 20 cm; weight: 9 kg). Figure 2.9 shows a schematic illustration of the set up. The cylindrical casing was mounted onto a metal grid of 70 cm by 70 cm, which was lowered to the sea bottom by a line from a boat. The casing was connected via a metal loop at one corner of the grid to an anchor sack (sand-filled bag) and a buoy at the sea surface — as a location mark as well as for retrieval purposes. The anchor decouples the sensor from buoy tugging. The grid and loop at the corner were to assist the lifting under potential sedimentation or burying expected in the near-shore zone over the period of deployment. The battery pack allowed for deployment of up to 40 days. The recorder required GPS time synchronization before and after deployment to allow for drift correction in the internal clock. The 24-bit A/D converter contained in the recorder continuously recorded at 200 samples

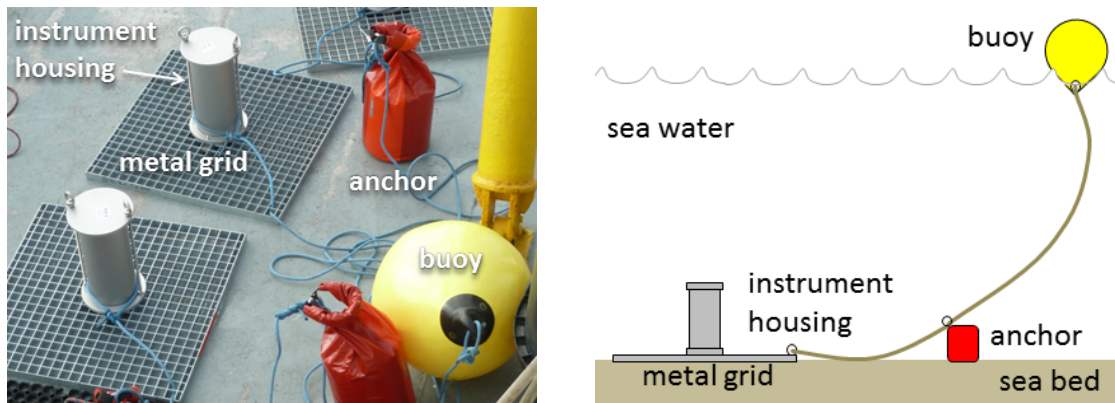


Figure 2.9: Instrument design: **(left)** A photograph of the instrument set up on deck and ready for deployment. This includes the watertight casing, metal grid for orientation, sand-sack anchors, and buoys. **(right)** A schematic illustration of a deployed sensor. Adapted from [Overduin et al., 2015a].

per second (sps). The data was stored on a 16 GB SD card. The watertight container permitted safe operations down to 100 m water depth. The metal grid served to guarantee approximately upright positioning of the instrument, which translates to the sensors being level. As some tilting could not be ruled out, and no gimbal system was employed to automatically level sensors, a calibrating signal was used to correct for a possible tilt-influence on the sensors. Tilt would particularly affect the horizontal components of the sensor. A calibrating signal was imposed to the geophones every day (24 h), the response function was calculated [Rodgers et al., 1995], and the time-series data of the three components corrected with a restitution filter [Scherbaum, 1996]. The approach was capable of accounting for time-varying transfer functions for potentially varying tilting by changing water currents, storms, etc. In general, only minor temporal changes in the tilt of individual sensors were observed, but a few stations recorded small, but abrupt changes in the sensor's eigenfrequencies and damping factors (represented in the response function), possibly due to a change in the grid position. All in all, the recording equipment is relatively small in size and could be deployed from a small-size boat, which was important for operation in shallow water.

In two 4-week-long field work periods, between 15 May until 11 June in 2012 and 25 March until 26 April in 2013, six submarine sensors were tested around Sylt island in the North Sea, Germany. The profile of the second period is shown in Fig. 2.10. Four additional sensors were deployed in the dunes on the land surface between the profiles to the east and west side of the island. The main purpose of these field works was to familiarize with the equipment and measurement routines as well as testing and improving the handling and design of the instruments in operation

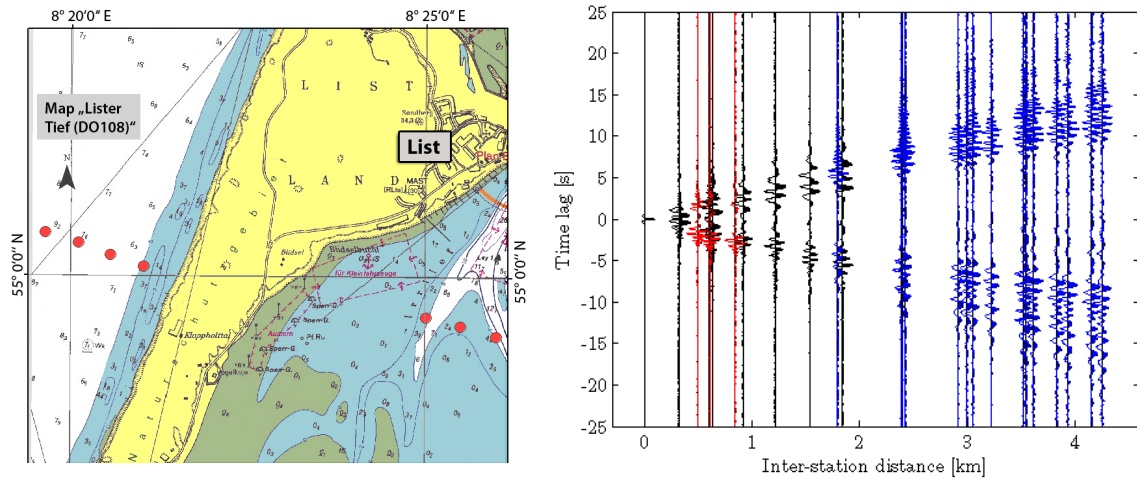


Figure 2.10: Test site around Sylt island in the North Sea, Germany, during the 2013 field works: **(left)** Location of the submarine sensors in two profiles to the east and west of the island. **(right)** Results of the seismic interferometry technique: Crosscorrelograms for different inter-station distances. Black traces are land-land station pairs, blue are land-ocean and red are ocean-ocean station correlations.

in a marine, ship-based environment. Deployment was successful, and no major faults were recognized. Due to the subsurface configuration around Sylt with mostly sandy sediments and not representing the simple 2-layer scheme necessary, testing of the H/V method was prohibited. However, crosscorrelations between the receiver stations could be calculated and are shown in Fig. 2.10. For details of the processing see Sect. 2.5. In a procedure of crosscorrelating all receiver-receiver pairs, virtual sources are successively created at each receiver position and the response at all other receivers is retrieved. The cone of a direct surface wave is well visible in the crosscorrelograms of different inter-receiver distances. This verified the ability of the passive seismic interferometry data acquisition and processing technique.

2.5 Arctic feasibility test site around Muostakh Island

Study site

Are [2003] identifies the shoreface and near-shore zone of rapidly retreating coasts as the most ideal setting to study inundated permafrost and the associated processes from its inception onwards. Here, distance from the shore represents a time scale, and degradation of permafrost may be observed from the time of inundation. Muostakh Island as the Arctic study area for this geophysical approach is selected for its well established long-term rapid erosion record, existing borehole observations in the near-shore zone from the 1980s [Slagoda, 1993] and available geoelectric measurements

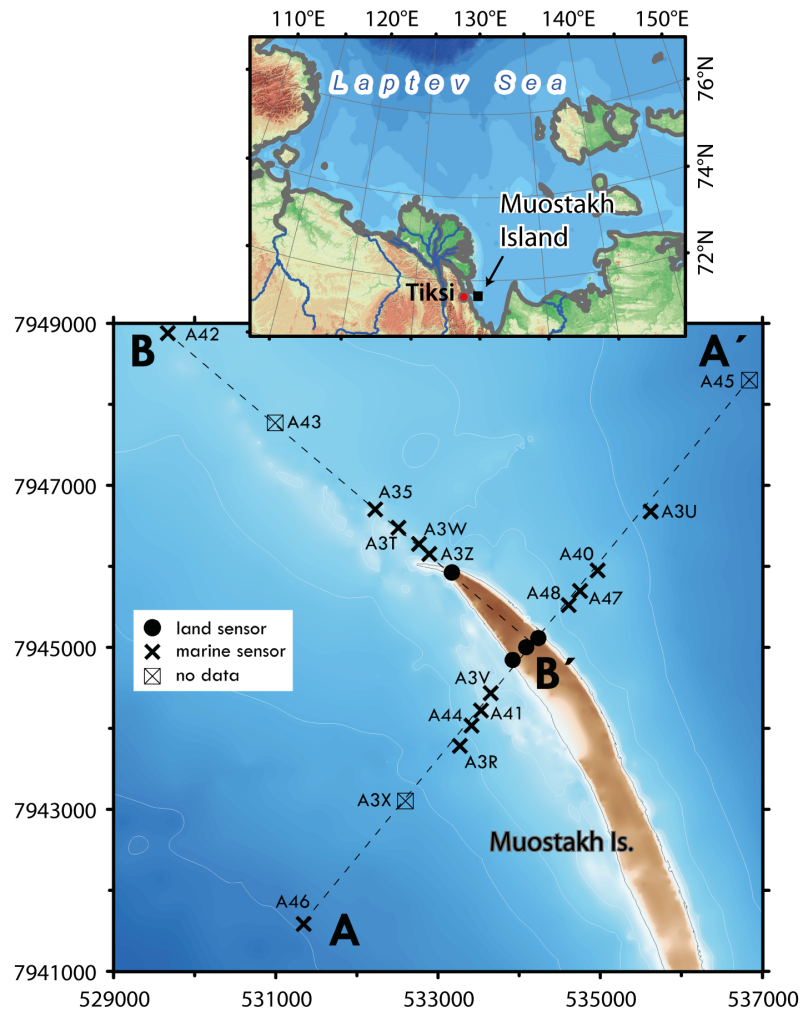


Figure 2.11: Elevation map of the north end of Muostakh Island showing the submarine and land sensor positions along the two profiles A-A' and B-B', respectively. (Inset) Location of Muostakh Island in the Laptev Sea. Adapted from [Overduin et al., 2015a].

[Overduin et al., 2016]. Muostakh Island lies in the central Laptev Sea, Russia (Fig. 2.11), within the zone of continuous permafrost (Fig. 1.1), and has one of the longest records of rapid coastal erosion in the Arctic [Günther et al., 2015]. Maximum values of shoreline retreat are up to 25 m per year, occurring at the northern spit of the island. While the entire eastern coast facing the open ocean is generally eroding, most of the more occluded western shore is relatively stable with individual shoreline sections exhibiting smaller rates of no more than 1–2 m per year. The bathymetry around Muostakh Island is shallow, seabed inclination perpendicular to the shore is between 0 and 0.7%. The subsurface sediment composition is observed in coastal exposures. In the western and central Laptev Sea, as well as on the New Siberian Islands, these generally exhibit Holocene deposits covering late Pleistocene Ice Complex deposits. These silty, ice-rich deposits extend down to within 10 m of the modern sea level (either above or below). At Muostakh, they extend below the

modern sea level. Below lie alluvial sandy silt to silty sand deposits [Günther et al., 2015] which are of up to 100s of meters in thickness [Drachev et al., 1998]. Thus, the study site of Muostakh Island offers a variety of coastal retreat rates (and therefore inundation rates) within a small local setting, in which the sediment composition characteristics are not expected to vary greatly.

On 8–9 August 2013, 17 underwater sensors were deployed around Muostakh Island along two profiles which stretch in three directions (Northwesterly, Northeasterly, and Southwesterly) offshore from the coastline to points about 4 km distant on the shelf (see Fig. 2.11 and Table 2.2). Additionally, land sensors were deployed on the surface of the island, and were coupled to the ice-bonded permafrost table below the seasonally thawed soil of the active layer. All sensors were reacquired almost four weeks later, on 4 September 2013. Burying from sedimentation and likely shifting sands in the shallow waters in the vicinity of the northern spit point impeded manual recovery of the closest instrument to the shoreline and necessitated use of an electrical crane and winch. Opening of the containers, GPS synchronization and data download were performed in the field. The raw data were converted to miniseed format. The calibration signals were removed from the time series. From the calibration, actual sensor characteristics of eigenfrequencies and damping factors were determined, and using these values, the data were restituted (see in Sect. 2.4). Generally, the data quality was good and only one marine station failed (sensor A43, Fig. 2.11).

H/V processing

The H/V spectral ratios were calculated as averages on 30 min time intervals. The processing procedure was in accordance with standard procedures [SESAME, 2004] and conducted using Matlab and Geopsy [<http://www.geopsy.org>] software. Specifically, the data period was divided in 60 s time windows with 50 % overlap. On each window, DC removal and tapering were applied before the power spectra were obtained by discrete Fourier transformation. The vertical (V) and two horizontal (H_x and H_y) spectra were smoothed using the Konno and Ohmachi [1998] smoothing function, which encompasses symmetric smoothing windows of constant width in the logarithmic frequency analysis performed here. To take into account the low-frequency limitation of the instrument sensors [Guillier et al., 2008, Strollo et al., 2008a,b], the frequency band for the analysis is limited to 0.5 Hz to 65 Hz. The H/V

ratio computation followed Eq. 2.10

$$\frac{H}{V} = \frac{\sqrt{|H_x|^2 + |H_y|^2}}{|V|} \quad (2.10)$$

All 60 s time windows were averaged over 30 min time segments. The results of these average H/V spectral ratios are shown as time-frequency plots where the 30 min slices are plotted along the time axis (see Fig. 2.12 a). This temporal display was used to check data quality.

The temporal variability of observations was assessed in order to distinguish effects in the H/V plots from weather (wind, rain), tides (currents around the island) and other disturbances — that may have affected the recordings at the shallow sea floor stations — from the structural response of the subsurface. Figure 2.12 a shows the exemplary results for one station over the entire acquisition period of almost 4 weeks. Strong variability in average H/V was observed for most stations. This included short-lived transient and long-lasting broadband disturbances. The transient ones were probably related to sea surface wave motions and connected to wind while the broadband high amplitude H/V values of longer duration were probably caused by currents. However, observed periods of strong H/V amplitudes could not be correlated to weather conditions during the observation period. On the other hand, the plots of H/V ratios also display an underlying pattern of stable features, i.e. peaks and troughs, that can be followed for hours and sometimes even for days between periods of higher variability (see Fig. 2.12 a, b). These stable parts of the H/V plots are conceptually related to the structural response of the subsurface in this study (see Sect. 2.3.1). In order to enhance the stable response parts a manual selection of time slices was performed. All selected 30 min time segments were subsequently stacked/averaged and the variability distribution statistically evaluated. A stacked H/V curve is illustrated in Fig. 2.12 c including the estimated variability bounds.

When evaluating the time-frequency plots and the stacked H/V curves by considering the means and variances, lower frequencies had long-term stable contributions for most of the stations in the study. This was also true even for frequencies below the corner frequency of the sensors. Based on the good resolution of the digital converter (see Sect. 2.4, effectively 21 bits at 200 samples per second), it is the opinion of this author that sensor recordings around 1 Hz can still be interpreted in most of the observations in this study. Beyond the first peak, H/V peaks were observed at very high frequencies. Some of these shifted frequency slowly with time. Generally, this frequency range was associated with a larger variance in the H/V curve while low frequencies (approximately between 1 and 10 Hz for most stations) showed a much

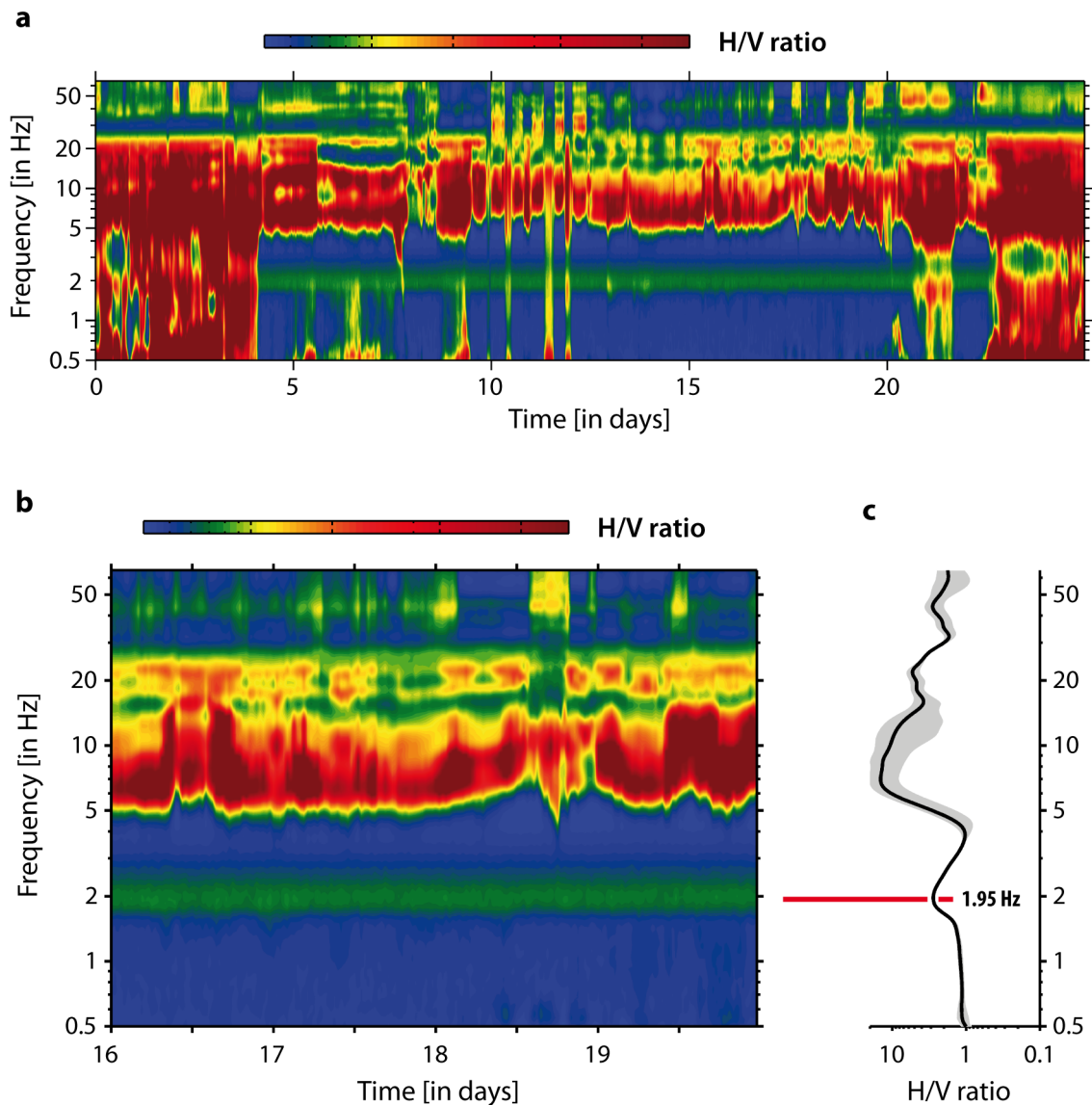


Figure 2.12: (a) H/V time-frequency plot for station A46 on profile AA', covering the whole 26-day observation period. (b) A stable part between days 16–19. (c) Stacks of the record in (b). The shaded area denotes the standard deviation. The retrieved peak frequency is also denoted.

lower variance. In this frequency range, a flat H/V spectrum with a comparably small amplitude peak and a neighbouring trough could be observed. This can also be seen in Fig. 2.13 which shows the H/V curves for stations along the profile B-B'. Higher frequency contributions may be related to ambient wavefield composition (see Sect. 2.3) and to the additional presence of a water layer, which deviates from the simple 2-layer configuration (see Appendix A).

Finally, for each station the mean position of the first maximum including the standard deviation evaluated from all stable segments was determined (Fig. 2.12c and Table 2.2). In the case of A3X and A45, no clear peak could be identified, and

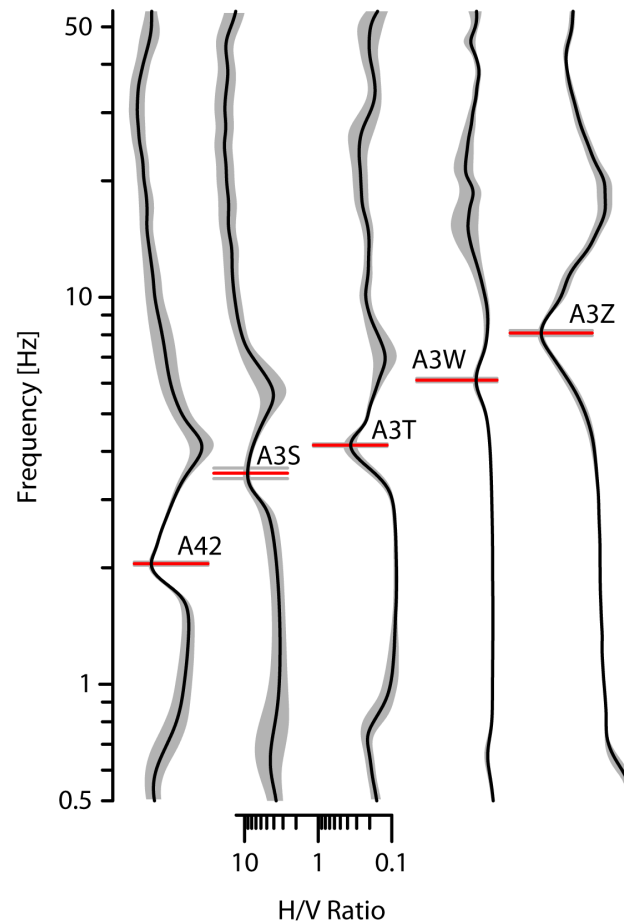


Figure 2.13: H/V spectral ratio for receiver stations along profile B-B' with uncertainty bounds for the H/V curve. Red bars indicate the position of the peak frequency.

the H/V data from these stations was removed from further interpretation. Such stations and failed instruments are marked accordingly in Fig. 2.11.

Processing of seismic interferometry data

Seismic interferometry was used for the calculation of the shear wave velocity of the unfrozen sediment layer offshore. In a procedure repeated for each receiver location, virtual sources are created at the position of this single receiver and the response at all other receivers is retrieved. Thus, a 'shot gather' for varying distances (corresponding to different inter-receiver distances) is obtained. A dispersion curve analysis of these ambient noise crosscorrelations yielded an estimate of the shear wave velocity of the unfrozen sediment layer.

The data analysis adhered mostly to the procedure outlined in Bensen et al. [2007], and was applied to the recorded vertical noise field component in order to subdue Love wave and enhance Rayleigh wave type contributions in the analyzed wavefield. For

each receiver pair, the continuous data was divided into daily slices. The respective spectra were then whitened, and the data one-bit normalized. The crosscorrelations of all slices for a station pair were computed in the frequency domain and then stacked. The band-passed result of the crosscorrelations for all inter-station receiver pairs in the experiment around Muostakh Island is presented in Fig. 2.14. The correlogram has a time-positive and a time-negative branch. The correlation function is defined for positive and negative correlation times, thus it represents waves propagating from one station to the other as well as vice versa. The functions are generally dominated by surface waves (Sect. 2.3.2).

In the figure, the coherent signals have a dominant signal period T of about 1.5 s. Their velocity derived from the diagram is approximately $v = 1.3 \text{ km s}^{-1}$. They represent surface waves, or more accurately interface or Scholte waves (as they propagate along the interface between sediment and water instead of along the free, subaerial surface) which penetrate into the sediment on a length scale proportional to their wavelength. Penetration is effectively between one-third and one-half of a wavelength, and a typical criterion for the penetration depth is the 0.4λ estimation. Based on this, these waves are estimated to be sensitive to depths down to:

$$0.4 \cdot \lambda = 0.4 \cdot \left(\frac{v}{f}\right) = 0.4 \cdot (v \cdot T) = 0.4 \cdot (1850 \text{ m}) = 750 \text{ m}$$

Therefore, these interface waves probe much of the upper part of the deeper permafrost layer, and their velocity is dominated by the frozen ground properties. Thus, this velocity can be used to obtain a rough estimate of the shear wave velocity in the lower permafrost layer.

In order to obtain the shear wave velocity of the unfrozen, unconsolidated soft sediment layer above the ice-bonded permafrost, an analysis of the dispersion curve of the interface waves in the crosscorrelograms was conducted. The technique of frequency-time analysis of Dziewonski et al. [1969] was employed. The analysis consists of bandpass-filtering the crosscorrelation function by a narrow frequency range of 0.25 Hz for successive center frequency traces between 1 and 7 Hz, retrieving the arrival time of the associated interface wave group in each trace, and converting into velocity. This analysis was performed on the crosscorrelation function of several submarine station pairs that showed well-defined dispersion in interface wave arrivals (the red traces between 200–600 m distance offset in Fig. 2.14). Figure 2.15 a shows the crosscorrelation function of one of these pairs (A3R–A44), the corresponding result of the dispersion curve analysis for this receiver pair is given in Fig. 2.15 b. Between a signal frequency of 1.5 Hz and 5 Hz, a distinctly disperse interface wave can be seen with decreasing velocity for increasing frequency, i.e. decreasing penetration

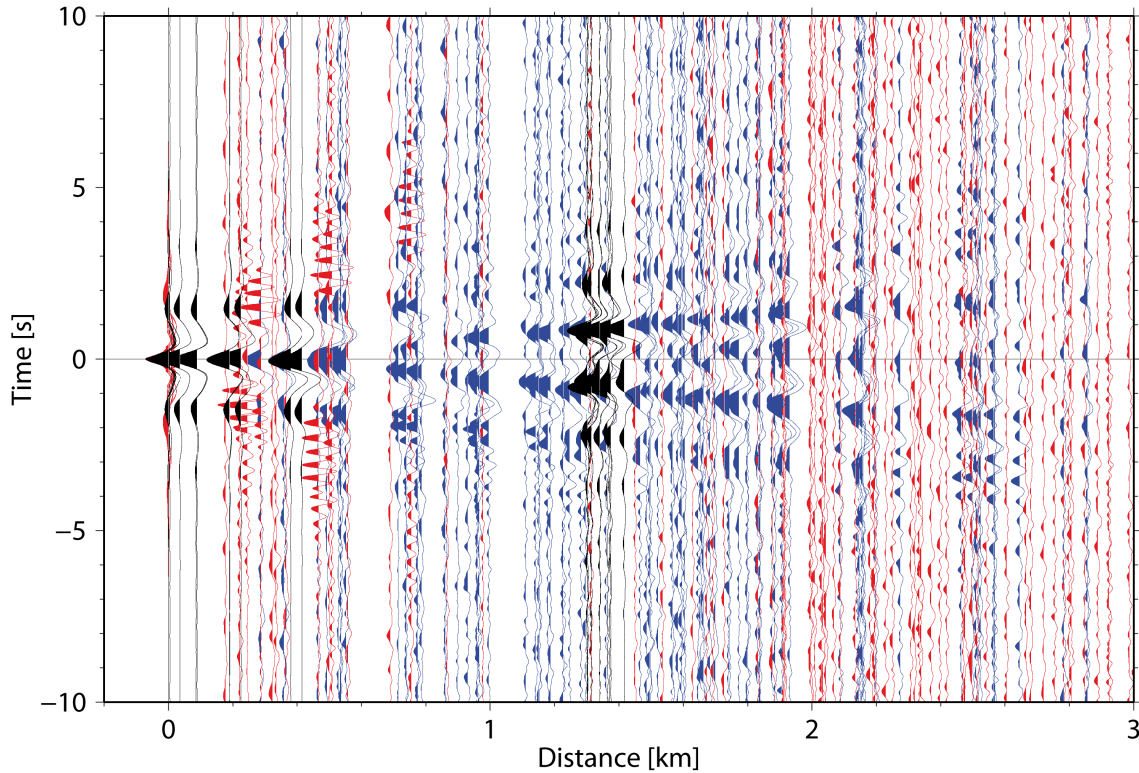


Figure 2.14: Crosscorrelation data of all receiver pairs band-passed between 0.5 and 5 Hz. The black traces denote land-land station pairs, blue are mixed land-ocean station pairs, and red are ocean-ocean station pair crosscorrelations. Adapted from [Overduin et al., 2015a].

depths of the interface wave into the sediment. It should be noted that the asymmetric amplitude retrieval in the crosscorrelation function was caused by a non-uniform distribution of ambient noise sources surrounding the receivers. This is traced to the asymmetric recovery of the negative time branch in the dispersion curve. Nonetheless, the corresponding travel times of interface waves from one direction between the receivers and vice-versa are essentially the same. The high-frequency part of the dispersion curve is associated with interface waves that propagate only in sediments at shallow depth, thus probing only the uppermost, unfrozen, soft sediment layer. By the 0.4λ estimation, these interface waves penetrate only about the first 10–14 m into the sediment. Therefore, this study uses the high-frequency part of the dispersion curve to yield the Scholte wave group velocity of the interface waves that only probe the top unfrozen layer. For higher signal frequencies (center-frequencies), the extracted group velocity approaches values down to approximately 100 m s^{-1} .

There is no simple direct conversion formula from group velocity dispersion information of interface waves to material velocities in the subsurface (shear wave and P-wave velocity). Among others, the relationship depends on frequency and water depth. However, for the high frequency limit of the dispersion curve, the group

velocity (v_g) can be related to the shear wave velocity of the shallowest layer using a simple factor. This factor depends slightly (to a few percent) on the $\frac{v_p}{v_s}$ ratio of the respective medium. In this study, a value of 0.85 is used as a proxy conversion factor. Thus, the shear wave velocity in the topmost unfrozen marine layer was estimated to be around 120 m s^{-1} , which is comparable to other observations [Stoll, 1977, Dong and Hovem, 2011, Vanneste et al., 2011]. Evaluation of the dispersion analysis for other station pairs resulted in similar group velocities of $\pm 10\%$. Therefore, a shear wave velocity of $120 \text{ m s}^{-1} \pm 10\%$ was used as a regional value in the conversion of H/V peak frequencies to layer thicknesses.

Lastly, using the same assumption of $v_g \approx 0.85 v_s$ for the signal dominated by the material properties of the permafrost layer, the shear wave velocity in this permafrost layer v_s can be estimated to 1.5 km s^{-1} . This fits well with values reported for seismic velocities in permafrost-affected sediments [Zimmerman and King, 1986] where shear

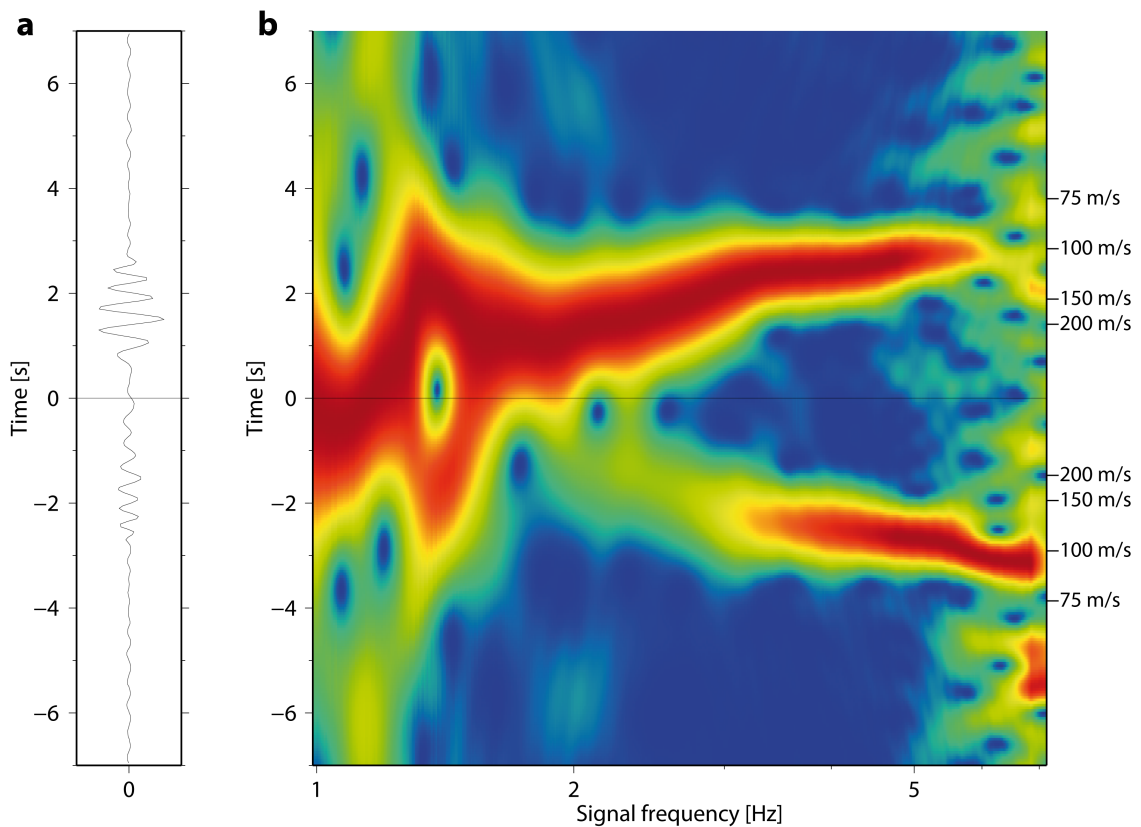


Figure 2.15: (a) Positive and negative time-branches of the crosscorrelation function for the station pair A3R–A44. Their interstation distance was 288 m. (b) The associated dispersion curve analysis of narrow band-filtered group waves. Traces are normalized within each frequency band. Red indicates high, blue low amplitudes. The time axis is recalculated using the receiver distance to yield velocity values. Two surface wave phases can be seen. The group velocities of the surface waves at higher frequencies ($> 5 \text{ Hz}$) approach values down to approximately 100 m s^{-1} . Adapted from [Overduin et al., 2015a].

wave velocities ranging from 0.9–2.3 km s⁻¹ (depending on sediment composition and saturation) were observed. Therefore, these results confirm a sharp acoustic impedance contrast in the configuration.

H/V peak interpretation in the presence of the overlaying water layer

The existence of a strong impedance contrast between the unfrozen upper sediment layer and the permafrost below has been confirmed from the data analysis. However, while the sediment configuration of our subsea permafrost resembles the simple 1-dimensional, two-layer configuration with high impedance contrast ideal for the applicability of the H/V method, the presence of the water layer instead of a free surface may have a deviating impact. In the conventional 2-layer applications, sensors are typically placed on the free surface of the sediment/atmosphere boundary. In this case of subsea permafrost detection, the sensors were deployed at the sediment/sea water interface instead. Previous work on the physical cause of the H/V spectral ratios and the interpretability in terms of fundamental resonance frequency does therefore not necessarily hold [Atakan and Havskov, 1996, Boore and Smith, 1999, Bussat and Kugler, 2011, Frontera et al., 2010]. In a cooperation with the University of Potsdam (Dr. Matthias Ohrnberger) forward modelling is performed to test the influence of the overlying water layer. This model can be summarized in that it considers a three-layer configuration (sea water – unfrozen sediment – an infinite halfspace of permafrost). It employed forward modelling of seismic sources, calculated spectral ratios, and processed the H/V data. It allowed comparison of the H/V peak frequencies from the full wave field to the $\lambda/4$ resonance calculation for pure vertical incident SH-reverberations in the unfrozen layer. Assessment was conducted for water layers with varying depth and varying thickness of the unfrozen sediment layer. Variation of the water depth ranged from 2 to 30 m, according to the field site bathymetry. Details and results can be found in the Appendix A.

In order to interpret the modelled results, A.1 b shows a low-frequency peak in the H/V spectrum that shifts with varying unfrozen sediment thickness. It closely resembles the fundamental resonance frequency ($n = 0$ in Eq. 2.1), as expected for shear wave resonance in an unconsolidated sedimentary layer in the two-layer case [Malischewsky and Scherbaum, 2004]. Equation 2.1 for $n = 0$ can be rearranged to yield the depth dependence of the peak frequency

$$d = \frac{v_s}{4 \cdot f_0} \quad (2.11)$$

where d is unfrozen layer thickness in m, v_s is the shear wave velocity of the unfrozen sediment in m s^{-1} , and f_0 is the peak frequency in Hz.

In addition to this low-frequency peak, a complex pattern of peaks and troughs was observed at higher frequencies in the modelled results. For the modelled parameter range, these higher frequency H/V peaks remained clearly separated from the primary, fundamental unfrozen layer signal, both for increasing water depth (Fig. A.1 a) and increasing unfrozen layer thickness (Fig. A.1 b). In the higher frequency part of the HV spectrum, an increasing water depth exhibits increasing resonances. No shear forces exist in the water body. Thus, a contribution of P wave resonance in the water layer is suggested, but no contribution at frequencies interfering with the fundamental H/V peak frequency occurred for water depths in the modelled parameter range.

Thaw depths results and discussion

Based on the numerical modelling results, the low-frequency peaks were related to the unfrozen sediment layer between the seafloor and the ice-bonded permafrost body. The retrieved frequency of fundamental H/V peak varied between 1.45 and 8.08 Hz in the study area. Using Eq. 2.11, the retrieved H/V peak frequencies were converted to unfrozen layer thicknesses. The necessary shear wave velocity of this layer is taken from the dispersion curve analysis, which yielded an average Scholte wave group velocity of $100 \pm 10 \text{ m s}^{-1}$ for the high-frequency part of the dispersion curve associated with sediments at shallow depths. This corresponds roughly to layer shear velocities v_s of $120 \pm 12 \text{ m s}^{-1}$. Assuming that this value is representative for the whole study area, the layer thickness d of the unfrozen marine sediment layer could be estimated. This is the depth of the top of ice-bonded permafrost below the seafloor. These thaw depths ranged from $3.7 \pm 0.5 \text{ m}$ to $20.7 \pm 2.6 \text{ m}$ in the study area. Table 2.2 lists all stations along the profiles including the retrieved H/V peak frequency and estimated top of ice-bonded permafrost depth.

Profile	Station	Water depth	f_0 (Hz)	Top of Ice-Bonded Permafrost Depth ^a		Permafrost Depth 2011 (m bsl) (Geoelectric Sounding) ^b	Permafrost Depth 1983 (m bsl) (Borehole Observation) ^c
				(m bsf)	(m bsl)		
B-B'	A42	3.2	2.05 ± 0.02	14.7 ± 1.8	17.9 ± 1.8	-	-
	A43	3.1	-	-	-	18.4 ± 0.7	16.2
A-A'	A3S	3.0	3.45 ± 0.11	8.6 ± 1.1	11.6 ± 1.1	11.0 ± 3.6	8.6
	A3T	2.2	4.15 ± 0.03	7.2 ± 0.9	9.4 ± 0.9	13.8 ± 1.6	6.6
	A3W	3.3	6.11 ± 0.06	4.9 ± 0.6	8.2 ± 0.6	8.7 ± 0.8	3.2
	A3Z	2.4	8.09 ± 0.12	3.7 ± 0.5	6.1 ± 0.5	5.4 ± 0.6	0
	A46	8.0	1.95 ± 0.06	15.5 ± 2.0	23.5 ± 2.0	-	-
A-A'	A3X	6.7	-	-	-	-	-
	A3R	5.2	1.47 ± 0.12	20.7 ± 2.6	25.9 ± 2.6	-	-
	A44	4.1	1.61 ± 0.07	18.9 ± 2.4	23.0 ± 2.4	-	-
	A41	2.6	1.51 ± 0.07	20.0 ± 2.5	22.6 ± 2.5	-	-
	A3V	2.3	2.15 ± 0.03	13.9 ± 1.7	16.2 ± 1.7	-	-
	A48	4.7	4.04 ± 0.05	7.4 ± 1.1	12.1 ± 1.1	-	-
	A47	4.9	3.31 ± 0.05	9.1 ± 1.2	14.0 ± 1.2	-	-
	A40	4.7	2.60 ± 0.03	11.5 ± 1.5	16.2 ± 1.5	-	-
	A3U	6.7	1.58 ± 0.03	19.0 ± 2.4	25.7 ± 2.4	-	-
	A45	7.8	-	-	-	-	-

^a Calculated assuming $v = 120 \text{ m s}^{-1}$.

^b Overduin et al. [2016].

^c Slagoda [1993].

Table 2.2: List of station positions in the two profiles and their characteristics. A comparison of the depth to ice-bonded permafrost calculated from H/V frequency to those from resistivity methods and drilling data is given (bsf - below sea floor; bsl - below sea level).

This method primarily assumes that (i) the shear wave velocity is the same in the whole study region, and (ii) a constant seismic velocity prevails within the unfrozen sediment layer. If strong lateral variations of the shear wave velocity in the unfrozen sediment layer were present, additional measurements of sediment velocities at each measurement point would be necessary. The same would hold for a possible depth dependence of the shear wave velocity within the unfrozen sediment layer. The retrieved estimates of the seismic velocity from the dispersion curve analysis were rough and limited in vertical resolution. However, they agree with values derived from other geophysical experiments at the sea bottom and from theoretical studies [Stoll, 1977, Dong and Hovem, 2011, Vanneste et al., 2011]. Moreover, regarding seismic interferometry, the stabilization of the normalized averaged correlation functions in our 26 one-day time segments period suggests that the resulting illumination is diffuse, and totally or partially equipartitioned. This agrees well with the assumption that the distribution of ambient noise sources randomizes when averaged over longer times, of which not more than a few hours for frequencies higher than a few hertz were also needed to stabilize the crosscorrelation functions in the studies of Pilz et al. [2013] and Sanchez-Sesma et al. [2011]. The derived upper layer thickness is larger than the effective penetration depth of the interface wave in the high-frequency part of the dispersion analysis, i.e. > 18.9 m vs. 10–14 m at stations A3R and A44, asserting that the interpreted velocity is in fact associated only with the unfrozen layer. This validates that the combination of both methods yielded consistent results. Concerning the error estimates from both quantities in Eq. 2.11, uncertainties of the peak frequencies f_0 are negligible relative to the uncertainties in the shear wave velocity v_s . The modelling, however, suggested that the $\lambda/4$ resonance frequency was systematically offset from the modelled H/V peak frequency for any given model scenario. This resembles the results presented by Malischewsky and Scherbaum [2004] for strong shear wave contrasts. From the parameters of the modelling that were used – and which resemble all encountered field conditions in this test study – this offset was less than 20 % in all cases. Nonetheless, offset dependence on unfrozen layer thickness and velocity could be the subject of further investigation.

Furthermore, a note should be made about the interdependence between deployed sensor type and field conditions. The peak frequency depends on the two quantities of unfrozen layer thickness and average velocities (Eq. 2.11). Sensor sensibility must be chosen according to the local conditions. In this study, the maximum estimable depth to ice-bonded permafrost below the sea bottom was about 30 m, based on reliable sensor sensitivity down to c. 1 Hz. Other conditions, e.g. smaller shear velocities or larger thaw depths, could require a different choice of sensor type.

Figure 2.16 presents the thaw depth along the two crosssections through Muostakh

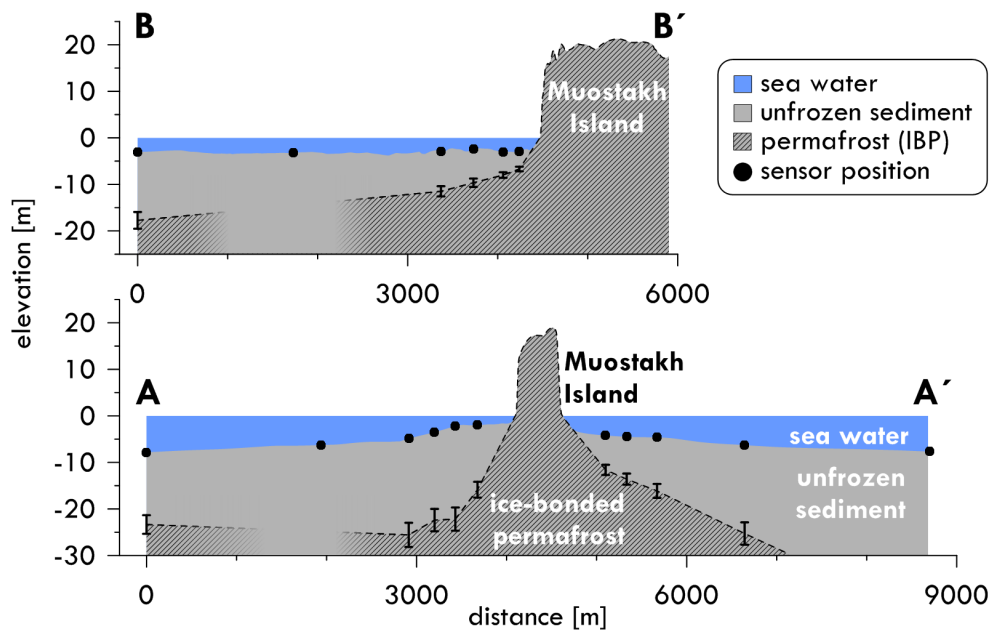


Figure 2.16: Resulting crosssection of Muostakh Island, sea floor and subsurface. (top) Along the profile B-B'. (bottom) Along the profile A-A'. The black circles indicate station locations including the depth of the top of ice-bonded permafrost below, as calculated in this study. Illustration adapted from [Overduin et al., 2015a].

Island. The distribution of the values showed a consistent pattern and smooth spatial trends in these crosssections, with lower values close to the island and higher values at greater distance from the shore. On Muostakh Island, ice-bonded permafrost reaches the surface (with the exception of the seasonally thawing, active layer), which corresponds to 0 m thickness of the overlying unfrozen layer. The crosssections reveal the asymmetrical subsurface structure around the island, with a gentler slope off the NE shore and more abrupt deepening towards the SW. This is consistent with more rapid mean annual coastal erosion rates on the eastern shore (2.32 m a^{-1}) than along the western shore (0.23 m a^{-1}) between 1951 and 2012, where profile A–A' intersects the shoreline [Günther et al., 2015]. To the NW, the permafrost is found at shallower depth than on either side of the island. Along the profile section B–B', the depths of ice-bonded permafrost derived by the H/V and interferometric methods agree to within 50–70 cm with the values derived by geoelectric sounding in 2011 [Overduin et al., 2016]. Only at station A3T was a larger difference of 4.4 m observed. This good agreement is remarkable when keeping in mind that the depth estimates were derived with completely different methods and, moreover, without using constraining information or calibration from other direct measurements. Furthermore, profile B–B' was chosen to coincide with several boreholes drilled in 1983. In these 1983 boreholes, the ice-bonded permafrost was encountered at depths listed in Table 2.2 [Slagoda, 1993]. Only four borehole observations of depth to ice-bonded permafrost are available that correspond to the determinations of the thickness of the overlying unfrozen

sediment (data failure occurred at instrument station A43 in this experiment). In all cases, the observations from 1983 are lower than or equal to our determinations. This is consistent with a degrading top of ice-bonded permafrost. If all values are assumed to be correct, then mean annual permafrost degradation rates over the 28 year period are 13, 6, 2, and 0 cm a⁻¹ in increasing distances from the shoreline (1100, 740, 410, and 230 m from the shoreline in 2013, respectively), based on the changes in depth position observed between drilling in 1983 and the 2013 measurements presented in this study. These values are consistent with observed subsea permafrost degradation rates near the coast (between 1 and 15 cm a⁻¹ in less than 10 m water depth) for 12 sites with varying geomorphology and coastline change rates in the Laptev and East Siberian Seas [Overduin et al., 2007b]. The trend of decreasing mean permafrost degradation rates with increasing distance from the shore is also consistent with observations of permafrost degradation following inundation [Hutter and Straughan, 1999]. Considering the use of the combined H/V and interferometry method for subsea permafrost mapping, a calibration measurement (e.g. from boreholes or geoelectric sounding) could be included in a future application. This might serve as an improvement, in particular, to constrain factors affecting the velocity of the unfrozen layer.

2.6 Arctic deployment for wide area detection around Muostakh Island

In order to collect as much data as possible around Muostakh Island, a second survey was conducted during an expedition in the summer of 2016. The same set of underwater seismic devices was deployed at new station positions around the island on 23 August 2016, and reacquired on 11 September 2016. The pattern of station positions was chosen to cover a wider area around the island's northern part, and to complement the locations from the 2013 expedition. The data was processed following the same procedure (see Sect. 2.5). 13 stations yielded additional estimates for the depth to the top of ice-bonded permafrost around Muostakh Island. Three station sensors failed during deployment due to a malfunction in at least one sensor component (vertical) as determined by the analysis of the calibration signal. This unfortunately rendered their recordings untenable for H/V ratio computation, and their data was removed from further interpretation. One station was lost. Table 2.3 summarizes all stations' positions around Muostakh Island deployed in the 2013 and 2016 expeditions, including the retrieved H/V peak frequency and estimated top of ice-bonded permafrost depth. Both data sets are mapped together in Fig. 2.17.

The retrieved data from 2016 shows a consistent pattern and smooth spatial variations, both within its own data set and when intersecting profiles from 2013. The general trend of lower values of thaw depths close to the island and higher values at greater distance is confirmed and spatially extended to the wider area around the northern part of the island. The trend of larger thaw depths closer to shore, i.e. a more abrupt deepening on the western shore, compared to the eastern shore is also confirmed. In summary, the collected data set presented here can be used in the future as reference (or baseline) to monitor possible continued changes of subsea permafrost. Furthermore, the extended data on subsea permafrost around Muostakh Island, combined with its well established history of geological and geomorphological data, can be used when applying modelling to study and assess the involved processes and, thus, help to improve our understanding of the degradation rates (see Chap. 3).

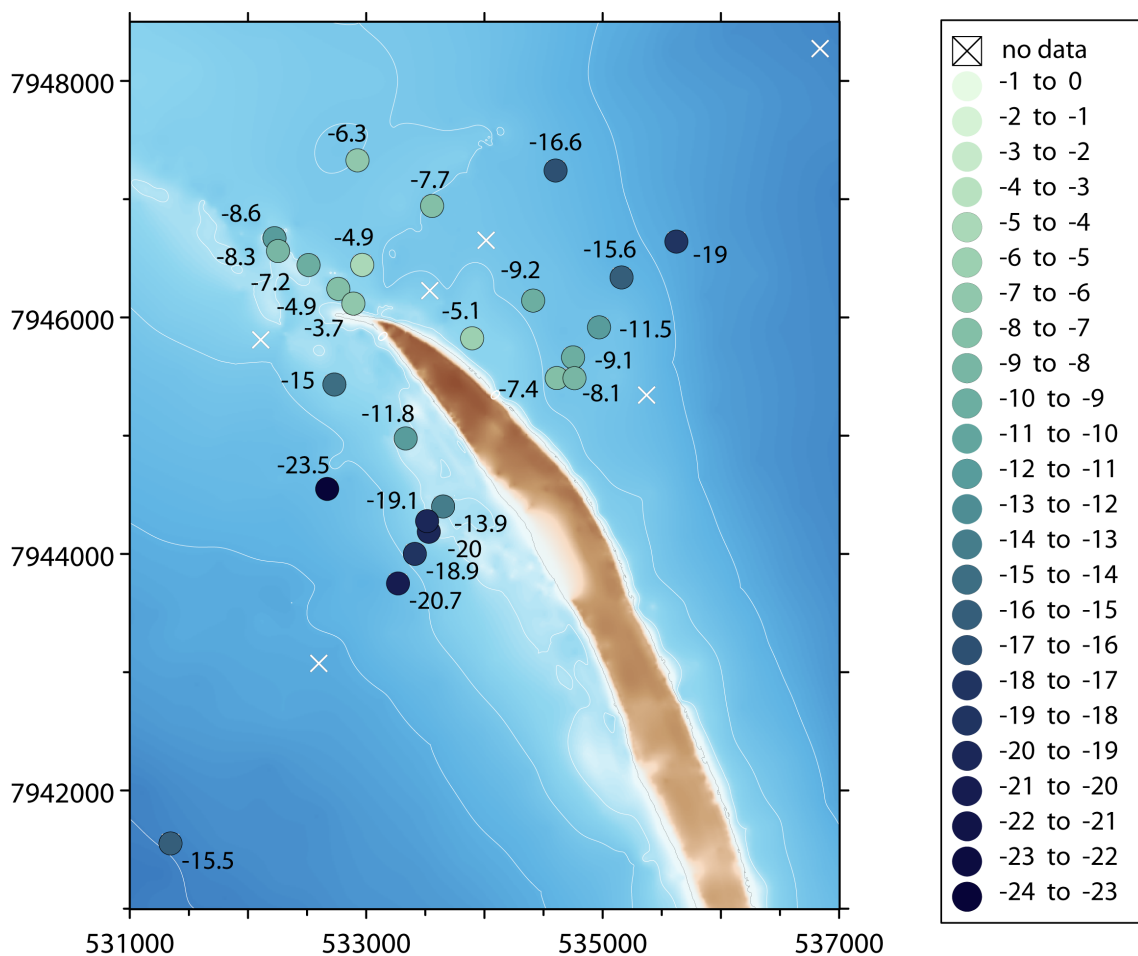


Figure 2.17: Elevation map of the north end of Muostakh Island showing the compiled 2013 and 2016 data sets of sensor positions and derived depth of the top of ice-bonded permafrost below the sea floor. White X denote failed station positions.

Year	Latitude	Longitude	Water depth	f_0 (Hz)	Top of Ice-Bonded Permafrost Depth ^a	
					(m bsf)	(m bsl)
2013	71.63904379	129.8438997	3.2	2.05 ± 0.02	14.7 ± 1.8	17.9 ± 1.8
	71.62894145	129.881091	3.1	-	-	-
	71.61921206	129.9156299	3.0	3.45 ± 0.11	8.6 ± 1.1	11.6 ± 1.1
	71.61713776	129.9237189	2.2	4.15 ± 0.03	7.2 ± 0.9	9.4 ± 0.9
	71.61529225	129.9307888	3.3	6.11 ± 0.06	4.9 ± 0.6	8.2 ± 0.6
	71.61416309	129.9343388	2.4	8.09 ± 0.12	3.7 ± 0.5	6.1 ± 0.5
	71.57344042	129.8885004	8.0	1.95 ± 0.06	15.5 ± 2.0	23.5 ± 2.0
	71.58686183	129.9247101	6.7	-	-	-
	71.59289158	129.9440207	5.2	1.47 ± 0.12	20.7 ± 2.6	25.9 ± 2.6
	71.5951127	129.9481692	4.1	1.61 ± 0.07	18.9 ± 2.4	23.0 ± 2.4
	71.5967724	129.9516009	2.6	1.51 ± 0.07	20.0 ± 2.5	22.6 ± 2.5
	71.59867361	129.955139	2.3	2.15 ± 0.03	13.9 ± 1.7	16.2 ± 1.7
	71.60827065	129.9829098	4.7	4.04 ± 0.05	7.4 ± 1.1	12.1 ± 1.1
	71.60981922	129.9869092	4.9	3.31 ± 0.05	9.1 ± 1.2	14.0 ± 1.2
	71.61206384	129.9932691	4.7	2.60 ± 0.03	11.5 ± 1.5	16.2 ± 1.5
	71.61846553	130.0121896	6.7	1.58 ± 0.03	19.0 ± 2.4	25.7 ± 2.4
	71.63284637	130.0475286	7.8	-	-	-
2016	71.603875	129.946396	3.1	2.54 ± 0.02	11.8 ± 1.5	14.9 ± 1.5
	71.597582	129.951231	2.7	1.57 ± 0.02	19.1 ± 2.4	21.8 ± 2.4
	71.600139	129.92736	5.8	1.28 ± 0.05	23.5 ± 3.1	29.3 ± 3.1
	71.608051	129.929481	3.8	2.00 ± 0.02	15.0 ± 1.9	18.8 ± 1.9
	71.611461	129.911951	4.3	-	-	-
	71.618231	129.916436	3.5	3.62 ± 0.07	8.3 ± 1.0	11.8 ± 1.0
	71.617081	129.936609	5.5	6.13 ± 0.37	4.9 ± 0.7	10.4 ± 0.7
	71.61499	129.95275	4.9	-	-	-
	71.611388	129.962742	4.9	5.83 ± 0.03	5.1 ± 0.6	10.0 ± 0.6
	71.60824	129.987165	6.0	3.70 ± 0.05	8.1 ± 1.0	14.1 ± 1.0
	71.606807	130.004419	6.5	-	-	-
	71.615818	129.998872	6.2	1.92 ± 0.01	15.6 ± 2.0	21.8 ± 2.0
	71.614173	129.977542	6.0	3.27 ± 0.02	9.2 ± 1.1	15.2 ± 1.1
	71.618741	129.966472	5.5	-	-	-
	71.624004	129.98344	6.5	1.80 ± 0.02	16.6 ± 2.1	23.1 ± 2.1
	71.621472	129.953626	5.5	3.90 ± 0.04	7.7 ± 1.0	13.2 ± 1.0
	71.625017	129.935863	4.9	4.78 ± 0.04	6.3 ± 0.8	11.2 ± 0.8

^a Calculated assuming $v = 120 \text{ m s}^{-1}$.

Table 2.3: Combined list of all positions with observed thaw depth in 2013 and 2016 around the northern part of Muostakh Island in the central Laptev Sea, obtained by the passive seismic technique.

CHAPTER 3

Modelling of subsea permafrost degradation processes

Numerical modelling is a powerful method to infer the occurrence of a phenomenon based on the prevailing environmental conditions and the governing underlying physical processes, which connect such conditions to the phenomenon. Due to the sparsely distributed measurements of subsea permafrost (i.e. temperature, salinity, and distribution), the current understanding of the extent, thermal state and stability of permafrost in the Laptev Sea shelf is primarily based on modeling results [Nicolosky et al., 2012]. The scarcity of data is due to a variety of reasons as discussed in Chap. 1, and include the limited access of large research vessels to the shallow near-shore zone of the shelves and hampered instrumentation by the dynamic nature of the transitional zone to the marine environment. In particular, shifting sediments and seasonal sea ice movement inhibit instrumentation during key periods for their ability to destroy measurement devices, moorings, and data cables. Physical process-based modelling therefore provides the best estimate for the distribution of subsea permafrost on large areas up to the pan-Arctic scale in the absence of direct observational data.

In turn, the accuracy of such a model approach fundamentally depends on two facts: (i) all relevant physical processes are understood and implemented, and (ii) observations or assumptions exist of the dominating input parameters for the governing physical processes, i.e. the necessary environmental conditions. The modelling approach then promises to provide a physically sound prediction of permafrost evolution on the Arctic continental shelf. For such a scheme, a physical or numerically parameterized description must exist for the different prevalent processes. Limitations are introduced if not all occurring processes are incorporated – due to complexity or simply lacking knowledge –, and by the uncertainty in the input parameters which drive the physical processes. In practise, however, some physical influences impact a system more than others, so that a generally good estimation can be derived if at

least the dominant parameters are well known. Nonetheless, it is essential to validate the correctness of the model before applying it to large scale estimations and the varying input parameters around the Arctic. In summary, modelling can thus serve two purposes: to infer the regional extent of permafrost and to study processes that drive its degradation.

3.1 An overview on subsea permafrost modelling

Numerical simulations have played a major role in the efforts to extend our understanding of the phenomenon of subsea permafrost and its extent on the Arctic continental shelves. To this aim, the dynamics of subsea permafrost after inundation have been explored with model calculations of growing complexity. Models can be classified by which physical processes are included. Broadly, models either (1) use a Neumann solution-type with a simple moving phase boundary or a more continuous variation of the physical permafrost properties at the phase boundary in a partially frozen zone and (2) do not include salt or include static effects of salt on the thermal state or incorporate salt transport.

Employing a Neumann solution-type and not treating salt, Lachenbruch [1957] analytically studies the thermal response (a moving thawing front at which all freeze/thaw processes occur) of a frozen homogeneous half space under the influence of a sea water body after a succession of step transgressions in a very simplified shoreline setting of flat topography. Subsequently, Harrison and Osterkamp [1978] carry out an early quantitative investigation generalizing the Stefan problem to include salt diffusion. They solve the coupled equations analytically for a simple limiting case to the conditions at Elson Lagoon and Prudhoe Bay in the Alaskan Beaufort Sea to discuss the breakdown of the diffusive regime in salt and heat transport. Delisle [2000], in an attempt to explain geoseismic permafrost interpretations in the Laptev Sea, undertakes thermal modeling and also discusses scenarios of paleoriver influence and the gas hydrate stability zone. The model achieves regional climatic forcing, but does not include saline freezing point depression nor salt transport. Romanovskii and Hubberten [2001] and Romanovskii et al. [2003] include a simplified salt influence by distinguishing a constant freezing point depression between marine and terrestrial deposits, leaving out only salt diffusion and its effect on the upper permafrost table. They show that permafrost on the Laptev Sea shelf has been preserved throughout transgressions of the last four glacial-interglacial cycles.

In a next step, models included the ‘mushy’, i.e. plastic, partially frozen transition zone due to the existence of liquid water in soils at below 0 °C temperatures. Oster-

kamp [1987] introduces a transition layer to the originally 2-layer Neumann solution. Nixon and Halliwell [1983] and Nixon [1986] also model permafrost temperatures while directly calculating the liquid water content in soils at cryotic conditions. Similarly, Taylor et al. [1996] employ a thermal diffusion model with liquid water parameterization, saline freezing point depression, but no salt transport, in order to interpret the paleoenvironmental history of the Beaufort Shelf, Canada. To reconcile the sparse permafrost observations with sediment properties and the paleoenvironment, Taylor et al. [2013] demonstrate that the last 125,000 years were sufficient to develop the present permafrost base depth and seaward extent on the Canadian continental shelf. Open taliks below previously developed thermokarst lake taliks on the East Siberian Arctic Shelf are created when including salt contamination in simulations [Nicolosky and Shakhova, 2010]. Most recently, Nicolosky et al. [2012] provide a comprehensive subsea permafrost distribution map on the Laptev Sea shelf using numerical modeling which incorporates an up-to-date paleo-geographic scenario and geological structure. Figure 3.1 shows their results as the most current, modelled distribution of subsea permafrost on the Laptev Sea shelf. Their model consists of thermal conduction considering liquid water fraction as well as altered physical properties due to the presence of salt, but no salt transport. They identify sediment salinity and unfrozen water parameterization as being critical to the evolution of subsea permafrost and emphasize the need to account for the coupled distribution mechanisms of salt in the subsurface.

Finally, a description of salt transport has been attempted in numerical models of subsea permafrost. Vasil'ev et al. [1995] develop a generalization of the Stefan problem numerically including salt diffusion and the plastic region of partially frozen sediments where salt diffusion occurs in the liquid water fraction. Lucas [2001] presents modeling of thawing and freezing of a finite porous slab in contact with an

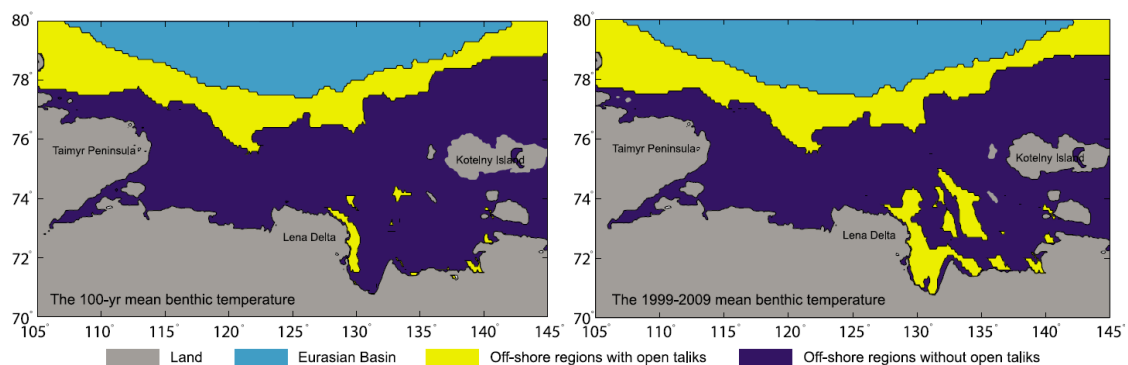


Figure 3.1: The modelled distribution of permafrost on the Laptev Sea shelf, illustrating the areas where taliks may exist. Two scenarios of benthic temperature forcing are shown. (Graph taken from Nicolosky et al. [2012].)

external saline solution, extending the resolution for a wide range of temperatures and solute concentrations, while considering purely diffusional mass transport in the liquid phase. Recent work [Dmitrenko et al., 2011] incorporates salt diffusion and suggests that observed bottom water warming will decrease permafrost thickness and gas stability on the eastern Siberian shelf by the end of the next millenium.

3.2 Salt distribution - mechanisms beyond diffusional transport

Salt infiltration constitutes the primary mechanism for downward degradation of ice-bonded subsea permafrost [Osterkamp et al., 1989]. Pore water salinity affects the thermal capacity, alters the freezing characteristic curve (the unfrozen water content as a function of negative temperature), depresses the freezing point and drives permafrost thaw under the slightly sub-zero temperatures in the Arctic shelf sediments. A complex suite of processes in the marine environment potentially impacts this transportational regime of infiltrating pore water (Sect. 1.1.4).

Beyond diffusion, water flow in the thawed and partially thawed pore spaces can also transport salt downward into the sediment. This advective regime is recognized to be important to the degradation of the upper permafrost table [Harrison and Osterkamp, 1978]. It is established that heat transport may remain diffusive while salt transport can simultaneously be advective due to several orders of magnitude difference in the respective diffusivities [Harrison and Osterkamp, 1978, Musgrave and Reeburgh, 1982, Ingebritsen et al., 2007]. Advecting water, though not appreciably contributing to heat transport, thus affects the thaw rate because it determines salinity and consequently the phase change temperature and position of the ice-bonded permafrost table [Harrison and Osterkamp, 1982]. One mechanism for advective flow is free (gravity-driven) convection of the interstitial water in the thawed layer [Musgrave and Reeburgh, 1982, Harrison and Osterkamp, 1982, Harrison, 1982]: Here, water flow is driven by the density difference between dense sea water on top of relatively fresh and buoyant water from melting ice at the permafrost table, with rapid salt transport into the thawing sediment for relatively permeable sub-seabottom sediments. Field observations at Prudhoe Bay, Alaska, reveal a well-developed convective regime and a thin boundary layer, where salt transport transitions to a purely diffusive regime above the phase boundary. Characteristic vertical pore water velocity is estimated to be of the order of a few tenths of a meter per year at the site. Pressure data also supports the interpretation of pore water motion, but the driving source remains unclear [Swift et al., 1983]. Both energy considerations and numerical

calculations [Swift and Harrison, 1984] yield that gravity driving alone cannot account for observations and demonstrate the need to consider so far unidentified processes. Another similar aspect are reports on laboratory measurements of salt fingering on a small scale of centimeters as a potential mechanism for rapid salt transport especially in the near-shore zone of seasonal sea bed freezing and bottom-fast sea ice [Baker and Osterkamp, 1988]. As these indicate higher pore fluid velocities consistent with field measurements of pressure gradients and as conditions at Prudhoe Bay, Alaska are shown sufficient to initiate this process [Gosink and Baker, 1990], these authors suggest that the laboratory experiments potentially offer more satisfactory explanations of observed permafrost degradation depths. Based on the Stefan-type model of Swift and Harrison [1984], gravity-driven convection has subsequently been studied to determine critical Rayleigh numbers for its onset [Galdi et al., 1987, Payne et al., 1988, Hutter and Straughan, 1997, Budu, 2001] or analyze necessary scalings to fit specifically to field conditions at Prudhoe Bay [Hutter and Straughan, 1999]. However, Hutter and Straughan admit that a non-horizontal phase boundary may explain observations better, and further physical processes may contribute through the interactions between ocean circulation and pore water flow field.

Are [2003] finds that salt transport in subsea sediments generally cannot be accounted for by diffusion alone. Next to free convection, a complex suite of other marine processes potentially influences pore water velocities or solute distribution in the sediments: Near bottom currents or reciprocating wave movement in the water column hydraulically initiate pore water movement. This is especially significant for coarse sands. Other sources of forced advection are cryogenic pressure during adfreezing of bottom-fast sea ice and moisture migration to the freezing zone. Further distribution processes include saline brine injection from freezing saline water during adfreezing of bottom-fast sea ice or active layer freezing in the near-shore zone. Additionally, large wave or storm perturbation of the fine-grained upper portion of the sea bottom sediments can lead to thorough mixing with sea water in the pore space. The scale of affected sediment depth is unknown, but remote sensing shows sediment stir in the water column after storms to water depths of about 10 m.

3.3 Open questions in salt transport and permafrost degradation

Although the importance of accurately capturing the infiltration mechanisms of salt into the subsurface after ocean inundation has been demonstrated, we lack mathematical models of mass transfer coupled with subsea permafrost dynamics.

A mathematical development of all participating physical and chemical processes is difficult [Are, 2003]. In-situ investigations to study the marine processes have not been carried out. Accounting for salt transport processes beyond diffusion in modelling efforts has been primarily limited to gravity-driven convection. However, free convection has only been evaluated in the context of a Stefan-type impermeable moving phase boundary, but remains unstudied in sediments with significant partially frozen regions and their associated retained liquid water fractions. It has further been shown not to account for all observations [Swift and Harrison, 1984], emphasizing the relevance of the other processes potentially influencing pore water velocity and solute distribution in the sediments. Other transport and coastal processes have not been included in any modeling effort of subsea permafrost. Realistic salt transport incorporations in model calculations are needed that describe the observations of permafrost degradation after inundation.

Variable degradation rates and trends in slopes of permafrost table offshore are observed at several locations in the Russian Arctic [Overduin et al., 2007b], indicating that differences in the locally prevailing degradation processes occur. Capturing the fundamental driving processes during the transition to the marine environment is the essential requirement for the ability to eventually extend numerical calculation to large-scale regions. It is therefore important to dissect involved physical transport processes and identify the dominant drivers. To this aim, numerical modelling of processes on the local scale can be constrained by detailed local data and allow for an assessment of marine processes and their relative impacts in subsea permafrost degradation. It further allows to assess our ability to explain local observations, and therefore validate the sufficiency (with respect to the inclusion of all relevant processes) of the physical process-based model for subsea permafrost evolution.

Currently, state-of-the-art subsea permafrost models applied to large regions remain based solely on thermal physical processes (heat conduction and static saline effects on the thermal state), and focus on refining the input parameters in the paleoenvironmental boundary conditions to these processes. However, salt infiltration constitutes the primary mechanism for downward degradation of ice-bonded subsea permafrost. Salt transport within the sediment is driven by a complex suite of potential processes, but quantitative mathematical development is lacking [Are, 2003]. Furthermore, questions on the sufficiency of salt transport mechanisms in the process-based models remain unresolved, due to a lack of areas with sufficient information and observational measurements to fully test model predictions [Osterkamp, 2001]. Improved understanding of the driving processes on a local scale is a prerequisite to the prediction of subsea permafrost occurrence and how perforated it is, i.e. its state in temperature and pore ice content, on the Arctic scale.

3.4 Modelling objectives

This study utilizes the only two well-documented data sets of permafrost borehole transects in the Laptev Sea region that comprise both onshore and near-shore (offshore) boreholes at the same location: The COAST transect drilled 5 boreholes into the subsea permafrost in the western Laptev Sea in 2005 [Overduin et al., 2007a], and in 2012 two boreholes were drilled at Buor Khaya Bay [Günther et al., 2013b]. With its higher number of boreholes, the former data set may potentially yield information on the different stages (i.e. zones) during the transgression. Additionally, modelling is evaluated against the newly acquired geophysical data set from Muostakh Island (Chap. 2).

These three local data sets allow the investigation of permafrost evolution coupled with salt transport and distribution processes, and thus, to evaluate the role of processes that potentially influence degradation based on local-scale numerical modelling. By better capturing salt infiltration processes in near-shore studies, the model aims to represent a more complete picture of the transition of permafrost from terrestrial to submarine conditions. In light of our current inability to develop full mathematical models of these complex processes, this study proposes to investigate these dynamics and their effect on permafrost degradation rates, thaw depth, ice content and salt distribution in parameterized implementations in a model of reduced complexity.

The objectives of this chapter are to

- (i) develop a numerical model for subsea permafrost evolution, coupling heat transport and salt effects. The model encompasses latent heat effects in partially unfrozen sediments and the effect of saline pore waters on the liquid water curve in porous sediments.
- (ii) assess the relative impact on degradation depths, rates and salt distribution of the inundation processes. Tested parameters include initial temperatures, sea bottom temperatures, cliff erosion, and coastline retreat rates. Modelling is constrained by borehole data from the COAST drilling transect and from Buor Khaya and by the newly collected geophysical data. A focus is set on four processes potentially affecting the salt transport in the offshore sediments. The processes include (i) purely diffusive regime, (ii) advective component (as posed by e.g. buoyancy-driven convection), (iii) sediment porosity, and (iv) the presence of prior saline layers.

3.5 Study sites

Are [2003] identifies the shoreface and near-shore zone as the most ideal setting to study inundated permafrost and the associated processes from its inception onwards. Here, local observations can serve as validation and can help test the impact of a variety of influences in modelling studies. All three study sites are shown in Fig. 3.2. The primary study site is located at Mamontov Klyk and comprises the data set of most detail; two secondary study sites are located at Buor Khaya Bay and Muostakh Island, respectively, and were used to supplement the evaluation of model results.

3.5.1 Primary study site: Cape Mamontov Klyk

Cape Mamontov Klyk lies in the Western Laptev Sea approximately halfway between the Anabar and Olenek Rivers. The coastal lowlands were once part of the large, late Pleistocene accumulation plains, stretching northward from the modern coastline. In this region 20–30 m thick ice-supersaturated Ice Complex deposits overlie less ice-rich fluvial silts and sands with peat layers [Schirrmeister et al., 2008]. A 65.1 m deep onshore core (C1: 73°36'21.5"N, 117°10'38.5"E) as well as four offshore cores (C2–C5) with depths up to 77 m below sea level (bsl) were drilled in April 2005 as part of a coastal and offshore drilling program [Overduin et al., 2007a]. This north-south transect (along 117°10'E) of five boreholes perpendicular to the shoreline is the primary source for modelling of the transgressional history and the different stages of inundation. The onshore borehole is located on a bluff on the coastal plain where thermokarst and lakes affect about 50% of the coastal plain landscape [Grosse et al., 2006]. The upper stratigraphy of the borehole is Ice Complex deposits of Late Pleistocene origin with ground ice content of up to and exceeding 80% by volume. The subsurface is mostly silty sand with relatively high organic content [Schirrmeister et al., 2008]. The thawing coastal bluff is 25–30 m high. In the Western Laptev Sea, upper Cretaceous-Cenozoic sandy-silty deposits several kilometers thick overlie the bedrock. At Cape Mamontov Klyk, at least 2 km of these sandy silts are inferred from seismic-geological profiles [Schwamborn, 2004, Grigoriev et al., 1996]. Hinterland is gently inclined, dipping slightly towards the sea in the north at a mean angle of 0.1° [Schirrmeister et al., 2008]. The low dip angle of less than 0.05° continues offshore, as evidenced in the bathymetry at the site of the transect, for the next 13 km. Figure 3.2 b shows a cross-sectional overview of the COAST transect. The offshore boreholes ranged between 1.5 and 6 m water depth, including bottom-fast ice conditions encountered at the borehole closest to the coast. The furthest borehole was located 11.5 km offshore. Ice-bonded permafrost was encountered at depths

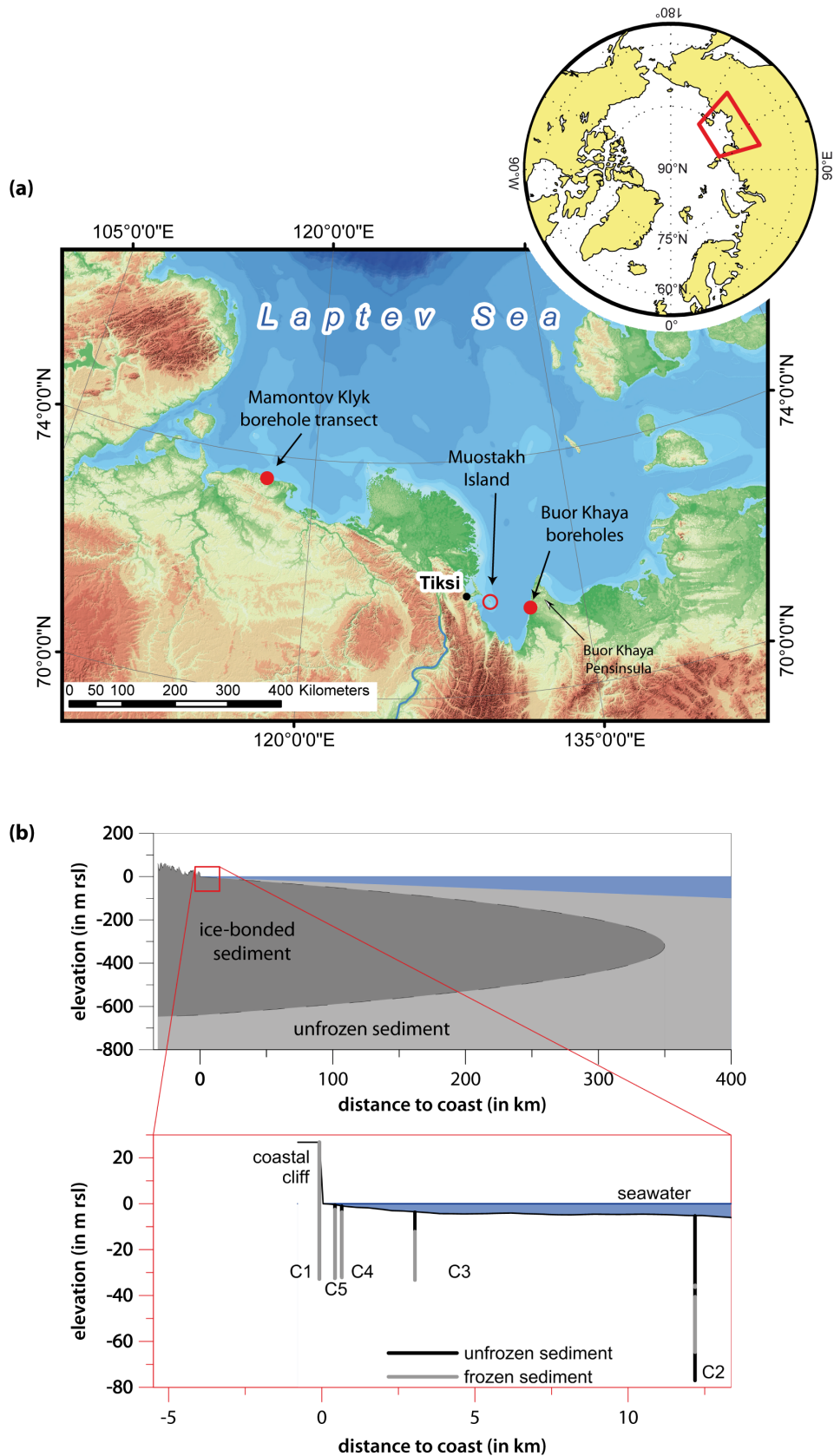


Figure 3.2: (a) Laptev Sea with the location of the three study sites: At Cape Mamontov Klyk in the western Laptev Sea, and at Buor Khaya Bay and on Muostakh Island in the central Laptev Sea. (b) Cross-sectional overview of the borehole transect at Mamontov Klyk in the COAST Drilling Campaign.

between 2.8 and 35 m bsl. Profiles of pore water salinity from laboratory analysis are given by Overduin et al. [2007a]. Borehole sediment composition, including organic, mineral, and water contents, is given by Winterfeld et al. [2011]. Most publications regarding the COAST transect to date [Rachold et al., 2007, Winterfeld et al., 2011, Mitzscherling et al., 2017] base coastal erosion rates at Mamontov Klyk on current coastline retreat rates of relatively rapid 4.5 m a^{-1} [Grigoriev, 2008] compared to an average of 2.5 m a^{-1} for Ice Complex coastlines in this region [Arctic Coastal Dynamics Project Team, 2008, Grigoriev and Rachold, 2003]. However, Günther et al. [2013a] observes short-term and long-term coastline retreat, and confirms current short-term erosion rates of $4.6 \pm 1.2 \text{ m a}^{-1}$, but finds mean long-term (c. 40 a) erosion rates of 2.9 m a^{-1} . Based on the current mean rate and distance offshore, the five boreholes offer snapshots of the degradation stages after approximately 108, 217, 652, and 2500 years. Based on the 40-year mean rate, the farthest offshore borehole in the transect would already have been flooded 3965 years ago.

3.5.2 Secondary study sites: Buor Khaya & Muostakh Island

Two sites provide a less extensive data set on the transgressional history: Two boreholes (one onshore, one offshore) on the western coast of the Buor Khaya Peninsula ($71^{\circ}25'13.0''\text{N}$, $132^{\circ}06'38.0''\text{E}$) and the geophysical detection area around Muostakh Island ($71^{\circ}35'\text{N}$, 130°E). The former yields only a transition between the two boreholes without access to different intermediate stages, but does provide sediment composition from borehole analysis; the latter provides several, spatially distributed locations of degradation depth, but does not include a ground-truthed data set of site-specific sediment composition, and modelling must rely on a synthetic core profile.

In the Buor Khaya Bay, two boreholes were drilled in April 2012 off the coast west of the Buor Khaya Peninsula in the framework of the Drilling Expedition Buor Khaya [Günther et al., 2013b]. The peninsula is part of the Yana-Omoloi interfluvium. It is an uplifted block bordered by two grabens which dissipate north of the Buor Khaya Cape [Imaeva et al., 2007]. The coastal landscape is covered by thermokarst depressions (9–14 m above sea level (asl)) and Yedoma/Ice Complex hills (up to 37 m asl), and generally characterized by an eroding Ice Complex and shoreline retreat. Isolated Yedoma remnants remain in only 15% of the area [Günther et al., 2013a]. The hinterland is dipped slightly towards the north with a mean angle of 0.05° . One onshore borehole (18.9 m deep) is located at the peak of a small Yedoma hill (35 m asl), being actively eroded at the coast; the offshore borehole (51 m deep below the sea ice surface) was drilled about 750 m offshore in 4.3 m deep water from the sea ice

cover. Ice-bonded sediment is encountered in the offshore borehole at 24.75 m below the sea floor. Sediment composition is given by onshore outcrop data [Strauss et al., 2017, Schirrmeister et al., 2017] and offshore borehole data [Overduin et al., 2015b]. The bathymetry and bottom water along the transect sampled at 8 locations is given by Günther et al. [2013b]. The mean annual erosion rate along a segment closest to the borehole site has been $1.4 \pm 0.8 \text{ m a}^{-1}$ for the past c. 40 years [Günther et al., 2012, Overduin et al., 2015b]. Based on the borehole distance from the modern coastline and on the mean erosion rate, the time period of inundation at the offshore borehole is about 530 a.

Muostakh is a small island about 40 km offshore Tiksi in the Buor Khaya Bay of the central Laptev Sea. The island is elongated and narrow in form, about 7.5 km long and less than 500 m wide. The island was originally connected with the Bykovsky Peninsula further in the north, but is now separated by 15.8 km of ocean [Grigoriev, 1993, Grosse et al., 2007, Overduin et al., 2016]. Both Bykovsky and Muostakh represent remnants of the Late Pleistocene accumulation plain, which remained after sea levels had reached their current level in the Holocene transgression, and has been largely destroyed by coastal thermo-erosion since. Muostakh consists mainly of Late Pleistocene Ice Complex deposits (ground ice content is 87% by volume [Günther et al., 2015]) underlain by ice-poor sands of Pliocene-Early Pleistocene age [Slagoda, 2004]. On Muostakh, the thickness of the Ice Complex deposits is 31 m and extends 10 m below the sea level [Kunitsky, 1989, Grigoriev, 1993, Günther et al., 2015]. More information on the island, coastal erosion rates and depth to ice-bonded permafrost are given in Sect. 2.5. Regarding the area of collected geophysical data, the northern spit area and its associated complex sediment repositioning potentially impair the assumption of steady coastal retreat rates. Therefore, this study used the west-east transects (A-A' in Fig. 2.11) furthest to the south, and perpendicular to the shoreline to evaluate against modelled permafrost degradation. Based on the distance of the furthest instrument off the coastline (about 2 km), and on the mean annual erosion rate (2.32 m a^{-1}), the furthest point in the east transect was flooded around 882 a ago. The west transect ranges 4 km offshore, with mean annual erosion rates of 0.23 m a^{-1} .

The Laptev Sea climate is Arctic continental and characterized by 8–9 month harsh winters and short cold summers of 2–3 months. Thick one-year land fast sea ice covers the coastal sea for most of the year [Günther et al., 2013a]. Ice formation begins between September and October with melting starting between late May and early June. Generally ice free conditions prevail in August and September, with sea-ice free conditions lasting 20% in the eastern, and only 14% of the year in the western Laptev Sea [Dunaev and Nikiforov, 2001]. However, ice formation is of high

interannual variability.

3.6 Developing a model for subsea permafrost

3.6.1 Thermal regime of the subsurface: governing equations of conductive heat transfer

In this section, the governing equations for heat transfer within the soil are derived, following loosely Jury and Horton [2004] and Westermann [2010], and focussing on soil freezing processes in the saturated sub-sea floor sediments.

Given a volume V of soil, its internal energy $E(t)$ is $E(t) = \int_V e(\vec{x}, t) d^3x$, with the energy density $e(\vec{x}, t)$. Local thermodynamic equilibrium is assumed in all elementary volumes in the volume integration, so that the definition of a local temperature and associated internal energy per unit volume is meaningful.

Conservation of energy yields that a change in the internal energy of the volume over time must equal the energy flux $\vec{j}_e(\vec{x}, t)$ across the surface S of the volume:

$$\begin{aligned} \frac{d}{dt} E(t) &= \int_V \frac{d}{dt} e(\vec{x}, t) d^3x \equiv - \oint \vec{j}_e(\vec{x}, t) \cdot \vec{n} d^2x \\ &= - \int_V \nabla \cdot \vec{j}_e(\vec{x}, t) d^3x, \end{aligned}$$

where \vec{n} is the unit vector normal to the surface, and Gauss's Theorem was applied in the last step. The equation must be satisfied for any arbitrary V , thus one obtains

$$\frac{d}{dt} e(\vec{x}, t) + \nabla \cdot \vec{j}_e(\vec{x}, t) = 0. \quad (3.1)$$

Regarding the first term in equation 3.1, in the case of permafrost soil, the internal energy e is a function of temperature T and the volumetric fractions $\Theta_{w, i, a, o, s}$ of water, ice, air, organic, and the solid matrix. For constant volumetric fractions, the term becomes

$$\frac{de}{dt} = \frac{\partial e}{\partial T} \frac{\partial T}{\partial t} = c_h \frac{\partial T}{\partial t}$$

with the specific volumetric heat capacity c_h . c_h can be expressed as the weighted

sum of the heat capacities $c_{w,i,a,o,s}$ of the individual soil constituents:

$$c_h = \Theta_w c_w + \Theta_i c_i + \Theta_a c_a + \Theta_o c_o + \Theta_s c_s.$$

In general, however, the volumetric fractions are not constant. In permafrost soils, specifically, phase change of pore water or infiltration of water results in variable composition fractions. In the saturated conditions of the subsea sediments, the air constituent and infiltrating water can be neglected. The phase change of interstitial water, i.e. freezing of water and thawing of ice, however, must be explicitly considered, in order to account for the associated latent heat effects.

Assuming Θ_o and Θ_s to be constant, and the sum of Θ_w and Θ_i to be constant, one needs to further consider that not all water in a porous medium such as soil or sediment does freeze at the freezing temperature of free water. Instead, a fraction of unfrozen water persists at subzero temperatures, due to the interfacial energy between water and the solid matrix, with a generally decreasing trend with decreasing temperature. The result is a functional relationship between the unfrozen water content Θ_w and temperature, the so-called soil freezing characteristic (see Sect. 3.6.1.2). The change along this curve can be used to describe the latent heat effects as a function of temperature in a definition of an effective heat capacity. Defining $e = 0$ at $T = 0^\circ\text{C}$ and all water in the liquid phase, and only considering the phase transition from liquid water to ice, e is given by $e = T \cdot (\Theta_w c_w + \Theta_i c_i + \Theta_s c_s + \Theta_o c_o) - L_f \Theta_i$, with L_f the volumetric latent heat of freezing/fusion [Ippisch, 2001]. The first term in equation 3.1 then becomes

$$\begin{aligned} \frac{de(T, \Theta_w(T), \Theta_i(T))}{dt} &= \frac{\partial e}{\partial T} \frac{\partial T}{\partial t} + \frac{\partial e}{\partial \Theta_w} \frac{\partial \Theta_w}{\partial T} \frac{\partial T}{\partial t} + \frac{\partial e}{\partial \Theta_i} \frac{\partial \Theta_i}{\partial T} \frac{\partial T}{\partial t} \\ &= c_h(T) \frac{\partial T}{\partial t} + c_w T \frac{\partial \Theta_w}{\partial T} \frac{\partial T}{\partial t} + (c_i T - L_f) \left(-\frac{\partial \Theta_w}{\partial T} \right) \frac{\partial T}{\partial t} \\ &= \left[c_h(T) + (L_f + (c_w - c_i)T) \frac{\partial \Theta_w}{\partial T} \right] \cdot \frac{\partial T}{\partial t}, \end{aligned} \quad (3.2)$$

where c_h is now a function of temperature (because of the varying ice and water contents). The relation $\frac{\partial \Theta_i}{\partial T} = -\frac{\partial \Theta_w}{\partial T}$, obtained by differentiating the constant sum of Θ_w and Θ_i , was used in the second line. At reasonable temperatures, the term $(c_w - c_i)T$ can be neglected against the volumetric latent heat of fusion L_f , as it is much smaller, and the term can be omitted. Thus, one can define an effective volumetric heat capacity

$$c_{\text{eff}}(T) = c_h(T) + L_f \frac{\partial \Theta_w}{\partial T} \quad (3.3)$$

in order to account for the phase change at temperatures below 0 °C in the heat transport equation.

The second term in equation 3.1 regards the heat fluxes out of and into the soil volume V . The main mechanism for heat transfer in soil and sediments generally is by conduction, while contributions of mass fluxes of liquid water remain negligible at the typically prevailing flow rates (Peclet number $\ll 1$, which provides a measure of the relative strength of convective versus conductive heat transfer) [Ingebritsen et al., 2007, Majorowicz et al., 2004, Harrison and Osterkamp, 1978]. Fourier's law of heat conduction yields the conductive ground heat flux \vec{j}_g

$$\vec{j}_g = -\lambda_h(T)\nabla T, \quad (3.4)$$

with λ_h the thermal conductivity of the sediment. λ_h is parameterized according to the de Vries [1963] model and modified by Ippisch [2001] and Campbell et al. [1994]: The thermal conductivity of a porous medium with components of water, ice, air, organic and mineral matrix depends on the composition, but also on the distribution of these phases and the geometry of the pore space. de Vries [1952] developed an empirical relationship to describe the total thermal conductivity as a function of the composing conductivities λ_i of the five phases $i = w, i, a, o, m$

$$\lambda_h = \frac{\sum_i f_i \Theta_i \lambda_i}{\sum_i f_i \Theta_i}.$$

Weighting factors f_i are used to describe the distributional effect of these phases with their associated individual conductivities. The concept behind it [Campbell et al., 1994] introduces one of the component phases as interconnected and continuous, while the other components occur as discontinuous domains embedded in the continuous phase. Weighting factors are given by

$$f_i = \left[1 + \frac{1}{3} \left(\frac{\lambda_i}{\lambda_{\text{cont}}} - 1 \right) \right]^{-1},$$

in which, for simplicity, the sediment particles have already been assumed spherical [Ippisch, 2001]. For the varying water and ice contents in permafrost sediments, a transition of the continuous phase from water to ice is implemented as suggested by Campbell et al. [1994], which specifies λ_{cont} in the equation. This method can also deal with a non-zero air fraction by interpolating between three such bi-component transitional systems (only air-water, air-ice, and ice-water), which span a three-dimensional space [Ippisch, 2001]. Thus, the thermal conductivity λ_h , like the heat capacity, is a function of the volumetric fractions of the sediment constituents, and

consequently, of temperature.

Finally, heat conduction in soil or sediments is approximated as a one-dimensional problem in this study, i.e. with a temperature gradient only in the vertical z -direction. Substituting Eqs. 3.2 and 3.4 in Eq. 3.1, the governing equation for conductive heat transfer in soil or sediment is obtained:

$$c_{\text{eff}}(z, T) \frac{\partial T}{\partial t} - \frac{\partial}{\partial z} \left(\lambda_h(z, T) \cdot \frac{\partial T}{\partial z} \right) = 0, \quad (3.5)$$

incorporating the phase change between water and ice.

3.6.1.1 Instructive example: solution with periodic forcing

It is instructive to consider a simplified case of heat transfer to provide some qualitative insights into fundamental aspects of heat transport in permafrost: Considering a semi-infinite half-space of soil with uniform thermal parameters (heat capacity and thermal conductivity constant with depth), and the phase change of water is neglected, then the governing heat conduction equation becomes a simple one-dimensional diffusion equation for temperature

$$\frac{\partial T(z, t)}{\partial t} - d_h \frac{\partial^2 T(z, t)}{\partial z^2} = 0, \quad (3.6)$$

with the thermal diffusivity $d_h = \frac{\lambda_h}{c_h}$. Assuming a constant-temperature initial condition may be written as $T(z, 0) = T_0 = \text{const}$. Imposing a periodic forcing at the surface boundary $T(0, t) = T_0 + T_{\text{ampl}} \cdot \sin(\omega t)$, with the angular frequency $\omega = 2\pi f$, and a lower boundary of unchanged constant temperature at infinite depth, i.e. $\lim_{z \rightarrow \infty} T(z, t) = T_0$, the diffusion equation can be solved. For example, an oscillation period at the surface $\frac{1}{f}$ of one day would represent the diurnal cycle, while one year would be a seasonal cycle. The solution can be obtained as

$$T(z, t) = T_0 + T_{\text{ampl}} e^{-kz} \sin(\omega t - kz) \quad \text{and} \quad k = \sqrt{\frac{\omega}{2d_h}}, \quad (3.7)$$

with the wave number k .

The surface amplitude is damped for the oscillation at depth (damping factor $D(z) = e^{-kz}$) and a phase shift is introduced ($\phi(z) = kz$). Both are a function of depth. The phase velocity of the downward-propagating heat wave is $v_{ph} = \omega/k = \sqrt{2d_h\omega}$. The penetration depth is defined by the depth where the surface amplitude is damped to

a fraction of $1/e$ and given by

$$k^{-1} = \sqrt{\frac{2d_h}{\omega}}. \quad (3.8)$$

Thus, the temperature oscillation at depth is also a sine wave with damping factor and phase shift. Both are a function of depth, but also of angular frequency (the wave number k depends on ω). A higher-frequency fluctuation at the surface, compared to a lower-frequency one, shows a larger phase shift ($\phi \sim \sqrt{\omega}$) and penetrates faster into the ground ($v_{ph} \sim \sqrt{\omega}$), but is simultaneously attenuated more rapidly and damped away in more shallow subsurface layers ($k^{-1} \sim \omega^{-\frac{1}{2}}$).

For a typical thermal diffusivity for soils $d_h = 0.5 \cdot 10^{-6} \text{ m}^2\text{s}^{-1}$ (see also Table 4.1), the daily temperature cycle would be rapidly attenuated with a penetration depth of approximately only 0.12 m. The seasonal (annual) temperature oscillation would experience the same attenuation at about 2.2 m. Of course, the situation in real permafrost soils and sediments is more complicated, including e.g. the latent heat of the phase change of water. Nonetheless, the qualitative statement remains valid, in that only long-term average temperatures determine the evolution of temperature in deeper (permafrost) layers. Short temperature cycles decay closer to the surface, and for sufficiently large thaw depths above the permafrost, the shorter cycles no longer contribute to (deeper) permafrost temperature changes. While typical terrestrial active layer depths in the continuous permafrost zone of the Laptev Sea are on the order of decimetres and only diurnal temperature cycles play diminished roles in further development of permafrost temperature changes, the subsea permafrost displays generally increasing thaw depths with time, i.e. distance offshore, for example on the order of 10 m for 1–2 km offshore around Muostakh Island (Chap. 2). Here, also the role of annual temperature variations on further permafrost temperature evolution will diminish with distance to the shoreline.

This special case solution has important implications beyond the simple one-frequency forcing. Variable upper boundary conditions, i.e. an arbitrary surface forcing, can be handled by a Fourier decomposition: Due to the linearity of the differential equation, any arbitrary surface signal may be decomposed in a convenient way. One such way is Fourier decomposition into periodic functions. The arbitrary forcing can thus be solved as the superposition of the solutions to the single-frequency periodic forcing. The insights and significance of this special case, thus, transfer to the general solution of the heat transfer equation. In order to incorporate complicating processes such as the latent heat effects of the freezing characteristic in pore water and varying sediment thermal properties with depth, numerical solving schemes are employed in

this study to simulate permafrost evolution based on Eq. 3.5.

3.6.1.2 Liquid water content and freezing characteristic in porous media

Porous media retain some pore water in liquid form even under cryotic conditions (temperatures below 0 °C). The amount of liquid water depends mainly on the particles' specific surface area and grain arrangement - other governing processes are the applied pressure, the particles' mineralogical and chemical composition and the density as well as the composition of the pore fluid [Hivon and Segoy, 1995, Nixon and Halliwell, 1983]. In general, with decreasing grain size and with increasing deviation from a free water body, surface adsorption effects increasingly decrease the phase change temperature of remaining pore water from the freezing temperature of free water.

Specifically, the internal energy and its associated various representations of thermodynamic potentials of water (i.e. either free or in a porous matrix) determine the equilibrium thermodynamic state and describe, among others, the melting and evaporation curve. Equilibrium state, in this context, implies that the relaxation times of all relevant system parameters are much shorter than the time on which the corresponding environmental variables change. In porous media, when compared to free water, the contribution of interfaces to the internal energy is no longer negligible. One of the consequences is the presence of liquid, unfrozen water at subzero temperatures. Similar to solutes in a liquid, the chemical potential of the liquid phase is reduced by a term which, in this case of a porous matrix, is inversely proportional to the pore radius, due to the attraction by the mineral surface and by the interfacial tension between the liquid and solid water phase. The reduction shifts the intersection of the chemical potentials of the solid and liquid phase of water in a porous medium from the one of free water, and results in a depressed freezing point with decreasing radius of a pore. Thus in a porous medium, as temperature decreases below 0 °C, liquid water in the largest pore voids freezes first and the liquid-ice interface moves into pore spaces with smaller radii. Therefore, the reduced chemical potential in a permafrost soil leads to a depressed freezing point and retained fractions of liquid pore water even at subzero temperatures.

For coarse grained materials the effect is lower than for fine-grained, which have higher capillary and adsorption forces and retain comparatively larger fractions of liquid water at a given subzero temperature. A 'freezing characteristic' is the relationship between temperature T and liquid water content fraction $\Theta_{w,liq}$ for a given sediment material. A typical example in permafrost is shown in Fig. 3.3. In the model, freezing characteristic curves for each sediment layer were used to account

for phase change energy by assessing the latent heat changes necessary during each model time-step (Eq. 3.2).

The phenomenon of unfrozen water in the cryotic sediment results in plastic but ice-bearing sediments in a transition zone between thawed (ice-free) and ice-bonded (cemented) sediments. It affects the subsurface temperature field by changing bulk sediment thermal properties and by extending the spatial and temperature range of significant latent heat effects. This liquid water content greatly influences permafrost dynamics by retarding its thermal response and affecting the development of thermal gradients [Nicolson et al., 2007, Romanovsky and Osterkamp, 2000].

In this study, the material-specific freezing characteristic curve was parameterized by a second order polynomial [Langer et al., 2013]

$$\Theta_{w,liq.}(T) = \begin{cases} \Theta_{w,min} + \frac{\Theta_{w,max} - \Theta_{w,min}}{(1-a \cdot T + b \cdot T^2)} & \text{for } T < 0 \\ \Theta_{w,max} & \text{for } T \geq 0 \end{cases},$$

with maximum and minimum liquid water contents $\Theta_{w,max}$ and $\Theta_{w,min}$, respectively, and where a and b are empirical factors. The factors are given by Langer et al. [2011], based on fitting to Time-Domain-Reflectometry measurements of liquid water content versus temperature for sandy-silty soils in the Laptev Sea study region ($a = 19$ and $b = 4$).

At submarine conditions, the saline pore water introduces an additional element of freezing point depression, which results in larger liquid water fractions than for

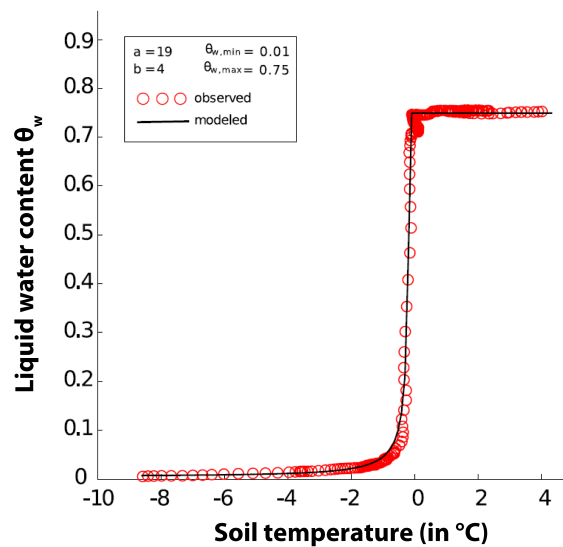


Figure 3.3: The soil freezing characteristic curve from the Laptev Sea study region. Measurements of volumetric water content and a material-specific fit are shown. (adapted from Langer et al. [2011])

freshwater pore waters. Corresponding to their concentration, dissolved solutes in the liquid phase decrease the chemical potential and, analog to above, shift the intersection point that represents the freezing temperature (see Sect. 3.6.3.1).

3.6.2 Model definitions: concentration and thaw depth

Salt content in the sediments is generally given by pore water salt concentrations or salinities. Concentrations can be given in various terms, i.e. mass concentration, molar concentration, and with respect to either solvent volume (yielding densities) or mass (yielding mass fractions). Distinguishing between the different types is essential regarding mass conservation in the governing equations. A mass concentration per volume $c_{m,V}$ (kg of solute per volume; density-concentration) is related to the mass concentration per solvent mass $c_{m,m}$ (kg of solute per kg of solvent; mass-fraction-concentration) by the density ρ of the solvent: $c_{m,V} = \rho \cdot c_{m,m}$. Salinity is the mass fraction concentration of kg salt per kg of sea water.

Two concentrations/salinities are further important in this context: the ‘total’ and the ‘in-situ concentration’. In-situ concentration is the concentration in the remaining liquid water phase. Most distribution processes depend on gradients in this concentration, thus, the in-situ concentration governs the salt transport equations. Total concentration is defined as the concentration that would exist in the liquid phase if all ice in the volume were melted. Thus, total concentration is the concentration with respect to the maximum water content of the (unfrozen) volume. Typically, this concentration would be measured in a sample if it were completely thawed before concentration determination. Note that this definition differs from other works, where ‘total’ often refers to the whole volume of porous medium. Contrastingly, in this study and the context of subsea permafrost, total is not given with respect to total volume V , but to total water content fraction volume ($\Theta_{w,\max} \cdot V$). Both total and in-situ concentrations are apparently related by converting the mass to the respective volumes. Given the in-situ density-concentration c (kg m^{-3}), the porosity Θ as the maximum water content fraction in saturated sediments, and the unfrozen water fraction Θ_w , mass conservation yields: $c_{\text{tot}} \cdot (\Theta V) = c_{\text{in-situ}} \cdot (\Theta_w V)$. Substituting the mass-fraction-salinity s using $c[\text{kg m}^{-3}] = \rho \cdot s[\text{kg m}^{-3}]$ yields the same relation for s :

$$s_{\text{tot}} = s \cdot \frac{\Theta_w}{\Theta}, \quad (3.9)$$

where s (without index) is used to refer to in-situ salinity.

Thaw depth, i.e. the depth of the transition to ice-bonded permafrost sediments, is typically determined by the observable change in mechanical resistance to penetration by a probing metal rod in the field. Once the sediment grains are cemented together, the mechanical resistance of the sediments increases dramatically. While terms such as ‘ice-bonded’ are used frequently in descriptive terms, no quantitative definition is known to this author in the modelling literature. However, this is indispensable in the context of this study which attempts to model and compare subsea permafrost thaw depths to field observations. Therefore, this study suggests a threshold definition for ‘ice-bonded’ permafrost conditions in terms of pore ice content. The relationship is based on the mechanical transition, which is reflected in seismic velocity as a primary diagnostic. Seismic velocity is (primarily) sensitive to the solid matrix portion (see Sect. 2.1) and, thus, is the suitable physical property in the context of ice-bonded conditions. The saturation of ice in the pore space is given by the fraction of ice content with respect to the pore space volume, i.e. the total water content of the unfrozen volume. Seismic velocity in ice-bearing sediments strongly depends on this saturation. A threshold of 40% reflects the onset of cementation of sediment grains with rapidly increased velocities [Brothers et al., 2012], and, thus, marks the threshold saturation value for ice-bonded sediments. Theoretical calculations [Johansen et al., 2003], observations in hydrate bearing sediments [Yun et al., 2007], and measurements [Zimmerman and King, 1986, Rogers and Morack, 1980] of seismic velocities support this value. This definition allows to assess thaw depth consistently compared to other geophysical methods such as seismics, and with mechanical solidity observations in the field. The model assessment of thaw depths in Sect. 3.7 was based on this value.

3.6.3 Saline effect on the state of permafrost

3.6.3.1 Liquid water content and freezing characteristic with saline pore water

The presence of salt in the marine realm alters the amount of unfrozen water twofold: (i) by the solute-concentration dependent depression of the freezing point and (ii) the increasing solute concentration during continued freezing in the continuously decreasing liquid water fraction. In a porous medium both effects change the non-saline freezing characteristic curve by (i) shifting the onset of freezing and (ii) retarding the decrease of liquid pore water fraction with decreasing temperature.

Different methods of incorporating salinity effects into the freezing characteristic curve have been suggested [Patterson and Smith, 1985, Nixon, 1986]. Hivon and Sego [1995] compare several methods with laboratory TDR-measurements and confirm best

agreement by simply summing a field-determined zero-salinity freezing characteristic curve and the theoretically calculated freezing point depression from the phase diagram of the pore water solution. For the zero-salinity part, we adopted TDR-field measurements of unfrozen water content of terrestrial sands of the Laptev Sea region, used in the studies of Langer et al. [2013, 2011]. We calculated the saline term of the freezing characteristic curve by using an adapted parameterization of the solution equilibrium line (sometimes also called liquidus curve) separating the ice and solution phases in the phase diagram (Fig. 3.4 and Eq. 3.10).

It is assumed that local thermodynamic equilibrium between the ice and the solution is retained on the time scale of the heat flow. Also, inclusion of salt into the ice and mineral precipitation out of the liquid phase during freezing are assumed to be negligible. Then, the NaCl concentration in solution follows the solution equilibrium line during freezing. Given a specific initial amount of salt (equivalent to ‘total concentration/salinity’, i.e., given with respect to the total water content assumed unfrozen), the freezing point depression and final point on the equilibrium line associated with a subzero temperature can be determined. This yields the ‘in-situ salinity/concentration’, i.e. the actual concentration in the remaining pore fluid, and the remaining liquid water content is given by the ratio of initial amount of salt and final concentration.

Parameterizations based on the sodium chloride (NaCl)–water (H₂O) binary phase diagram [Marion, 1995] and a marine mixture of solutes from the FREEZEBRINE

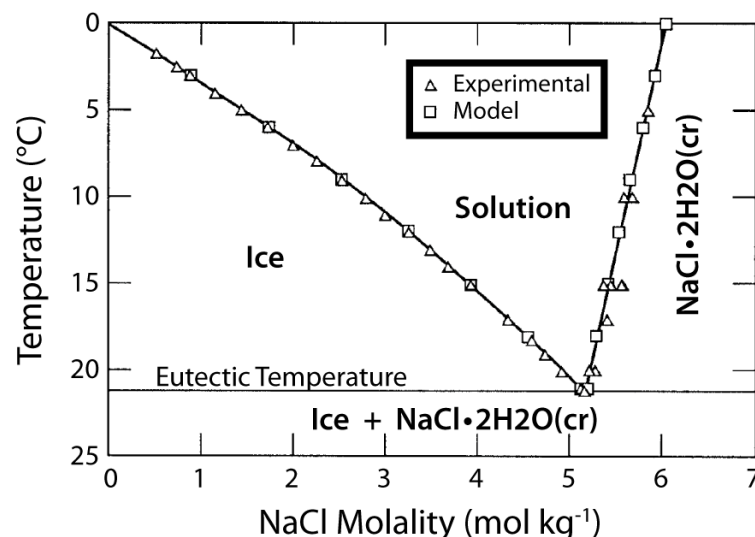


Figure 3.4: Phase diagram for the NaCl–H₂O system at subzero temperatures (adapted from Marion [1995]). The ice-solution equilibrium line and the solution–NaCl·2H₂O equilibrium line are shown, as well as the eutectic point (–21.7 °C and 5.17 mol kg^{–1}) below which the residual solutions solidifies as a mixture of ice and NaCl·2H₂O.

model [Komarov and Kiyashko, 2012] yield identical results, and, the former parameterization was used in this model. The second order polynomial expression must be adapted to enforce zero-point crossing. Deviation is small (less than 0.13°C) and is required to avoid numerical instabilities by the sudden step change. To better capture the mixture of salts in sea water, an effective molar mass instead of NaCl molar mass was used to convert to salinity. This effective $M_{NaCl, \text{eff}}$ is based on the ion molality of standard sea water composition at salinity 35 [DOE, 1994, McDougall and Barker, 2011]. In general, the molality vs. salinity relationship is not linear for higher salinities (TEOS-10 [McDougall and Barker, 2011]). However, unfrozen water content depends on the total salinity, not the concentrated salinity in the remaining pore liquid (see above). Arctic Ocean total salinities are comparatively low (<30), even brine concentrations beneath sea ice are below the range of significant deviations from linearity (less than approximately 100), and the linear approximation is well suited to the modelled salinity domain. The parameterization as a function of salinity s (g of salt per kg of sea water) is given by:

$$\Delta T = -5.078(\pm 0.007)10^{-2} \cdot s - 5.312(\pm 0.027)10^{-5} \cdot s^2. \quad (3.10)$$

Figure 3.5 shows freezing characteristic curves with varying pore water salinity, as used in the model. The stated salinity is referenced to the total water content of the unfrozen sample. At freezing temperatures, the in-situ salinity in the remaining pore water liquid can be substantially higher. The curves show that the onset of freezing,

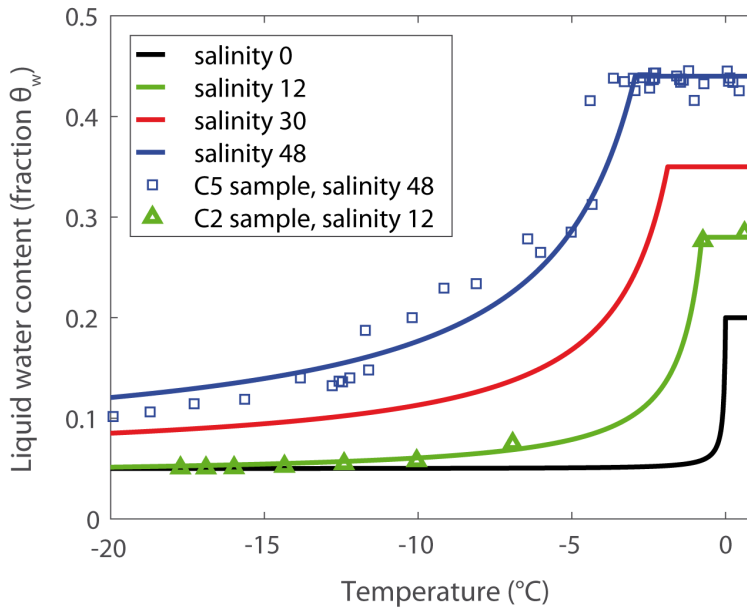


Figure 3.5: Freezing characteristic curves in the model (solid lines for various salinities) and TDR measurements at samples from the Mamontov Klyk boreholes.

i.e. when partial freezing and decrease in water content begin to occur, is shifted to lower temperatures for increasing salinity. Equally for higher salinities, a larger amount of liquid pore water is retained at the same subzero temperature below this onset temperature.

The liquid water content $\Theta_w(T, s_{\text{tot}})$ is now also a function of salinity, specifically of the total salinity as expressed by the amount of salt with respect to the entire water volume considered unfrozen. The heat transfer equation therefore couples to any transport/distribution equation that governs the pore water salinity field in the subsurface sediments. This couples the salt transport equation to the heat equation by the salinity effect on the liquid water content and on the thermal parameters. In a formal derivation, this changes the first term in Eq. 3.1. Equation 3.2 becomes

$$\frac{de(T, \Theta_w(T, s_{\text{tot}}), \Theta_i(T, s_{\text{tot}}))}{dt} = \frac{\partial e}{\partial T} \frac{\partial T}{\partial t} + \frac{\partial e}{\partial \Theta_w} \frac{\partial \Theta_w(T, s_{\text{tot}})}{\partial t} + \frac{\partial e}{\partial \Theta_i} \frac{\partial \Theta_i(T, s_{\text{tot}})}{\partial t}.$$

The water and ice fraction derivatives now include an additional term for changing salinity: $\frac{\partial \Theta_w(T, s_{\text{tot}})}{\partial t} = \frac{\partial \Theta_w}{\partial T} \frac{\partial T}{\partial t} + \frac{\partial \Theta_w}{\partial s} \frac{\partial s}{\partial t}$, and equivalently for $\frac{\partial \Theta_i(T, s_{\text{tot}})}{\partial t}$. Evaluation analog to Eq. 3.2 yields an extra term:

$$\frac{de}{dt} = \left[c_h(T) + L_f \frac{\partial \Theta_w}{\partial T} \right] \cdot \frac{\partial T}{\partial t} + L_f \frac{\partial \Theta_w}{\partial s} \frac{\partial s}{\partial t}, \quad (3.11)$$

which explicitly couples the heat transfer equation to the salinity transport equation.

3.6.3.2 Thermal properties

Salinity effects on thermal conductivity are negligible (1 % difference between fresh water and sea water) and thus not considered in the model [Osterkamp, 1987]. Salt effects on the thermal heat capacity of the saline liquid pore water are more complex. This study used a parameterization of sea water heat capacity vs. salinity for negative temperatures, given by [Komarov and Kiyashko, 2012]. For positive temperatures, a constant heat capacity was used.

3.6.4 Salt transport: governing equation & parameterizations

Salt profiles, i.e. the depth distribution of salt in the pore water, depend on several factors, such as sea bottom salinity, the injections of brines in shallow waters (where the salinity of the sediment can be much larger than sea bottom water salinity),

diffusion of salt, convection in the pore space, sediment turbation by waves, and the rate of permafrost thaw.

In this section, the governing equations for diffusive and advective mass transfer within the porous sediment are derived and the parameterizations used in the subsea model are described for these and other processes that affect the salinity distribution. These include diffusive (Sect. 3.6.4.1) and advective (Sect. 3.6.4.2) transport, and prior saline layers (Sect. 3.6.4.3).

Given a volume V of porous sediment, where solute transport occurs exclusively in the liquid water phase fraction, the mass of salt M_s in V is given by $M_s = c \cdot \Theta_w \cdot V$, where c is in-situ mass concentration in the liquid water phase volume $\Theta_w \cdot V$. Expressed in the in-situ salinity mass fraction concentration s , M becomes: $M_s = \rho \cdot s \cdot \Theta_w \cdot V$. The governing equation for diffusive and advective salt fluxes across the surface S of the volume can be derived analog to Eq. 3.1 by salt conservation and the continuity equation, stating that the change over time of the mass density $m_s = M_s/V$ is given by the divergence of the in- and outward fluxes through the surface of V . The result for the macroscopic variables in the far-field (i.e., few tens of grains, equivalent to a few millimeters [Roth, 2012]) and for variable transport volume fraction Θ yields [Roth, 2012, Ingebritsen et al., 2007]:

$$\frac{d}{dt} \overbrace{[\Theta \rho s]}^{m_s} + \nabla \cdot [\Theta \rho v s] - \nabla \cdot [\Theta \rho D_{\text{sed}} \nabla s] = 0, \quad (3.12)$$

where v is the effective downward pore water velocity and D_{sed} is the effective diffusion coefficient of salt in the porous media. Here, s refers explicitly to the in-situ salinity and ρ to the solvent density. In the saturated, partially frozen subsea sediments, the transport volume is equivalent to the unfrozen water content, and thus varies with time and space. If we assume ρ approximately constant (and given by the density of water), the density cancels in all terms and the equation is valid for concentration per volume as well as for salinity [Ingebritsen et al., 2007].

Regarding thus the first term in Eq. 3.12, the time derivative of the salt mass density $m_s = \Theta_w \cdot s$ is a function of in-situ salinity s and the volumetric fraction Θ_w of liquid water. This becomes

$$\begin{aligned} \frac{dm_s(s, \Theta_w(T, s))}{dt} &= \frac{\partial m_s}{\partial s} \frac{\partial s}{\partial t} + \frac{\partial m_s}{\partial \Theta_w} \left(\frac{\partial \Theta_w}{\partial T} \frac{\partial T}{\partial t} + \frac{\partial \Theta_w}{\partial s} \frac{\partial s}{\partial t} \right) \\ &= \Theta_w \frac{\partial s}{\partial t} + s \left(\frac{\partial \Theta_w}{\partial T} \frac{\partial T}{\partial t} + \frac{\partial \Theta_w}{\partial s} \frac{\partial s}{\partial t} \right) \\ &= \left[\Theta_w + s \frac{\partial \Theta_w}{\partial s} \right] \cdot \frac{\partial s}{\partial t} + s \frac{\partial \Theta_w}{\partial T} \frac{\partial T}{\partial t}, \end{aligned} \quad (3.13)$$

where Eq. 3.9 must be further used to obtain $\frac{\partial s_{\text{tot}}}{\partial s}$ in the term $\frac{\partial \Theta_w(s_{\text{tot}})}{\partial s} = \frac{\partial \Theta_w(s_{\text{tot}})}{\partial s_{\text{tot}}} \frac{\partial s_{\text{tot}}}{\partial s}$.

Thus, analog to Eq. 3.11, the temperature dependence of Θ_w couples to the available fluid volume for flow in the transport equation, and yields the last term in Eq. 3.13. This term explicitly couples the salt transfer to the heat transfer equation, therefore giving the coupled transport equations of heat and salt in subsea permafrost sediments.

The two flux terms in Eq. 3.12 were implemented in a numerical flux-conserving finite volume scheme, which provided higher order accuracy without spurious oscillations in the advection solution [Dullemond and Springel, 2012]. The treatment of the two terms and the implemented process is given in the following sections.

The basic formulation for a one-dimensional flow through a pipe with crosssection S is given by cells with centers at z_i with volume $V = \Delta z \cdot S$, and cell interfaces at $z_{i+\frac{1}{2}}$. Mass of salt M_s is the conserved quantity. In explicit formulation, the quantity can only be changed by moving in- and outflow through cell interfaces with flux $f_{i+\frac{1}{2}}$, yielding the discrete form for the salt mass density m_s :

$$\begin{aligned} \frac{d(M_s)_i}{dt} &= \frac{d(m_s \cdot S \cdot \Delta z)_i}{dt} = (f_{i-\frac{1}{2}} - f_{i+\frac{1}{2}}) \cdot S \\ \frac{d(m_s)_i}{dt} &= \frac{f_{i-\frac{1}{2}} - f_{i+\frac{1}{2}}}{z_{i+\frac{1}{2}} - z_{i-\frac{1}{2}}}. \end{aligned} \quad (3.14)$$

This is valid for non-regular grid spacing and for non-constant porosity. For the formulation of the fluxes, the underlying concept [Dullemond and Springel, 2012] introduces different assumptions to obtain an estimate for the average state of all time-dependent variables at the interface. With these, additional numerical stability at higher order accuracy is obtained, especially in the advection solution where numerical instability or numerical diffusion of the advected front otherwise produce spurious oscillations or upstream information flow and, thus, deviations from the physical solution.

3.6.4.1 Diffusion processes

For the diffusive flux term in Eq. 3.12, f is given by:

$$f^{\text{diff}} = -\Theta D^{\text{sed}} \frac{\partial}{\partial z} s. \quad (3.15)$$

In this case, a simple assumption, the so-called donor-cell scheme [Dullemond and Springel, 2012, Alhumaizi, 2007], is sufficient, and the spatial derivative is discretized

as centered-differences over the half-grid point, yielding [Dullemond and Springel, 2012, Alhumaizi, 2007]:

$$\begin{aligned} f_{i+\frac{1}{2}} &= -\Theta_{i+\frac{1}{2}} D_{i+\frac{1}{2}}^{\text{sed}} \frac{s_{i+1} - s_i}{z_{i+1} - z_i} \\ f_{i-\frac{1}{2}} &= -\Theta_{i-\frac{1}{2}} D_{i-\frac{1}{2}}^{\text{sed}} \frac{s_i - s_{i-1}}{z_i - z_{i-1}}. \end{aligned} \quad (3.16)$$

Regarding the salt diffusion coefficient, macroscopic spreading in a porous medium is limited in contrast to molecular diffusion D^m in a free water volume due to the convoluted path (referred to as tortuosity). This results in a reduced effective diffusion coefficient D^{sed} for salt within the subsea sediments. A number of parameterizations exist, however, generally with rather weak experimental support, and often only transposed from results of gas diffusion in porous media [Roth, 2012]. This study restrains to parameterizations which apply to water flow in porous sediments. Reported parameterizations of D^{sed} are given in Table 3.1. Note that in the literature, such effective D^{sed} is often given to include the Θ in Eq. 3.15. Thus, the exponents given here may deviate by a factor of Θ . Nonetheless, no data were available to support either type of parameterization over another for the study site. Model sensitivity to the choice of diffusion parameterization was tested in Sect. 3.7. A reference estimate of molecular diffusion D^m for NaCl was used, corrected for sea water and temperature according to Li and Gregory [1974], of about $8 \cdot 10^{-10} \text{ m}^2 \text{ s}^{-1}$. In an effective parameter approach, higher values were also used later in this study. D^m is therefore replaced by the effective parameter D , and always referred to as the effective diffusion parameter in this study. Thus implicitly, any further diffusive contribution is also subject to the tortuosity of pathways on the pore scale.

Table 3.1: Parameterizations of effective diffusion coefficients in porous media.

D^{sed} parameterization		source
$D^m \cdot \frac{1}{\tau}$	tortuosity factor $\tau = \frac{\pi}{2}$	[Lucas, 2001]
$D^m \cdot (\Theta_w)^{\frac{1}{3}}$		[Roth, 2012]
$D^m \cdot (\Theta_w)^n$	$\begin{cases} n = 1..2 \text{ (sands)} \\ n = 2..4 \text{ (silts)} \end{cases}$	[Frederick and Buffett, 2015]
$D^m \cdot \left(\frac{1}{1-2 \ln(\Theta_w)}\right)$		[Boudreau, 1997]

3.6.4.2 Advective processes and numerical scheme

For the advective flux term in Eq. 3.12, f is given by:

$$f^{\text{adv}} = \Theta s v. \quad (3.17)$$

In this case, a slightly more complicated assumption, a so-called piecewise-linear scheme [Dullemond and Springel, 2012], is required. The underlying idea is that the state of the variables $[\Theta s]$ is assumed as a piecewise linear function of position. This assumption poses a subgrid reconstruction, as only information about the variable at the cell center is given. This gives the state at the beginning of the time step t_n within each cell as:

$$[\Theta s](z, t = t_n) = \Theta_i s_i^n + \sigma_i^n (z - z_i).$$

By good choice of the slope σ , numerical oscillations and overshoots near sharp fronts can be prevented. For $v > 0$, the state of the top cell is advected downwards. Substituting and calculating the average flux over the time step $\Delta t = t_{n+1} - t_n$ by $\frac{1}{\Delta t} \int_{t_n}^{t_{n+1}} f(t) dt$ yields [Dullemond and Springel, 2012, Alhumaizi, 2007]:

$$\begin{aligned} f_{i+\frac{1}{2}} &= v_{i+\frac{1}{2}} \Theta_i s_i + v_{i+\frac{1}{2}} \sigma_i \left((z_{i+\frac{1}{2}} - z_i) - \frac{1}{2} v_{i+\frac{1}{2}} \Delta t \right) \\ f_{i-\frac{1}{2}} &= v_{i-\frac{1}{2}} \Theta_{i-1} s_{i-1} + v_{i-\frac{1}{2}} \sigma_{i-1} \left((z_{i-\frac{1}{2}} - z_{i-1}) - \frac{1}{2} v_{i-\frac{1}{2}} \Delta t \right). \end{aligned} \quad (3.18)$$

Different choices of slope limiters are given by Alhumaizi [2007]. Due to its efficient ability to prevent the numerical development of oscillations and overshoots near very strong concentration gradients, the superbee slope limiter was applied in this study [Dullemond and Springel, 2012, Roe, 1986]:

$$\begin{aligned} \sigma_i &= \text{maxmod} \left(\sigma_i^{(1)}, \sigma_i^{(2)} \right) \\ \sigma_i^{(1)} &= \text{minmod} \left[\frac{q_{i+1}^n - q_i^n}{\delta x}, 2 \cdot \frac{q_i^n - q_{i-1}^n}{\delta x} \right] \\ \sigma_i^{(2)} &= \text{minmod} \left[2 \cdot \frac{q_{i+1}^n - q_i^n}{\delta x}, \frac{q_i^n - q_{i-1}^n}{\delta x} \right], \end{aligned} \quad (3.19)$$

where $q = \Theta s$, and minmod and maxmod are given by:

$$\text{minmod}(a,b) = \begin{cases} a & \text{if } a \cdot b > 0 \text{ and } |a| < |b| \\ b & \text{if } a \cdot b > 0 \text{ and } |a| > |b| \\ 0 & \text{if } a \cdot b \leq 0 \end{cases}$$

$$\text{maxmod}(a,b) = \begin{cases} a & \text{if } a \cdot b > 0 \text{ and } |a| > |b| \\ b & \text{if } a \cdot b > 0 \text{ and } |a| < |b| \\ 0 & \text{if } a \cdot b \leq 0. \end{cases}$$

Figure 3.6 compares the pure advection solution in the model without and with the slope limiter scheme. The implementation of the superbee limiter effectively prevented the non-physical numerical diffusion at the advection front.

As this model is a one-dimensional scheme, thus, the advective contribution to salt transport is parameterized by an effective downward velocity v . A main mechanism is density-driven, convective flow which depends on the concentration difference between the denser, high salinity sea water above and the newly thawed, fresh pore water at the thawing front below. The development of real convection cells with up- and downward flows would require at least two-dimensional treatment. In order to capture this mechanism in the one-dimensional model, the velocity

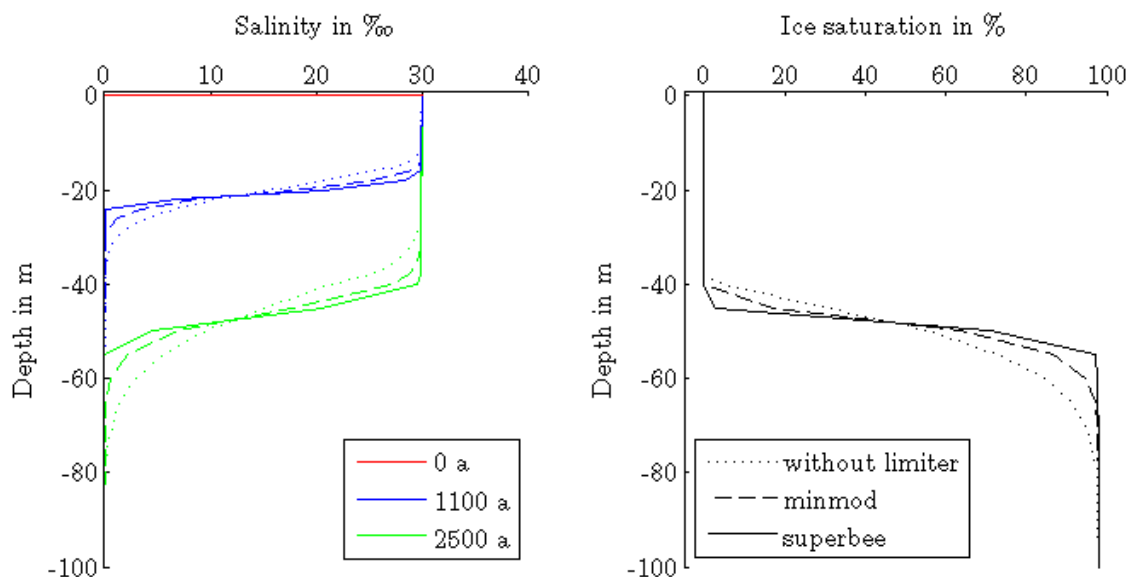


Figure 3.6: Salinity profiles (**left**) with a downward-advecting front and ice saturation (**right**) for different time points in a sediment column of constant porosity. The numerical diffusion of the sharp concentration front is apparent in the case without a slope limiter implementation, and affects the sharpness of the transition in ice saturation. The effect is lessened in the case of the so-called minmod limiter, while the case of the superbee slope limiter displays the most effective reduction.

parameter v was scaled to reflect that the actual flow rate depends on the salinity difference between the cells above the current permafrost table and the maximum salinity in the completely thawed column above. Usually, this maximum will be the ocean water salinity at the top. Thus, flow diminished and eventually ceased if the bottom cell accumulated to the same salinity, and therefore density, as the cells above. Furthermore, due to the varying porosities in the sediment column, the flow velocity was limited in the model to the smallest porosity in the unfrozen sediment column. This effectively precluded the non-physical accumulation of salt above the permafrost table, and yielded a simple, effective process parameterization in the one-dimensional model. Thus, the effects of density-driven flow were captured in the model, which included convective transport through the unfrozen sediment column to the ice-bearing sediment layer, and infiltration into the frozen sediments by diffusion [Harrison and Osterkamp, 1982].

Additionally, using this effective parameter description, further advective or diffusive contributions to the transport process can be included by variation of the effective parameters v and D : Wave-induced pore water motion could be another component of advective transport. It can be described by a dispersion term in an effective diffusivity [Harrison et al., 1983], thus, it can be incorporated in the model by an effectively larger parameter D . Salt fingering is another density-driven mechanism, which can occur from the thawing boundary upward or from the seabed downward. Gosink and Baker [1990] have shown that this process can initiate under typical density gradients that occur at least seasonally at the sea bed. Such additional components can be equally captured in the model by an effectively larger parameter v . Typical downward velocities in thawing subsea permafrost given by Harrison and Osterkamp [1982], Swift et al. [1983] and Swift and Harrison [1984] are on the order of a few tenth of a meter per year.

3.6.4.3 Prior saline sediment layers

The presence of prior saline layers in the inundated permafrost sediments would allow for taliks – unfrozen pockets in the frozen permafrost body. Information about such layers in the Laptev Sea region is tentative. Ponomarev [1940] reports three water-bearing horizons offshore in Kozhevnikov Bay, and an unfrozen layer is discovered at the bottom end of the COAST C2 borehole [Rachold et al., 2007, Winterfeld et al., 2011]. However, the presence of several layers has been reported in the Canadian Beaufort Shelf [Blasco, 1995]. These are interpreted as eight transgression/regression cycles (see Sect. 1.1.1 and Fig. 1.4). Marine mud deposits are thought to have been preserved between terrestrial deposits, and potentially provide zones of liquid

water content at relatively cold temperatures. Ice-bonded permafrost degradation outwards from these zones might contribute to degradation dynamics, for example under the warmer conditions during the following transgression cycles. Such layers might also affect the apparent degradation rate in observations, when such a layer is encountered during downward migration of the ice-bonded permafrost table. In the model, the marine layers of the Blasco core were used to assess such a layer effect on subsea permafrost evolution dynamics at Mamontov Klyk.

3.6.5 Modelling approach

In this study, heat and salt transport were modelled at the mesoscale (10^1 – 10^2 m of spatial and 10^3 years of time scale) and compared with borehole data from the Laptev Sea. The coupled system of diffusive heat transfer and advection-diffusion equation of salt transport in the porous subsea sediments was solved numerically in a one-dimensional flux-conserving finite volume scheme. Combining Eqs. 3.11 and 3.4 in Eq. 3.1, and 3.13 and 3.9 in 3.12, the coupled governing equations are given by:

$$\begin{aligned} c_{\text{eff}}(z, T) \cdot \frac{\partial T}{\partial t} &= \overbrace{\frac{\partial}{\partial z} \left(\lambda_h(z, T) \cdot \frac{\partial T}{\partial z} \right)}^A - \left(L_f \frac{\Theta_w}{\Theta} \frac{\partial \Theta_w}{\partial s_{\text{tot}}} \right) \frac{\partial s}{\partial t} \\ \left(\Theta_w + s \frac{\Theta_w}{\Theta} \frac{\partial \Theta_w}{\partial s_{\text{tot}}} \right) \cdot \frac{\partial s}{\partial t} &= \underbrace{\frac{\partial}{\partial z} \left(\Theta D_{\text{sed}} \frac{\partial s}{\partial z} - \Theta v s \right)}_B - \left(s \frac{\partial \Theta_w}{\partial T} \right) \frac{\partial T}{\partial t}, \end{aligned} \quad (3.20)$$

The spatial derivatives in A and B were solved using the Donor-cell and slope limiter discretizations. Equation 3.20 was solved for $\frac{\partial T}{\partial t}$ and $\frac{\partial s}{\partial t}$.

Freeze-thaw processes were considered in a three-phase heat capacity/conductivity model based on de Vries [1963] and modified by Ippisch [2001] to incorporate the phase change between water and ice (Eq. 3.2). The thermal model approach was based on simulations previously used in studies on terrestrial permafrost [Langer et al., 2013, Westermann et al., 2011, 2013]. The effective heat capacity was pre-calculated in a lookup table to increase modelling speed. The salt transport discretization scheme yielded higher order accuracy without spurious oscillations in the advection solution.

Model setup: sediment composition

Thermal parameters in the heat capacity/conductivity model were assigned based on the sediment composition analysis of the borehole. At Mamontov Klyk, heat

capacity and thermal conductivity were derived from the sediment composition of the core recovered from the onshore borehole [Winterfeld et al., 2011]. At Buor Khaya, sediment composition analysis of the deep offshore core was combined with data from Yedoma outcrops at the coast (up to 30 m asl) [Strauss et al., 2017] to obtain one continuous, composite data set from the bluff surface downwards to a depth of 51 m bsl. Care was taken to convert typically retrieved wt-% to Vol-% in the sediment composition. At Muostakh Island, subsea permafrost data was provided by the geophysical detection only, and a synthetic core was established using a local three layer model (1 m active layer, 33 m Yedoma, sands below). Mean values for the Holocene cover and the Pleistocene sands of the pre-Eemian floodplain are given by [Schirmer et al., 2011b, Kunitsky, 1989], while Yedoma composition is given by [Strauss et al., 2017]. For all three sites, sandy unconsolidated sediment was assumed below the borehole observations to the modelled depth of 1000 m. Porosities in the sandy-silty permafrost sediments below the ice-rich surface layers typically range between 20–40 %, with porosity expected to decrease with depth. Consistent to the observed trends in porosity at the bottom of the boreholes at Mamontov Klyk and Buor Khaya, a linear decrease to 20 % porosity at 200 m and constant porosity below was used in the model. Average mineral thermal values $\lambda_{min} = 2.9 \frac{W}{mK}$ and $c_{min} = 2 \cdot 10^6 \frac{J}{m^3K}$ were used [Hillel, 1982].

Figure 3.7 shows the resulting effective heat capacity, thermal conductivity and thermal diffusivity as a function of depth. At all three sites, the thermal properties profiles show a rather constant, steady trend with depth. Mean values for heat capacity, thermal conductivity, and thermal diffusivity are between 2.06–2.08 MJ m⁻³ K⁻¹, 2.19–2.38 W m⁻¹ K⁻¹, 1.06–1.15 · 10⁶ m² s⁻¹ with maximum deviations along the profile of less than 10 %, 10 %, and 14 %, respectively. These small variations are in line with the observed, rather homogeneous sandy-silty lithologies of the boreholes (right-hand side in Fig. 3.7).

The subsea sediments were considered to be porous media saturated with ice and/or liquid water of varying salinity. Any gas phase present in the sediment was neglected. By using sediment composition data from boreholes, the sediment organic content onshore and offshore was naturally included in the model. The inclusion of a surface organic layer with its associated lower conductivity is critical for accurate simulation of thawing from above [Nicolson et al., 2007].

Initial and boundary conditions

A temperature profile at the terrestrial borehole of the Mamontov Klyk drilling campaign is available from field measurements [Overduin et al., 2007a]. The borehole

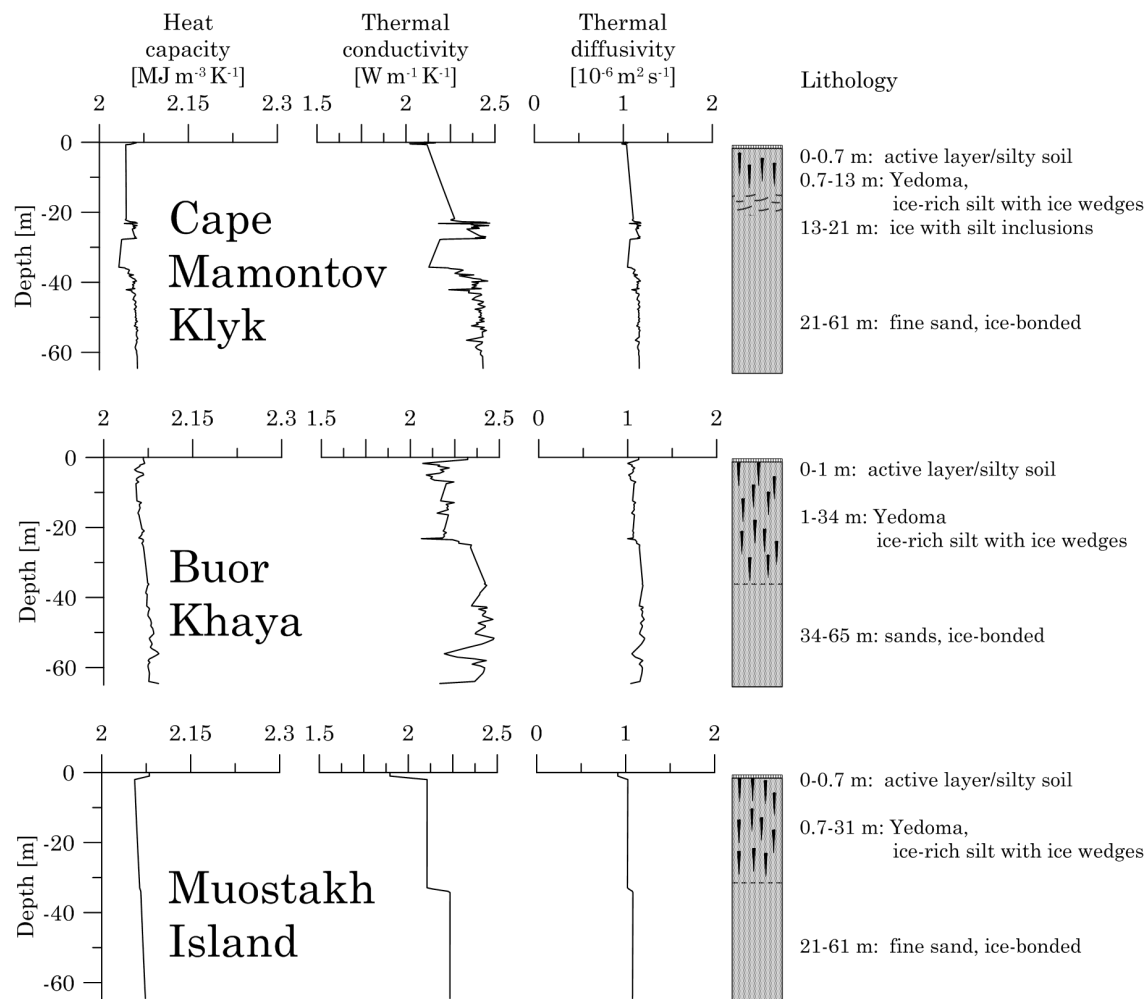


Figure 3.7: Thermal parameters in the subsea permafrost model for (**top**) Mamontov Klyk, (**middle**) Buor Khaya and (**bottom**) Muostakh Island: Effective heat capacity, thermal conductivity and thermal diffusivity. Shown to the right are the subsurface lithologies.

data suggested an equilibrium profile corresponding to a surface temperature of roughly -14.2°C at the assumed time of inundation 2500 years ago. This was close to the current average annual air temperature in the Lena Delta of -14.7°C [Wagner et al., 2003] and is consistent with the slight cooling trend since the Holocene optimum some 8000 years ago. At the other two locations, no deep temperature data existed to indicate equilibrium surface temperature. The initial equilibrium surface temperature was approximated by a latitude-dependent shift to the Mamontov Klyk value. In general, the latitude-MAGT (mean annual ground temperature) relationship varies between regions and landscape conditions due to, e.g., influences by ocean currents on climate and elevation. However, due to similar site characteristics (such as vegetation, soil conditions, coastal proximity), local scale MAGT variations based on landscape conditions could be considered negligible in this study [Romanovsky et al., 2010b]. Moreover, contemporary MAGT in the study region shows a spatial variation of

about 1 °C for each degree of latitude [Romanovsky et al., 2010a]. Assuming that the latitude-MAGT relationship remained the same during the past millenia, a 2.2 ° and 2.0 ° latitude shift was applied for Buor Khaya and Muostakh Island, respectively.

Ocean water salinities at Mamontov Klyk are given by Overduin et al. [2007a] and are about 30 ‰. Salinities around Muostakh Island and in the Buor Khaya Bay are much lower due to the strong influence of freshwater discharge from a major channel of the Lena river, and around 10 ‰ [Charkin et al., 2017].

Inundation occurs by coastal retreat, which erodes the coastal cliff. Correspondingly, the upper 25 m, 35 m, and 16–19 m of ice-rich deposits, which were used to obtain the initial temperature profile, were initially removed from the soil column by the model at the Mamontov Klyk, Buor Khaya, and Muostakh Island location, respectively.

The upper boundary temperature following inundation corresponded to the bottom water temperature of the Laptev Sea shelf. We used OCSEAP temperature data [Harrison and Osterkamp, 1977] as a function of water depth for Mamontov Klyk conditions away from river influences. The OCSEAP data (Fig. 3.24) captured temperatures throughout the shallow transition zone. The temperature curves were shifted to match the observations of warmer annual sea bottom temperatures [Overduin et al., 2016] in the warmer regions at Muostakh Island and Buor Khaya Bay, which are influenced by river discharge. Model sensitivity to this factor and impact were tested in Sect. 3.7. The lower boundary condition was set to a geothermal flux of $Q = 53 \text{ mW/m}^2$ [Pollack et al., 1993, International Heat Flow Commission (IHFC), 2011]. The 1-dimensional soil model was solved as a mixed boundary-value problem with the upper boundary being forced by the external temperature variable itself (Dirichlet boundary condition) while the lower boundary was specified by the gradient of temperature (Neumann boundary condition) [Ingebritsen et al., 2007].

The heat stored in the subsurface could be underestimated if the bottom boundary condition (BBCP) were too shallow and perturb the subsurface temperature field [Stevens et al., 2007]. Based on Smerdon and Stieglitz [2006], the necessary BBCP in the model was identified to be at least 400 m lower than the region of interest, i.e. the permafrost body, to prevent boundary condition-related amplitude-attenuation for the millennial scale period of the simulations. Model tests confirmed that no influence of the BBCP at the 600 m deep base of permafrost was detectable when the bottom boundary condition was placed at 1000 m or deeper. This therefore achieved a depth larger than the decay length of the heat wave on the scale of the model run time [Nicolosky et al., 2007].

The approach included the effect of pore water salinity on phase state and thermal

properties, as detailed in Sect. 3.6.3 and 3.6.4, in order to show the impact of solute transport mechanisms into the sediment. Sediment temperature, pore water salinity, sediment volumetric liquid water and ice contents are calculated for each scenario.

Model applicability and assumptions

Model simplifications restrict its application and must be stated explicitly. The model implicitly assumed that (i) advective heat transport was negligible, (ii) there were no internal heat sinks or sources in the sediment, and (iii) frost heave and the effect of volume changes associated with the freeze/thaw phase transition (about 10%) were negligible. These assumptions are reasonable regarding subsea permafrost due to typically small Peclet numbers for heat transport and to excess ice existing predominantly in the initially eroded near-surface deposits. Further complicating near-shore processes were explicitly considered within the assessment in Sect. 3.6.4 and 3.7.

3.6.6 Model testing

In this section, the model algorithms are verified for mass conservation of salt and grid size sensitivity.

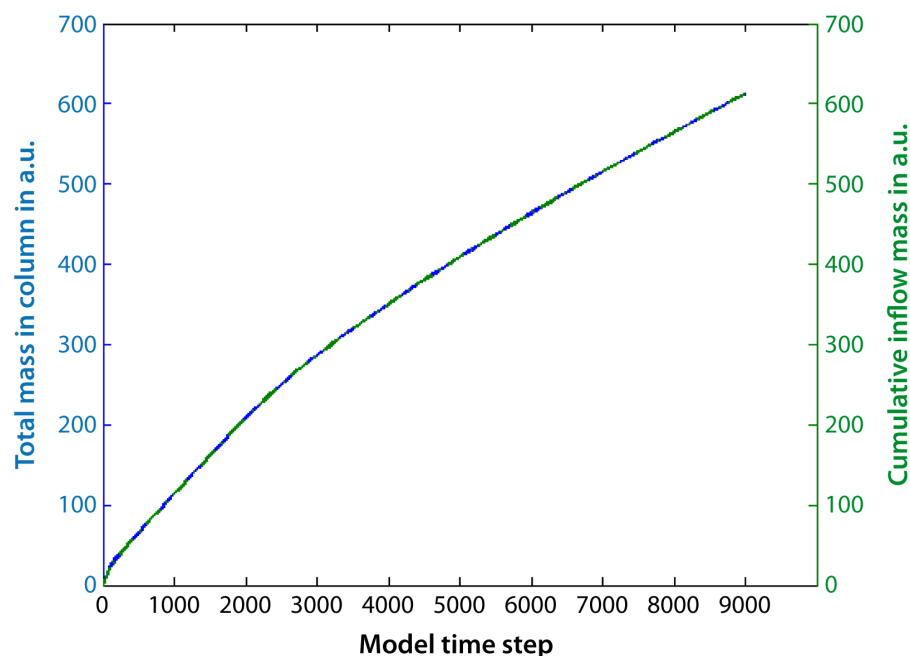


Figure 3.8: Cummulative mass influx of salt into the top cell of the model from the ocean above (**green**) equals the total amount of salt mass present at each model time step (**blue**).

Salt conservation in the model was ensured by accounting for both the total mass in the sediment column as a function of time and the cumulative influx into the column at the top boundary from the overlying reservoir of sea water. Careful consideration of the irregular grid cell volumes was required in the case of the former. Figure 3.8 shows the result for both as a function of model time step. Given the initially fresh pore water in the sediment, both salt quantities agreed with each other at every time step, thus, confirming the salt conservation within the model.

Grid independence was tested using logarithmically-scaled grid spacings with total numbers of cells of 150 to 1000 (Fig. 3.9). Sensitivity of the thaw depths to grid size was generally small. Only for very few grid cells of 250 and less was a trend to shallower thaw depths apparent. This was expected, as altogether larger cell volumes take longer for enough salt to accumulate before thawing to levels below the ice saturation threshold, yielding apparently retarded thaw depths compared to finer resolved grid cells. Therefore, this study used 350 cells.

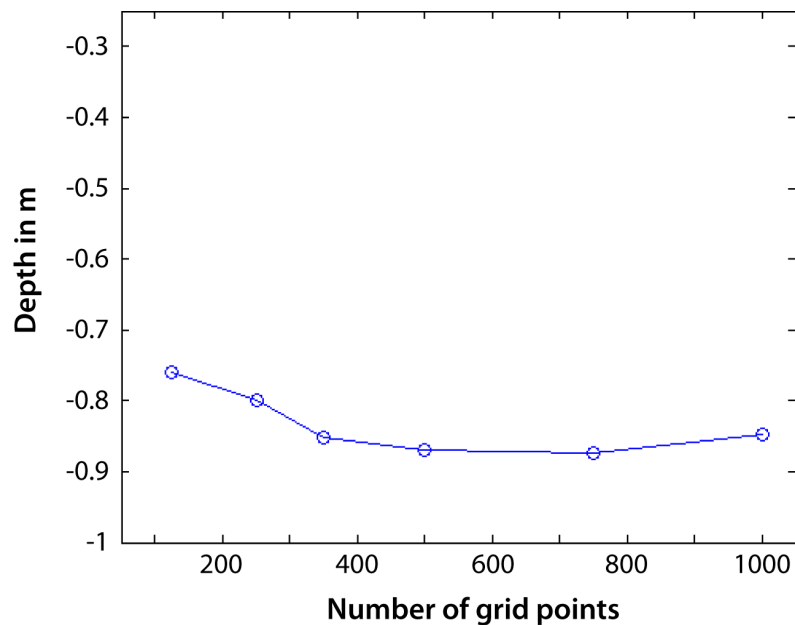


Figure 3.9: Depth of ice-bonded permafrost table after 109 a for varying model grid sizes.

3.7 Results: Influence of model parameters on subsea permafrost degradation

The state of permafrost during the transition and inundation from terrestrial to subsea conditions is influenced by a range of potentially important factors. These encompass, on the one hand, general inundation parameters such as the initial ground temperature and associated initial conditions, the eroding coastal cliff, altered temperature conditions by the sea bottom temperatures after inundation, and the coastal shoreline retreat rate which governs the progression speed of the inundation. Other factors, on the other hand, are directly related to salt infiltration influences such as stratigraphic salt distribution, and effective diffusion and advection transport mechanisms.

In order to facilitate a quantitative understanding of these processes, therefore, the impact of these inundation parameters was assessed using the developed subsea permafrost model. In the following, these parameters are treated, starting with a model based solely on heat conduction to assess the thermal impact of inundation, of the initial ground temperature before inundation, and of the initial cliff erosion. Subsequently, model results are presented of four stratigraphic scenarios that assessed the influence of salt distribution in the sediments. Lastly, based on the coupled model of heat and salt transport, the impact of factors on the downward degradation of the ice-bonded permafrost table was assessed. These included the choice of salt diffusion parameterization within the sediment, the sea bottom temperatures after inundation, the coastal shoreline retreat rates and, finally, the effective diffusion and advection parameters.

Thermal response to inundation

The permafrost temperatures change greatly after inundation. Figure 3.10 shows the temperature evolution in the sub-bottom sediments, based solely on heat conduction, for 3965 a after inundation. This represented the approximate time period for the C2 borehole at Mamontov Klyk under the influence of sea bottom temperatures at the top and the geothermal heat flux at the bottom. The entire temperature profile within the permafrost became almost isothermal relatively quickly: Within 1500 a, the temperature profile was nowhere lower than -3°C at any depth in the permafrost; after less than 2500 a, temperatures throughout the permafrost were above -2°C . These results are consistent with the measured temperature profile in the C2 borehole at the time of drilling (see in Fig. 3.11), which displayed temperatures roughly between

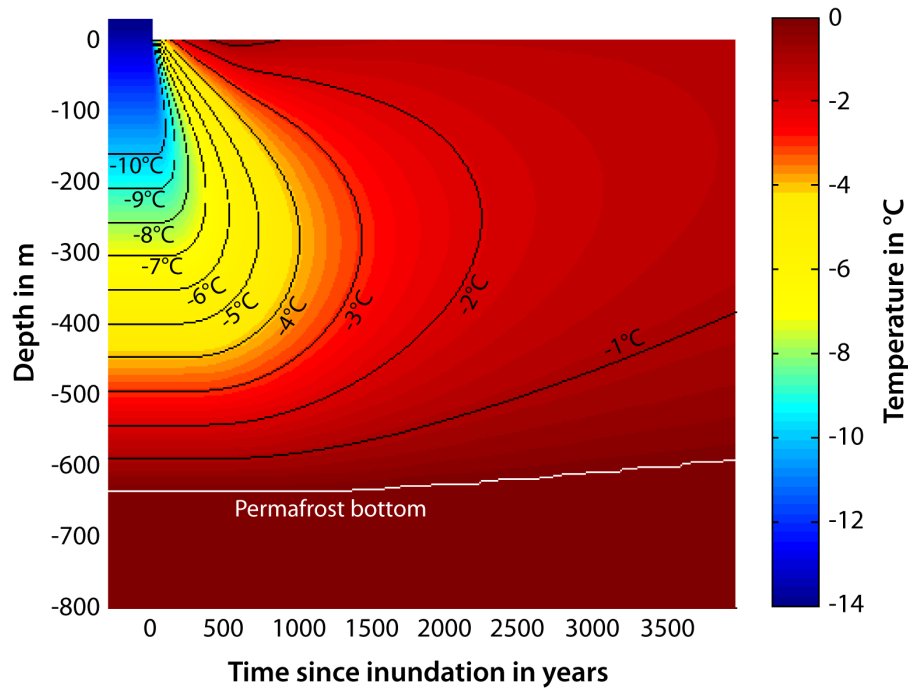


Figure 3.10: Modelled temperatures for 3965 a after inundation (C2), based on heat conduction and without salt infiltration. The bottom table of permafrost is indicated in white. Temperature isolines are indicated in black.

-2 and -1 °C down to a depth of 67.5 m. Heat conduction yielded no ice-related degradation due to continued subzero temperatures. The freezing temperature of sea water with the salinity of 30 ‰ is depressed to approximately -1.8 °C. The temperature profile after 2000 a was warmer than this threshold temperature.

Initial ground surface temperature

The influence of the initial ground surface temperature on the permafrost thickness after 2500 a was investigated using varying initial surface temperatures T_{ini} . Due to the assumed initial steady-state temperature profile, T_{ini} determined the initial temperature conditions in the sediment column. Figure 3.11 shows the final temperature profiles 2500 a after inundation for different T_{ini} , including the corresponding bottom depth of permafrost. The permafrost thickness was very sensitive to the initial ground surface temperature. A 2 °C variation in T_{ini} resulted in a shift of the bottom depth of permafrost of about 100 m.

Cliff erosion

The eroding coastal cliff is associated with a loss of the upper part of the sediment column. This exposes the sediment at the base of the cliff as the new top of the

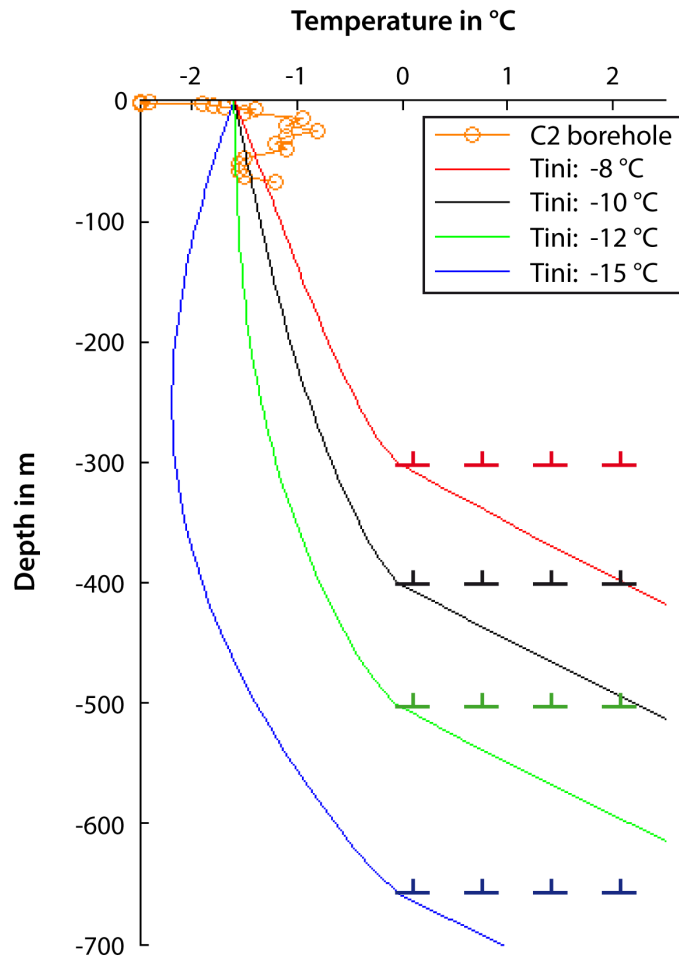


Figure 3.11: Influence of the initial surface temperature on the final temperature profiles 2500 a after inundation. The bottom table of permafrost is indicated for each case of T_{ini} . The measured temperature profile of the C2 borehole is also plotted (yellow circles).

submerged sediment column. As this potentially alters the temperature profile that the marine processes act upon, the influence of an eroding cliff of 30 m height at Mamontov Klyk on the bottom boundary of permafrost was studied using two modelled temperature profiles: with and without an initial soil column cut prior to inundation. Figure 3.12 compares the final temperature profiles at the end of the model runs. Although a slightly warmer temperature profile resulted from the initial cliff erosion, both temperature profiles yielded almost equally isothermal conditions throughout the profile. The difference in depths between the bottom permafrost table was also about 30 m. Thus, the influence of the eroding cliff prior to inundation is effectively limited to a shift of the same height in the overall thickness even after a few thousand years.

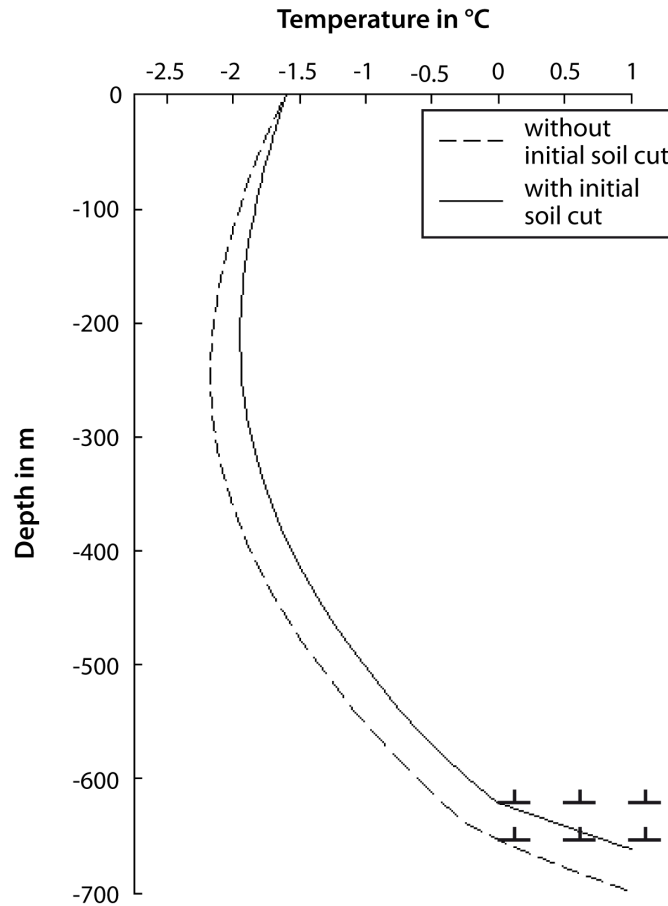


Figure 3.12: Influence of coastal cliff erosion: The modelled final temperature profiles after 2500 a for two cases, one with the top 30 m of soil eroded prior to inundation (solid line), and one without (dashed line).

Stratigraphic salt scenarios

The influence of the presence of salt in the subsea sediments was tested using four different stratigraphic scenarios: (i) a purely fresh sediment column with no salt infiltration from above, (ii) the same, but a salt infiltration implemented as the simple mean rate determined from the 35 m depth of ice-bonded permafrost table at C2 of about a cm per year, (iii) prior saline sediments in the entire column, and (iv) prior saline layers based on the Blasco [1995] layers. All model runs were based on constant sea bottom temperatures of -1.6°C after inundation, and based solely on the static influence of the salt presence in the liquid water content and latent heat effects. The resulting profiles of temperature and ice saturation for all four scenarios after 2500 a are shown in Fig. 3.13. The permafrost temperatures remained unchanged with included simple salt infiltration from above by a fixed infiltration rate, compared to the no salt scenario. While the thawed state of the top 35 m could be seen in the corresponding ice saturation, this had negligible effect on the temperature

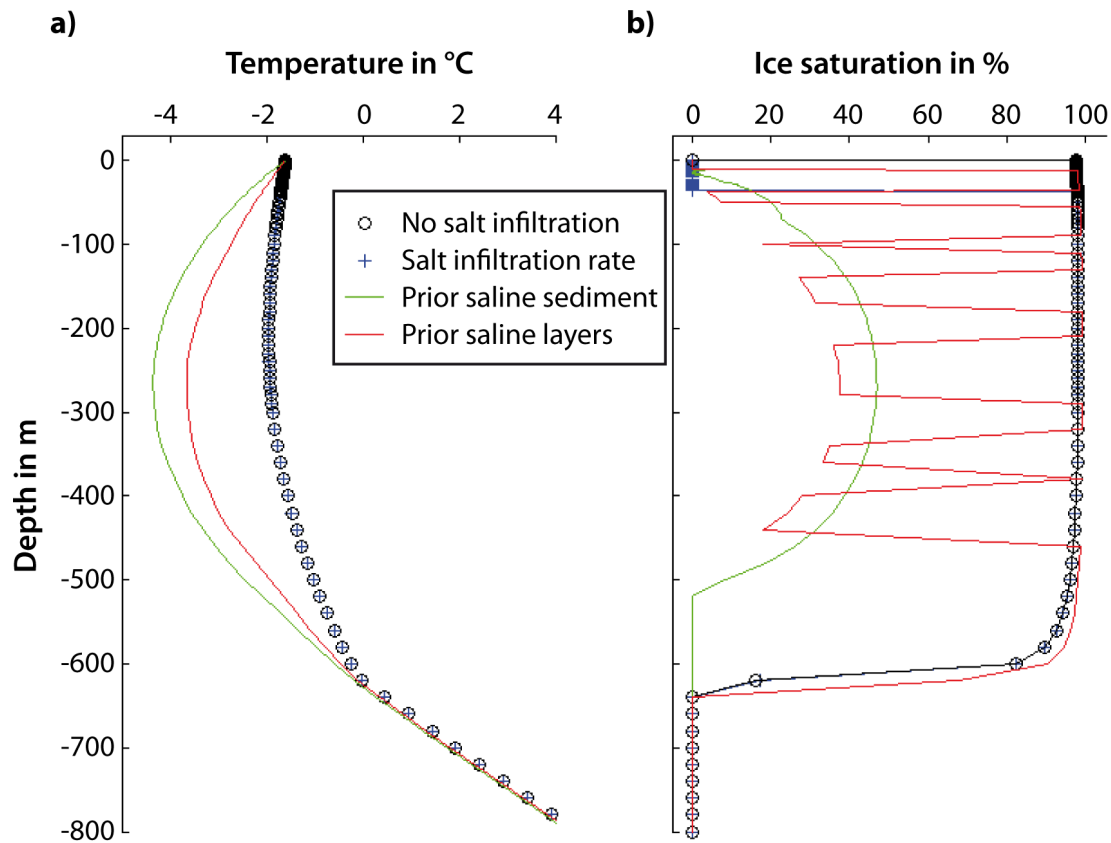


Figure 3.13: The effect of four stratigraphic scenarios of salt distributions in the subsea sediments on temperature (a) and ice saturation (b) profiles after 2500 a.

profile. In the same time period of inundation, the permafrost temperatures for the stratigraphy of prior saline sediments remained lower by maximally 2.4 °C. The temperatures in the profile of the saline layer stratigraphy were between these cases of fresh and completely saline sediments, and maximally lower by 1.7 °C. This is an expression of the latent heat that the saline sediment requires at already lower temperatures. The corresponding profiles of ice saturation, on the other hand, differed largely from the fresh sediment stratigraphy scenario. In the case of prior saline sediments, ice saturation decreased during the inundation period throughout the entire permafrost column. A maximum ice saturation of 47 % at around 270 m depth, and ice-bonded conditions between only about 140–400 m were found, and indicated a largely degraded permafrost state. The layer-scenario differed again. The ice saturation profile varied between lower values in the saline layers similar to the saline sediments case and the high values of the fresh sediment scenario in the regions between these layers. For this case, the ice saturation in all saline layers of the permafrost column had dropped to levels below 40 % after 2500 a, indicating degraded, not ice-bonded conditions. Thus, widely differing ice content conditions corresponded to relatively similar temperature profiles in the subsea sediments depending on the

stratigraphic scenario of salt distribution.

Sediment diffusion coefficient

In order to additionally consider the coupled diffusion transport of salt in the sediments after inundation, a diffusion coefficient in the porous medium D^{sed} must be used (Sect. 3.6.4.1). The influence of the diffusion parameterization was studied using the parameterizations in Table 3.1. For the Frederick and Buffet parameterization $n = 1, 2$ and 4 were tested (Fig. 3.14 a). Figure 3.14 b shows the associated salt concentration profiles after 2500 a. As expected for the small porosities in the subsea sediments, parameterizations with higher D^{sed} at small porosities generated more rapid salt infiltration. However, the difference between thaw depths in the ice saturation profiles was negligible (Fig. 3.14 c): Except for the $n = 4$ case, all parameterizations yielded relatively similar depths of ice-bonded permafrost (within 18%), of about 4 m in 2500 a. Sensitivity to this factor was therefore low. The Boudreau [1997] parameterization was subsequently used in this study.

With this diffusion implementation, the impact of the following inundation parameters on the downward degradation and resulting thaw depths was assessed: sea bottom temperatures, shoreline retreat rates, and effective diffusive and advective salt transport parameters. To clarify the individual impacts, only one factor was varied in each assessment. In the case of the former two factors, a model employing solely the reference mass diffusion as salt transport mechanism was used ($8 \cdot 10^{-10} \text{ m}^2 \text{ s}^{-1}$). While in the case of the latter two parameters, a model employing the reference values of bottom water temperatures (OCSEAP) and retreat rates (long-term rates) was used.

Sea bottom temperatures

The sea bottom temperatures after inundation govern the temperature evolution at the top of the submerged permafrost. Sensitivity to differing sea bottom water temperature was tested: Specifically, the influence on the degradation depth was studied using the OCSEAP data, the OCSEAP data shifted by $+1 \text{ }^\circ\text{C}$, and a constant temperature scenario (see data plots in Fig. 3.24). Results are presented in Fig. 3.15. The degradation depth in the constant temperature scenario began to decrease with time from the onset of inundation, while degradation remained at shallower depths for the first few hundred years in the OCSEAP data scenarios, due to the initially very cold temperatures in the latter. However, both OCSEAP scenarios overtook the degradation depth of the constant scenario after only 126 a and 213 a, respectively.

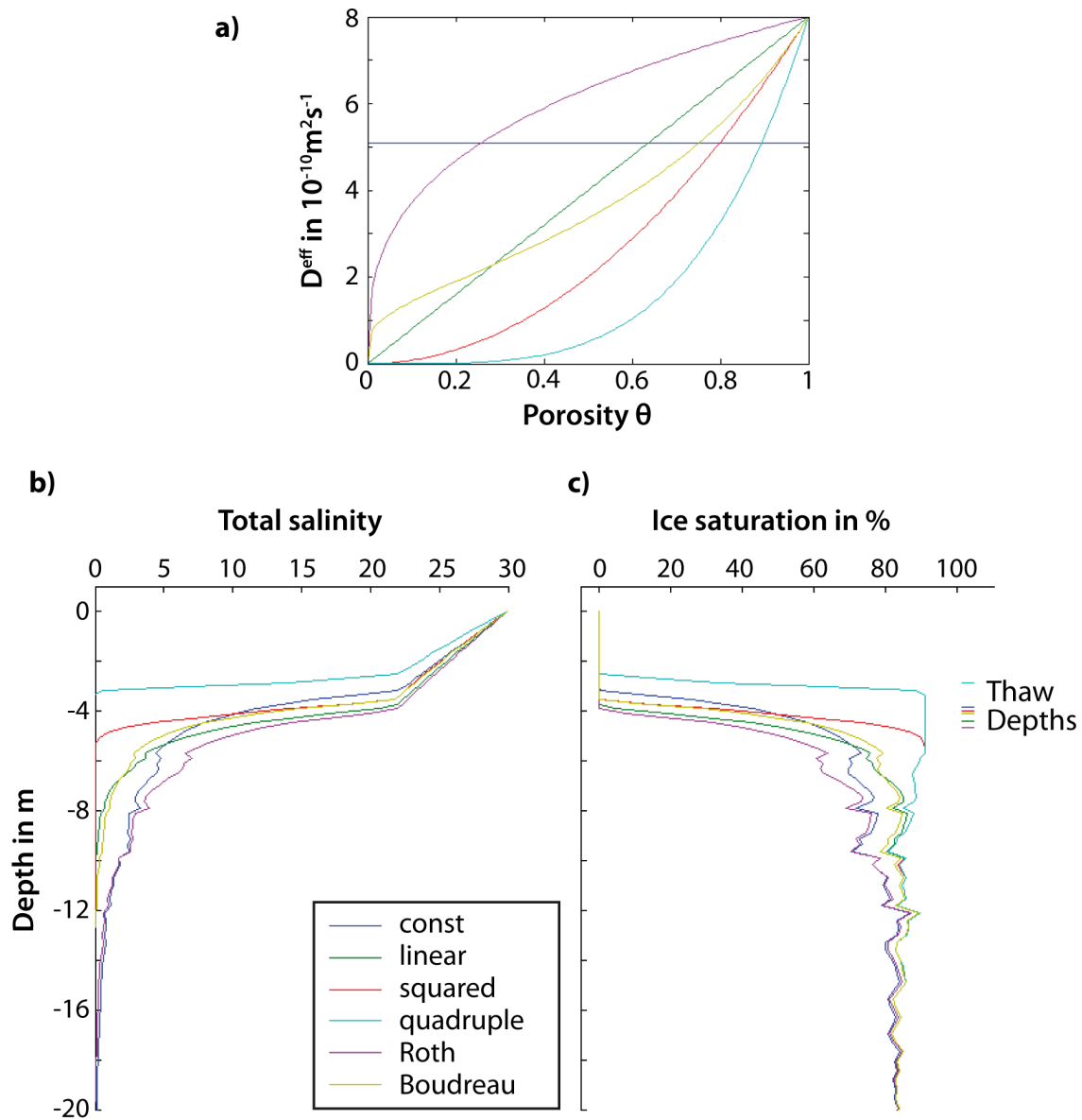


Figure 3.14: Sensitivity to the parameterization of the effective diffusion coefficient: (a) The parameterization with respect to porosity, and the corresponding profiles of total salinity (b) and ice saturation (c) in the sediment. The associated thaw depths (40 % ice saturation) after 2500 a are indicated on the right-hand side of the ice saturation profiles.

The OCSEAP scenario, although consisting of subzero, and only slightly warmer temperatures by less than maximally 1 °C between 2 and 6 m water depths compared to the constant scenario, yielded a larger degradation depth after 2500 a by a factor of about 2: 4.43 m vs. 2.19 m. A shift in the OCSEAP scenario by 1 °C resulted in a further progressed degradation depth of 11.44 m after 2500 a. Thus, the degradation rate and depth to the ice-bonded permafrost table as a function of time or distance offshore responded strongly to variations in sea bottom temperatures.

Shoreline retreat rates

The rate of local shoreline retreat governs the progression speed of inundation of the land by the Arctic Ocean. While known to be variable in space and time, local retreat rates are generally assumed to have remained similar to the present-day rates, mainly due to the lack of records on the time scale of the inundation. The influence of variation and uncertainty in the coastal retreat rates was investigated using the long-term retreat rate of 2.9 m a⁻¹ as reference for the Mamontov Klyk site. The high modern retreat rate of 4.6 m a⁻¹ was used as an upper bound. A rate as low as 2.3 m a⁻¹ was assessed to yield a lower bound (see discussion in Sect. 3.8). At Buor Khaya and Muostakh Island, inundation time points based on the observed long-term retreat rates of 1.4 m a⁻¹ and 2.32 m a⁻¹, respectively, were more recent. Here, a factor of 2 was used to investigate the influence of variation and uncertainty. Model runs for each rate were performed and the thaw depth as a function of distance offshore was analyzed. Figure 3.16 shows the resulting depth of the ice-bonded permafrost table at Mamontov Klyk for the long-term retreat rate and both lower and upper bound rates. While this thaw depth for the long-term rate reached 5.27 m at 11.5 km offshore, these depths differed by 24 % and 22 % for the lower and upper rate limit, respectively. These deviations – as given by the upper and lower bounds of the retreat rate – were obtained with salt transported diffusion only. However, when the rate of downward infiltration is larger, e.g. with an advective contribution or larger effective diffusion, the impact of the different retreat rates is also enlarged. To test the effect at higher salt infiltration, Table 3.2 shows the impact for a range of speculative, higher effective diffusion parameters. The table lists the difference in thaw depths at the borehole locations between the upper and lower retreat rates. Salt infiltration of the highest tested D parameter of $350 \cdot 10^{-10} \text{ m}^2 \text{ s}^{-1}$ was closest to observational thaw depths at C2 (see Fig. 3.17). The impact at the end of the model runs (at the C2 borehole location) increased significantly, from about 2.5 m to over 12 m. An increase of the same magnitude was found for higher effective v parameters (see in Fig. 3.20 b; about 12 m variation in thaw depths at the highest tested v).

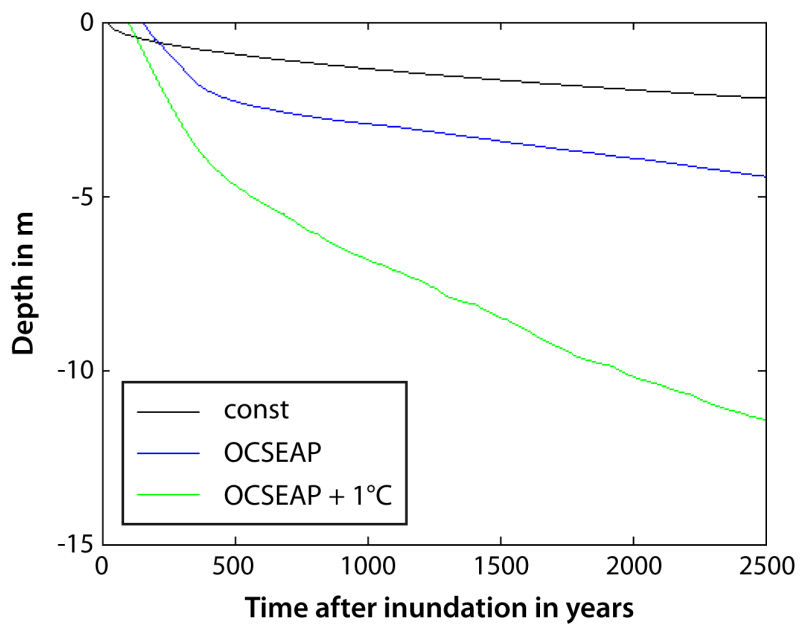


Figure 3.15: Impact of sea bottom temperatures on the depth of the ice-bonded permafrost table after 2500 a.

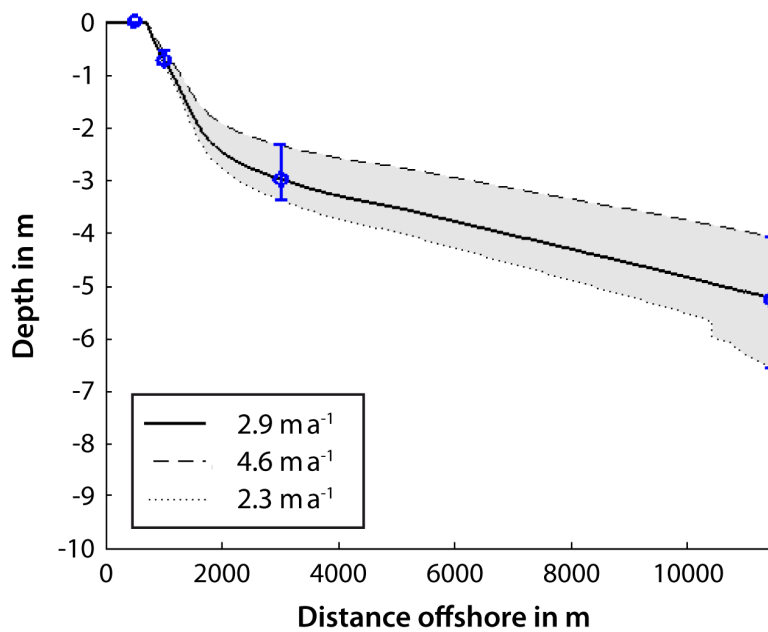


Figure 3.16: Impact of coastline retreat rate on the depth of the ice-bonded permafrost table. The model curves are based on the reference salt diffusion coefficient ($D = 8 \cdot 10^{-10} \text{ m}^2 \text{ s}^{-1}$). The range in degradation depths is highlighted at the distances of the boreholes C5, C4, C3, and C2 at about 0.5, 1, 3, and 11.5 km offshore, respectively.

Impact of the shoreline retreat rate therefore increased with salt infiltration rates, and was significant at the observed infiltration conditions.

Assessment of salt transport processes: diffusion

Based on fixed functions for bottom water temperatures and the long-term mean shoreline retreat rates at the three study sites, the influence of the effective salt transport parameters was assessed. First, the impact of an increased effective diffusion parameter D was tested using model runs with only diffusive transport ($v = 0$) and increasing D . The results are presented in this section. In the next section, the impact of increasing advection at constant D is assessed.

Figure 3.17 shows the modelled depths of the ice-bonded permafrost table for increasing effective diffusion parameters D . Stars mark the observed table depths. Table 3.3 lists the specific depths for the borehole locations at Mamontov Klyk. The reference salt diffusion coefficient of $D = 8 \cdot 10^{-10} \text{ m}^2 \text{ s}^{-1}$ yielded thaw depths in the sub-seabed sediments of 2.99 m and 5.27 m at the C3 and C2 borehole locations at about 3 km and 11.5 km, respectively. These underestimated the observed thaw depths by a factor of about 4 and 6.6, respectively. Increased effective D parameters of 25 and $100 \cdot 10^{-10} \text{ m}^2 \text{ s}^{-1}$ continued to fall short of the observed depths at these two borehole locations. The observed thaw depth at C3 was reached (14.15 m) by the highest tested parameter of $350 \cdot 10^{-10} \text{ m}^2 \text{ s}^{-1}$. However, the observed depth at C2 was only approximately obtained using the lower bound retreat rate, i.e. the longest assumed period of inundation, even for this D parameter magnitude. The modelled depths of the ice-bonded permafrost table were not consistent with the observations for the closest boreholes of C5 and C4 for any of the tested effective D

Table 3.2: Impact of coastline retreat rate for higher salt infiltration. The effective D parameters correspond to those used in Fig. 3.17. The difference in modelled thaw depths between upper and lower boundary rates is given at the COAST borehole locations. Distance offshore is given in brackets.

	Difference in depth to ice-bonded permafrost table in m:			
	C5 (0.5 km)	C4 (1 km)	C3 (3 km)	C2 (11.5 km)
$D = 8 \cdot 10^{-10} \text{ m}^2 \text{ s}^{-1}$	0	0.24	1.04	2.47
$D = 25 \cdot 10^{-10} \text{ m}^2 \text{ s}^{-1}$	0	0.43	1.76	4.51
$D = 100 \cdot 10^{-10} \text{ m}^2 \text{ s}^{-1}$	0	0.70	4.33	7.11
$D = 350 \cdot 10^{-10} \text{ m}^2 \text{ s}^{-1}$	0	1.00	5.67	12.30

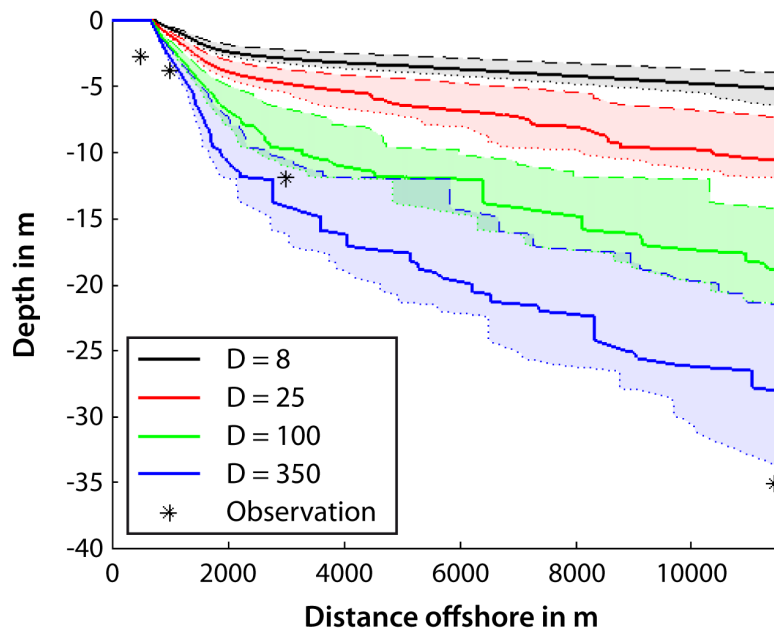


Figure 3.17: Impact of effective diffusion parameter D on the depth of ice-bonded permafrost table as a function of offshore distance for Mamontov Klyk. D is given in units of $10^{-10} \text{ m}^2 \text{ s}^{-1}$. The solid lines show the thaw depths for the long-term retreat rate of 2.9 m a^{-1} , while the dashed and dotted lines represent the bounding retreat rates of 4.6 m a^{-1} and 2.3 m a^{-1} , respectively. Observations of ice-bonded permafrost table depth from the COAST boreholes are also displayed (starred symbols).

Table 3.3: Modelled depth to ice-bonded permafrost table at the COAST borehole locations for various effective D parameters. Results are for the long-term coastline retreat rate of 2.9 m a^{-1} .

effective input parameter D (in $10^{-10} \text{ m}^2 \text{ s}^{-1}$)	Depth to ice-bonded permafrost table at:			
	C5 (in m)	C4 (in m)	C3 (in m)	C2 (in m)
8	0	0.74	2.99	5.27
25	0	1.23	4.87	10.68
100	0	2.08	9.80	18.98
350	0	2.89	14.15	28.09

parameters. These are located in the very near-shore zones 3 and 4 (see Fig. 1.7), and within 1 km of the shoreline.

Depth of the ice-bonded permafrost table with distance offshore for the other two sites at Muostakh Island and Buor Khaya are shown in Fig. 3.18. Modelled results for four different D parameters are shown. The corresponding thaw depth measurements from the geophysical detection along the eastern transect at Muostakh Island (see Chap. 2) and from the borehole at Buor Khaya are marked by stars. The $D = 8 \cdot 10^{-10} \text{ m}^2 \text{ s}^{-1}$ curve in panel b displayed lowered thaw depths beyond an offshore distance of about 400 m, which was unexpected because it surpassed the depth for the higher D parameter of $25 \cdot 10^{-10} \text{ m}^2 \text{ s}^{-1}$. Model testing related the effect to the value of ocean salinity, but the exact cause remained unknown. Nonetheless, at both sites, the same trend as at the Mamontov Klyk site was found. The observed depths to the ice-bonded permafrost table were severely underestimated by the implementation of the pure salt diffusion coefficient ($D = 8 \cdot 10^{-10} \text{ m}^2 \text{ s}^{-1}$). For Muostakh Island, modelled depths were 2.63, 3.06, 3.75, and 5.39 m at the four station locations at 514, 736, 1072, and 2048 m offshore, respectively. These were thus lower than the corresponding measured depths by a factor of about 2.8, 3.0, 3.1, and 3.5. For Buor Khaya, modelled depth at the borehole at 740 m offshore (8.34 m) was lower than the observation by a factor of 3.

Modelled profiles of salt concentration of the interstitial waters in the subsea sediments at the C3 and C2 borehole locations of Mamontov Klyk are presented in Fig. 3.19.

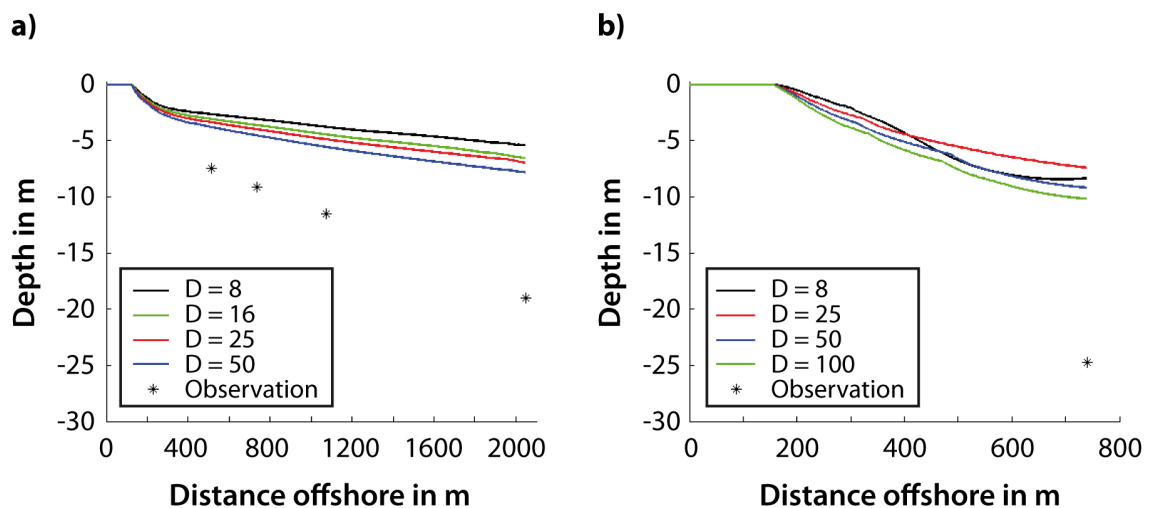


Figure 3.18: Impact of effective diffusion parameter D on the depth of ice-bonded permafrost table as a function of offshore distance for (a) Muostakh Island and (b) Buor Khaya. D is given in units of $10^{-10} \text{ m}^2 \text{ s}^{-1}$. Model results are based on the long-term retreat rate at the respective site. Observations of ice-bonded permafrost table depth are also displayed (starred symbols).

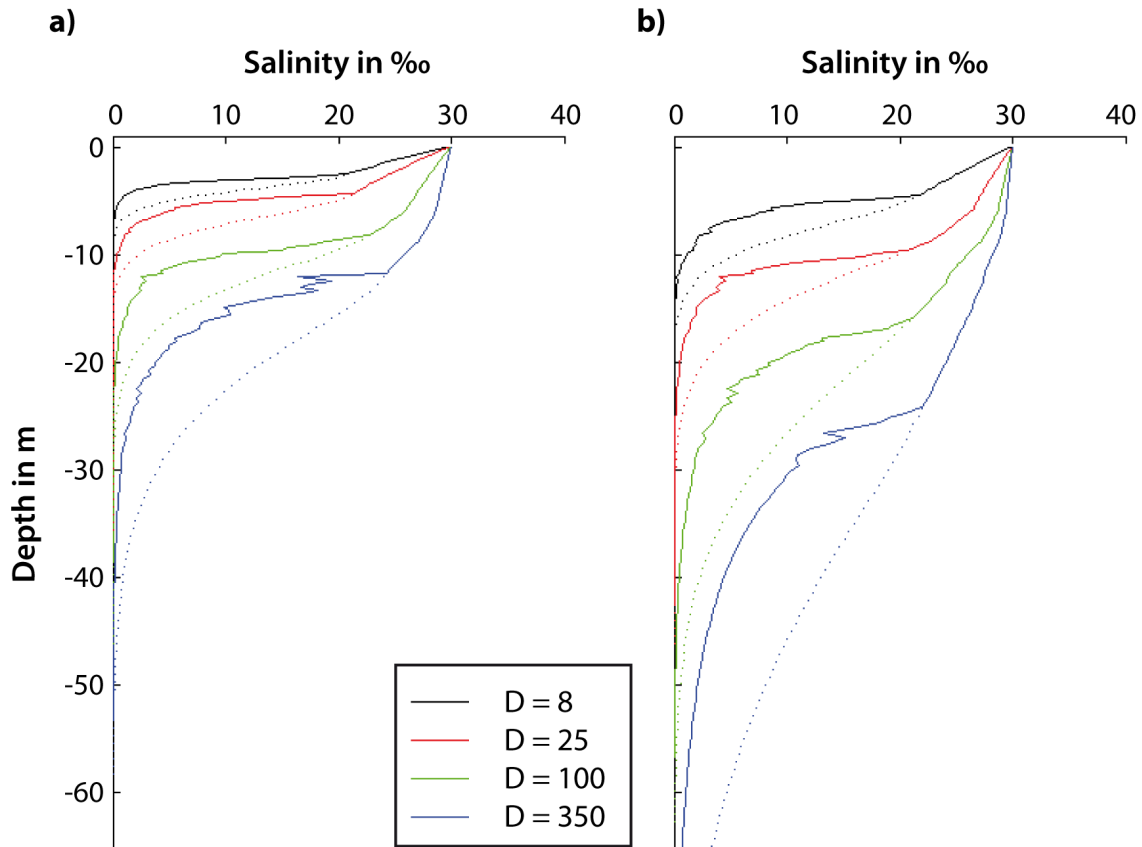


Figure 3.19: Modelled salinity profiles for purely diffusional salt transport: Resulting profiles are given for the same D parameter values as in Fig. 3.17, and for (a) C3 and (b) C2 at Mamontov Klyk. Solid lines represent total salinities, dashed lines in-situ salinities.

Salinity profiles are shown corresponding to the same D parameters as in Fig 3.17 and Table 3.3. Both in-situ salinities and total salinities are plotted for each case. While in-situ salinity profiles showed typical diffusive curves of smoothly decreasing trends away from the ocean source into the subbottom, total salinity profiles displayed a much more rapid decrease and differing, sharp salinity gradients above the ice-bonded permafrost table in the ice-bearing permafrost zone. The total concentration profiles also exhibited less smooth curves with sharp kinks. These were the result of variations in the sediment composition, i.e. the porosity change as a function of depth. The ice-bearing zone was recognized in these salt infiltration scenarios. This zone of partially frozen sediments (ice saturation between 0 and 100%) can be readily recognized in the salinity profiles as the region where total and in-situ salinities diverge. At C2, the modelled thickness of the ice-bearing layer above the ice-bonded permafrost table (40% ice saturation) varied between 0.79 m and 3.98 m for the cases of $D = 8 \cdot 10^{-10} \text{ m}^2 \text{ s}^{-1}$ and $D = 350 \cdot 10^{-10} \text{ m}^2 \text{ s}^{-1}$, respectively.

Assessment of salt transport processes: advection

Based on the salt diffusion coefficient ($D = 8 \cdot 10^{-10} \text{ m}^2 \text{ s}^{-1}$), the influence of additional advective salt transport was assessed using models of increasing effective parameter v . Figure 3.20 a shows the modelled depths of the ice-bonded permafrost table for different v . Stars mark the observations of table depths at the borehole locations. The mean in-situ flow velocities observed in the model run corresponding to these input parameters v are given in Table 3.4. The table also lists the specific thaw depths for the borehole locations at Mamontov Klyk. The $v = 0$ case corresponds to the model run with reference salt diffusion coefficient and no additional advective component (black line in Fig. 3.17). For higher input parameter v , the obtained thaw depths were successively deeper, too. However, for higher v , the gain in additional thaw depth began to decrease around $v = 50 \cdot 10^{-10} \text{ m s}^{-1}$. Beyond a v of approximately $100 \cdot 10^{-10} \text{ m s}^{-1}$, no significant further impact of increased parameter v was found. This ‘saturation’ of obtained thaw depths and in-situ flow velocities expressed the density-driven character of the advective mechanism: As this process is density-driven, its effect is limited by the occurring density differences. v sets a magnitude of flow for maximum density gradients between pore water of low salinity above the permafrost table and the ocean water of high salinity. For very high v , the density differences within the sediment column were equalized more quickly, but no significant further deepening of the thaw depths was found. This is represented in the modelled salinity profiles at C3 and C2 (Fig. 3.22). Higher v values corresponded

Table 3.4: Overview of effective input parameter v , corresponding mean in-situ flow velocities in the model v_m , and depth to ice-bonded permafrost table at the COAST borehole locations. Results are based on the reference salt diffusion coefficient ($D = 8 \cdot 10^{-10} \text{ m}^2 \text{ s}^{-1}$).

effective input parameter v (in $10^{-10} \text{ m s}^{-1}$)	mean in-situ flow velocity v_m (in cm a^{-1})	Depth to ice-bonded permafrost table at:			
		C5 (in m)	C4 (in m)	C3 (in m)	C2 (in m)
0	0	0	0.74	2.99	5.27
1	0.09	0	0.75	3.30	6.72
5	0.41	0	0.78	4.45	11.48
15	0.80	0	0.87	6.68	17.98
50	1.08	0	1.07	8.96	22.81
100	1.16	0	1.21	9.81	24.19
400	1.23	0	1.37	10.40	25.38
1200	1.26	0	1.43	10.60	25.56

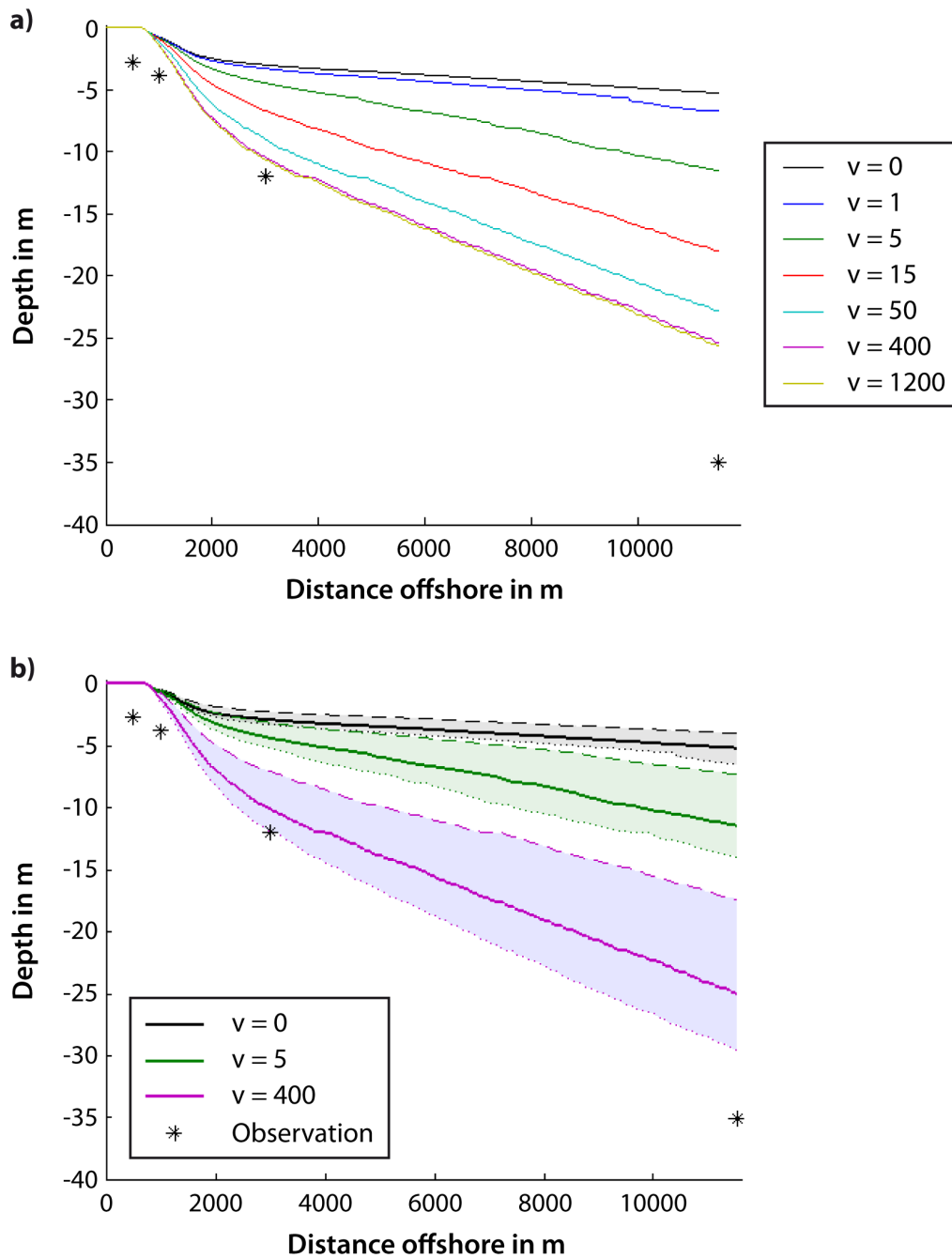


Figure 3.20: (a) Impact of effective advection parameter v on the depth of ice-bonded permafrost table as a function of offshore distance for Mamontov Klyk. v is given in units of $10^{-10} \text{ m s}^{-1}$. (b) Impact of coastline retreat rates on the depth of ice-bonded permafrost table for three input parameters v . The solid lines show the thaw depths for the long-term retreat rate of 2.9 m a^{-1} , while the dashed and dotted lines represent the bounding retreat rates of 4.6 m a^{-1} and 2.3 m a^{-1} , respectively. Observations of ice-bonded permafrost table depth from the COAST boreholes are also displayed (starred symbols).

to profiles with constant, uniform salinity of about 30 all the way down to the permafrost table. The smallest density gradient was quickly equalized, but did not result in further increases in thaw depth. Since in-situ flow velocity would cease once the density difference was eradicated, the mean in-situ velocities confirmed this process-inherent ‘saturation’ limit (Table 3.4). The mean in-situ flow velocities observed in the model increased quickly to values of about 1 cm a^{-1} with increasing effective input parameter v until about $v = 50 \cdot 10^{-10} \text{ m s}^{-1}$. Beyond this, a threshold was reached and no rapid increase was found. Mean in-situ transport velocities did not exceed maximum values of 1.26 cm a^{-1} . Thus, mean in-situ transport velocities in density-driven processes in these subsea conditions were on the order of maximally cm a^{-1} .

The addition of a density-driven, advective component of salt transport yielded thaw depths in the sub-seabed sediments of maximally about 10 m and 25 m at the C3 and C2 borehole locations, respectively. Using a parameter just below the threshold of ‘saturated’ velocity conditions ($v = 25\text{--}50 \cdot 10^{-10} \text{ m s}^{-1}$) yielded corresponding thaw at these locations of around 8 m and just above 20 m, respectively. These underestimated the observed thaw depths, which were higher by a factor of about 1.6. The modelled depths of the ice-bonded permafrost table were again not able to yield consistent results with the observations for the closest boreholes of C5 and C4 for any of the tested effective v parameters. Figure 3.20 b shows the difference in thaw depths between the bounding shoreline retreat rates as a function of distance offshore. The impact of uncertainty in the shoreline retreat rate at the higher salt infiltration rates was again high (about 12 m for mean in-situ flow velocities of 1.23 cm a^{-1} at input parameter v of $400 \cdot 10^{-10} \text{ m s}^{-1}$; refer to earlier results in the section on shoreline retreat rates).

Depth of the ice-bonded permafrost table with distance offshore for the other two sites at Muostakh Island and Buor Khaya are shown in Fig. 3.21. Modelled results for different v parameters as well as the observations are shown. At both sites, the same trend as at the Mamontov Klyk site was found. The observed depths to the ice-bonded permafrost table were also underestimated by the addition of the advective transport component. For Muostakh Island, modelled depths ($v = 50 \cdot 10^{-10} \text{ m s}^{-1}$) were 4.18, 5.16, 6.50, and 9.94 m at the four station locations, respectively. These were thus lower than the corresponding measured depths, which were higher by a factor of about 1.77, 1.76, 1.77, and 1.91. For Buor Khaya, observed depth at the offshore borehole at 740 m offshore was higher than the model result (11.72 m) by a factor of 2.1.

Modelled profiles of salt concentration corresponding to five selected v parameters

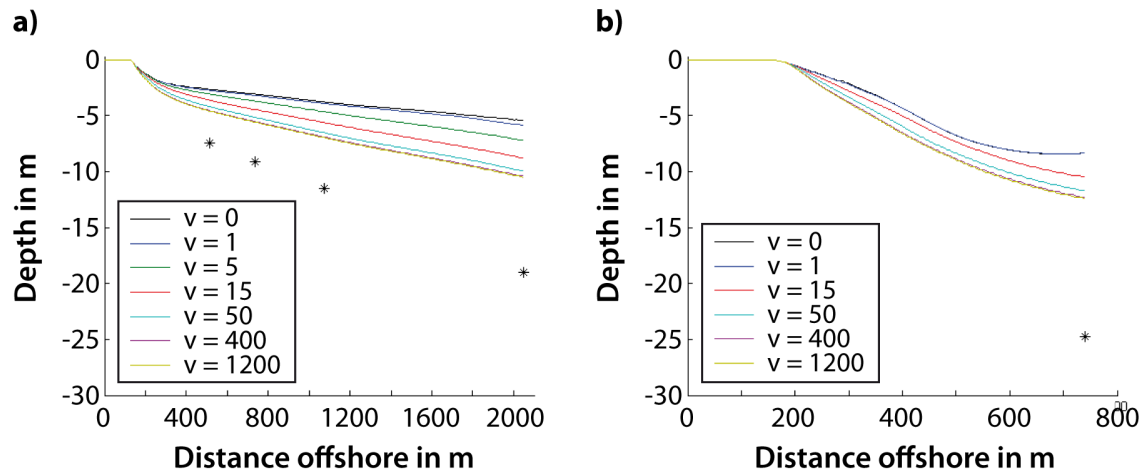


Figure 3.21: Impact of effective advection parameter v on the depth of ice-bonded permafrost table as a function of offshore distance for (a) Muostakh Island and (b) Buor Khaya. v is given in units of $10^{-10} \text{ m s}^{-1}$. Model results are based on the long-term retreat rate at the respective site. Observations of ice-bonded permafrost table depth are also displayed (starred symbols). Note the different spatial scales (x-axis) between the plots of the different sites.

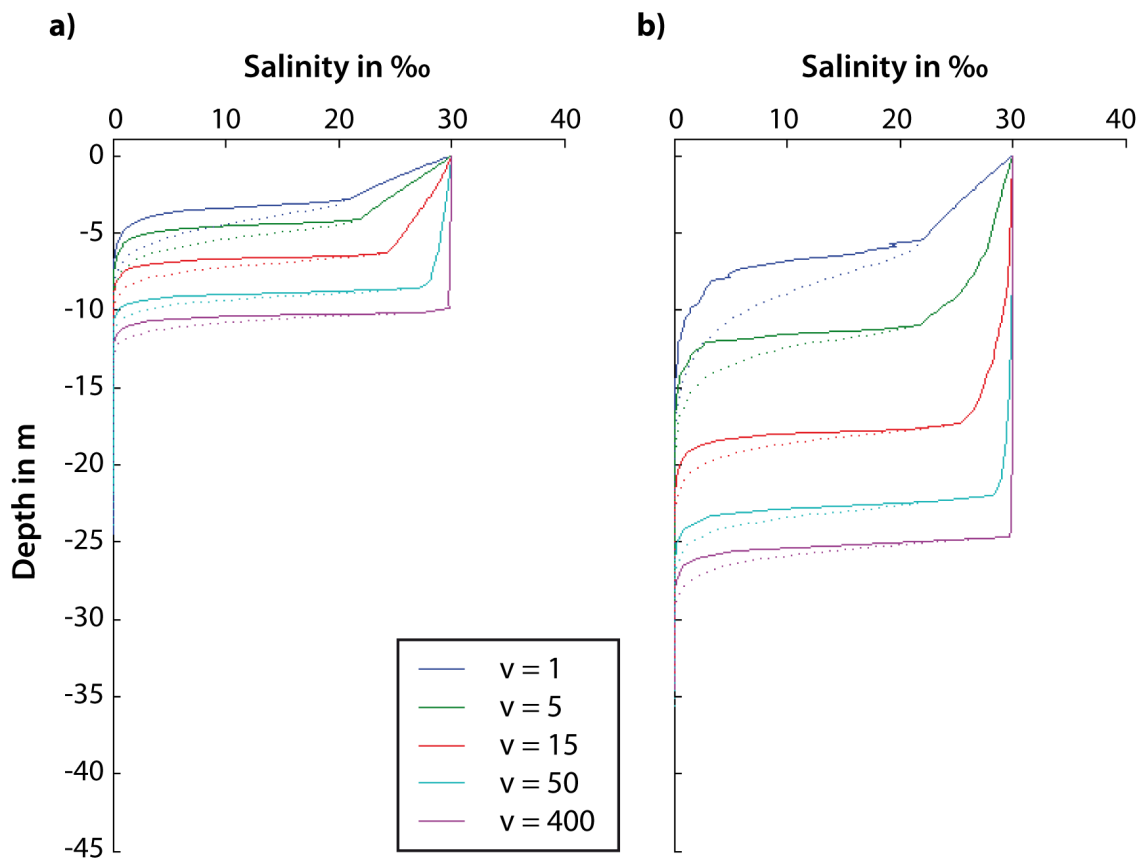


Figure 3.22: Modelled salinity profiles for different magnitudes of advective salt transport: Resulting profiles are given for (a) C3 and (b) C2 at Mamontov Klyk. Solid lines represent total salinities, dashed lines in-situ salinities.

($v = 1, 5, 15, 50, 400$) are presented in Fig. 3.22. Total and in-situ salinity profiles are given for the C3 and C2 borehole locations of Mamontov Klyk. Compared to the pure diffusion case, the in-situ salinities show less smooth trends with depths. Instead, higher salinities within the thawed sediment column and a relatively sharp decrease at a salinity front were characteristic of the advective case. The higher v , the more uniform salinities down to the depth of the ice-bonded permafrost table were found (see above). The concentration profiles did not display pronounced kink or bump features as in the diffusion case (Fig. 3.19), at least for v larger than $v = 1 \cdot 10^{-10} \text{ m s}^{-1}$. Thus, most salinity differences, caused by porosity variations with depth, were quickly overridden by the relatively fast advective flow. The differences between in-situ and total salinity profiles were also less pronounced, compared to the pure diffusion case. The modelled thickness of the ice-bearing layer above the ice-bonded permafrost table was therefore smaller, only 0.34 m and 0.37 m at the C3 and C2 locations, respectively.

Combined advective and diffusive salt transport

Finally, a combination of processes was modelled to seek an effective parameter combination to match the observed thaw depths from the field. Furthermore, the influence of a talik at the site of inundation and its potential to lower the observed depth of the ice-bonded permafrost table compared to an intact Yedoma layer was modelled.

Figure 3.23 shows the thaw depths and associated salinity profiles at the C3 and C2 borehole location for models with different parameter combinations in four cases. Field observations of thaw depths are also given in the figure. A v parameter just below the onset of saturation was used to model the advective component of salt transport ($v = 25 \cdot 10^{-10} \text{ m s}^{-1}$). A base case is given by the reference salt diffusion coefficient ($D = 8 \cdot 10^{-10} \text{ m}^2 \text{ s}^{-1}$). Higher effective D parameters ($D = 50$ and $100 \cdot 10^{-10} \text{ m}^2 \text{ s}^{-1}$) were used to yield results for thaw depths similar to the field observations. As previously indicated, the base case underestimated the field observations of thaw depth at all four borehole locations, by 100 %, 76 %, 35 %, and 41 % at C5, C4, C3, and C2, respectively. Additional contribution by an increased effective D of between $50 \cdot 10^{-10}$ and $100 \cdot 10^{-10} \text{ m}^2 \text{ s}^{-1}$ would yield thaw depth which met the observations at the two further offshore boreholes. Deviations at C3 and C2 were only $\pm 5\%$ and $\pm 7\%$, respectively. At the same time, these cases continued to fall short by about 50 and 100 % at the two near-shore boreholes C4 and C5. In order to also show the potential influence of pre-deteriorated permafrost conditions prior to inundation, results are shown for an initial temperature profile similar to

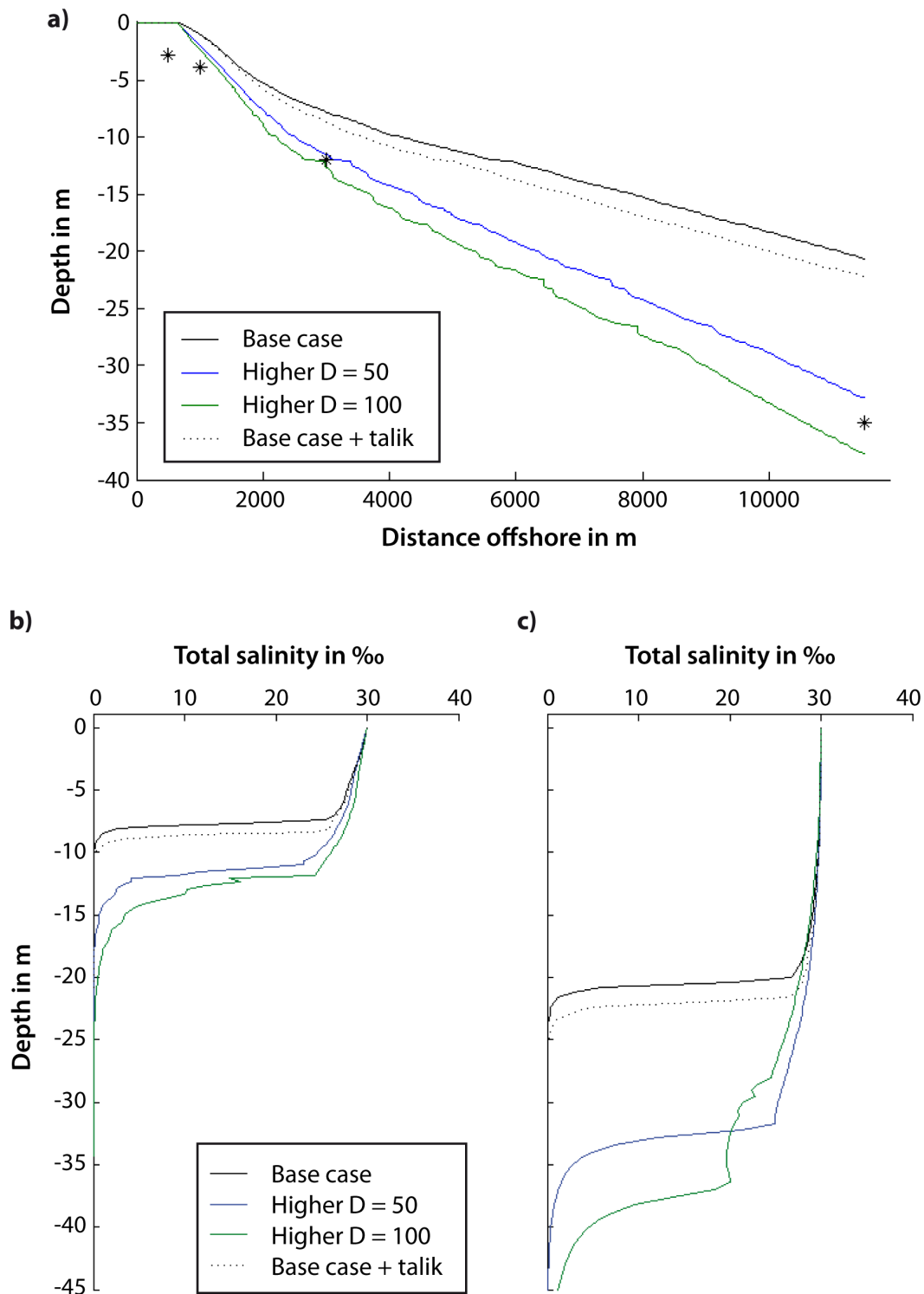


Figure 3.23: Depth of the ice-bonded permafrost table as a function of offshore distance (a) and modelled total salinity profiles at Mamontov Klyk for C3 (b) and C2 (c) for different combination scenarios of processes: (i) base case of $(v,D) = (25,8)$, (ii) higher effective D cases of $(v,D) = (25,50)$ and (iii) of $(v,D) = (25,100)$, and (iv) base case with initial talik conditions. Star symbols indicate observations.

that of a thermokarst lake with a bottom water temperature of 3 °C [Lenz et al., 2016] and an approximately 30 m deep talik after 1500 a. The talik scenario yielded only slightly lower thaw depths compared to the base case, with depths lower by 0.8–1.6 m between C3 and C2. Specifically for later inundation stages, the trend was almost uniformly shifted to the base case at offshore distances beyond about 3 km. This indicated that the talik affected thaw depths during the initial inundation stages, but its effect on longer time scales was given by a constant offset.

The total salinity profiles (Fig. 3.23 b and c) also showed only a small downward shift of the salinity front for the talik scenario compared to the base case at both C3 (shift by c. 0.8 m) and C2 (by c. 1.6 m). While both higher D scenarios showed relatively sharp fronts at C3, the higher relative role of diffusion in the $D = 100 \cdot 10^{-10} \text{ m}^2 \text{ s}^{-1}$ case was apparent at C2, with lower salinity values between 28–36 m. It was also reflected in the appearance of small kinks, a response of diffusion to changes in sediment stratigraphy, in the profile compared to the lower D cases.

3.8 Discussion and implications

3.8.1 Modelled inundation parameters

Temperature, i.e. the thermal response of permafrost modelled initially in this study, is usually used to assess changes to permafrost, especially in traditional terrestrial permafrost. Assuming that modern long-term coastline retreat rates represent past mean rates, the modelled temperatures were similar to the measurements of temperature in the offshore borehole at a distance of 11.5 km (C2 in Fig. 3.2 b): Measured temperatures were slightly warmer and varied with depth by less than 1 °C compared to uniform model results. This may be the result of the heat disturbance from drilling, which perturbed sediment temperatures at the time of measurement [Junker et al., 2008]. If true, this would mean that measured temperatures were overestimated, which would be consistent with the slightly colder model profiles of temperature. The modelled permafrost thickness offshore of Mamontov Klyk is shown in Fig. 3.10. The depth of the permafrost bottom is in agreement with Romanovskii et al. [2004]’s model results, who give a permafrost thickness of 500–600 m for the near-shore zone at that site. Warming of subsea permafrost has three important consequences:

Firstly, no rapid permafrost degradation was suggested by the model. Subsea permafrost displayed almost isothermal temperature profiles of above -2 °C within only 2000 a after its inundation.

Secondly, whereas the initial cliff erosion hardly changed permafrost thickness, subsea permafrost thickness was highly sensitive to the initial ground surface temperature (by about 100 m per 2 °C). This is plausible, as T_{ini} mainly governs the initial permafrost thickness prior to inundation and degradation. These results suggest that accurate modelling of subsea permafrost depends on good knowledge of the state of permafrost prior to inundation. This emphasizes the importance of a good understanding of regional temperature forcing when attempting to assess subsea permafrost extent on any larger, i.e. regional or Arctic, scales. This prerequisite of the regional understanding of the initial conditions is, thus, subsequently studied in Chap. 4 of this thesis.

Thirdly, in contrast to observation, the thermal models yielded no thawed sediment layer overlying frozen permafrost (degrading ice-bonded permafrost). Field observations, however, clearly indicate a thawed layer and degradation of ice-bonded permafrost from the top downwards with increasing distance offshore. Therefore, the thermal implementation alone is insufficient to explain subsea permafrost degradation. Modelling must include the influence of salt in a further step to describe the observed degradation. The presence of salt and its infiltration would thaw the ice-bearing permafrost. The warmed, isothermal temperature profiles of above -2 °C are considerable, since the freezing temperature of sea water with the salinity of 30 ‰ is depressed to approximately -1.8 °C. This agrees with Osterkamp et al. [1989] who state that the degradation of subsea permafrost at subzero temperatures is driven by the salt infiltration. Our results indicate that these volatile thermal conditions are attained in the entire subsea permafrost column after only a few thousand years at Mamontov Klyk.

Considering stratigraphic scenarios of different salt distributions in the subsea sediments is an intermediate step to understand the influence of the presence of salt on the state of subsea permafrost. Four scenarios were tested: purely fresh sediments with and without a uniformly prescribed salt infiltration rate as well as prior saline sediments in either the entire column or in specific layers, as suggested by alternating transgressions and regressions [Osterkamp, 2001, Blasco, 1995, Ponomarev, 1940]. The resulting profiles of temperature and ice saturation in the subsea sediments (Fig. 3.13) show distinctly that, while temperature trends in the subsurface are similar in all four scenarios, they correspond to vastly different ice saturation profiles, and therefore degradation states of permafrost. Specifically, even though small differences in temperatures were found between the two saline scenarios, their temperature profiles are indistinguishable from freshwater sediment that has not been inundated quite as long. Nonetheless, permafrost degradation differs between these scenarios as shown in their ice saturation profiles. Permafrost vulnerability to

degradation, including development of a through-going talik, depends on ice-content, and, therefore, sediment salinity. Thus, two major implications of these findings are (i) that the information of a temperature profile is not sufficient to assess the (ice-related) degradation state of subsea permafrost sediments, and (ii) that the salt distribution in the sediments has a large impact on the resulting degradation state. The assumption of prior saline sediments throughout the entire column has been made by modellers of subsea permafrost maps in the Laptev Sea [Nicol'sky et al., 2012]. Our modelling results suggest that open taliks may develop in such cases (see the ice saturation profile for this scenario in Fig. 3.13 b). The ice saturation decrease will vary with the salt concentration present in the sediments. Furthermore, in contrast to Nicol'sky's assumption, the analysis of the COAST and Buor Khaya boreholes did not support completely saline sediments prior to inundation (Fig. 3.25). Their assumption therefore represents an extreme case with maximum potential permafrost degradation. Given the implications above, these scenarios thus highlight the necessity of implementing salt transport in subsea permafrost models and of correctly representing sediment stratigraphy.

Model sensitivity to tortuosity parameterization for the salt diffusion in porous sediments was low. Using the constant parameterization of tortuosity, modelled thaw depth ranged at the lower end of the tested parameterizations, while apparently generating increased liquid water fractions in the sediments below the ice-bonded permafrost table. However, changing ice content changes the tortuosity in a complex manner depending on pore size distribution, geometry, and connectivity. A parameterization of tortuosity in terms of Θ_w is intended to capture this complexity better than a constant tortuosity factor. This is also the more prevalently used approach. Nonetheless, current knowledge of the specific mechanisms of diffusion within sediments on the pore scale is limited. Thus, low model sensitivity to this parameter is good news. Boudreau [1997] states that ‘...the important point is [not the background theory, but] whether [the parameterizations] explain tortuosity data.’ Only laboratory measurements of local sediment samples would elucidate this question, but the low sensitivity supports that this is negligible. Instead, the Boudreau parameterization is proposed in this study, as it has shown the best fit to widespread, fine-grained, marine and lacustrine sediments [Boudreau, 1997].

For a modelled salt transport solely based on diffusion, and using the reference salt diffusion coefficient of $D = 8 \cdot 10^{-10} \text{ m}^2 \text{ s}^{-1}$, the depth of the ice-bonded permafrost table as a function of distance offshore yields a parabolic, which agrees with simple Stefan theory for homogeneous conditions [Harrison, 1982]. The modelled shallow thaw depths at the onset of inundation and a transition zone of more rapid, almost linearly increasing thaw depth preceding the parabolic shape are similar to obser-

variations at Prudhoe Bay, and due to the lower sea bed temperatures in the shallow water zone [Osterkamp et al., 1989]. However, the model severely underestimates the observed thaw depths at the C3 and C2 borehole locations (Table 3.3), and accounted for only about 25 % of the observed depth at the closer borehole at 3 km offshore, and even lower 15 % at the further offshore borehole at 11.5 km. At Buor Khaya, this model accounted for only 33 %, at Muostakh Island only for 36, 34, 33, and 28 %, at the observation locations offshore, respectively. Thus, solely diffusional salt transport underestimates thaw depths. This agrees with the findings by Harrison and Osterkamp [1978], who report for Prudhoe Bay, Alaska, that purely diffusional transport theory thawed a layer only about 4 m thick after approximately 3370 years of inundation. The observed thickness was at least 40 m. This is similar to the situation for C2 in the COAST transect in this study. Therefore, contributions from other salt transport processes must be active. In the following, several factors are discussed that may affect or contribute to salt transport: the indirect factors of sea bottom temperatures after inundation and variation in the shoreline retreat rate, as well as factors that effectively increase the diffusion coefficient or add advective contributions.

The sea bottom temperatures after inundation govern the temperature evolution at the top of the submerged permafrost, and may therefore affect downward degradation.

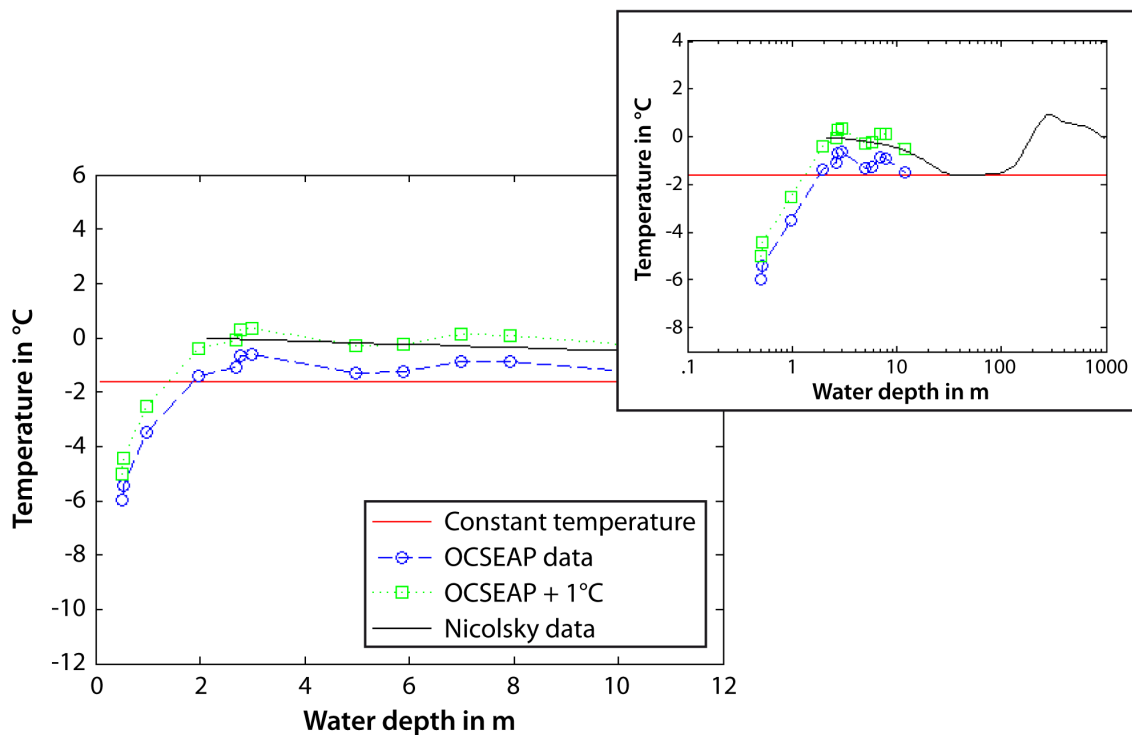


Figure 3.24: Sea bottom water temperatures: OCSEAP data adapted from Harrison and Osterkamp [1977], Laptev Sea data adapted from Nicolsky et al. [2012].

Some large-scale models of subsea permafrost evolution assume a simple, constant sea bottom temperature on the shelf after inundation (e.g. Romanovskii et al. [2004]). The red line in Fig. 3.24 indicates the constant assumption of $-1.6\text{ }^{\circ}\text{C}$. This assumption, however, is not always valid for the shallow near-shore zone. Mean annual sea bed temperatures as a function of water depth are available from Prudhoe Bay and Barrow, Alaska (OCSEAP data, blue line in the figure). Temperatures were slightly warmer, but subzero for depths larger than 2 m, but drop much lower landwards of the 2 m isobath to $-6\text{ }^{\circ}\text{C}$. Very shallow waters are therefore still affected by the colder air temperatures. Thermal coupling of the sea bed through bottom-fast sea ice results in colder mean annual temperatures. Observations of long-term (100 year mean) bottom water temperature as a function of water depth for the Laptev Sea shelf region are given by Nicolsky et al. [2012] and by Dmitrenko et al. [2011]. However, their focus is set around the Lena River region. Data on the general shelf region are more sparse, and especially so in the near-shore zone below 10 m water depth. The data (black curve in inset of Fig. 3.24) show constant bottom water temperatures of $-1.6\text{ }^{\circ}\text{C}$ on the outer shelf in water depths larger than about 25 m out to the shelf edge at 120 m. In shallower waters, benthic temperatures are warmer. Observational data are not available for water depths below 2 m in the Laptev Sea data, due to the bottom-fast sea ice zone. The Nicolsky data are 0.5 to $1\text{ }^{\circ}\text{C}$ warmer than the OCSEAP data. The Laptev Sea data (large-scale spatial average) encompasses warmer river discharge in the central Laptev Sea. However, Cape Mamontov Klyk was chosen to minimize river influence. While the assumption of constant sea bottom temperatures probably holds for water deeper than 25 m, it is likely too high landwards of the 2 m isobath, and too low in water depths in between (2–25 m). This study used the OCSEAP data for Mamontov Klyk, and shifted temperature curves to match observations in the warmer water regions at Muostakh Island and Buor Khaya Bay [Overduin et al., 2016], which are warmed by Lena river discharge. Degradation depth increased from about 4 to 11 m for an increase of $+1\text{ }^{\circ}\text{C}$ in the sea bottom temperatures (green curve in the figure). We thus expect differences in degradation between areas with warmer surface waters – as associated with river discharge –, and areas away from any such influences. Or in areas with bathymetry that affects benthic temperatures close to shore. Furthermore, the assumption of constant temperatures in other studies underestimates degradation rates, by missing the rapid initial degradation in water depths below 25 m. Therefore, any large-scale modelling effort of subsea permafrost evolution must represent the benthic temperatures well (i.e., capture the variability due to rivers and bathymetry).

The rate of local shoreline retreat and sea level rise govern the progress of inundation. Since we use assumed rates to estimate inundation periods, uncertainty in this

parameter generates uncertainty in the period of exposure to (degrading) submarine conditions. Coastal retreat rates are highly variable in space and time [Günther et al., 2013a]. They have been recorded directly only for recent decades. In the Laptev Sea region, remote sensing based on aerial photography covers a period of about 40 a. There are only few places, such as at Muostakh Island, where an annual scale record exists. Since we have no data pre-dating this relatively short period, we assume that past retreat rates were similar to present-day rates. Temporal variability, however, remains high even within this period [Günther et al., 2013a]. In this study, the long-term retreat rate of 2.9 m a^{-1} was used as reference for the Mamontov Klyk site. The high modern retreat rate of 4.6 m a^{-1} was used as an upper bound. A rate as low as 2.3 m a^{-1} was assessed to yield a lower bound, as this rate would yield a time of inundation of the 11.5 km offshore C2 borehole almost 5000 a before the present. This rate would place inundation right at the transition period when sea levels reached their present-day level (see Fig. 1.2). Placing the inundation even earlier than this would certainly have seen larger transgression rates due to the addition of sea level rise to coastal thermo-erosion, making 2.3 m a^{-1} the lower bound estimate. Our results showed that the impact of this factor on modelled thaw depths increased considerably with salt infiltration rates. Therefore, the impact is likely significant at the observed infiltration conditions of 35 m at 11.5 km offshore. This corroborates the importance of good knowledge of the local coastline retreat rates when an assessment of subsea permafrost evolution is sought on any scale, from local to regional to circum-Arctic.

Both factors of sea bottom temperatures and shoreline retreat rate, however, could not explain the difference between the diffusion model and observation. Thus, concerning salt transport, further processes may result in additional infiltration, such as wave-induced pore water motion. The effect of sea surface wave action on salt transport into the subsea sediments has been shown to be important depending on hydraulic conductivity, sediment thickness, wave action characteristics, and water depths [Harrison et al., 1983]. As it can be described by a dispersion term in an effective diffusivity, this study assessed the effect of a range of effectively larger model parameters D against the observed degradation. However, our results show that a contribution of wave action over 40 times larger than salt diffusion would be required to obtain thaw depths consistent with the observations at the C3 and C2 boreholes (D of at least $350 \cdot 10^{-10} \text{ m}^2 \text{ s}^{-1}$ in Fig. 3.17). Theoretical considerations based on typical subsea permafrost conditions of hydraulic conductivity, sea surface wave amplitude, wavelength, and water depth conclude that the contribution to permafrost thawing at Prudhoe Bay is negligible [Harrison et al., 1983]. Sediments in that study were coarser-grained making it less likely that wave-induced transport is important at

our Siberian sites. The short Arctic wave season (open water period) would further reduce the total impact. A contribution of a factor of 40 larger than salt diffusion would be highly improbable under these conditions. A different mechanism, to which such strong diffusive/dispersive transport could be attributed, is currently unknown to this author.

Gravity-driven convection is another candidate salt transport mechanism. It has been inferred to occur in subsea permafrost sediments on the U.S. Beaufort Sea shelf, e.g. offshore of Prudhoe Bay [Harrison and Osterkamp, 1978, 1982, Harrison, 1982]. Characteristic vertical pore water velocities reported by Harrison and Osterkamp [1982], Swift et al. [1983] and Swift and Harrison [1984] exceed a few tenths of a meter per year (by observations and numerical modelling results). Based on theoretical considerations, Swift and Harrison [1984] find that free convection alone cannot account for observations. Swift et al. [1983] and Gosink and Baker [1990] argue that the associated velocities are inconsistent with the release of freshwater at the thawing permafrost table. Salt fingering is proposed as a viable additional, density-driven mechanism for salt water transport in thawing subsea permafrost [Gosink and Baker, 1990]. These authors have shown that salt fingering can initiate under typical density gradients that occur at the sea bed through excess salinity by salt rejection and concentrated brines below sea ice and brines in the reduced water volume of the re-frozen topmost layer of the seabed sediments in very shallow water depths at the end of winter. Once initiated, wedge-like flow upward from the thawing boundary can penetrate up to 5 m above the thaw interface at relatively rapid flow rates of maximally 1 cm h^{-1} ; and downward from the seabed at a predicted maximum velocity of 1 m d^{-1} [Gosink and Baker, 1990]. These rapid events, though seasonal in nature, may contribute to a significantly larger mean effective velocity of advective transport. However, our model assessment of arbitrarily high, density-driven, advective transport yielded maximal interstitial velocities on the order of just above 1 cm a^{-1} . The threshold limit in modelled mean interstitial velocities as well as in attainable thaw depths for higher input velocities v can be explained by the density-driven character of the advecting mechanism. Increased v simply leads to quicker equalization of the occurring salinity gradients. But after equalization, interstitial velocities cease, thus no further increase in thaw depth can be obtained by arbitrarily high advective contributions, as long as they are based on density differences.

No observations of in-situ interstitial velocities exist at our study sites. However, these interstitial velocities in the model differ slightly from observations in the Alaskan subsea permafrost: Based on Osterkamp and Harrison [1980], who estimate an order of magnitude upper limit for the interstitial velocity of 0.3 m a^{-1} , our velocities would

indicate either a hydraulic conductivity one order of magnitude lower or further, non-density-driven contributions to interstitial velocities, not captured by this model. While the latter is supported by the continued underestimation of thaw depths in the model results, the former would likewise be reasonable due to the fine-grained, sandy-silty sediments of the Laptev Sea subsea permafrost. Thus, the available observations are not sufficient. If in-situ interstitial velocities could be estimated in the field at our sites, a clearer indication whether additional velocity mechanisms are missing would be possible.

Our effective parameter approach includes all potential advective contributions to salt transport which are driven by density gradients. However, the model results show that by the addition of such density-driven, advective mechanisms to salt diffusion ($D = 8 \cdot 10^{-10} \text{ m}^2 \text{ s}^{-1}$), even maximal thaw depths continue to underestimate the observations, accounting for merely 88 % and 70 % at C3 and C2, respectively (Fig. 3.20). For more realistic interstitial velocities below the threshold, 65 % and 58 % of observed thaw depths are accounted for. The same bias is found at Buor Khaya (45 %) and Muostakh Island (49–52 %) (Fig. 3.21). Therefore, our results suggest that not only is free convection unable to account for thaw depths, but also that any further kind of density-driven mechanism including effective salt fingering would be insufficient by itself to explain the observations and account for the discrepancy seen in the pure diffusion models.

We consider these more realistic interstitial velocities of the order of cm a^{-1} and a pure salt diffusion coefficient ($D = 8 \cdot 10^{-10} \text{ m}^2 \text{ s}^{-1}$) as a base case that combines diffusion and advection transport. Only the assumption of additional diffusive/dispersive contribution, i.e. an increased effective diffusion coefficient of about $D=75 \cdot 10^{-10} \text{ m}^2 \text{ s}^{-1}$, resulted in modelled thaw depths at both C3 and C2 consistent with the observations (Fig. 3.23). The comparison of thaw depth curves to the case of increased advection (Fig. 3.20) shows that the latter, for extreme values of v , may almost explain the thaw depths at C3, but falls short of the observation at C2, due to the slope of the curve with distance offshore. Only the increased D parameter also yielded the necessary slope change that would meet both C3 and C2 observation depths. However, it is likely that the relative contribution of transport mechanisms varies over time (Fig. 1.7).

Salt concentration variation over depth should differ between diffusive and advective transport. The major differences are apparent in the in-situ salinity profiles of the corresponding two model cases (Figs. 3.19 and 3.22): a smoothly decreasing trend with depth for diffusion versus uniform concentrations with depth to a sharp concentration front for advection. However, measured salinity profiles are obtained

as total salinity because salt concentration is typically determined in the total water content of the thawed sediment core sample. The resulting total salinity profiles in the two model cases are strikingly similar – with now much sharper fronts for the diffusion case. The effect of sediment porosity on the salinity profile is thus equivalent to what would be expected for the advective shape of the profile, and effectively prevents the quantitative distinction between respective diffusive and advective contributions for the present data set of observed total salinity profiles. This could be overcome, if not only total salinity observations were available, but actual in-situ salinities could be measured. This would require the knowledge of the exact current liquid water fractions at the time of sampling (e.g. by exact temperature measurements at better depth resolution, or by direct in-situ sampling). Then, in-situ salinities could be inferred, and a chance of quantitatively assessing relative contribution of diffusive and advective transport based on concentration profiles would be possible.

Measured salinity profiles along the COAST transect and at the Buor Khaya offshore borehole (BK2) show the variability that exists in the observed salinity profiles in subsea permafrost sediments (Fig. 3.25). Nonetheless, measured salinity along the COAST transect and, specifically, at C2 – keeping the limitations discussed above in mind – broadly hints at a profile similar to diffusion at depth below 10 m, including bumps and kinks. These would not be expected if advection were to dominate over diffusion, as can be seen in the salinity profiles for the combined cases of diffusion and advection (Fig. 3.23 b and c). If this were the case, two questions remain unresolved, however:

Firstly, such D values as required to meet further offshore observations for diffusional transport would suggest an additional source of diffusive transport greater than the magnitude of pure salt diffusion by a factor of about 9, i.e. almost an order of magnitude greater. The source of such high D remains unresolved. No processes to justify the high D values required are known to this author. Bumps and kinks could be equivalently produced by prior saline layers, but were shown in these results to also be caused simply by the porosity variation with depth.

Secondly, the underestimation of observed thaw depths was particularly pronounced for the very near-shore boreholes in zones 3 and 4 in all modelled scenarios (Figs. 3.17, 3.18, 3.20, 3.21, 3.23). For these zones, even the higher D cases produced underestimates. Therefore, we must consider missing processes, that are not represented in the model, which might also contribute to the discrepancy between modelled and observed results.

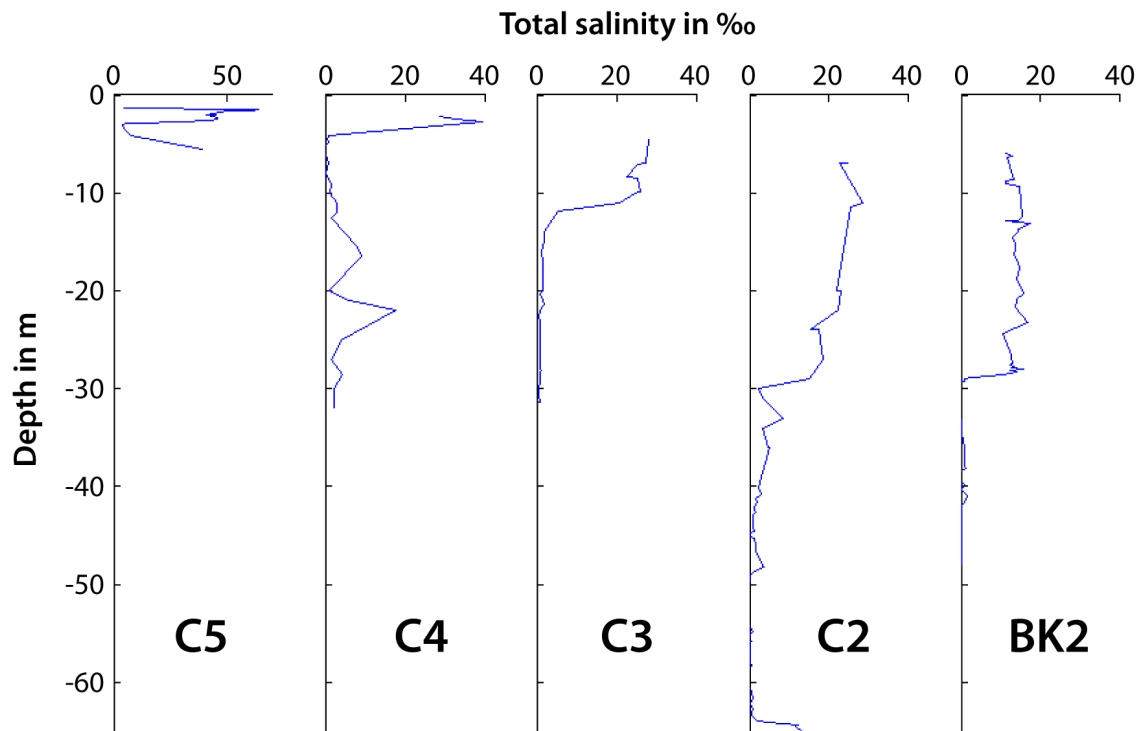


Figure 3.25: Observed salinity profiles for the offshore boreholes at Mamontov Klyk (C5–C2) and at Buor Khaya (BK2). See Fig. 3.2 b for the location of the COAST boreholes within the transect. The measured salinity corresponds to total salinity. Note the different x-scale for C5. Mamontov Klyk data: [Overduin et al., 2007a], Buor Khaya data: [Overduin et al., 2015].

3.8.2 Further factors affecting subsea permafrost degradation

Our three sites are separated by hundreds of kilometers. They have similar ice-rich sediments, but different local climate influences, river discharge, bottom water temperatures, salinities, erosion rates, and potential pre-inundation conditions. Nonetheless, with maximally realistic, density-driven flow velocities and reasonable salt diffusion coefficients, our model results underestimate thaw depths at all sites by similar amounts. Thus, it is unlikely that local factors are responsible for the underestimation. Rather, this author suggests that a supra-regional process may be responsible for the discrepancy either by affecting permafrost pre-inundation or post-inundation, or both. Possible relevant processes missing in current model implementations are:

- **Bottom-fast Sea Ice:** Initially after inundation, sea ice freezes to the bottom some time in winter or fall (zone 3 in Fig. 1.7). The effect of this seasonal ad-freezing of the sea ice cover to the seabed is twofold: It allows thermal coupling of cold aerial winter temperatures to the seabed, which cool the sediments [Harrison and Osterkamp, 1978, Solomon et al., 2008]. Simultaneously, salt rejection during sea ice formation and restricted circulation below the

sea ice lead to high salt concentrations. Thus, brines can be injected into the sediment sometimes under elevated hydraulic pressure, especially during bottom ad-freezing. These lower the freezing point and cause permafrost thaw. Additionally, in the short summer, the shallow water temperatures remain relatively warm. Thus, in zones extending to water depths of about 1.5–2 m, an active layer of thawing in summer and re-freezing in winter can develop. Observations of shallow thaw depths near Prudhoe Bay in that zone [Osterkamp et al., 1989] indicate that seasonal refreezing reaches the ice-bonded permafrost so that the depth of the ice-bonded permafrost table is seasonally variable. As our study implemented only cold seabed temperatures in that zone, the resulting underestimation of thaw depth to the observations at C5 and C4 indicate that brines injected during active layer development cause at least some increased thaw depth progression. The measured salinity profile at C5 also suggests that sediments refroze, since elevated salt concentrations were found below the observed ice-bonded permafrost table. Bottom water salinity in the borehole (> 100 [Overduin et al., 2007a]) and sediment total salinities of up to 64 (Fig. 3.25) support the presence of injected brines. The extent of bottom-fast sea ice is controlled by bathymetry. Assuming as first order approximation that rates of sediment removal from the shore face, subsidence by ice melting, and shoreline retreat rates remained constant, the present-day bathymetry would move with the shoreline retreat ('equilibrium shoreface profile'). The period following inundation, during which the sediment is subject to these influences, is then estimated by the bathymetry, not as a function of distance offshore, but as time since inundation using the retreat rate as conversion factor (Fig. 3.26). While the time periods for Mamontov Klyk and Buor Khaya are similar in length, Muostakh Island is the site with the shortest duration in that zone of the three sites. Thus, we would expect Muostakh Island to show the least effect of bottom-fast ice processes. These processes, however, cease beyond zone 3. Beyond the 2 m isobath, the expected effect is only a constant shift by an offset in thaw depth. For example, assuming a shift of the base case (black curve in Fig. 3.23) of about 3 m down would remove the deviation between modelled and observed thaw depth at C4, which is located just beyond the grounding threshold isobath. But such an offset would only yield a parallel shift and could not account for the increased slope necessary to explain the observation depth at C2. Only the curves for increased D parameter also yielded the necessary slope change that would meet both C3 and C2 observation depths (see Sect. 3.8.1). Thus, this process is not expected to help explain further offshore discrepancies.

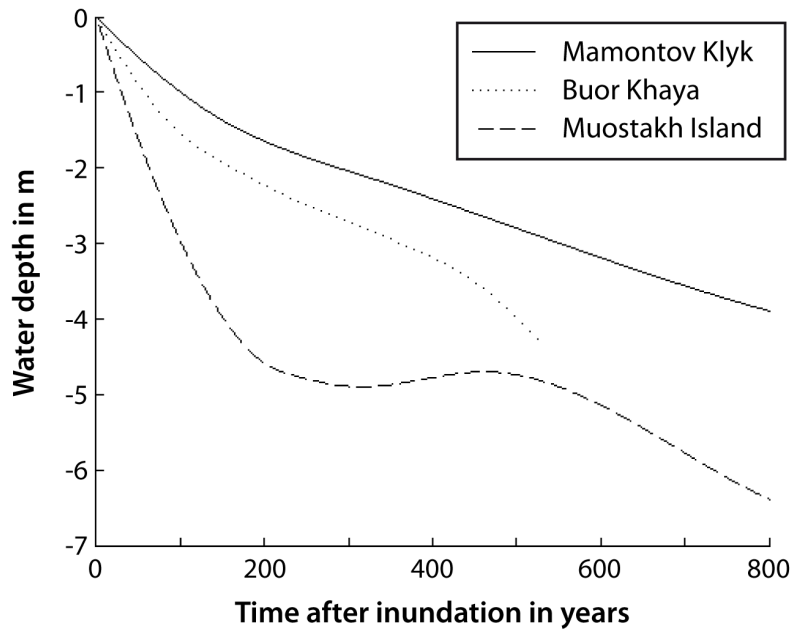


Figure 3.26: Bathymetry at the three sites, Mamontov Klyk, Buor Khaya, and Muostakh Island. Water depths is plotted as a function of time after inundation, instead of distance offshore. Conversion is determined by the local long-term shoreline retreat rate.

A fully implemented, explicitly formulated implementation of these initial processes would, however, help assess these opposing thermal and brine related processes, and whether they fully account for the modelled deviations at C5 and C4. This assessment would require further input parameters such as seasonal data on the sea bed temperatures and local winter air temperature trends of the last c. 200 a (the approximate time period of bottom-fast sea ice occurrence at Mamontov Klyk).

- **Sediment re-suspension events:** Large storm or wave events can perturb the fine-grained upper portion of the unfrozen sea bottom sediments and lead to thorough mixing with sea water in the pore space. Remote sensing shows suspended particles in the water column after storm events for near-shore areas of up to about 10 m water depth [Heim et al., 2014]. Such a process cannot be included in effective transport parameters v and D and would have to be implemented separately. Potential of thorough mixing of the topmost unfrozen layer could be modelled by defining a maximum mixing depth \hat{z}_{mix} and event frequency f_{mix} , and the salinity manually mixed in the affected column at the intervals given by f_{mix} . Such a process might be responsible for the higher salinities at C2 down to about 11 m, and at C3 for depths to about 7 m (Fig. 3.25), where salinities are similar to marine salinities.
- **Ice scouring:** Gouging by drifting ice pressure ridges redistributes and mixes

sediment. Scour marks have been observed widespread on the sea bed in the Arctic shelf seas [Ogorodov et al., 2013, Smalls et al., 2015, Hequette et al., 1995] in water depths out to about 65 m and with the most intensive gouging near the fast ice rim (e.g. corresponding to 5–12 m water depth in the Kara Sea [Ogorodov et al., 2013]). Therefore, their effect may be present at our Laptev Sea sites, but is not expected to greatly affect permafrost degradation in the near-shore zone landwards of C2, which is protected from larger ice bodies by its shallowness.

- **Sedimentation:** Sedimentation is neglected in the model. This process would maximally contribute a shift by the bathymetry at the furthest borehole C2. This would also not be enough to singly explain the discrepancy of the base case.
- **Talik prior to inundation:** The model assumes an intact Yedoma cliff, consistent with the landfall of the borehole transect. However, the coastal plain's landscape has thermokarst landforms that include lake basins [Grosse et al., 2006, Günther et al., 2013a]. Whether the sites of the boreholes or geophysical stations had been affected by thermokarst prior to inundation is unknown. A thermokarst lake would have warmer initial temperatures when inundated. Such prior permafrost warming and talik development would result in greater thaw depths. Such effects may have affected either only some individual sites or may have been so widespread that it could practically act as a systematic contribution at all locations. Warmer sub-thermokarst lake temperature profiles are subjected to colder temperature conditions after lake drainage or inundation (see OCSEAP data, Fig. 3.24) and sediments do not thaw further and begin to freeze from above. No infiltration of salt occurs under these conditions and there is a uniform shift in thaw depths in the long-term due to the warmer initial temperatures. However, the effect might differ significantly for conditions where taliks reach lower than sea level. Ice-rich Yedoma thickness in the Laptev Sea region extends down to about sea level ± 10 m [Günther, 2013]. At Muostakh Island, this results in significant subsidence and lake beds below sea level; at Buor Khaya and Mamontov Klyk, the beds are generally some meters above sea level and lakes are drained when breached by the shoreline erosion. Unfrozen taliks would extend well below sea level under these conditions prior to inundation and have a large impact on the subsequent subsea permafrost thaw depths after inundation.
- **A-priori saline sediment layers:** Some partially destroyed ice complex deposits, associated with a previous regression, and covered by several meters

of ocean sediments are observed in the East Siberian Arctic Shelf [Soloviev et al., 1987]. In the Laptev Sea, three water-bearing horizons in Kozhevnikov Bay [Ponomarev, 1940] and an unfrozen layer at the bottom of the C2 borehole [Winterfeld et al., 2011] are found. Alternating layers of marine and continental sediments are also found in the Beaufort Sea [Blasco, 1995]. Although deeper stratigraphic information is sparse in the Laptev Sea, marine mud deposits are thought to have been preserved between terrestrial deposits in onlapping layers of transgressive sediment [Forbes et al., 2014]. The sub-seabottom sediments of the Laptev Sea shelf probably have a complex structure of salt contamination, frozen and thawed regions, layered with some remnant ice complexes [Nicolosky et al., 2012]. Modelled results for a stratigraphic layer scenario (Fig. 3.13) suggest that such saline layers would be unfrozen under the relatively quickly attained, isothermal temperatures of the inundation, e.g. at C2. Thaw depth would instantaneously increase if the ice-bonded permafrost table thawed down to such a layer. This would affect the apparent mean degradation rate, which would appear larger than what the salt transport mechanisms of diffusion or advection actually provided. Our model results showed that the stratigraphic scenario could therefore affect quicker complete degradation of ice-bonded permafrost and the development of a through-going talik.

The real cause of observed thaw depths and salinity profiles in the boreholes, naturally, may be a mix of all discussed processes. Interpretation is furthermore not unique, as for example, the apparent change in slope discussed above could be equally explained by higher effective diffusion coefficients, by a talik prior to inundation at the location of C2, or a saline layer at C2 within these first 35 m that rapidly progressed the apparent thaw depth. Additionally, details of potential inundation parameters at the borehole locations such as the presence and position of saline layers or of taliks prior to inundation remain speculative at present.

3.8.3 Implications

In summary, the results in this study suggest that observed degradation rates of ice-bonded permafrost are higher than can be accounted for with a model of coupled heat and salt transport incorporating freeze/thaw processes, the saline influence on the freezing characteristic, sediment diffusion coefficient correction, reasonable effective salt transport parameters for diffusion and advection, and best available estimates of initial conditions, shoreline retreat rates, sea bottom temperatures and salinity. Additional processes, in superposition with the factors modelled in this study, may play a role but are difficult to constrain. Relative contribution of processes

might differ significantly with time. More information, especially regarding bottom water temperatures, shoreline retreat rates, saline layers, pre-inundation conditions, and implementation of further post-inundation processes such as bottom-fast sea ice is needed. Our results also point to the necessity to consider potentially unrecognized processes to corroborate high effective diffusion coefficients. Their identification would promise great benefit for our understanding of the driving mechanisms of subsea permafrost degradation. All of these are essential to our efforts to better predict and understand the current state, vulnerabilities and risks related to degraded subsea permafrost and their development under climate change in the future.

The main implications for subsea permafrost degradation from our model are:

- (1) Sediment temperature profiles are not sufficient to identify the position of the top of the ice-bonded permafrost or the ice-related degradation state of subsea permafrost. Salt transport has a large impact on the resulting ice saturation, and must be implemented in subsea models.
- (2) Three key factors for the degradation of subsea permafrost were identified: bottom water temperatures, inundation period (as related to estimates of shoreline retreat rates), and the initial conditions. Variations and/or uncertainty in these factors had a large influence on the modelled depth of ice-bonded permafrost table. Other tested inundation parameters, on the other hand, such as cliff erosion and the parameterization of the diffusion coefficient in the sediments showed little influence on degradation rates.
- (3) We showed that the use of constant sea bottom temperatures underestimates the initial degradation taking place for periods up to thousands of years.
- (4) No generally saline subsea sediments were found in the studied near-shore zone of the Laptev Sea. Instead terrestrial freshwater permafrost was found.
- (5) Any density-driven advective mechanism of salt transport downward was insufficient to explain the discrepancy between diffusion-driven thaw depths and observations. This confirmed studies by Swift and Harrison [1984] that free convection can not account for the difference, and goes beyond to show that salt fingering is effectively insufficient as well.
- (6) The bias at all three sites with their local differences in environmental conditions implies that a trans-regional process is missing rather than just a local deviation. This process can be either pre- or post-inundation in character, or both.
- (7) Modelling suggests that an additional diffusional or dispersive process about an order of magnitude larger than salt diffusion could explain the discrepancy. However,

a transport mechanism to which such characteristics could be attributed remains unclear.

(8) For the full picture of the transition to subsea permafrost, we identified the importance of (i) gathering field data on sea bottom temperatures, salinity and shoreline retreat rates to constrain modelling well, and (ii) to develop further model implementations of the bottom-fast sea ice zone, of pre-inundation processes and initial conditions, and of identifying the specific stratigraphic structure of the subsea sediments prior to inundation in terms of saline inter-bedded layers. The latter implementations require the former constraining field data such as seasonal sea bottom and air temperatures of at least the last few hundred years.

(9) Our findings show that the current process-implementation in models of subsea permafrost evolution underestimate thaw depths. Current studies therefore may underestimate the degradation and the development of through-going taliks. This would have large implications for the development of pathways for gas and fluid flow through the subsea sediments on the Laptev Sea shelf, and would directly affect the contribution of destabilized greenhouse gases to the atmosphere.

CHAPTER 4

From local to regional scale: Amending sparsely distributed temperature records

Paleoclimate and paleotemperature reconstructions are important in many applications in the climate system. As tools they are valuable for assessing the current climatic changes in the context of past variability as well as for improving our understanding of interactions in the climate system. By understanding climate responses to conditions in the past, driving processes can be assessed and predictions made for changing conditions in the future.

The local surface temperature history is an overarching factor in the context of subsea permafrost as it affects two related aspects. On the one hand, it constitutes the main driver of terrestrial permafrost thaw and determines the state of permafrost and its degradation features prior to inundation. Next to the marine influences discussed in Chap. 3, which act on the permafrost after the onset of the transgression, the initial conditions that the inundation encounters represent an additional large influence. This is documented in the geophysical observation of talik depressions in the subsea permafrost table below thaw lake and pingo-like features on the inundated sea floor [Shakhova et al., 2017, Rekant et al., 2015, Portnov et al., 2013]. It is also further corroborated in the numerical evaluation of the effect that taliks (developed in the pre-inundation landscape) have on the formation of through-going taliks during subsea permafrost degradation. Salt transport was not even necessary to infer that open taliks could have formed from the pre-developed landscape in the Dmitry Laptev Strait [Nicolosky and Shakhova, 2010].

On the other hand, the local surface temperature history also continues to affect subsea degradation in the first stages of the transition to the marine environment (as discussed in Chap. 3): In the shallow water depths of the early near-shore zones 2–3, it still affects bottom water temperatures and through bottom-fast sea

ice, atmospheric winter temperatures penetrate to the ocean-bottom sediments. Information on the local temperature history at our site of the COAST transect at Cape Mamontov Klyk provides the basis for any future assessment of more complex marine processes during the transition from terrestrial to submarine conditions, such as bottom-fast sea ice occurrence.

Regarding to its role in permafrost thaw, it is a proxy of the initial landscape and initial temperature conditions in the soil profile prior to inundation, on a local as well as on the larger scale. Knowledge of the local conditions and to which degree they differ from the larger scale trend in a region is essential for moving from local scale to larger Arctic scale distribution modelling of subsea permafrost. Local temperature history information is an instrument to judge the spatial variability of these influences on a larger regional scale. This will be a necessary prerequisite later to any meaningful simulation of the evolution of subsea permafrost degradation on the scale of the entire shelf area. The specific underlying question is: Were the driving temporal changes of synoptic scale and consistent over the whole region, or did spatial variations exist, either regional or local? To reduce complexity, the assumption of the former has so far been used in large scale studies of permafrost distribution in the Russian Arctic, where a global trend of temperature was used with only an offset for different locations [Romanovskii et al., 2003, 2004, Nicolsky et al., 2012]. Differences in this driving parameter would imply that using a global uniform input in permafrost models introduces errors and does not capture the actual temperature changes that led (i) to local observations of degradation that are used as validation or constraint and (ii) to the actual extent of permafrost on the shelf.

In order to provide this basis, this chapter concerns the reconstruction of the local temperature history at sites that are relevant to the subsea permafrost transition, i.e. the coastal tundra in the high Siberian Arctic. Temperature reconstructions are a means to access information on past temperature changes beyond the time period for which direct observations were recorded or for locations where none exist. To achieve this, reconstructions utilize different datable proxy information that can be associated with the prevalent temperature. These include, among others, isotope variations in ice core layers (fractionation of isotopes during evaporation of ocean water reflects the prevalent temperature), growth rate of tree rings (the width of seasonal growth reflects temperature in the growing season) and pollen in layered lake sediments (prevalent flora occurrence reflects mean temperatures). Other proxies that correspond to temperature have been employed, such as glacier length or the archive of temperature fluctuations in the profile of deep glacier or terrestrial boreholes (remnants of surface changes slowly propagating downward into the subsurface).

Temperature reconstructions: Global perspective

Global and northern hemisphere temperature reconstructions have been very successful at illustrating the anomalous character of recent 20th and 21st century warming in the context of the natural variability of the last millenia [Mann et al., 1999, Crowley, 2000, Briffa et al., 2001, Esper et al., 2002, Jones and Mann, 2004, Moberg et al., 2005, Oerlemans, 2005, PAGES 2k Consortium, 2013] and investigate the cause of warming, supporting anthropogenic over naturally occurring forcing [Mann et al., 1999, Crowley, 2000]. The average northern hemispheric temperatures were warmer than temperatures for at least the last 1300 years [Mann and Jones, 2003, Mann et al., 2008] and more variable than the best estimate of temperature changes for the last interglacial [Crowley, 2000]. Details of the last 2000 years of the northern hemisphere temperature history from a comprehensive global proxy data set include a Medieval warm period that remains below recent levels [Mann et al., 2008], a ‘Little Ice Age’ cooler period in the centuries prior to the 20th century warming which begins as early as 1850 [Ljungqvist, 2010], and reconstructions of up to annual resolution [Shi et al., 2013]. Subsurface borehole temperature archives complement available proxy records. Huang et al. [2000] and Pollack and Smerdon [2004] address differences between estimates of the two approaches and integrate various record sources [Huang, 2004]. Global mean temperatures constructed beyond the last two millennia with lower frequency resolution (millennial-scale) [Marcott et al., 2013, Huang et al., 2008, Jouzel et al., 2007] show that the steady rise of the last 150 years reversed a long-term cooling trend of the previous 5000 years taking temperatures from near the coldest to the warmest of the entire Holocene. An anomalous signal in the warmth of the late Holocene might even suggest anthropogenic influences on Earth’s pre-industrial climate, e.g. early agriculture [Ruddiman et al., 2016]. Based on these centennial-to-millennial-scale records, recent centennial scale warming is a global phenomenon that is most rapid in the north.

Regional & local temperature reconstructions in Siberia

Regional studies improve global reconstructions of temperature and reveal spatial deviations from the larger scale mean. In addition, while global scale reconstructions prove useful in assessing the predictions of current large-scale climate models, e.g., their underestimation of the Medieval Warm period [Shi et al., 2013], regional-scale models might require less spatially averaged temperature parameters. Siberia, in particular, is the site of rapid change, including warming and sea ice loss, but few data that permit temperature reconstructions exist. Briffa et al. [2001] find that

summer temperatures reconstructed based on tree ring proxies in northern Siberia differed from the global average in that 15th century summers were warmer than summers in the 20th century. Pollack et al. [2003] find a similar trend when studying deep borehole reconstructions from three regions in Russia with northeast Siberia exhibiting anomalously warmer temperatures than the other regions in Russia from the 16th to the 19th century. Thus, strong regional or even local differences in past temperature changes may exist in Siberia, but their seasonal (annual, summer, or winter) as well as spatial character remain unknown.

The Arctic

Given that temperature change in the Arctic is 3–4 times more rapid than the global mean [Hansen et al., 2010], there is special interest in the region, but temperature history is sparsely documented [Kaufman et al., 2009]. In addition, Arctic climate change may be significantly impacted by internal climate variability. Opel et al. [2013] report that regional temperature fluctuations in the last millennium in the Barents and Kara Seas region contain abrupt warming and cooling changes suspected to be connected through sea ice cover to shifting atmospheric circulation patterns. McKay and Kaufman [2014] compiled a circum-Arctic paleotemperature reconstruction of the last 2000 years. The compilation's density of records is highest in northeast Canada and Greenland and most sparse in Arctic Russia (Fig. 4.1). This uneven spatial coverage gives more weight to western hemisphere temperature changes potentially irrelevant to the thick Pleistocene permafrost of Siberia. In addition, the only Russian proxies included are tree ring data, which are primarily sensitive to summer temperatures and other biological stressors. Meyer et al. [2015] have shown that winter paleotemperature trends recorded in ice wedge stable isotopes may not follow summer trends. Poor coverage in the Russian Arctic may also affect Huang et al. [2000]'s continental scale reconstructions based on deep boreholes. Again, temperature data are sparsest in Asia and no sources are from Arctic Russia.

A knowledge gap in the Russian Arctic

Understanding past temperatures in central Siberia is important, because organic carbon reserves stored in Pleistocene permafrost are sensitive to temperature changes [Schuur et al., 2009]. In addition to its impact on subsea permafrost in this study, warming and thawing of the terrestrial permafrost releases frozen organic carbon to degradation, mineralization and release into the atmosphere as greenhouse gas [McGuire et al., 2009]. Although strong regional and local differences in variability

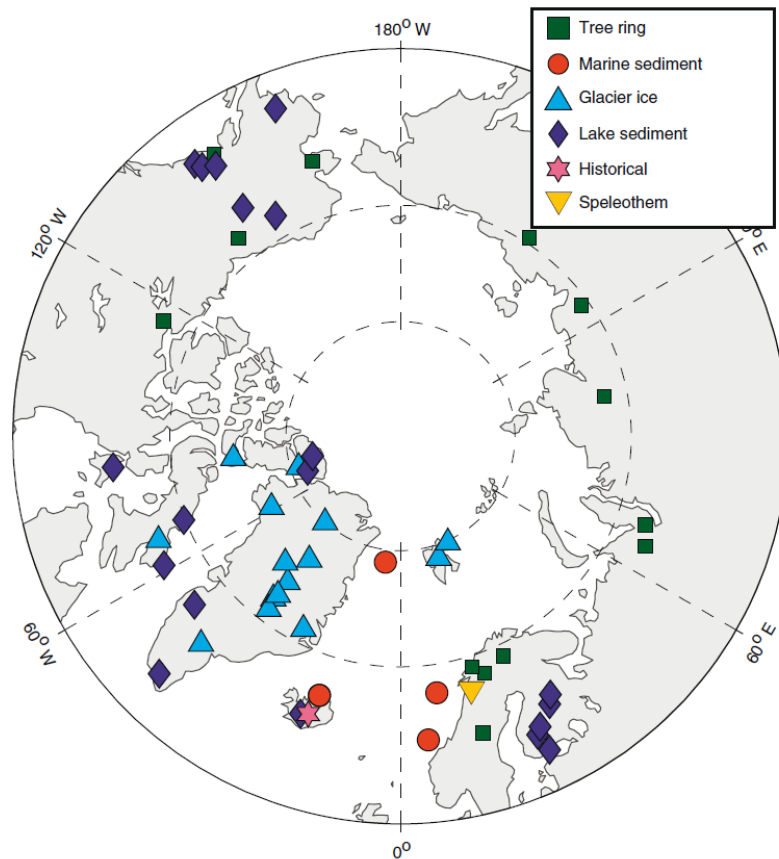


Figure 4.1: The locations of archives and their respective type included in the PAGES Arctic 2k reconstruction, graph adapted from [McKay and Kaufman, 2014].

in the climate system in the Arctic region have been found to exist, local arctic temperature histories in the ice-rich permafrost areas of the remote Russian Arctic are sparsely known or based on proxy data with potential biases and underrepresented in circum-Arctic reconstructions. Since these local temperature changes have driven past permafrost warming and cooling, they are critical to assessing permafrost interactions with other climate components. In addition, temperature reconstructions from borehole data can provide an independent data set for testing local and regional permafrost model parameterization.

For the case of the Cape Mamontov Klyk COAST drilling site, relatively short records of direct observational temperature exist only in distances of over 470 km, e.g. in Tiksi and Khatanga. Similarly, it is remote from other sites of longer local proxy reconstructions, which moreover have strongly differing local environments to the coastal tundra lowlands (oxygen isotope based reconstructions from ice core data north of the Taimyr Peninsula over 900 km to the northwest [Opel et al., 2013] and tree ring based near Khatanga to the south [Briffa et al., 2007, Naurzbaev and Vaganov, 2000]).

In the absence of trees and multi-decadal ice as provider of proxy data in the Arctic tundra, there is a need for other sources to fill the gap between usually longer time scale proxy temperature information from lake sediments such as chironomids, pollen (1 or 2 data points in the last 1000 a [Kurek et al., 2009, Andreev et al., 2004]) or ice wedge isotopes (centennial resolution and omitting the recent first few centuries due to age control [Meyer et al., 2015]) and direct observational data (if available, reaching back several decades at best). Geothermal reconstructions from permafrost boreholes could help overcome this limitation. While borehole depths of 300 m are estimated to be necessary to reconstruct the temperature of the last 500 a [Jaume-Santero et al., 2016], shallower permafrost boreholes present a more frequent albeit not widespread possibility for reconstructions of the last few centuries. For many remote permafrost sites of interest with no observational record, these may yield temperatures of the recent past with relatively good resolution for the first time. In addition, geothermal reconstructions from boreholes respond to the temperature signal throughout the year instead of a seasonal bias.

4.1 An overview of borehole temperature reconstruction

Information of the changes in temperature history at the ground surface is preserved in the subsurface temperature field: When temperature at the surface changes, the temperature of the ground (rock, soil, or ice) will start to change in response as heat is transferred vertically by diffusion, and in the case of water flow, by advection. Thus, a signal of surface temperature change is transported as a heat wave slowly into the ground. The time scale on and depth to which a signal penetrates the ground depends on the period of the temperature signal (Sect. 3.6.1.1). Long-term slow changes penetrate deeper, while shorter time-scale changes such as the daily or annual cycle are damped out at shallower depths. Inverting the depth information of temperature to reveal past changes at the surface is the idea behind borehole temperature reconstructions.

Generally the thermal regime is as follows: At larger depths, borehole temperatures are dominated by the geothermal heat flux — which results from the cooling of the Earth's core and from radioactive decay — and a rather uniform geothermal gradient in the profile prevails. The geothermal heat flux varies only on large geologic time scales, and is regarded constant on the time scale of the much shorter-term climate variations. At shallower levels, temperature variations at the surface propagate as heat waves into the ground. Surface temperature varies in a complicated way. The signal comprises dominant diurnal and annual periodicities, but also lower

frequency quasi-periodic contributions from decadal variations (examples are the North Atlantic Oscillation or the El-Niño-Southern Oscillation) and superimposed temperature excursions such as the Little Ice Age (about 1550–1850) or the Medieval Climate Optimum warm period (about 800–1300). Glacial/interglacial cycles make up even longer-period components. Due to the low thermal diffusivity of the ground on the order of $10^{-6} \text{ m}^2\text{s}^{-1}$, ground surface temperature changes propagate slowly downward with phase velocities of $v_{ph} = \omega/k = \sqrt{2d_h\omega}$ and are observed as transient perturbations to the quasi-steady state gradient. As shown in Eq. 3.7, the further down, the more the temperature reflects influences of longer periods of surface variations due to the Earth’s damping higher angular frequency periods first. The different components of the surface signal are thus separated due to their different characteristic damping depths $k^{-1} = \sqrt{2d_h/\omega}$. Beyond a certain depth, damping renders the fluctuations’ amplitudes negligible and the geothermal gradient dominates. In a homogeneous half space medium with uniform thermal properties (thermal conductivity, capacity, and diffusivity), typical characteristic damping depths are shown in Table 4.1 for two representative materials, rock and soil respectively.

Table 4.1: Characteristic damping depth values given by Eq. 3.8 for the characteristic time of various events. Calculation for two homogeneous media with uniform thermal diffusivities $d_h = 3 \cdot 10^{-6} \text{ m}^2\text{s}^{-1}$ and $d_h = 0.5 \cdot 10^{-6} \text{ m}^2\text{s}^{-1}$, representative of solid rock and soil respectively (see also in Roth [2012]).

event	time [a]	k_{rock}^{-1} [m]	k_{soil}^{-1} [m]
diurnal cycle	$2.7 \cdot 10^{-3}$	0.28	0.12
annual cycle	1	5.5	2.2
Little Ice Age	~300	95	39
Last Glacial Maximum	17500	726	296

The thermal properties of the ground impact the subsurface temperature field. The steady-state background profile (vanishing first term in Eq. 3.5) depends on the geothermal heat flux and the thermal conductivity. Thus, thermal conductivity governs the gradient variations at the quasi-steady geothermal heat flux Q_{geo} in the background profile. In a heterogeneous subsurface with different layers of materials, the derivation of the temperature anomaly from the quasi-stationary background depends strongly on the accurate representation of the thermal parameters. Otherwise, excursions in the temperature profile are misinterpreted as warming or cooling signals. The assumption of uniform thermal parameters is usually not valid for the topmost unconsolidated layers, and must be taken into account in the thermal forward model of the reconstruction. Thermal diffusivity $d_h = \frac{\lambda_h}{c_h}$, on the other hand, controls the transient-state heat conduction with characteristic damping depths and phase velocities of the penetrating surface wave signals. Additionally, the thermal

parameters depend not only on sediment composition, but also on water content. Water has both high volumetric heat capacity and low conductivity. An increase in porosity under saturated conditions thus results in a particularly strong influence on diffusivity, which decreases.

Figure 4.2 illustrates the effect of step changes in the surface temperature history on the subsurface temperature profile in homogeneous ground conditions. In the left panel, the response over time to a simple step change warming event shows the downward propagating perturbation of the previous long-term equilibrium profile. Conversely interpreted from the ground temperature profile, an observed warmer deviation in the upper profile represents the response of the ground to recent warming of the mean long-term surface temperature T_0 . Likewise, an observed cooler deviation is associated with recent surface cooling. In the right panel, two combinations of subsequent warming and cooling events, termed (a) and (b), complicate the response in the resulting temperature profile, but the individual components remain visible in the deviations with depth. For example, the earlier cooling in case (b) starting 500 a ago is connected with a negative deviation further down at 220 m and much more attenuated than a positive deviation at shallow depth around 30 m. The latter is associated with the more recent warming event beginning 200 a ago.

In summary, surface temperature fluctuations at the surface are transported slowly into the subsurface and get damped exponentially with depth. The characteristic penetration depth increases proportionally to the square root of the fluctuation's period. The thermal properties in a heterogeneous ground and potential phase transitions of water in the soil column further complicate this simple regime. However, the separation of different components means that there is information on the temperature changes at the surface archived in the subsurface temperature field. Heat transport by fluid movement is negligible in the case of frozen ground; and even in most cases in temperate regions, the main mechanism for heat transfer is conduction due to a very small Peclet number [Majorowicz et al., 2004]. Adapting the heat conduction equation to include non-uniform thermal parameters with depth in a one-dimensional model and implementing phase change processes is then generally solved numerically to recover a ground surface temperature (GST) history (see details in Sect. 4.6.1).

The geothermal reconstruction method is limited by the physics of diffusive heat transfer. The surface temperature signal is progressively and irrevocably smeared (broadened peak and attenuated amplitude) in the subsurface with transfer to depth and in time. This diffusive spreading and overlap of signal components results in several implications:

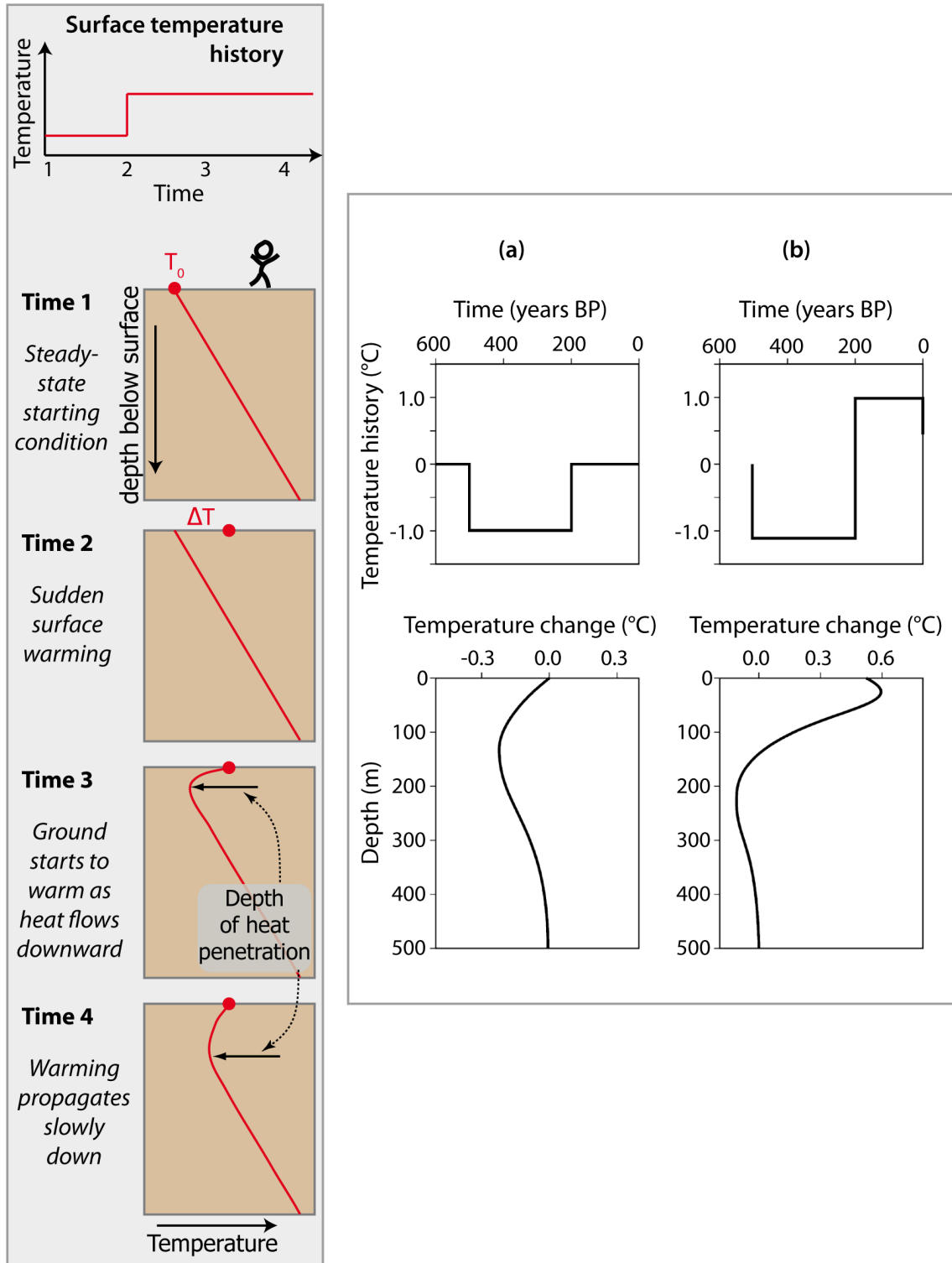


Figure 4.2: The effect of changes in the surface temperature history on the subsurface temperature profile in a simple homogeneous medium: **(left)** A step change warming event leads to a perturbation of the previous linear background, which propagates downward with time. **(right)** Two combinations of subsequent warming and cooling events, (a) and (b). Note that the lower graphs here show only the deviation from the previous long-term equilibrium, not the complete profile. Graph adapted from [Majorowicz et al., 2004].

1. The inversion problem is non-unique. The temperature at a specific depth is influenced by a multitude of time points in the surface history. An infinite number of surface histories exist that would explain the profile perfectly and complex inversion techniques are necessary to infer the most likely solution. The details of the individual inversion scheme will reflect in the character of the best solution found [Shen et al., 1992].
2. The diffusive attenuation and phase shift are frequency dependent. This prevents direct inference of surface trends from trends in underground time series data. Only incorporating the physical processes in full inversion schemes accounts for the physical effects of heat transfer and allows correct surface temperature trend reconstruction.
3. The underground degradation of the signal, specifically the diffusive spatial spreading, inherently decreases the resolution backward in time. The temperature value in the surface history reconstructed for time τ before logging represents an average over a time interval, the length of which is proportional to τ [Clow, 1992] and typically estimated over about 0.5τ [Majorowicz et al., 2004]. This physical limit on the retrievable information must be considered particularly for real surface temperature histories that are more complicated than the previous simple step change examples, and where typical inversion techniques are employed to recover the temperature history. For boreholes in rock and permafrost, this resolution is a few decades at the start of the 20th century and decreases to a few centuries at 1500 [Committee on Surface Temperature Reconstructions for the Last 2,000 Years, National Research Council, 2006]. Borehole temperatures therefore reconstruct long-term temperature averages and trends prior to the period of instrumental records, but not decadal variations or specific years, except for the most recent ones. However, this simultaneously means that for our remote sites with no instrumental record in the Arctic tundra, this method reveals the temperature history with still good resolution of a few decades around 1900 and increasing resolution to the present.

The main other methodological limitation is the one-dimensional, purely conductive model description in all existing inversion algorithms. Lateral inhomogeneities of the thermal parameters of the ground and any departures from the conductive mode of heat transfer are effects not captured by this method. Furthermore, the GST variations are traditionally assumed to track the long-term surface air temperature (SAT) changes. If the reconstructed results are also to be transferred beyond spatial variability of ground thermal conditions and to infer long-term climatic variability,

the validity of this assumption is important.

In the following, a brief overview of the various methods used for inversion studies is given. The reconstruction of ground surface temperature history from subsurface temperature profiles presents an ill-posed inverse problem. The history must be estimated from measured temperature profiles and thermophysical properties. In order to reduce complexity, all techniques assume one-dimensional conductive heat transfer in a homo- or heterogeneous medium. The existing inversion schemes frequently employ a forward model of heat transfer in the ground or ice sheet and optimize a surface temperature history that fits to the observed subsurface temperature profile (minimizes the mismatch between simulated and observed temperature profile). The method the inversion uses to find an optimized update to the temperature history in each step can be broadly classified in three categories [Orsi et al., 2012]: (i) generalized least-squares inversion methods, (ii) random inversion approaches, referred to as Monte-Carlo methods, and (iii) especially in the case of ice core temperature inversions, the inclusion of water isotopes as additional proxy constraints. For terrestrial boreholes, one method of the first category is the functional space inversion (FSI) technique [Shen and Beck, 1992, 1991]. It uses a Bayesian approach, i.e. the measured temperature profile, the thermophysical model parameters and the surface temperature history are random quantities in a probabilistic model and driven within given standard deviations from a-priori estimates to an a-posteriori configuration with maximum probability. Another method is given by the singular value decomposition (SVD) [Mareschal and Beltrami, 1992, Beltrami, 2002, Jaume-Santero et al., 2016]. Similar results in most cases considered in comparisons [Beck et al., 1992, Wang, 1992] have been shown for these two methods. The inversion based on the Tikhonov regularization method [Zagorodnov et al., 2012, Nagornov et al., 2006, 2001, Tikhonov and Samarskii, 1990] also falls into this category. Other examples of this wide class can be found in MacAyeal et al. [1991], Muto et al. [2011], Huang et al. [1996, 2000], Pollack et al. [1998], Orsi et al. [2012] and a computationally very efficient approach in Roberts et al. [2013]. Monte Carlo based approaches to explore the range of possible solutions have been used by Dahl-Jensen et al. [1998, 1999], Hopcroft et al. [2007], Barrett et al. [2009] and Roberts et al. [2013]. Examples of optimizations of the third category that use the relationship between surface temperature and stable water isotope ratios are Johnsen [1977], Cuffey et al. [1995], Cuffey and Clow [1997] and Johnsen et al. [1995]. For the terrestrial borehole temperature records in the Laptev Sea, two methods [Roberts et al., 2013] from the first two categories are employed in this study.

4.2 On the transferability of ground to air temperatures

Ground surface temperatures generally do not equal surface air temperatures. Accurately, the borehole temperature profile is a direct measure of the surface energy balance [Majorowicz et al., 2004]. Ground temperatures respond to surface air temperatures, but also to other processes that influence the energy balance, such as vegetation changes [Balobaev, 1973], radiative forcing, snow cover or phase changes from thawing and freezing. Especially the insulating effect of snow cover can contribute to an offset between long-term air and ground temperatures. Generally, ground temperatures are warmer than air temperatures due to solar radiation effects in the summer and the insulating effect of snow cover during the winter [Bartlett et al., 2004]. Locally different surface conditions can therefore lead to differences in subsurface temperatures even for a common transient SAT signal, but the trends, i.e. changes, would remain comparable. Amplitude damping and phase shifting of surface signals precludes direct trend comparison with ground temperature time series, but inverted reconstructions of surface history explicitly take these physical processes into account, making trends comparable [Lesperance et al., 2010]. Long-term systematic variation in the offset between surface air and ground temperature would produce biased inferences of climate change. For example a shorter snow cover duration would lead to apparent ground warming relative to SAT trends [Bartlett et al., 2004] or a decrease in cold season snow cover leads to increased cooling of the ground and an apparent underestimation of SAT warming [Mann and Schmidt, 2003]. Known differences occur over daily and seasonal periods [Stieglitz et al., 2003, Bartlett et al., 2004] but only longer (than annual) systematic changes are relevant for borehole reconstructions [Pollack et al., 2005, Smerdon et al., 2004]. At centennial time scales, air and ground temperatures are well coupled in mid-latitude [Harris and Chapman, 2001] and hemispheric studies [Pollack and Smerdon, 2004, Chapman et al., 2004] and confirmed by model simulations [Gonzalez-Rouco et al., 2006, Garcia-Garcia et al., 2016]. Beltrami et al. [2005] find for 4 boreholes in Quebec, Canada, that subsurface temperatures track the variations of the surface air temperature for at least seven decades of SAT data despite changes to snow cover and soil moisture. Their results indicate air-ground coupling at decadal to centennial time scales and that geothermal reconstruction anomalies are robust long-term change indicators under conditions of conductive heat transport.

4.3 Reconstruction objectives

Our objectives in this chapter are to

- (i) reconstruct temperature histories for past few hundred years in our Laptev Sea, Russian Arctic, study region using shallow (100 and 65 m deep) permafrost borehole temperature records and
- (ii) evaluate the results by comparing them to larger scale reconstructions from this region.

In this study, two inversion methods (least-square QR and particle swarm optimization) are used to reconstruct the local ground surface temperature history at two sites: Cape Mamontov Klyk and Sardakh Island, located in the western Laptev Sea and in the Lena River Delta, Russia, respectively (Fig. 4.3).

4.4 Borehole sites and climate

The Laptev Sea is located in central Arctic Siberia, between the Taimyr Peninsula and the New Siberian Islands (Fig. 1.1). The general climate in the Laptev Sea region is Arctic continental with 8–9 month winters and short summers of 2–3 months. Winter temperatures are severe, with mean January temperatures of -30 to -32 °C and mean July temperatures of 3 – 4 °C [Atlas Arktiki, 1985]. Annual precipitation is between 200 and 300 mm [Andreev et al., 2011]. In winter, cyclones are rare and already in their filling stage. Cloudiness and precipitation are less than in the other Arctic regions affected by the Atlantic or Pacific to the east and west. In summer, winds subside and atmospheric circulation weakens. High relative humidity and fogs are common [Timokhov, 1994].

The Laptev Sea coastal region is part of the northern tundra zone [Atlas Arktiki, 1985, CAVM Team, 2003]. Active layer thickness in this zone of continuous permafrost is around 30–40 cm [Atlas Arktiki, 1985]. Vegetation is dominated by moss-grass/low-shrub tundra with vascular plants, mosses, and lichens [Andreev et al., 2011].

The borehole locations (Fig. 4.3) were chosen to represent different subsurface compositions:

Cape Mamontov Klyk lies in the Western Laptev Sea approximately halfway between the Anabar and Olenek Rivers. Details on the 65.1 m-deep onshore core ($73^{\circ}36'21.5''\text{N}$, $117^{\circ}10'38.5''\text{E}$), primarily consisting of silty sands, with ice-rich Ice Complex deposits making up the upper 20–30 m, are given in Sect. 3.5.1.

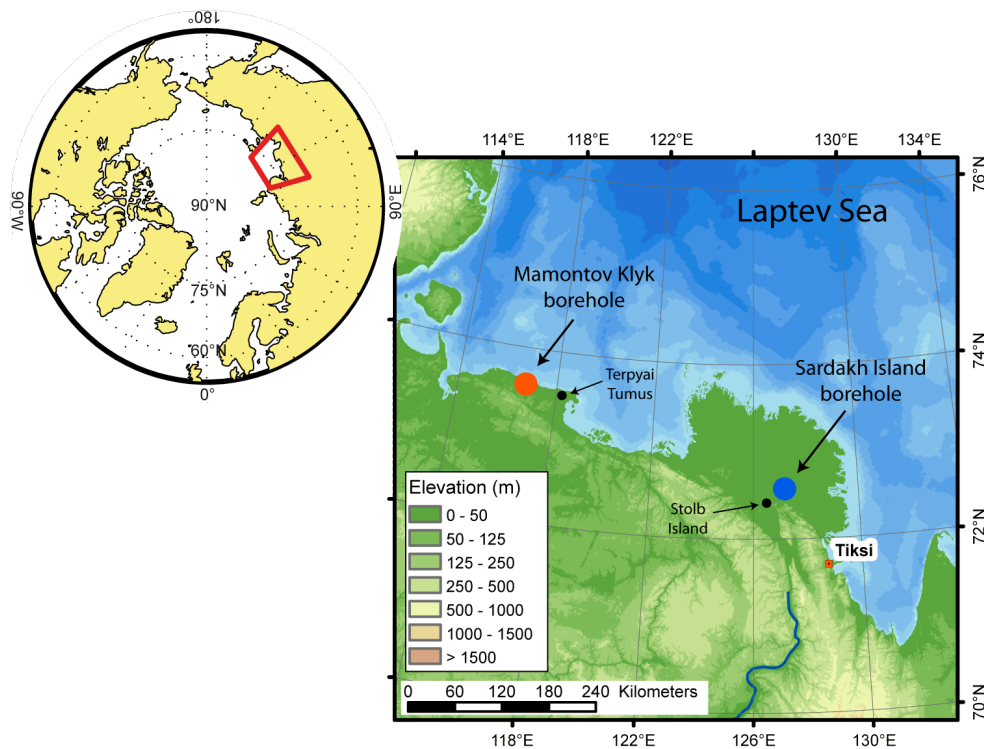


Figure 4.3: Western Laptev Sea with the location of the two boreholes: At Cape Mamontov Klyk (65.1 m deep) and on Sardakh Island in the Lena River Delta (100 m deep). Adapted from [Kneier et al., 2018].

Sardakh Island lies in the southern part of the Lena Delta. A 100-m-deep borehole ($72^{\circ}34'17.6''\text{N}$, $127^{\circ}14'29.4''\text{E}$) was drilled in April and May 2009. The Lena Delta has been subdivided into three geomorphological terraces, the oldest of which is exposed in fragments in the southern part of the delta and formed in the middle to late Pleistocene. The second terrace makes up the western part of the delta, a region called Arga Island, and formed in the late Pleistocene to late Holocene, while the eastern terrace is the currently active part of the delta and has been formed since the middle Holocene with shallow modern flood plains [Wagner et al., 2003, Schwamborn et al., 2002, Are and Reimnitz, 2000]. Ice wedge polygons in various stages of development are characteristics of the landscape in the delta [Mueller, 1997]. In the central delta, bedrock outcrops are scattered like islands near the surface. Sardakh Island formed around one of these outcrops [Grigoriev, 1993]. Sediments on Sardakh Island consist of Pliocene and neo-Pleistocene deposits of the southern part of the delta. They are ice-rich deposits of loamy sand and overlie actively deformed layers of sedimentary/carbonate rocks and conglomerates, sand, pebbles, and boulders of Devonian age, indicating intensive pre-Pliocene reworking [Grakhanov et al., 2013]. These can contain lithified organic material and even large pieces of lithified wood [Grigoriev, 1993, Galabala, 1987]. Bedrock may lie close to the surface as suggested by gravity data [Kogan, 1974], but its depth below

the surface is unknown. Sardakh Island is undergoing current neotectonic uplift [Grigoriev et al., 1996] and its elevation of currently about 40 m is comparable to the oldest terrace (though different in genesis). The island's surface is characterized by ice wedge polygons of presumably late Pleistocene origin [Grakhanov et al., 2013] and a few thermokarst lakes of 30–500 m in diameter.

In contrast to Mamontov Klyk, meteorological data are available from the southern Lena delta: Wagner et al. [2003] report mean annual air temperature of -14.7°C and mean annual precipitation of 190 mm. The nine month winter with average and minimum temperatures of -30 and -48°C , respectively, brings heavy snowstorms, while the summer period following break-up of the Lena River end of May [Rivera et al., 2006] has average and maximum temperatures of 7 and 18°C [Wagner et al., 2003]. Recently, Boike et al. [2013] report slightly warmer annual mean air temperatures of -12.5°C from 1998 to 2011.

4.5 Borehole temperatures

Both boreholes are part of the Global Terrestrial Network for Permafrost (GTN-P) with IDs 'RU 148 DE02' and 'RU 149 DE03', for Cape Mamontov Klyk and Sardakh Island respectively. At both sites, thermistor chains were installed, recording at 1 h interval (Mamontov Klyk) and 6 h interval (Sardakh). As a rough estimation, the return to the equilibrium state after the thermal disturbance of drilling is completed in a period that is 10–20 times greater than the duration of drilling [Majorowicz et al., 2004]. Three year time series after logging were available for this study and safely allow recovery to equilibrium between the well-filling air and the surrounding permafrost. Mean temperature profiles for the last year of available data from both boreholes are presented in Table 4.2. They are used as the target temperature profiles in the temperature reconstructions. This study discards the top measurement, which lies in the active layer. Removing top measurement depths potentially influences the most recent time in the reconstruction. The effect here, however, is negligible, as even the annual temperature signal penetrates much deeper than these missing target depths.

The deepest temperatures recorded by the logger chain at Sardakh Island varied annually by about 0.05°C , although they were below the damping depth for annual surface signals. These variations were probably a result of cooling and warming of the data logger at the surface. Therefore, only longer than annual trends are regarded when using sensor time series data below 20 m. On Sardakh Island, thermokarst around the borehole was recorded in the summer of 2012 for the first time, and a

Mamontov Klyk		Sardakh Island	
Mean		Mean	
depth [m]	Temperature [°C]	depth [m]	Temperature [°C]
0.1	-9.36	0	-8.68
1.1	-9.34	0.4	-8.66
2.1	-9.63	0.8	-8.71
3.1	-9.78	1.2	-8.80
4.1	-10.04	1.6	-8.93
5.1	-10.26	2	-8.91
6.1	-10.50	2.5	-9.04
8.1	-10.84	3	-9.14
12.1	-11.37	4	-9.24
14.1	-11.57	5	-9.36
16.1	-11.71	7	-9.58
18.1	-11.85	9	-9.73
20.1	-11.93	11	-9.86
22.1	-12.08	13	-10.02
30.1	-12.21	15	-10.11
35.1	-12.29	20	-10.33
40.1	-12.43	30	-10.56
45.1	-12.50	40	-10.59
50.1	-12.54	50	-10.52
55.1	-12.53	60	-10.53
60.1	-12.54	70	-10.38
65.1	-12.54	80	-10.24
		90	-10.20
		100	-10.19

Table 4.2: Mean temperature of observed borehole profiles from 14.08.2010 to 13.08.2012 (Mamontov Klyk) and 23.08.2011 to 22.08.2012 (Sardakh Island).

larger pond had developed by 2014 (Fig. 4.4). This process will affect temperatures in the upper several meters after 2012, but remains negligible for the time period analyzed in this study.



Figure 4.4: The borehole on Sardakh Island photographed after installation in 2009 (left) and in 2014 (right). Photographs by Julia Boike.

4.6 Inversion method

To estimate temperatures at times prior to the start of direct observation, the diffusive slow transfer of heat into the ground to different depths on different time scales can be taken into account, and a surface temperature history can be reconstructed that is consistent with the observed temperature profile in the borehole.

In this study, an adaption of two inversion methods previously applied to temperature measurements from ice core sites was used [Roberts et al., 2013]. The inversion scheme employed a flux-conserving finite volume numerical soil model for heat conduction in the subsurface. This forward model was used to calculate temperature vs. depth profiles from surface temperature histories. The inversion schemes optimized temperature history in a least-square sense: they minimize the deviation of the forward model output from the observed temperature profile in the borehole, i.e., the unweighted root-mean-square (RMS) error:

$$E_{rms} = \left(\frac{\sum_{i=2}^{i_{max}} (T_{model}(i) - T_{obs}(i))^2}{i_{max} - 1} \right)^{0.5} \quad (4.1)$$

to yield a best fit solution for the surface temperature history, where T_{model} is the modelled temperature distribution and T_{obs} the observed temperature data, as shown in Table 4.2.

4.6.1 Forward model

Diffusive heat transfer is solved numerically in a one-dimensional flux-conserving finite volume scheme (Eq. 3.5). Freeze-thaw processes are considered in a three-phase

heat capacity/conductivity model based on de Vries [1963] and modified following Ippisch [2001] to incorporate the phase change between water and ice (Eq. 3.3):

$$c_{\text{eff}} \cdot \frac{\partial T}{\partial t} = \frac{\partial}{\partial z} \left(\lambda_h \cdot \frac{\partial T}{\partial z} \right)$$

with $c_{\text{eff}} = \sum_i c_i \theta_i + L_f \frac{\partial \theta_w}{\partial T}$

where c is heat capacity, θ_i volumetric fraction of phase i (mineral, water, and ice), L_f latent heat of freezing, and λ_h thermal conductivity.

Sediment composition and thermal parameters for both sites

Subsurface thermal properties were retrieved from either the observed temperature field or the sediment composition analysis of the borehole.

Mamontov Klyk borehole: Heat capacities and thermal conductivities were assigned based on the sediment composition of the core recovered from the borehole [Winterfeld et al., 2011]. Sandy unconsolidated sediment was assumed below the borehole to the modelled depth of 1000 m and average mineral thermal values $k_{\text{min}} = 2.9 \frac{\text{W}}{\text{mK}}$ and $c_{\text{min}} = 2e6 \frac{\text{J}}{\text{m}^3\text{K}}$ were used [Hillel, 1982].

Sardakh borehole: Sediment composition and thermal parameters were derived numerically from the observed 3 years (2009–2012) of temperature data time series and from the lithology of the borehole [Rajeev and Kodikara, 2016]. By using 3 successive sensors, the bottom and top sensor temperature time series are used as boundary condition in a numerical implementation of 1-dimensional heat conduction. Initial thermal properties for the mineral fraction were chosen as Hillel's averages. For the shallow depths dominated by sand (Fig. 4.5), the fit to the middle sensor time series determined the best fitting sediment composition fractions for the block. For depths greater than 13 m, it was found that accounting for layers with different mineral thermal properties instead of Hillel's averages is required to fit the observed temperature time series. The values were fit using average literature values for thermal conductivity, heat capacity and porosity for limestone [Eppelbaum et al., 2014] initially. These values were allowed to vary in each layer independently within 50 % of the literature values and water content according to the lithological description to find the best fit in a RMS sense to the middle sensor time series.

Figure 4.5 shows the resulting effective heat capacity, thermal conductivity and thermal diffusivity as a function of depth for both borehole profiles. At Mamontov Klyk, the thermal properties profiles show a rather constant, steady trend with depth.

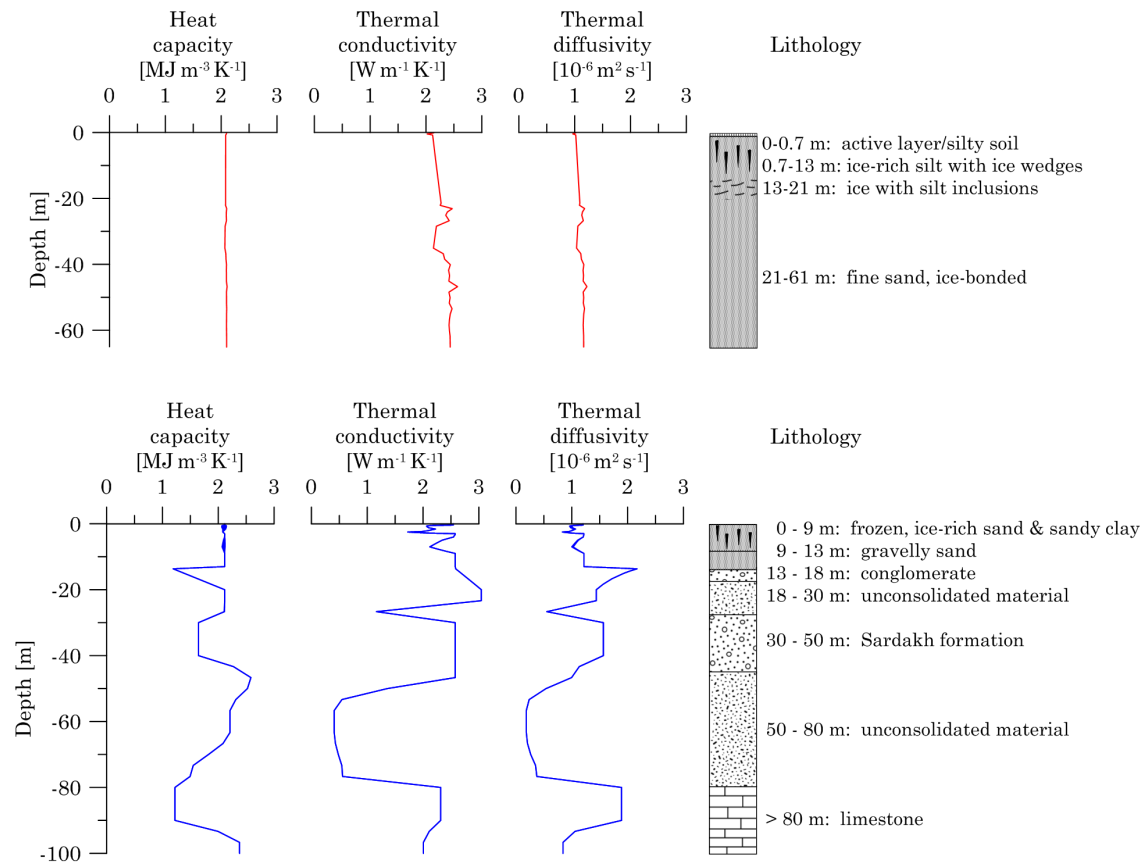


Figure 4.5: Thermal parameters in the forward model for **(top)** Mamontov Klyk and **(bottom)** Sardakh Island: Effective heat capacity, thermal conductivity and thermal diffusivity. Shown to the right are the subsurface lithologies. Adapted from [Kneier et al., 2018].

Mean values for heat capacity, thermal conductivity, and thermal diffusivity are $2.08 \text{ MJ m}^{-3} \text{K}^{-1}$, $2.25 \text{ W m}^{-1} \text{K}^{-1}$, $1.08 \cdot 10^{-6} \text{ m}^2 \text{ s}^{-1}$ with maximum deviations along the profile of less than 1%, 14%, and 13%, respectively. These small variations are in line with the observed lithology of the borehole, in which rather homogeneous sandy-silty conditions prevail along the entire depth of the profile. At Sardakh Island, the profiles of the thermal properties show much larger variations with depth. While the mean values of heat capacity, thermal conductivity, and thermal diffusivity are similar to those at Mamontov Klyk ($1.99 \text{ MJ m}^{-3} \text{K}^{-1}$, $2.13 \text{ W m}^{-1} \text{K}^{-1}$, $1.12 \cdot 10^{-6} \text{ m}^2 \text{ s}^{-1}$, respectively), the maximum deviations (up to 40%, 81%, and 94%, respectively) are over a factor of 7 larger. Most notable, a very pronounced, broad low-conductivity, and consequently, low-diffusivity zone occurs between approximately 50 and 80 m depth at Sardakh Island, associated with a layer of unconsolidated material. In general, the thermally inferred variations along the profile agree well with observed layer transitions in the lithology (right-hand side in Fig. 4.5).

Initial and boundary conditions

The time varying upper boundary temperature corresponded to the temperature history. The lower boundary condition was set to the geothermal flux of $Q = 53 \text{ mW/m}^2$ [Pollack et al., 1993, International Heat Flow Commission (IHFC), 2011]. The one-dimensional soil model was solved as a mixed boundary-value problem with the upper boundary being forced by the external temperature variable itself (Dirichlet boundary condition), while the lower boundary was specified by the thermal gradient (Neumann boundary condition) [Ingebritsen et al., 2007].

The heat stored in the subsurface could be underestimated if the bottom boundary condition placement (BBCP) was too shallow and perturbs the subsurface temperature field [Stevens et al., 2007]. Based on Smerdon and Stieglitz [2006], the necessary BBCP in our model was identified to be at least 550 m below the borehole to prevent boundary condition-related amplitude attenuation within the borehole. The bottom boundary condition was placed well below this threshold at 1000 m.

The initial temperature profile was constructed using temperature observations from a 500 m-deep borehole near Tiksi [Grigoriev, 1966]. Extrapolation below was done by extending the constant heat flux, taking into account the change in temperature profile slope below the permafrost for saturated sand conditions at Mamontov Klyk. Due to its rocky subsurface with low water content at depth, there was no such distinct change in the slope at Sardakh Island. The whole profile was shifted to match the bottom temperature at each site by adding a constant offset. Linear approximation from 20 m upwards to the surface was accommodated dynamically in the optimization process using the initial value of the currently valid surface temperature history.

The model implicitly assumes that (i) advective heat transport is negligible, (ii) there are no internal heat sinks or sources in the sediment, (iii) frost heave and the effect of volume changes associated with the phase transition of water and ice are neglected, and (iv) that there is no lateral heat flux.

4.6.2 Optimization

The inversion problem of surface temperature reconstruction does not have a unique solution due to the diffusive nature of heat transport. A heat pulse at the surface spreads spatially as it diffuses into the ground. Temperature at one specific depth, therefore, contains contributions of surface temperature from a range of past times. As a result, an infinite number of possible temperature histories can fit the observed

temperature profile perfectly [Clow, 1992] and the problem is underdetermined. The resolution power of borehole temperature reconstruction is limited by this diffusive spreading, which effectively smooths out extrema over time. The result is that the recovered temperature for a certain year in the past is effectively the weighted average of the temperatures in a range around that year. The width of that range grows larger with increasing time into the past [Orsi et al., 2012]. Using theoretical calculations in a homogeneous subsurface, Demezhko and Shchapov [2001] estimate the minimum event length resolved in the current ground temperature field to be $\pm 1/3 \cdot \tau$ around the time τ before the borehole observation. Consequently, this study chose methods that do not specify high-frequency changes in the past. In addition, a procedure of averaging with non-uniform running windows should be used whenever comparing temperature time series of constant temporal resolution (such as annual observations) to geothermal reconstructions [Demezhko and Gornostaeva, 2015]. To estimate the past surface temperature history T_j from the borehole temperature observations, two inverse methods (LSQR and Particle Swarm) were used with the forward soil model to optimize a surface temperature history for each of the borehole sites (Sects. 4.6.2.1 and 4.6.2.2). To estimate the time period for which information can be reconstructed from the borehole temperatures, the characteristic penetration depths of thermal heat waves were analysed using the forward model for the two sites (Sect. 4.7.1).

4.6.2.1 Least-squares method (LSQR)

The least-squares QR (LSQR) inversion is a generalized least-squares method. Its outcome is a single best solution with minimal variance, that is, the updates on the history to minimize E_{rms} are distributed as evenly over the time span as a locally linearized response allows.

In this method, a greedy algorithm iteratively decreases the largest deviation between the forward model run and the observed temperature profile by adding an update to the temperature history. Selection of the optimized update is done using the LSQR method [Paige and Saunders, 1982] and is based on a local linearization of the problem. In each iteration the algorithm determines the current deviation of the forward model run from the observed temperature profile and selects the largest temperature residual $T_{residual}(i^*)$ at depth i^* . An update δT_j to every time point in the surface temperature history is sought to reduce that largest residual. In a local linearization of the problem the response of the forward model at depth i^* to a small variation of the surface temperature at time j is calculated, i.e. the partial

derivative response matrix:

$$S_{ij} = \frac{\partial T_{model}(i)}{\partial T_j} \quad (4.2)$$

where $T_{model}(i)$ is the response of the temperature at depth i of the largest residual. To take into account the resolution power discussed above and that only longer wavelength heat waves penetrate to deeper depths with significant magnitudes, the surface temperature is varied over a minimum event duration [Demezhko and Shchapov, 2001] around j . The derivative response matrix S_{ij} is calculated using the complex-step derivative approximation [Martins et al., 2003]. Computation is numerically expensive and done only every few iterations so that S_{ij} is kept constant for those few iterations.

Here, the under-determination of the problem is reflected in the fact that:

$$T_{residual}(i^*) = \sum_j S_{i^*j} \cdot \delta T_j \quad (4.3)$$

has an infinite number of possible updates δT_j that decrease the residual and therefore minimize E_{rms} . The least square QR method is used to select the optimized update as the one with minimum variance from the multiple possibilities, as LSQR minimizes the Euclidian norm. The updated surface temperature history is used in the next iteration. The initial choice of surface temperature history was a linear interpolation of the observed temperature profile vs. depth mapped linearly to the reconstructed time domain.

4.6.2.2 Particle swarm optimization (PSO) method

In particle swarm optimization (PSO), a group (= swarm) of particles searches in the space of all possible temperature histories to find the best fit to the observed borehole temperature profile. The space of all possible histories is parameterized and the coordinates of a point in the space represent a temperature history. A group is randomly initialized with positions in the search space as well as with velocities with associated inertia keeping the particles on their current trajectories. Each particle evaluates its current position's temperature history and RMS error using the soil forward model. An iterative update to each particle's velocity is given by an attractive component drawing a particle in the direction of the position of the best fit so far evaluated by any swarm member, and determines the new position for the next iteration. Due to the combination of attraction and inertia, the method leads to a broad exploration of the search space while focussing specifically on regions

Optimization parameters	
Swarm size	30
Maximum generations	400
Attraction towards personal best	0.5
Attraction towards global best	3
Limit of velocity of particles	Limited to 10% of the parameter range.
Range of random initial positions	-16.2 to -10.2 °C

Table 4.3: Input optimization parameters for the particle swarm implementations.

with good overall match (RMS error) to the observation. The search terminates once a temperature history with E_{rms} below a specified input threshold is encountered. Many runs with different random initializations were performed and the resulting best fits analysed statistically. This swarm optimization approach is well suited to the nonlinear diffusive character of the problem and a large dimensional search space with potential multiple local and global minima. This study used a Matlab implementation of the PSO method by Ebbesen et al. [2012].

Systematic variation of the optimization parameters in the implementation resulted in values given in Table 4.3 to yield most robust search results, i.e., the probability of a single swarm reaching the specified input E_{rms} threshold. Palaeotemperature reconstructions for the northern hemisphere and for the Arctic predict anomalies on the order of <1 and 1–2 °C over the last 2000 years, respectively [Mann et al., 2008, McKay and Kaufman, 2014]. For the initial random particle positions a subspace of three times the larger Arctic range around the Tiksi air temperature average of 1961–1990 was chosen (Table 4.3).

To inhibit unresolved high-frequency variations, two choices of parameterizing the search space of possible temperature histories were applied:

(Four-segment PSO) The four-segment parameterization applied by Roberts et al. [2013] in his ice borehole reconstructions. The temperature histories were simplified to four consecutive linear ramps with transition points that were variable during optimization. In this eight-dimensional parameterization, the variables to be optimized are the time and temperature of the three transition points as well as the temperature of the start and end.

(Fix time point PSO) Fixed time points were spaced, such that the span of $\pm 1/3$ around them did not overlap adjacent spans. In this parameterization of the search space, only the temperatures at each fix time point varied. The advantage was effectively a higher number of segments which should be more stable at higher search

space dimensionality in the optimization as changes are fully independent of each other, which was not the case as fully in the four-segment parameterization (changing the location in time of an intermediate point simultaneously affects the temperature at the old point). A disadvantage is that temporal resolution is a-priori limited even if the temperature observations could offer more information. In addition, the resulting temperature history curve appears less smooth, because past temperatures are optimised at discrete time ranges.

For both (four-segment and fix time point), 500 stochastic runs of the swarm optimization with random swarm initializations yielded a population of temperature histories. The median was selected as the most likely temperature history and the variation about the median indicate uncertainty including potential short-term variations that are smoothed out by diffusion.

In contrast to the LSQR method, the PSO method employs a Monte Carlo approach to explore the range of possible solutions. Its outcome is a distribution of possible solutions with the freedom of producing sharper changes than the LSQR method. Therefore, the LSQR method is expected to smooth out sharper changes more than the PSO method.

4.6.3 Sensitivity analysis

Sensitivity of PSO median solution to the input E_{rms} threshold

The distribution of temperatures in the PSO inversion was calculated for decreasing values of specified input E_{rms} threshold. Table 4.4 shows the resulting values of E_{rms} and maximum error for the median solution. As expected both values decrease with lower input thresholds until a limit was reached beyond which agreement between the observation and the inversion was not possible. The ability of the specific history parametrization to capture the required history, measurement errors in the observed temperature profile, uncertainties in the sediment composition and non-diffusive heat transfer processes may all affect this threshold for the two methods. The lowest attained E_{rms} in the median solution for the fix time points PSO were $2.77 \times 10^{-2} \text{ }^\circ\text{C}$ and $2.66 \times 10^{-2} \text{ }^\circ\text{C}$, for Mamontov Klyk and Sardakh Island respectively. In comparison, the best thresholds attained in the four-segment-parameterized PSO inversion fall short of those for both LSQR and fixed time point PSO ($5.46 \times 10^{-2} \text{ }^\circ\text{C}$ and $4.28 \times 10^{-2} \text{ }^\circ\text{C}$ at the two sites, respectively). The residual maximal error in the profiles from the median solution with this method also remained higher by a factor of 2. In the four-segment PSO, the distribution of temperatures in the solution was

Mamontov Klyk					
FIX TIME POINTS PSO			FOUR-SEGMENTS PSO		
Input E_{rms} threshold [°C]	E_{rms} in median of PSO solutions [°C]	Maximum error in median of PSO solutions [°C]	Input E_{rms} threshold [°C]	E_{rms} in median of PSO solutions [°C]	Maximum error in median of PSO solutions [°C]
0.2	5.05×10^{-2}	11.17×10^{-2}	0.5	34.44×10^{-2}	67.50×10^{-2}
0.1	4.14×10^{-2}	9.20×10^{-2}	0.3	22.66×10^{-2}	38.05×10^{-2}
0.07	3.10×10^{-2}	7.17×10^{-2}	0.2	14.51×10^{-2}	25.15×10^{-2}
0.05	3.10×10^{-2}	7.85×10^{-2}	0.15	11.82×10^{-2}	19.19×10^{-2}
0.04	2.77×10^{-2}	6.28×10^{-2}	0.1	8.82×10^{-2}	19.14×10^{-2}
0.03	3.18×10^{-2}	7.09×10^{-2}	0.07	5.46×10^{-2}	11.32×10^{-2}
0.02	no solutions		0.06	no solutions	
Sardakh Island					
FIX TIME POINTS PSO			FOUR-SEGMENTS PSO		
Input E_{rms} threshold [°C]	E_{rms} in median of PSO solutions [°C]	Maximum error in median of PSO solutions [°C]	Input E_{rms} threshold [°C]	E_{rms} in median of PSO solutions [°C]	Maximum error in median of PSO solutions [°C]
0.2	8.40×10^{-2}	23.84×10^{-2}	0.2	19.27×10^{-2}	36.24×10^{-2}
0.1	5.49×10^{-2}	13.90×10^{-2}	0.1	7.13×10^{-2}	18.28×10^{-2}
0.07	3.90×10^{-2}	9.08×10^{-2}	0.07	5.04×10^{-2}	13.46×10^{-2}
0.05	3.27×10^{-2}	7.34×10^{-2}	0.06	4.64×10^{-2}	12.36×10^{-2}
0.04	2.93×10^{-2}	5.65×10^{-2}	0.05	4.21×10^{-2}	10.48×10^{-2}
0.03	2.66×10^{-2}	4.87×10^{-2}	0.04*	3.57×10^{-2}	8.79×10^{-2}
0.02	no solutions		0.03	no solutions	

(*) denotes a skewed distribution

Table 4.4: Sensitivity of PSO median solution with respect to the input E_{rms} threshold.

relatively skewed (skewness: 2–4), with even higher skewness at the lowest threshold at Sardakh Island. Optimal values for the E_{rms} input threshold were therefore chosen as 0.07 °C and 0.05 °C, for Mamontov Klyk and Sardakh respectively. For fix time points PSO at Mamontov Klyk, lowering the input threshold to 0.03 °C resulted in increased E_{rms} and maximum error in the median solution, unable even to meet the input threshold. Optimal values for the E_{rms} input threshold were therefore chosen as 0.04 °C and 0.03 °C, for Mamontov Klyk and Sardakh respectively. In the distributions obtained from the fix time point PSO, skewness was comparably absent (on the order of 0.3–0.5).

Sensitivity to initial temperature profile

Assuming an equilibrium initial temperature profile, the maximum warming during the recoverable period at Mamontov Klyk was reconstructed and a lower bound to our estimate of past temperatures established. This will likely underestimate past temperatures and the real temperatures may lie between this lower bound and the estimate adapting the pre-warmed conditions from Tiksi. For the equilibrium

scenario, the initial temperature profile is based on the steady state temperature profile given by the start temperature of the surface history and the geothermal heat flux. The initial temperature profile varies throughout the optimization process as the start temperature in the history adjusts. Fig. 4.6 shows the temperature history reconstructed from both scenarios using the LSQR inversion. Using the equilibrium initial condition, the general trend of temperature change remains unchanged, but with a 0.2°C higher maximum around 2000 CE and temperatures two centuries ago that were up to 0.4°C lower, indicating better agreement with the indicated colder past climates at Mamontov Klyk.

Sensitivity to seasonal freeze/thaw in active layer

Any departures from simple one-dimensional diffusive heat conduction can be treated as perturbation to the subsurface temperature field. In permafrost, non-conductive processes affect the thermal regime of the active layer and may impact the deeper permafrost temperature. The reconstructed temperature histories represent the ground temperature changes at the upper boundary of the heat conduction domain [Majorowicz et al., 2004]. Summer temperatures in the active layer can be lowered by non-conductive processes, e.g. evaporative cooling near the surface that diverts energy from the downward sensible heat flow. Although a more detailed study might incorporate additional heat flows in the ground close to the surface interface [Badache et al., 2016], the required meteorological input parameters were not observed at the sites. Temperatures $2\text{--}3^{\circ}\text{C}$ lower than expected by conduction alone were observed in the active layer at Barrow, Alaska [Hinkel et al., 2001]. Assessment of heat flux processes in the active layer on Svalbard and on the Tibetan Plateau find that non-conductive transport contribute only a maximum of 3% to the mean heat flux and indicate that heat conduction together with an appropriate freeze/thaw description already yields accurate results of thermal regimes [Weismüller et al., 2011]. Latent heat effects have further been speculated to mute annual GST signals during summer when the active layer thaws [Hinkel et al., 2001, Smerdon et al., 2004]. In order to estimate the effect that the seasonal freeze/thaw cycle has on the reconstructed temperature history, a simplified annual sine of 15°C amplitude was superimposed on the mean annual temperature history during the LSQR inversion at Mamontov Klyk (Fig. 4.6). The necessary higher temporal resolution in the forward model was numerically expensive, and in a simplification the derivative response matrix was kept constant throughout the inversion process. A solution of the inversion without seasonal variation was calculated using the same modification to assess the impact of freeze/thaw alone. The impact of seasonal freeze/thaw processes on the reconstructed

temperature history was small. Reconstructed temperatures were less than $0.2\text{ }^{\circ}\text{C}$ higher in the second half of the 20th century. In 2005 the minimum temperature is marginally higher ($-11.8\text{ }^{\circ}\text{C}$ instead of $-11.9\text{ }^{\circ}\text{C}$). The strongest deviation is seen at the end of the reconstructed period when temperatures were warmer by up to $0.8\text{ }^{\circ}\text{C}$ compared to the inversion without seasonal variations, which is reduced to $0.5\text{ }^{\circ}\text{C}$ when considering the non-seasonal solution with constant response matrix to assess the impact of freeze/thaw alone. Latent heat effects of freezing and thawing thus have only a small impact on the recovered temperature history beyond the most recent few years, and even then the impact is small compared to the reconstructed rapid increase on the order of $3\text{ }^{\circ}\text{C}$.

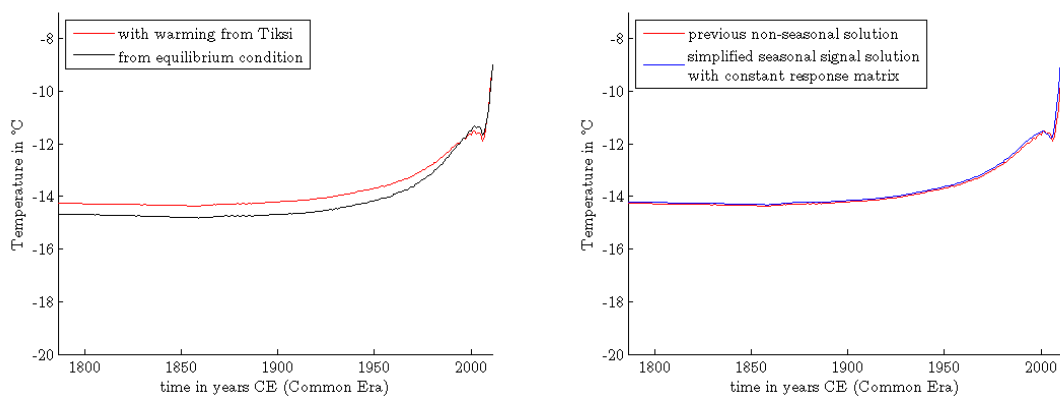


Figure 4.6: Assessment of various impacts on the reconstructed solution: **(left)** Effect of initial equilibrium subsurface temperature conditions on the LSQR reconstruction of the temperature history at Mamontov Klyk. **(right)** Comparison of LSQR reconstructions at Mamontov Klyk for the non-seasonal solution and the solution impressed with a seasonal sine. Adapted from [Kneier et al., 2018].

4.7 Results and discussion of the reconstruction from the permafrost boreholes

4.7.1 Recoverable period

At Mamontov Klyk, the recoverable period was approximately 450 a, based on the characteristic penetration depths. The reliably reconstructed period is limited by the LSQR method's design to $3/4$ of the forward model time domain due to the fact that for later times no full $\pm 1/3$ window fits into the model time span for the derivative response function. This study conservatively adopted $1/2$ of the model time length as the maximum recoverable period for the Mamontov Klyk borehole site (225 a). At Sardakh Island, the characteristic penetration depths led to a recoverable period

of 2500 a. This is not unexpected since the heterogeneous stratigraphy included a low conductivity layer from 50 to 70 m depth (see Fig. 4.5). This layer strongly attenuated propagating temperature signals. In the subsurface different surface signal frequencies are attenuated over different depths-distances, and this separation of time signals to different depths allows the reconstruction from borehole profiles. Such a strongly damping layer restricts the characteristic penetration depth of longer time scale signals to the borehole depth but simultaneously shifts the different depths to which individual signals are attenuated closer together. The diffusive nature of heat transport, i.e. the spreading of heat signals over depth, has a stronger relative effect at these depths below the layer, which limits the recoverable period. To deal with these limitations, LSQR calculations were performed with varying model time domain for Sardakh Island. For model time domains longer than 800 a, the LSQR solutions of surface temperature consistently changed only prior to 1750 CE, indicating that a maximum robust reconstruction period had been reached and that no additional information was recoverable from increased model time lengths (Fig. 4.7). This study therefore adopted 800 a as the model time domain and 260 a as the recoverable time period at the Sardakh Island borehole site.

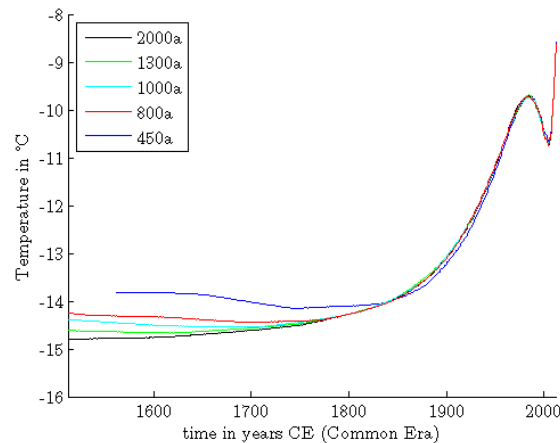


Figure 4.7: Sardakh Island LSQR solutions of temperature history for various model time lengths. Adapted from [Kneier et al., 2018].

4.7.2 Optimization

The LSQR implementation was run calculating updates to improve the E_{rms} and saving the result in 0.01 °C-steps of decreasing E_{rms} . The lowest attained limit was 0.04 °C at both sites. The distribution of temperatures in the PSO inversion achieved an E_{rms} in the median solution for the fix time points PSO of 2.77×10^{-2} and 2.66×10^{-2} °C, for Mamontov Klyk and Sardakh Island, respectively. In this respect, the four-segment-parameterized PSO inversion fell short of both the LSQR and the

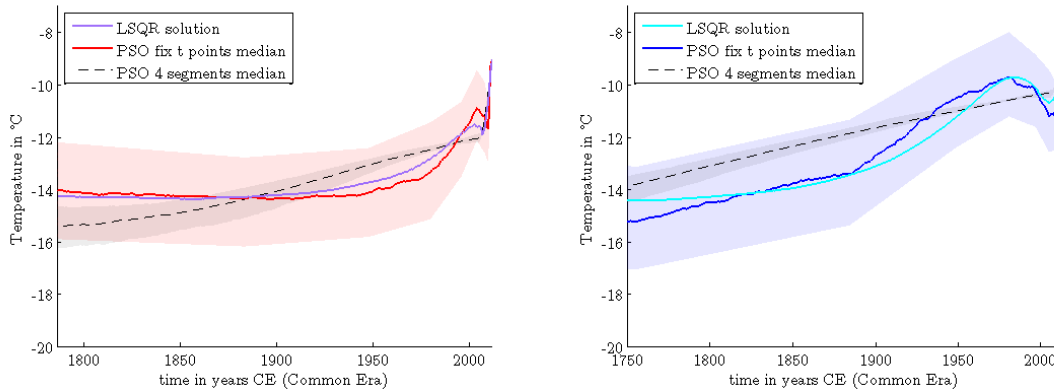


Figure 4.8: Reconstructed ground surface temperature history (**left:**) at Mamontov Klyk and (**right:**) at Sardakh Island using the LSQR and both PSO inversion methods. The shaded area gives the 25th and 75th percentile in the PSO distribution. Adapted from [Kneier et al., 2018].

fixed time point PSO (5.46×10^{-2} and 4.28×10^{-2} °C at the two sites, respectively) (See Sect. 4.6.3). The resulting optimal temperature histories are shown in Fig. 4.8.

4.7.3 Surface temperature reconstructions and fit

For the Mamontov Klyk site, the LSQR solution shows almost constant temperature levels of -14.2 °C starting before 1800 and continuing throughout the 19th century with only a small one tenth of a degree Celsius rise between 1860 and 1873. A gradual transition to rising temperatures begins in the first decade of the 20th century and warming increasingly in the second half of the century. A slowing of the warming occurs in the 1990s and a maximum of -11.5 °C is reached in 2002. A slight cooling of 0.4 °C follows until 2004 when a recent final strong linear increase sets in culminating the temperature history at -9 °C in 2011, the time of borehole logging. The median solution from the fix time points PSO exhibits a generally similar pattern with gradual deviations. Temperatures start around -14 °C before 1800 falling slightly but gradually by 0.25 °C per century throughout the 19th century before beginning to warm as well in the first decade of the 1900s. The warming rate, however, remains lower with temperatures up to c. 0.3 °C below the LSQR curve, the rate increasing only later in 1950 and again in the 1970s. The PSO shows warming eventually superseding the LSQR level and reaching a maximum 0.6 °C warmer around the same time (2003). The magnitude of the subsequent cooling is double the LSQR value and the cooling period lasts twice as long. The final increase occurs in the last 2 instead of 5 years. This solution thus shows the sharpest final increase of the three reconstruction methods. The four-segment PSO solution stands apart from the two

other solutions. It matches the feature of the recent temperature rise but appears to instead almost linearly decrease backwards prior to that going straight through the variations of the other two curves from 1800 to c. 1980, warming rather steadily by 3°C in two centuries.

For the Sardakh Island site, the LSQR solution shows almost constant temperature levels of -14.3°C during the 18th centuries with variations of only one tenth of a degree Celsius. A gradual warming begins in the course of the 19th century, significantly increasing in its rate after the turn to the 20th century. Temperatures rise continuously to a maximum of -9.7°C in the 1980s. The solution displays a subsequent pronounced drop of 1°C until 2004 before commencing a final large increase in recent years to a maximum of -8.6°C in 2012, the time of borehole logging. The median solution from the fix time points PSO is made up of coarser ramp periods than the LSQR solution, especially recognizably in the further past. Nonetheless, its solution again exhibits a similar pattern with a few notable deviations. Temperatures begin at a minimum of -15.2°C in the middle of the 18th century. Temperatures recover by 1.4°C per century until the end of the 19th century when a further increase in the warming rate to 4.6°C per century is evident until 1950. This warming continues to a maximum temperature of the same level as in the LSQR but attained slightly earlier in 1979. The subsequent cooling is broken into two consecutive steps, but the magnitude of the overall drop is again over one-and-a-half times as large as in the LSQR falling as low as -11.3°C . As the solution reaches the same final temperature, the last increase to -8.6°C is even larger, 2.7°C in 4 years. The four-segment PSO solution coincides only in the most recent sharp temperature increase, but shows a differing behavior before that point. It is characterized by an almost linear decrease backwards with -1.4°C per century cutting through the troughs and peaks of the other two curves.

Figure 4.9 presents the temperature profiles down the Mamontov Klyk and Sardakh Island boreholes from observation and by the forward soil model for the inversion solutions of all three methods. In general, forward modelled borehole temperatures from the LSQR and fix time point PSO solutions agree with the observation and with each other (Fig. 4.8) to within sensor accuracy. Borehole temperatures calculated from the four-segment PSO solution have the poorest agreement with temperature observations around a warmer excursion at 30 and 35 m depth for Mamontov Klyk and a similar excursion at 50m and a temperature overestimation at 20 m depth for Sardakh Island, though, due to poorer sensor accuracy at Sardakh, even the four-segment PSO profile lies within the uncertainty range. At Mamontov Klyk with its better sensor accuracy, four-segment PSO clearly does not agree to within observation uncertainty. Agreement to these features of the observational record

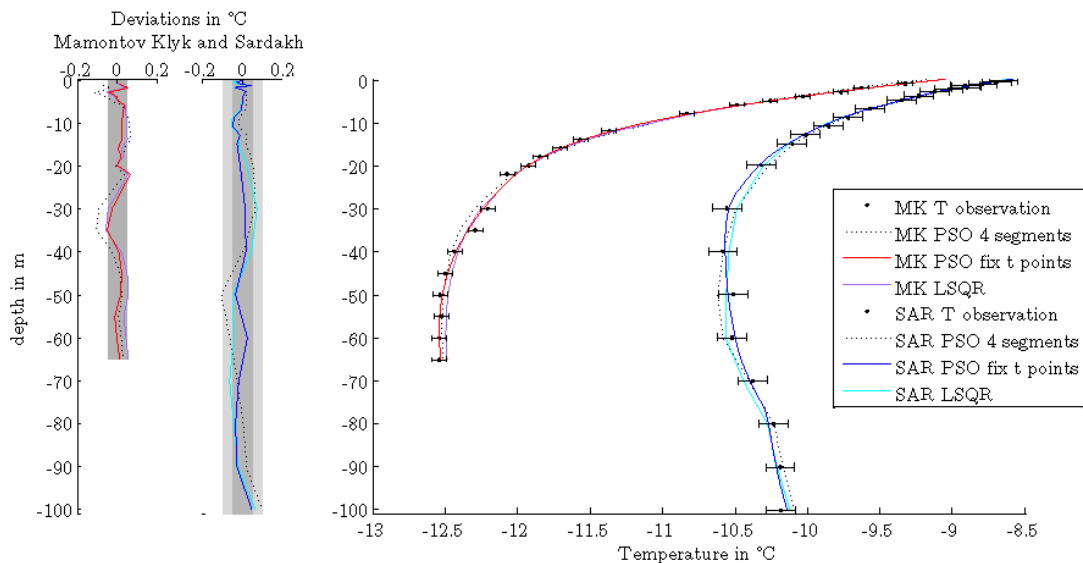


Figure 4.9: (Right) The temperature profiles down the two borehole sites from observation and by the forward soil model for the LSQR and both PSO median surface temperature reconstructions. Thermistor accuracy was $0.05\text{ }^{\circ}\text{C}$ at Mamontov Klyk but only $0.1\text{ }^{\circ}\text{C}$ at Sardakh Island. **(Left)** Deviations from observed profiles for both sites. The dark grey area represents $0.05\text{ }^{\circ}\text{C}$ deviation and the light grey area represents the larger uncertainty at Sardakh. Adapted from [Kneier et al., 2018].

in the reconstruction solutions of the other two methods was also only observed at the final lower E_{rms} thresholds, indicating that such agreement is connected with the ability to achieve lower E_{rms} limits than obtainable with the four-segment PSO inversion.

Thus, the LSQR and the fix time points PSO inversion solutions agree quite well with each other (to an RMS deviation between the two histories of 0.27 and $0.40\text{ }^{\circ}\text{C}$, at Mamontov Klyk and Sardakh, respectively) and with the observation (to an E_{rms} of less than $0.03\text{ }^{\circ}\text{C}$ and maximal errors of $0.05/0.06\text{ }^{\circ}\text{C}$ in forward modelled temperature) at both sites. The four-segment PSO reconstruction shows a generally differing temperature history (a three times higher RMS deviation to the other two solutions) and forward modelling yields a smoother temperature profile that captures variations in the borehole profile less well. This method is not able to resolve the temperature variations over the relatively long recoverable time period of modelling (Sect. 4.7.4).

For a comparison of the ground surface temperature histories of Mamontov Klyk and Sardakh Island, the temperature histories given by the optimal inversion solutions of the LSQR and the fix time points PSO were considered. Solutions at both sites showed a similar warming trend from the colder temperatures of the previous centuries, followed by a maximum and cooling in recent times and a sharp final

increase in temperature during the last half decade before 2011/2012. They differed, however, in the timing of the warming as well as the magnitude of the first warming and subsequent cooling in recent times. At the start of the reconstruction, both exhibited almost constant temperatures with variations of only a tenth of a degree and temperature levels are of similar magnitude of c. -14.2°C (Mamontov Klyk) and -14.3°C (Sardakh). Temperatures at Sardakh began to rise around 1850 and continued to a maximum of about -9.6°C at the start of the 1980s. This was followed by a pronounced cooling by $1\text{--}1.6^{\circ}\text{C}$ over the 13 years before 2004. At Mamontov Klyk, on the other hand, the transition to warmer temperatures commenced almost a century later and rose to a maximum of only -11.5 to -11°C in the first decade of the 21st century, three decades later than Sardakh. The subsequent cooling was also less ($0.4\text{--}0.8^{\circ}\text{C}$) and lasted only for half a decade. The final strong increase in temperatures began only between 2006 and 2009, when it rose to -9°C in just two years. In contrast, this most recent temperature increase commenced earlier at Sardakh (between 2004 and 2008). In addition, although prior maximum temperature levels here had been higher, due to its previous more pronounced cooling, the overall temperature change to the 2011/2012 maximum of -8.6°C was almost the same as at Mamontov Klyk ($2.1\text{--}2.8^{\circ}\text{C}$ vs. $2.6\text{--}2.9^{\circ}\text{C}$). The final (2011 at Mamontov Klyk, 2012 at Sardakh Island) ground temperatures at both sites were almost similar (-9 vs. -8.6°C).

4.7.4 Inversion method's impact on character of solution & sensitivity to temperature history parameterization

The three inversion methods used in this study differed from one another. The differences in how updates in their search for the optimal solution are obtained, is reflected in the character of the respective best solution found [Shen et al., 1992]. Minor differences were observed between the LSQR and fix time points PSO (such as the difference in the position of the first warming maximum of one and four years at the two sites), which result from the position of the fix time points in the latter's parameterization. The LSQR solution tends to smooth out the first warming transition period from 1900 to 2000 at Mamontov Klyk, and from 1800 to 1980 at Sardakh. Also, the fix time point PSO solution shows a colder temperature at 1750, suggesting a signature of cooler Little Ice Age conditions at Sardakh, whereas this colder period is unresolved in the LSQR solution. LSQR further underestimates the maximum and minimum variation in the temperature history in the first decade of the 21st century at Mamontov Klyk, and in the minimum around 2004 at Sardakh Island. This character was expected and is in part explained by the least variance

nature of the updates in the LSQR solution for this under-determined problem [Golub and Loan, 1990, Roberts et al., 2013]. Even the large deviations in the solution and temperature profile of the four-segment PSO inversion can be explained by the inability of the parameterization to capture the required variations over the particular time span of the reconstruction. Three, four and five-segment parameterizations of the temperature history were assessed for increased resolution in the reconstruction. The PSO implementation yielded no results for the five segment parameterization whereas fewer segments resulted in even more smoothing. Figure 4.10 shows the four-segment solution when the median is used to spin up the model to 150 a before 2012 and the inversion scheme is performed employing the four segments only over the time span of the last 150 a. The four-segment parameterization seems to improve its ability to show similar variations to the solutions of the other two inversion methods when the parameterization of four segments is used over a shorter time span. Therefore, the parameterization of Roberts et al. [2013]’s ice borehole study was found to be unsuitable for terrestrial permafrost boreholes due to the difference in the reconstructible time period. Even for similar borehole depths, this results from differences in thermal parameters and from differences in the physical forward model between the two applications.

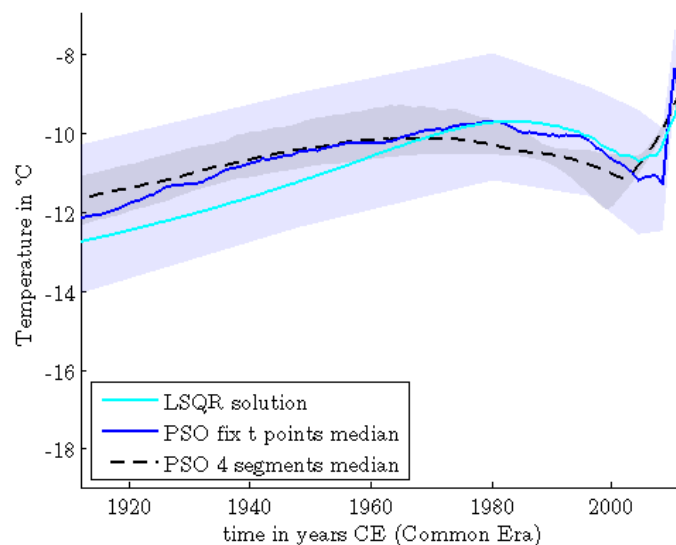


Figure 4.10: Comparison of the three inversion methods for the case that the four-segment PSO employed its parameterization over a shorter interval (150 a). The known median solution of the fix time point PSO was used to spin up the model for the first 300 a. Adapted from [Kneier et al., 2018].

4.8 Discussion of spatial differences and implications

4.8.1 Comparison to other temperature data

Figure 4.11 shows the trends of the resulting temperature histories at Mamontov Klyk and Sardakh Island in comparison to other local records from the region as well as to larger scale temperature trends. To be able to compare these records to the geothermal reconstruction, their annually resolved time series were averaged using the non-uniform running windows of the minimum event resolution referenced to the year 2011/2012 CE [Demezhko and Gornostaeva, 2015].

For the most recent time span, the results can be compared with direct observational data. The longest record of surface air temperature in the region is available from Tiksi (1930s to present), a shorter period record (1961–1996) from Cape Terpyai Tumus in the vicinity of Mamontov Klyk, and a short recent record from Stolb Island in the Lena Delta (2005–present). Of these, only the 60 a of observational data from Tiksi are long enough to indicate a trend. The observational period from Terpyai Tumus is enough to calculate the climatic 1961–1990 average, but the period is too short to clearly distinguish trends. The few years' record at Stolb did not allow for a 1961–1990 reference determination, but employing the Tiksi reference (located 118 km to the southeast) to calculate anomalies, they appear to match the Tiksi trend well, indicating that there is good agreement between these (relatively nearby) stations. Similarities can be seen to the reconstructed temperature history at Sardakh Island in the magnitude of the recent increase by 3 °C and in the earlier timing of the onset of the increase already in 2000. The higher temperatures in the middle of the 20th century in the Tiksi record also agree with the reconstructed Sardakh trend while contrasting the trend of lower temperatures at Mamontov Klyk.

A longer observational data set from 1850 CE onward is given by the spatially averaged northern hemispheric instrumental record of land air anomalies compiled by the Climate Research Unit of the University of East Anglia [Jones et al., 2012]. On this larger scale average, temperatures increase only slightly until the middle of the 20th century, after which significant continuous warming sets in. A plateau and slight cooling occur only in the first decade of the 21st century. These periods are reminiscent of the reconstructed Mamontov Klyk temperature trends albeit a factor of 2 lower in magnitude. However, while the Mamontov Klyk reconstruction began increasing again by 2011, the instrumental record shows a comparably rapid recent increase only in the four years up to 2016, following the borehole record (dotted line in Fig. 4.11 d). Mamontov Klyk is undergoing recent surface temperature increases

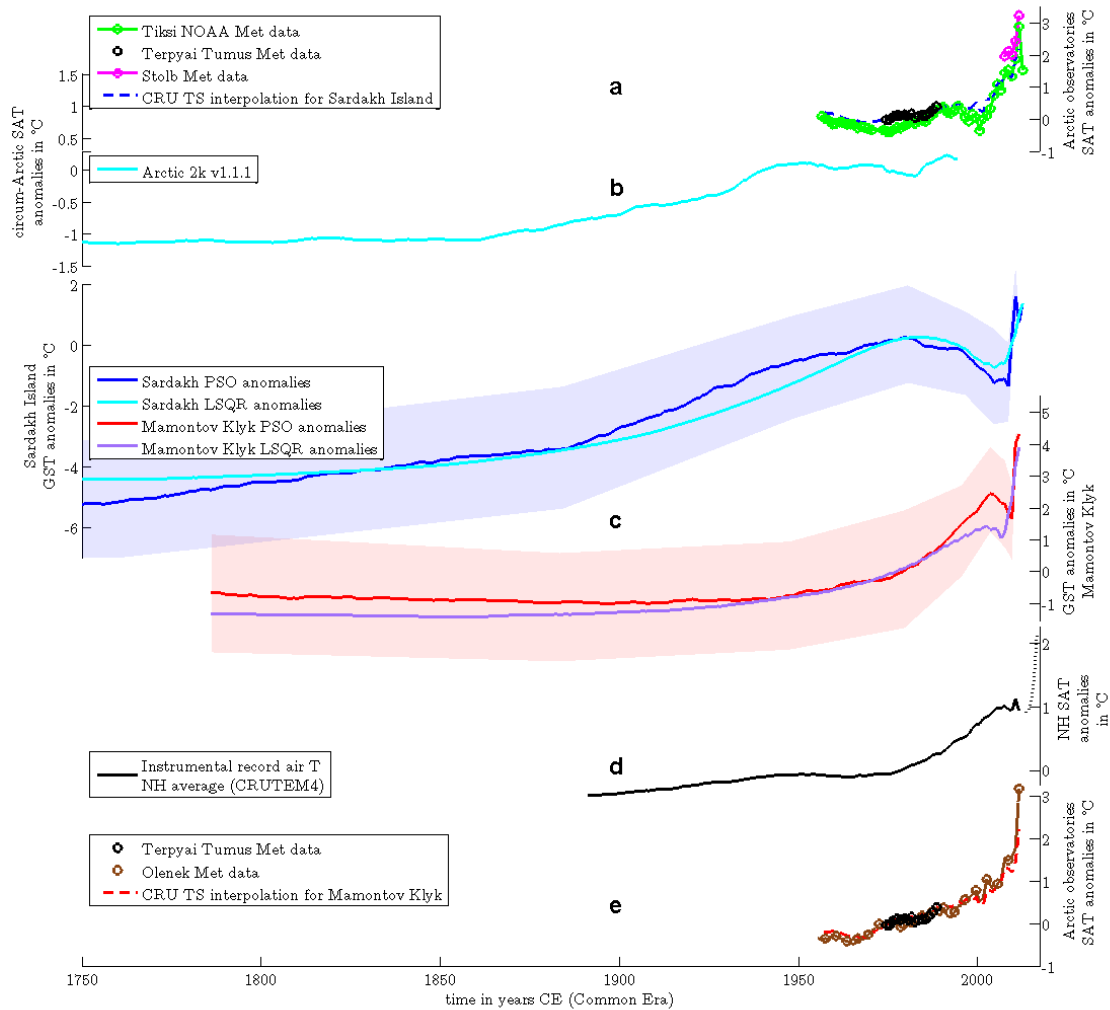


Figure 4.11: (a, e) Regional surface air temperature (SAT) anomalies at Tiksi [National Climatic Data Center, NOAA, 2015], Terpyai Tumus [Bulygina and Razuvaev, 2012], Stolb Island [Reliable Prognostics, 2017], Olenek (68.5°N, 112.43°E) [Lawrimore et al., 2011], and the CRU TS grid interpolation [Harris et al., 2014] for Sardakh Island and Mamontov Klyk. (b, d) Two longer scale records, (light blue) circum-Arctic proxy-based temperature compilation from PAGES 2k Consortium [2013], and (black) the northern hemispheric mean temperature anomalies of the instrumental record [Jones et al., 2012]. (c) Anomalies of the two reconstructed ground surface temperature (GST) histories at Mamontov Klyk (red) and Sardakh Island (blue) from the LSQR and fix time point PSO inversions. The Terpyai Tumus record is shown twice, in comparison to the Tiksi trend and the Olenek/Mamontov Klyk CRU TS trend. All anomalies are referenced to the 1961–1990 period where possible. The averaging process shortens the record lengths from the periods given in the text. Note the factor of 2 in the scale of the hemispheric and circum-Arctic larger spatial averages. Adapted from [Kneier et al., 2018].

that are ahead of the hemispheric trend but consistent with the Arctic synoptic trend. Olenek, a station located 500 km south of Mamontov Klyk (68.5°N, 112.43°E), exhibits a similar trend of a steady increase from the 1930s onward and with relatively low temperatures in the middle of the century.

For periods prior to the availability of direct observations, our temperature reconstructions can be compared to other borehole temperature or proxy-based climate reconstructions. Our 3–4 °C variation between 1900 and 2000 is within the range of other arctic site measurements. Lachenbruch and Marshall [1986] demonstrate that Alaskan permafrost subsurface temperatures indicate a spatially variable but widespread warming of the permafrost surface of 2–4 °C during the previous few decades to century. Subsurface borehole temperature reconstructions on a northern hemispheric scale show an increase of 0.9 °C from 1750 to 2000 [Pollack and Smerdon, 2004, Huang, 2004, Huang et al., 2000]. Given that Arctic warming is amplified and 3–4 times more rapid than the global mean [Hansen et al., 2010], our reconstruction's increase of 2.7 °C at Mamontov Klyk until 2000 and a 3.9 °C increase at Sardakh in the same period are reasonable. The variation at Sardakh within this period is, however, even higher with a maximum of 5 °C, placing it at the higher end of expected temperature change. A regional circum-Arctic proxy-based reconstruction with potential bias to western hemispheric influences is given by McKay and Kaufman [2014] for the period of 1–2000 CE (Arctic2k). This record overlaps the time span of the Tiksi observational record from 1956–1994. The Arctic2k and Tiksi anomalies have similar trends, but the Arctic2k varies less (by more than a factor of 2) than Tiksi, so that the larger scale mean is again more moderate than our local record. Nonetheless, both records indicate a warmer period beginning in the 1980s, a minimum in 1960, and warmer temperatures prior to that minimum. Therefore, this author suggests that the Tiksi record follows the circum-Arctic trend and furthermore that this region indicates temperature changes amplified over even the Arctic mean. Mean Arctic temperatures show warming from the 1850s onwards, reaching their warmest pre-2000 levels from the 1940s on. Together with the fit to the recent Tiksi record, these trends are similar to the reconstructed Sardakh Island temperature trends. Both begin to rise around 1850, a century ahead of such warming at Mamontov Klyk, both show elevated temperatures between 1931 and 2000, and a similar recent rise of 2.7–3 °C.

Despite their similarities, the reconstructed histories in the Laptev Sea region at Mamontov Klyk and Sardakh Island suggest some local differences in permafrost surface temperature history. While Sardakh Island is more similar to regional Arctic temperature trends, Mamontov Klyk is consistent with Arctic trends only in the most recent decade and is more similar to northern hemispheric scale mean trends before

then. There is consistency between our Sardakh reconstruction and observational records from Tiksi and Stolb. The only record from the vicinity of the Mamontov Klyk borehole is from Terpyai Tumus. This record is only 30 years and not long enough to correlate it with either reconstruction, but there is consistency between our Mamontov Klyk reconstruction and a record from Olenek (Fig. 4.11) albeit the latter being further south. In addition, consistency is indicated between our reconstructions and temperature data from the CRU TS grid, interpolating instrumental observations to the remote locations of Mamontov Klyk and Sardakh Island, with agreement to the two differing trend types, respectively.

Despite the differences between both borehole reconstructions, it is interesting to note that the final ground temperatures (2011 and 2012) at both sites were almost similar. The reconstructions' ground surface temperatures for both sites were also almost equal two centuries ago, i.e., levels of -14.2 and -14.3 °C, although the assumed climate as well as the deeper permafrost temperatures observed in the boreholes suggest a colder climate at Mamontov Klyk. This might indicate colder initial ground temperatures at Mamontov Klyk well before the time period reconstructed in this study.

4.8.2 Site differences

Reasons for the differences in the reconstruction between the two sites could be differences in environmental influences. The two borehole sites are about 350 km apart and differ in meteorology, atmospheric circulation including impact from snow cover, long-wave radiation, geothermal heat flux, sea ice, and river heat, which may influence their ground surface temperature history.

Mamontov Klyk is far from major river influences but directly at the coast of the Laptev Sea. Sea ice formation and its effect on climate might have a direct influence on the prevalent temperature history [Isaksen et al., 2007] and rapid sea ice loss has been connected with accelerated Arctic land warming [Lawrence et al., 2008]. Changes to advected heat will thus be sensitive to changes in sea ice cover or open water season duration and to surface water temperature changes. Both changes are difficult to quantify but consistent with warming over the past half century. In the central Laptev Sea, open water season has been reported to have increased by 15 days per year on average for the 2010–2012 period from the previous 20 year mean [Günther et al., 2015].

In contrast, Sardakh Island is located in the middle of a large delta. It is separated from the open ocean and its influences by more than 75 km of intervening deltaic

deposits, lakes, and river channels. It is adjacent to a major discharge channel of the Lena river which transports heat several hundred kilometers (year-round, in winter under up to 1.5 m river ice) from warmer southerly latitudes. Observational records suggest that both discharge [Peterson et al., 2002] and heat transport [Yang et al., 2005] are increasing. Additional lateral heat input could dominate over the surface temperature forcing if (i) a strong enough temperature difference between river and surface temperature exists over long time periods or during a sensitive season, e.g., warm river forcing could prevent winter cooling of the ground, altering the annual mean temperature to a more moderate magnitude than the meteorological trend would predict and (ii) the heat flux from the river at the borehole location is of comparable magnitude to the surface heat flux. To better understand the influence of the Lena River as a local heat source, observations of heat flux in the river bed and banks adjacent to the borehole would provide an indication of the temperature perturbation at the borehole, and support numerical modelling of heat conduction. In general, though, the river influence is not expected to strongly dominate due to the good agreement with SAT trends of the closest observatories in Tiksi and Stolb.

The trends of environmental changes at both Mamontov Klyk and Sardakh are consistent with reconstructed temperature records. Differences between their dominating environmental influences may be responsible for differences between the sites.

As part of the atmospheric circulation patterns, cloudiness during winter is another factor influencing the surface temperatures. In the surface energy balance, net radiation during the winter period is mainly determined by the long-wave radiation, with increased cloudiness leading to decreased outgoing long-wave radiation and warmer surface temperatures. Changes to cloudiness, i.e., the evolution of winter time cyclone activity at the sites, could drive the evolution of permafrost temperatures [Langer et al., 2011], but are difficult to assess. Vavrus et al. [2011] show increased autumn cloudiness associated with recent sea ice minima and further suggest that the rapidly declining Arctic sea ice will be accentuated by changes in polar clouds. The differences between the sites might indicate general differences in atmospheric circulation with cloud cover such as cyclonic activity.

Although geothermal heat flux has been shown to vary over very short spatial scales, e.g., in Antarctica by over 150 % over 10–100 km [Carson et al., 2014], the global map of heat flux in Davies [2013] gives values that differ only by less than 5 % between the sites.

Differences could potentially originate from snow cover impact and its influence on differences between ground and air temperatures. If long-term snow cover variation

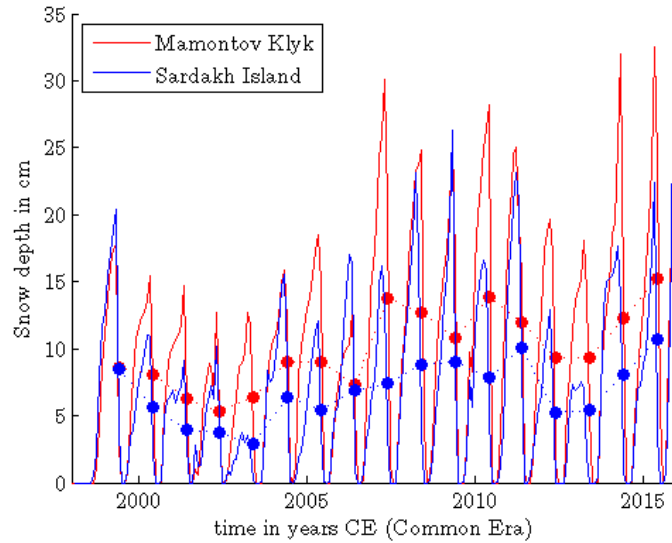


Figure 4.12: Monthly snow depth analysis data [Brown and Brasnett, 2015, updated annually] for the Mamontov Klyk and Sardakh Island locations. Dots represent the annual mean. Adapted from [Kneier et al., 2018].

differed spatially between the two sites, the same air temperature history could yield differences in the ground temperature history. Langer et al. [2013] report that 10 mm deviation in snow water equivalent could translate to up to 2.5 °C deviation in ground temperatures at 2.5 m depth on annual to decadal time scale. No long-term snow cover observations exist for either site. However, interannual variations of snow depth analysis data from the Canadian Meteorological Centre (CMC) for the period of 1998–2015 [Brown and Brasnett, 2015, updated annually] appear to be correlated (Fig. 4.12), suggesting that both sites are similarly affected by synoptic variations during this time period. During the data period, Mamontov Klyk exhibits a generally higher mean snow cover (10 vs. 7 cm) with only a few exceptions where severe winters at Sardakh lead to thicker snow cover relative to Mamontov Klyk (winter of 1998/99, 2005/6, 2008/9). Regarding the annual mean trend in snow depths, a general similar pattern at both sites is apparent. At decadal-to-centennial time scales, other borehole studies [Harris and Chapman, 2001, Chapman et al., 2004, Beltrami et al., 2005] (see Sect. 4.2) indicate air-ground coupling even with changes to snow cover and soil moisture.

4.8.3 Methodological considerations

In the geothermal method used, the borehole temperature profiles have a direct association with temperature in the GST history (since they are the direct physical remnants of past changes at the surface). This direct relationship removes ambiguity

related to the necessary calibration introduced in proxy record reconstructions, which affects temperature inference [Ho and Laepple, 2016]. The disadvantage in geothermal reconstructions, however, is a progressively lower resolution in the increasingly distant past. Differences between geothermal and various proxy-based reconstructions have been ascribed mainly to different seasonal sensitivities in their temperature biases. For example tree ring proxies are sensitive to the growing season and ice core isotopes respond to the snow season. Proxies tend to be biased towards a particular season, whereas borehole temperatures respond to the surface temperature signal continuously and throughout the year.

Ground temperatures respond to surface air temperatures, but also to other processes that may superimpose non-climatic energy perturbations on the climatic signal. As discussed in Sect. 4.2, a warmer season bias was implied in some studies, but the re-analysed data suggest that it contains both summer and winter effects, and additional data indicate that GST compares favorably to SAT trends even in the presence of snow and freeze/thaw cycles. Those results indicate air-ground coupling at decadal-to-centennial time scales and that geothermal reconstruction anomalies are robust long-term change indicators under conditions of conductive heat transport. Our reconstructed ground surface anomalies are thus interpreted to reflect SAT trends with the potential exception of the most recent decade, which might be affected by interannual variation in the offset between air and ground temperatures. The fact that both sites' histories are reminiscent of paleotemperature records suggests that the transferability to SAT is likely high, and that the differences between reconstructed temperature histories for the two sites most likely result from differences in meteorological conditions.

In the perennially frozen Arctic region, non-conductive processes affect the active layer. The reconstructed temperature histories represent the ground temperature changes at the upper boundary of the heat conduction domain [Majorowicz et al., 2004], which, in this permafrost setting, is the top of permafrost. Even in the active layer, however, heat conduction is found to be the dominant process, with non-conductive transport contributing less than 3% to the mean heat flux [Weismüller et al., 2011]. Their results indicate that heat conduction plus a process description of freeze/thaw is appropriate to explain the thermal regime in the active layer. To assess the impact that latent heat effects may have on deeper permafrost temperatures, the reconstructed temperature history was modelled with the superposition of a seasonal freeze/thaw cycle. The result (Fig. 4.6) shows that latent heat effects have only a small impact on the recovered temperature history (see Sect. 4.6.3 for more details).

The assumption of the initial subsurface temperature condition may bias our results. The equal levels of reconstructed surface temperature in the past at both sites, despite the observed colder deep permafrost temperatures at Mamontov Klyk, could also indicate that the initial conditions constructed from the deep Tiksi borehole were less appropriate for the Mamontov Klyk site. Mamontov Klyk is three times as far away from Tiksi as Sardakh, and its unconsolidated and relatively ice-rich subsurface differs in thermal diffusivity from the rocky Tiksi and Sardakh borehole sites, leading to potentially slower propagation of the Holocene transient warming signal. The Mamontov Klyk borehole is not deep enough to observe the geothermal gradient and the ambient quasi-steady-state temperature profile at the site. There are no other borehole data that could be used to evaluate the disparity between Tiksi and Mamontov Klyk. Nonetheless, transient Holocene warming is clearly visible in the borehole temperature record from Tiksi, indicating pre-warmed and not equilibrium conditions at the start of the reconstruction. The effect of equilibrium initial conditions is considered in Sect. 4.6.3.

While the character of the specific inversion methods is reflected in the respective solutions as expected, a shortcoming in the resolving ability of the parameterization of the temperature history has a large impact on the reconstructed solution (Sect. 4.7.4). The four-segment parameterization is only adequate to resolve the variations necessary in our reconstruction when used over a shorter time span of 150 a (Fig. 4.10). This shows that the choice of search space parameterization in optimization studies can be of high impact and must, therefore, be well considered. Nonetheless, the inversion solution of all three methods – when this limitation is taken into account – agree quite well with each other. The reconstructed temperature histories thus seem robust against variation of the chosen inversion method.

4.8.4 Implications

Borehole temperature reconstructions from shallow permafrost boreholes prove successful in filling the gap of recent (up to the previous 200–300 a), well-resolved temperature records in the absence of tree ring proxies in the Arctic tundra region. Resolution on the short time scale is good which overcomes poor age control in long-term radiometric dating techniques in this regard. For the Mamontov Klyk region, where no closer direct observations exist, this is the first time that a temperature record is recovered at this site of ongoing permafrost degradation. The reconstructed ground surface temperatures are directly valuable to permafrost models and to evaluating permafrost processes in the Siberian Arctic as they provide the temporal temperature changes at the permafrost table (the top of the mostly conductive

regime) or at the standard depth of permafrost temperature observation (20 m below surface). The former parameter is the necessary upper boundary condition for forcing model assessments of the evolution of permafrost.

Due to the increasingly limited temporal resolution further back into the past, these reconstructions do not provide a means of comparing amplitudes of temperature change in recent time intervals to those in intervals further in the past. Peaks here can be interpreted as a lower bound of temperature extrema. The uncertainty in the PSO solution distribution is a measure of the potential for short-term variation that is smoothed out by the diffusive processes. High frequencies are better resolved the more recent they are. As a consequence, the most current time span is the one with most detail. Nonetheless, the rapid recent increase is observed at both sites. Whether this signal will endure over longer time scales or remain transient (and be consequently smoothed out in future geothermal records as past transient high excursions may have today), will only become evident if the higher temperature persists in the future or by improving the resolution of the recovered temperature history. Combining the borehole temperature reconstructions with a proxy record with sensitivity to higher frequency modulations in the past of the temperature history could improve the resolution [Demezhko and Solomina, 2009]. Unfortunately, even oxygen isotope variations in ice wedges do not achieve the required decadal resolution [Meyer et al., 2015, Opel et al., 2017].

Implications for the Laptev Sea region include:

- (1) The reconstructed magnitude of changes is consistent with the observation that the region is amplified in its temperature changes even above the mean Arctic temperature change. This observation from the Tiksi SAT record is also in line with a recently reported c. 2.5 times higher warming rate for central Yakutia [Boike et al., 2016].
- (2) The spatial differences between the two sites imply that climate trends did not necessarily affect both sites in the same way. This suggests that regional-scale temperature reconstructions are not necessarily valid locally.
- (3) Despite the spatial variability, temperature histories at both sites are consistent with a recent rapid warming. This indicates that the recent warming signal is of synoptic scale and dominates over previous spatial variability.
- (4) Our reconstructions provide information on the differences in the temperature history from simply using a shifted regional Arctic or even global mean temperature curve for the entire region. Studies of subsea permafrost distribution in the Russian Arctic [Romanovskii et al., 2003, 2004, Nicolsky et al., 2012] for example so far have

utilized a global temperature trend curve adapted by offset for different locations due to the large-scale nature and the sparsity of data. However, our findings of spatial differences in the temperature trend during the last 200–300 a are a strong indicator that differences were probably present in earlier times, as well. Due to the spatial variability in the Laptev Sea region, site assessment of permafrost degradation might be strongly a-priori biased if a larger scale mean temperature history instead of these local reconstructions is used.

CHAPTER 5

Conclusion and outlook

In this thesis, three steps on the path to improved understanding of subsea permafrost degradation on the Arctic continental shelf, and specifically, in the Laptev Sea region have been identified: (I) innovative observational methods, (II) the role of salt infiltration and its implementation in modelled degradation, and (III) variability of potential regional differences in key driving parameters. In each area, a specific hypothesis was tested to advance the current shortcomings (Fig. 5.1 summarizes the answers and contributions of this thesis to the three areas).

Regarding improved detection capabilities, the strong shear wave velocity contrast between the unfrozen sedimentary layer and the ice-bonded permafrost below makes the application of passive seismic H/V analysis for mapping of subsea permafrost very suitable. Clear H/V peaks could be identified in the data set of ambient noise around Muostakh Island, and their relationship to frozen permafrost corroborated by numerical modelling. This study showed that the shear wave velocity of the unfrozen sediment, required to estimate layer thicknesses from the H/V frequency peaks, can be successfully obtained by seismic interferometry analysis of the ambient noise of the same data set. Therefore, the method is self-contained, i.e. almost entirely data-driven and based on the same set of observational data without the need to collect or assume additional subsurface information. Hypthesis 1 can thus be answered: Yes, ambient noise beneath the seabed was shown to contain information on thaw depths in the near-shore zone of the continental shelf.

The passive geophysical method has a great potential for mapping the permafrost distribution in large areas with reasonable efforts. Furthermore, monitoring of temporal changes could be achieved by time lapse measurements. A first baseline of thaw depths around the island is provided by this study's data set. The developed underwater instruments are low-cost, compact, and permit easy deployment from small ships and at minimal transportation cost and logistics. The method is non-invasive,

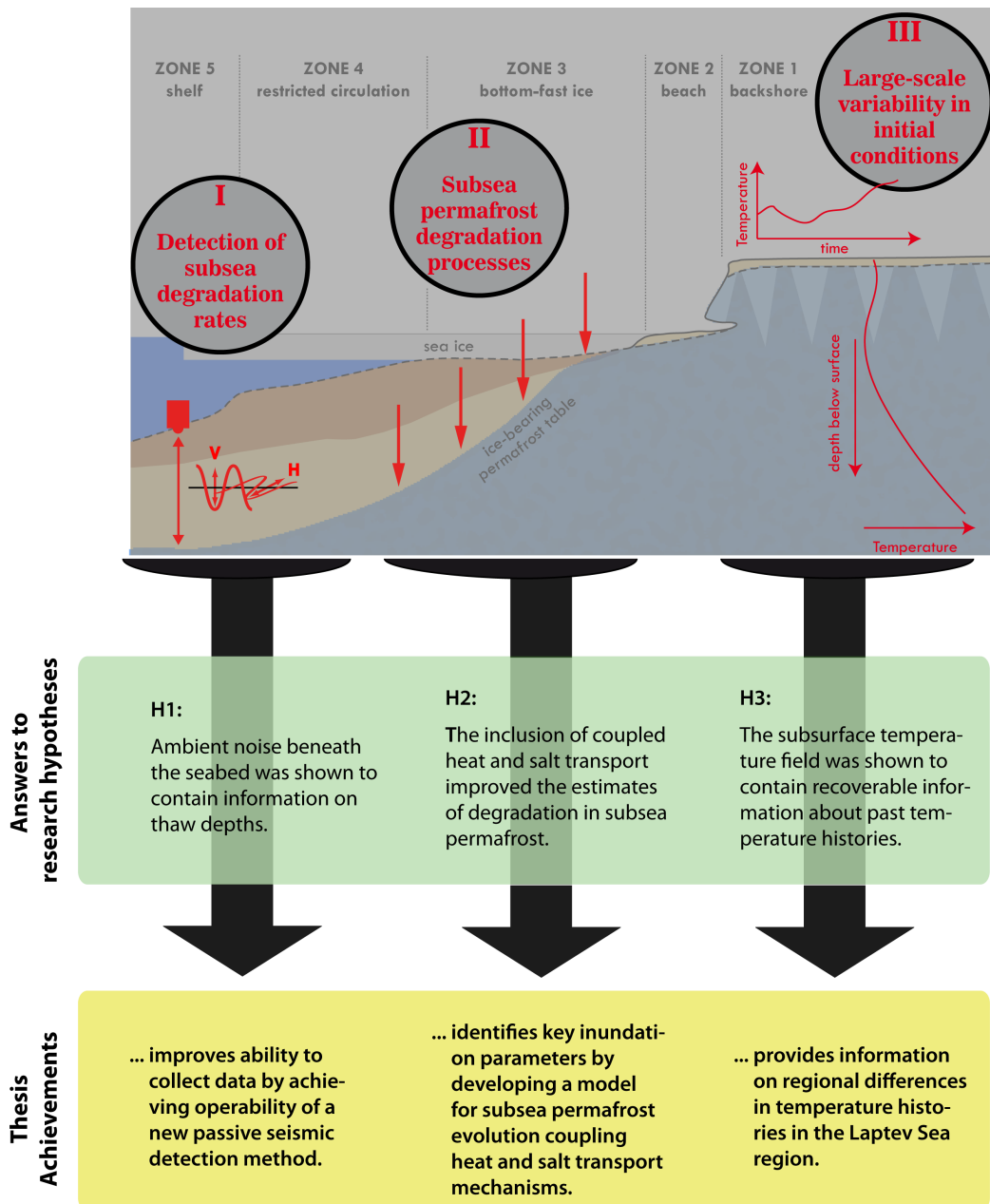


Figure 5.1: Key areas of corresponding research hypotheses. Answers to the research questions and achievements are given below.

environmentally friendly and does not need active seismic sources, circumventing the main permitting limits. Limitations of the method may include additional H/V peaks from the water layer interfering with the H/V peaks of interest. Moreover, further investigations of the velocities of the unfrozen sediment in future experiments (critical to estimate the depth of the ice-bonded permafrost) should be conducted. It is also possible that an arrangement of sediment and bedrock in the unfrozen zone above the permafrost does not fit the basic assumption of water/soft unfrozen sediment/frozen permafrost, i.e. the method would be limited to hard permafrost tables beneath soft

sediment columns. Finally, the sensor frequency characteristic should correspond to the expected H/V peak frequencies depending on the permafrost depth and the shear wave velocity of the sedimentary overburden.

Examining the influence of various inundation parameters (including saline pore water) on the permafrost evolution in Arctic shelf sediments was achieved by developing a one-dimensional permafrost soil model constrained by borehole data from the Laptev Sea. The model was validated with observed temperature profiles and previously reported permafrost thicknesses. Stratigraphic salt scenarios showed that the modelled salt, its distribution and its infiltration mechanism have a large impact on the state (thawed or frozen) of offshore permafrost. However, these processes are not sufficiently, if at all, included in current models of subsea permafrost evolution. Since key field parameters, such as interstitial water flow velocities, remain unknown, the model work successfully implemented a parameterized approach of salt transport mechanisms in simulations. In answer to hypothesis 2, the inclusion of coupled heat and salt transport improved agreement between modelled and observed depth of subsea permafrost thaw after inundation. Quantitatively, three parameters were identified that, when changed, shift the modelled depth of the ice-bonded permafrost table most strongly: bottom water temperatures, shoreline retreat rates, and the initial temperature before inundation. Consequently, any meaningful modelling of subsea permafrost would have to constrain these factors well. A focus should be set on understanding the regional differences in the key factors, in order to simulate variability in subsea permafrost degradation rates on the circum-Arctic scale.

Importantly, salt transport based solely on diffusion was shown to underestimate the observed thaw depths in the boreholes. By employing an effective parameter salt transport model, we could show that the gap cannot be accounted for with contribution from any density-driven mechanism. Free convections and salt fingering can therefore be only part of the solution to explain observations: A threshold for realistic interstitial velocities and attainable thaw depths by this mechanism was shown to exist and to merely account for about 50% of the observed thaw depths at offshore sites hundreds to thousands of years after inundation. Key parameters better constrained by observational data are required to improve this estimate of the discrepancy between the process implementation of current models and observed thaw depths. Nonetheless, this discrepancy suggests the importance of further mechanisms of salt penetration and thaw that have not been considered – either pre-inundation or post-inundation, or both. Identification of processes to explain these thaw depths on a local scale, such as in our Laptev Sea boreholes, is essential in order to eventually apply complete models (in terms of the driving processes) for a simulation of permafrost on the entire Arctic continental shelf. Our results quantify

what is missing to understand the full picture of the transition of permafrost from onshore to offshore conditions.

Ground surface temperature histories are key parameters for initial conditions prior to inundation. This study's reconstructions from borehole temperatures at two sites in the Laptev Sea region in the Russian Arctic show rapid recent warming. Local records of paleotemperature are sparse for this region, which is underrepresented in circum-Arctic temperature reconstructions. We used two inversion methods to find the most likely temperature histories required to generate the observed temperature profiles in the boreholes. Local differences, such as later warming and warming of higher magnitude, from current circum-Arctic temperature reconstructions were shown to exist between sites. Spatial differences in past temperature trends between both sites suggest that additional records will uncover local-to-regional-scale variability. Understanding this spatial variability will depend on data on the variability of potential influences such as sea ice and snow cover. The thesis results provide a basis for local surface temperature record parameterization of climate models and permafrost models in particular. Hypothesis 3 can now be answered: Yes, the subsurface temperature field was shown to contain recoverable information about regional differences in past temperature histories. Understanding these local differences in key parameters such as the initial conditions prior to inundation is required when simulating permafrost evolution and the degradation state on the regional Arctic scale.

Thus, in each area, this thesis advanced our abilities and current understanding by:

1. Improving our ability to collect data on subsea permafrost degradation. Achieving operability of a new passive-seismic detection method in the near-shore zone of the continental Arctic shelves.
2. Assessing a suite of inundation parameters for their ability to explain observational data on the Laptev Sea shelf, by developing a model for subsea permafrost evolution coupling heat and salt transport mechanisms. Key parameters influencing the permafrost degradation were identified.
3. Providing local-to-regional differences in temperature histories in the Laptev Sea region, essential as model constraints of initial conditions in larger-scale permafrost modelling on the shelf and as prerequisite input parameter for bottom-fast sea ice implementations.

5.1 Outlook

For the subject of degradation dynamics and current state of subsea permafrost discussed in this thesis, the three identified areas are essential. These advance our understanding of subsea permafrost based on field observations as well as our theoretical understanding of the participating processes of degradation in model studies on the local and regional spatial scale. From this study's findings, the next steps necessary to gain a thorough understanding of the distribution, driving processes, and, eventually, state of degradation on the circum-Arctic scale have become apparent: For reducing the identified knowledge gaps in each area, the following research opportunities would help to elucidate (i) details of local differences in subsea permafrost thaw by widespread data collection, (ii) the ability of yet unimplemented degradation mechanisms to explain the remaining observation discrepancies, and (iii) pre-inundation conditions, and specifically, regional differences in temperature histories beyond the Laptev Sea region.

After proving operability of the new passive seismic detection method during the feasibility study in this thesis, advancing development of the geophysical system will allow for fast and effective data collection. A remotely controlled, semi-automated vehicle is currently designed and construction is taking place at the project partner of the GFZ German Research Centre for Geosciences. Based on the underwater instruments used in this thesis, the vehicle will navigate to observation points, lower the instrument to the sea floor, conduct the measurement, and hoist the instrument after successful data collection. Thus, data for a grid of observation points could be collected with minimal effort. This thesis has shown that less than 5 minutes are sufficient for robust H/V peak measurements, making rapid data collection feasible. Optimally, a continuous reference measurement is simultaneously recorded in the study area over a longer, i.e., the entire period of data collection to ensure that stable conditions prevailed in the low-frequency band, and thus to assist in interpretation of the collected rapid measurements. This rapid, semi-automated detection system would provide a means to observe local variability in subsea permafrost thaw, which could further elucidate variations in prevailing degradation mechanisms.

Accounting for further degradation processes, pre- and post-inundation, in the model would promise to resolve the cause of the currently remaining discrepancy to observations. Implementing bottom-fast sea ice explicitly is the first apparent such process. During the time period in zone 3 (Fig. 1.7), seasonally resolved seabed temperatures and brine concentration are crucial input parameters. While extremely small liquid water volumes in seabed sediments prevail at cold conditions of bottom

ad-frozen sea ice in winter, highly concentrated salt solutions may infiltrate deep into the sediments in late fall and early spring. A simplified parameterization with few parameters promises the most efficient evaluation of the opposing thermal and brine-related effects on permafrost degradation. Field observations of the onset of brine concentration, trends in the time period until initial sea bed ad-freezing, and likewise for the period after sea ice breakup in spring would be required. Furthermore, air temperature trends from borehole reconstructions such as presented in this thesis could be used, where available, to drive boundary conditions during zone 3 (compare time period of less than 2 m water depth, Fig. 3.26, and reconstructed temperature history of 225 a at Mamontov Klyk). Accounting explicitly for bottom-fast sea ice in the model will elucidate the inability of current models to explain field observations in zone 3 (C5 and, partially, C4), as well as the long-term effect on degradation beyond that zone.

The effect of thermokarst on initial conditions would be elucidated by direct observations at a coastal site where shoreline erosion has breached a thermokarst lake, and thus, inundation occurs for alas (thermokarst depression) and Yedomas cliff conditions adjacent to each other. A transect of boreholes offshore for each setting would be optimal. Still, at least two boreholes to verify sediment composition for the model and a series of geophysical thaw depths observations in the near-shore zone of each setting would be sufficient. Optimally, the initial talik depths would be determined by an onshore borehole or geophysical measurement. Thus, local short-term thaw depths could be evaluated, and compared. Furthermore, data collection of high spatial resolution covering a larger area along the coastline as well as further offshore would provide a means to distinguish between the systematic or local nature of the model discrepancy discussed in this thesis. If the local, small-scale modelling yielded better agreement with observations, then the latter would provide better understanding of the nature of the pre-formed landscape prior to inundation, specifically, if the pre-inundated landscape had been affected by widespread thermokarst degradation (corresponding to a systematic nature in the discrepancy) or if only selected points had been degraded previously (local deviations in the discrepancy).

Sea bottom temperatures are identified as one key impact factor. However, local seabed temperatures remain highly uncertain. The used temperatures for Mamontov Klyk, Buor Khaya, and Muostakh Island are the best educated guesses of these environmental conditions available at this time in the absence of direct local observations. However, a new method to yield such data from field measurements could potentially be based on temperature reconstructions from short temperature logs in the shallow seabed. The methodology will be similar to the reconstruction method described in Chap. 4. The main difference would be to collect short temperature logs of a

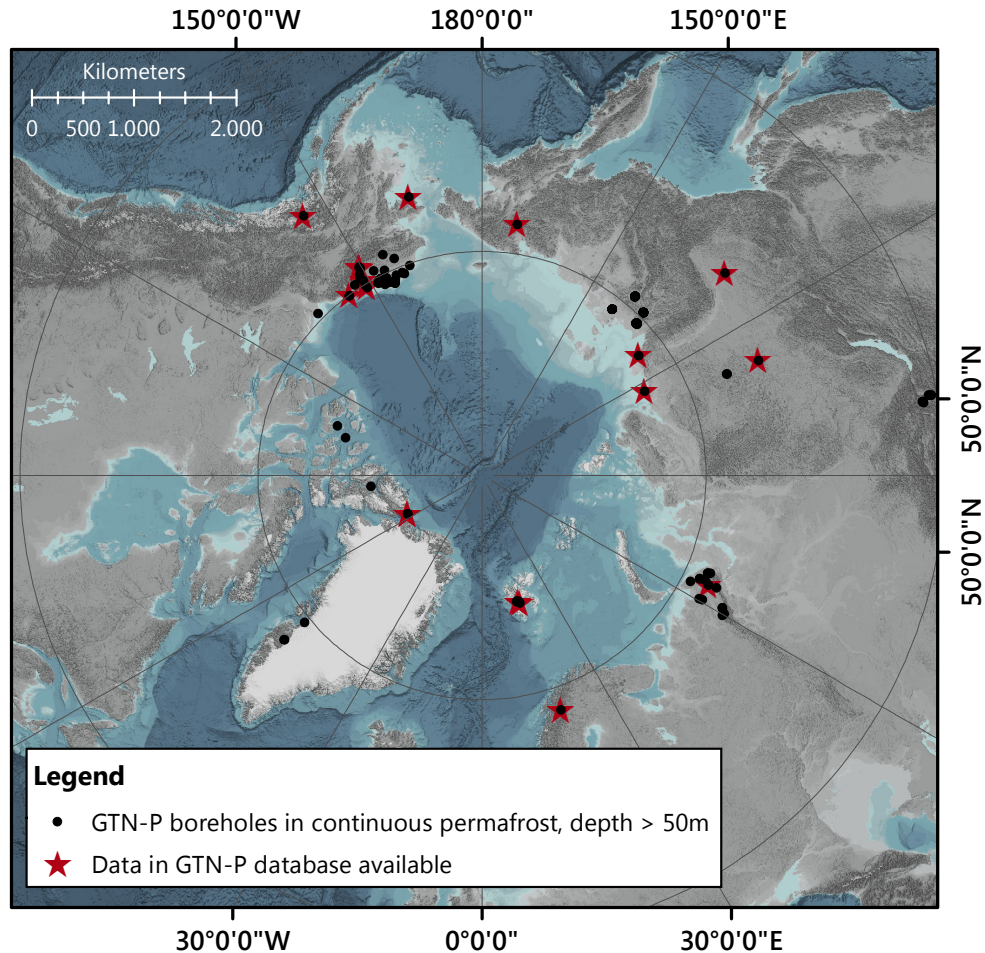


Figure 5.2: Locations of potential permafrost boreholes in the continuous permafrost zone with a depth exceeding 50 m (black dots). Red stars mark boreholes for which data is available in the GTN-P database. (Data source: Biskaborn et al. [2015])

few meters in a transect perpendicular to the coast, and reconstruct the seasonal cycle of seabed temperatures from the log. Successful application will depend on the ability of the ground model to capture thermal bottom-fast sea ice processes. Thus, even measurements collected during only one season potentially allow to reconstruct absolute temperatures for the whole annual cycle, and could be used as forcing parameters in the local subsea permafrost model.

Lastly, the Global Terrestrial Network on Permafrost (GTN-P), a network of permafrost boreholes distributed around the Arctic, could serve as basis to understand the regional differences in temperature histories. Boreholes with depths larger than about 65 m were found suitable in this thesis to reconstruct temperatures of a minimum of two centuries before present (depending also on the specific sediment composition). Figure 5.2 shows the location of GTN-P boreholes suitable to reconstructions based on their depths. Boreholes can be found spanning the entire region of the Arctic, from the Kara Sea, Laptev Sea, East Siberian Sea, Beaufort Sea to the Svalbard

Archipelago. Application of the reconstruction method, therefore, will provide a means to yield a consistent circum-Arctic picture of the regional temperature trends and their potential differences. Thus, with this knowledge as prerequisite, modelling of subsea permafrost evolution and estimation of its current state could be performed on the circum-Arctic scale. Knowledge of both – this spatial variability of initial conditions as well as a full process-understanding of degradation mechanisms – would finally bring within reach reliable mapping of the current extent and degradation state of subsea permafrost on the entire Arctic continental shelf. At last, this analysis would allow confident answers regarding the development of through-going taliks for gas migration (as presently discussed for the Laptev Sea shelf), and enable a quantitative evaluation of the vulnerability to past, present and future climate conditions, and, especially, to predicted climate change scenarios.

APPENDIX A

Modelling tests for H/V method configuration

Due to the controversy surrounding the cause of H/V peak interpretation, part of the feasibility project was to test the H/V peak response in modelling tests for our subsea configuration, which includes a third water layer and therefore may differ from the better-studied simple two layer setup of unfrozen on top of frozen sediments. This was conducted within a cooperation with the University of Potsdam and mainly contributed by Dr. M. Ohrnberger. Their results are presented/summarized here, loosely following [Overduin et al., 2015a].

To test the potential influence of the overlying water layer forward modelling of seismic sources was performed, spectral ratios calculated, and processed for H/V data. The structural model is a three-layer model consisting of a water layer of varying depth (2 to 30 m, based on the field site bathymetry), underlain by an unconsolidated soft sediment layer with variable thickness, which was underlain by ice-bonded permafrost that acts as a half space. For the forward computations the wave number integration method by Wang [1999] was used to compute seismograms for distinct subsurface models and observation distances. The modelling employed double-couple sources of arbitrary orientation located in shallow depth in the sedimentary layer to generate complete seismograms at a number of distances (200 m to 1 km). The unfrozen, unconsolidated layer was modelled with typical elastic properties for shallow marine environments [Stoll, 1977].

Figure A.1 shows the results of the modelling, indicating the main low frequency H/V peak associated with the unfrozen sediment overlying the frozen layer, clearly separated from several higher frequency peaks which represent higher modes and water column reverberations. Peak frequencies determined from model results (grey vertical lines) containing the full wave field response and the $\lambda/4$ calculations (red lines) for pure vertical incident SH-reverberations in the unfrozen sediment layer

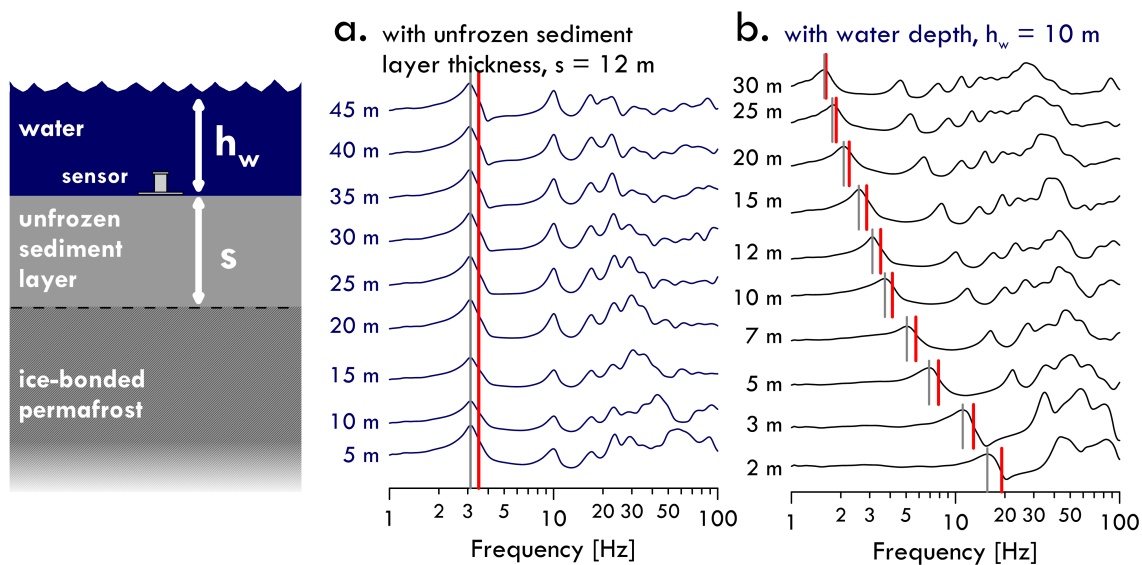


Figure A.1: Modelled H/V intensity (grey lines mark the f_0 peaks) vs. frequency for (a) constant thickness of the unfrozen sediment layer (12 m) and varying water depths, and (b) varying unfrozen sediment layer thicknesses and 10 m water depth. Red lines indicate the $\lambda/4$ resonance frequency. Adapted from [Overduin et al., 2015a].

show a systematically varying offset of not more than 20% which allows use of the $\lambda/4$ estimate as a first order proxy measure of sediment thickness. A decrease in the thickness of the unfrozen layer from 30 to 2 m beneath a constant water depth of 10 m results in a change in peak H/V frequency from approximately 1.5 to 20 Hz.

Bibliography

- Alhumaizi, Khalid. Flux-limiting solution techniques for simulation of reaction-diffusion-convection system. *Communications in Nonlinear Science and Numerical Simulation*, 12 (6):953–965, 2007. doi:10.1016/j.cnsns.2005.11.005. (cited on pages 85, 86, and 87)
- Andreev, Andrei; Tarasov, Pavel; Schwamborn, Georg; Ilyashuk, Boris; Ilyashuk, Elena; Bobrov, Anatoly; Klimanov, Vladimir; Rachold, Volker and Hubberten, Hans-Wolfgang. Holocene paleoenvironmental records from Nikolay Lake, Lena River Delta, Arctic Russia. *Palaeogeography, Palaeoclimatology, Palaeoecology*, 209:197–217, 2004. doi:10.1016/j.palaeo.2004.02.010. (cited on page 136)
- Andreev, Andrei A.; Schirrmeister, Lutz; Tarasov, Pavel E.; Ganopolski, Andrey; Brovkin, Viktor; Siegert, Christine; Wetterich, Sebastian and Hubberten, Hans-Wolfgang. Vegetation and climate history in the Laptev Sea region (Arctic Siberia) during Late Quaternary inferred from pollen records. *Quaternary Science Reviews*, 30:2182–2199, 2011. doi:10.1016/j.quascirev.2010.12.026. (cited on page 143)
- Arai, Hiroshi and Tokimatsu, Kohji. S-Wave Velocity Profiling by Inversion of Microtremor H/V Spectrum. *Bulletin of the Seismological Society of America*, 94(1):53–63, 2004. doi:10.1785/0120030028. (cited on page 31)
- Arai, Hiroshi and Tokimatsu, Kohji. S-Wave Velocity Profiling by Joint Inversion of Microtremor Dispersion Curve and Horizontal-to-Vertical (H/V) Spectrum. *Bulletin of the Seismological Society of America*, 95(5):1766–1778, 2005. doi:10.1785/0120040243. (cited on page 32)
- Arctic Climate Impact Assessment (ACIA). *Impacts of a Warming Arctic: Arctic Climate Impact Assessment*. Cambridge University Press, Cambridge, 2004. (cited on pages 12 and 14)
- Arctic Coastal Dynamics Project Team. The Arctic Coastal Dynamics (ACD) Circumpolar Coastal Classification, 2008. (cited on page 70)
- Are, F. E. Shoreface of the Arctic seas - a natural laboratory for subsea permafrost dynamics. In: Phillips, M.; Springman, S.M. and Arenson, L.U.(eds.), *Proceedings of the 8th International Conference on Permafrost, Zurich, Switzerland*, pages 27–32. Swets & Zeitlinger, Lisse, 2003. (cited on pages 13, 15, 43, 65, 66, and 68)
- Are, Feliks and Reimnitz, Erk. An Overview of the Lena River Delta Setting: Geology, Tectonics, Geomorphology, and Hydrology. *Journal of Coastal Research*, 16(4):1083–1093, 2000. URL <http://www.jstor.org/stable/4300125>. (cited on page 144)
- Are, Felix E.; Reimnitz, Erk and Kassens, Heidemarie. Cryogenic Processes of Arctic Land-Ocean Interactions. *Polarforschung*, 68:207–214, 2000. (cited on page 7)

- Atakan, Kuwet and Havskov, Lens. Local site effects in the northern North Sea based on single-station spectral ratios of OBS recordings. *Terra Nova*, 8(1):22–33, 1996. doi:10.1111/j.1365-3121.1996.tb00722.x. (cited on page 52)
- Atlas Arktiki. (*in Russian*). GUGK, Moscow, 1985. (cited on page 143)
- Badache, Messaoud; Eslami-Nejad, Parham; Ouzzane, Mohamed; Aidoun, Zine and Lamarche, Louis. A new modeling approach for improved ground temperature profile determination. *Renewable Energy*, 85:436–444, 2016. doi:10.1016/j.renene.2015.06.020. (cited on page 156)
- Baker, G and Osterkamp, T. Implications of salt fingering processes for salt movement in thawed coarse-grained subsea permafrost. *Cold Regions Science and Technology*, 15:45–52, February 1988. URL <http://linkinghub.elsevier.com/retrieve/pii/0165232X88900377>. (cited on page 65)
- Bakulin, Andrey and Calvert, Rodney. Virtual source: new method for imaging and 4D below complex overburden. In *2004 SEG Annual Meeting, October 10–15, 2004, Denver, Colorado*, pages 2477–2480. Society of Exploration Geophysicists, 2004. URL <http://link.aip.org/link/SEGEAB/v23/i1/p2477/s1&Agg=doi>. (cited on page 33)
- Balobaev, Veniamin Tikhonovich. Heat exchange between permafrost and the atmosphere in the presence of a vegetation cover. *NRC Technical Translation*, 1670, 1973. (cited on page 142)
- Bard, Pierre-Yves and SESAME participants. The SESAME project: an overview and main results. In *Proc. of 13th World Conf. on Earthquake Engineering, Vancouver, BC, Canada*, August 2004. Paper No. 2207. (cited on pages 27 and 31)
- Barrett, B. E.; Nicholls, K. W.; Murray, T.; Smith, A. M. and Vaughan, D. G. Rapid recent warming on Rutford Ice Stream, West Antarctica, from borehole thermometry. *Geophysical Research Letters*, 36(2):L02708, 2009. doi:10.1029/2008GL036369. (cited on page 141)
- Bartlett, Marshall G.; Chapman, David S. and Harris, Robert N. Snow and the ground temperature record of climate change. *Journal of Geophysical Research: Earth Surface*, 109(F4):F04008, 2004. doi:10.1029/2004JF000224. (cited on page 142)
- Bauch, H.A; Mueller-Lupp, T; Taldenkova, E; Spielhagen, R.F; Kassens, H; Grootes, P.M; Thiede, J; Heinemeier, J and Petryashov, V.V. Chronology of the Holocene transgression at the North Siberian margin. *Global and Planetary Change*, 31:125–139, 2001. doi:10.1016/S0921-8181(01)00116-3. (cited on page 2)
- Beck, A.E.; Shen, P.Y.; Beltrami, H.; Mareschal, J.-C.; Safanda, J.; Sebagenzi, M.N.; Vasseur, G. and Wang, K. A comparison of five different analyses in the interpretation of five borehole temperature data sets. *Palaeogeography, Palaeoclimatology, Palaeoecology*, 98(2):101–112, 1992. doi:10.1016/0031-0182(92)90191-7. (cited on page 141)
- Beltrami, Hugo. Climate from borehole data: Energy fluxes and temperatures since 1500. *Geophysical Research Letters*, 29(23):26–1–26–4, 2002. doi:10.1029/2002GL015702. 2111. (cited on page 141)
- Beltrami, Hugo; Ferguson, Grant and Harris, Robert N. Long-term tracking of climate change by underground temperatures. *Geophysical Research Letters*, 32(19):L19707, 2005. doi:10.1029/2005GL023714. (cited on pages 142 and 169)

- Bensen, G. D.; Ritzwoller, M. H.; Barmin, M. P.; Levshin, A. L.; Lin, F.; Moschetti, M. P.; Shapiro, N. M. and Yang, Y. Processing seismic ambient noise data to obtain reliable broad-band surface wave dispersion measurements. *Geophysical Journal International*, 169(3):1239–1260, 2007. doi:10.1111/j.1365-246X.2007.03374.x. (cited on pages 39 and 48)
- Bergmann, Uwe. *Interpretation of digital Parasound echosounder records of the eastern Arctic Ocean on the basis of sediment physical properties = Interpretation digitaler Parasound Echolotaufzeichnungen im östliche Arktischen Ozean auf der Grundlage physikalischer Sedimenteigenschaften*, volume 183 of *Berichte zur Polar- und Meeresforschung (Reports on Polar and Marine Research)*. Alfred Wegener Institute for Polar and Marine Research, Bremerhaven, Germany, 1996. (cited on page 25)
- Biskaborn, B. K.; Lanckman, J.-P.; Lantuit, H.; Elger, K.; Streletskiy, D. A.; Cable, W. L. and Romanovsky, V. E. The new database of the Global Terrestrial Network for Permafrost (GTN-P). *Earth System Science Data*, 7(2):245–259, 2015. doi:10.5194/essd-7-245-2015. (cited on page 181)
- Blasco, S. Origin and engineering implications of deep ice-bearing permafrost, Canadian Beaufort Shelf. Technical report, Geological Survey of Canada, Open File Report 3058, 1995. (cited on pages 4, 5, 89, 99, 116, and 128)
- Blasco, S.; Bennett, R.; Brent, T.; Burton, M.; Campbell, P.; Carr, E.; Covill, R.; Dallimore, S.; Davies, E.; Hughes-Clarke, J.; Issler, D.; Leonard, L.; MacKillop, K.; Mazzotti, S.; Patton, E.; Rogers, G.; Shearer, J. and White, M. 2010 State of Knowledge: Beaufort Sea Seabed Geohazards Associated with Offshore Hydrocarbon Development. Technical report, Geological Survey of Canada, Open File Report 6989, 2011. (cited on page 6)
- Boike, J.; Kattenstroth, B.; Abramova, K.; Bornemann, N.; Chetverova, A.; Fedorova, I.; Fröb, K.; Grigoriev, M.; Grüber, M.; Kutzbach, L.; Langer, M.; Minke, M.; Muster, S.; Piel, K.; Pfeiffer, E.-M.; Stoof, G.; Westermann, S.; Wischniewski, K.; Wille, C. and Hubberten, H.-W. Baseline characteristics of climate, permafrost and land cover from a new permafrost observatory in the Lena River Delta, Siberia (1998–2011). *Biogeosciences*, 10(3):2105–2128, 2013. doi:10.5194/bg-10-2105-2013. (cited on page 145)
- Boike, Julia; Grau, Thomas; Heim, Birgit; Günther, Frank; Langer, Moritz; Muster, Sina; Gouttevin, Isabelle and Lange, Stephan. Satellite-derived changes in the permafrost landscape of central Yakutia, 2000–2011: Wetting, drying, and fires. *Global and Planetary Change*, 139:116–127, 2016. doi:10.1016/j.gloplacha.2016.01.001. (cited on pages 7 and 172)
- Bonnefoy-Claudet, Sylvette; Cornou, Cecile; Bard, Pierre-Yves; Cotton, Fabrice; Moczo, Peter; Kristek, Jozef and Fäh, Donat. H/V ratio: a tool for site effects evaluation. Results from 1-D noise simulations. *Geophysical Journal International*, 167(2):827–837, 2006a. doi:10.1111/j.1365-246X.2006.03154.x. (cited on pages 28, 30, and 31)
- Bonnefoy-Claudet, Sylvette; Cotton, Fabrice and Bard, Pierre-Yves. The nature of noise wavefield and its applications for site effects studies: A literature review. *Earth-Science Reviews*, 79(3):205–227, 2006b. doi:10.1016/j.earscirev.2006.07.004. (cited on pages 28 and 31)
- Bonnefoy-Claudet, Sylvette; Köhler, Andreas; Cornou, Cécile; Wathelet, Marc and Bard, Pierre-Yves. Effects of Love Waves on Microtremor H/V Ratio. *Bulletin of the Seismological Society of America*, 98(1):288–300, 2008. doi:10.1785/0120070063. (cited on pages 30 and 32)

- Boore, David M. and Smith, Charles E. Analysis of earthquake recordings obtained from the Seafloor Earthquake Measurement System (SEMS) instruments deployed off the coast of southern California. *Bulletin of the Seismological Society of America*, 89(1):260–274, 1999. URL <https://pubs.geoscienceworld.org/ssa/bssa/article-abstract/89/1/260/120449/analysis-of-earthquake-recordings-obtained-from>. (cited on page 52)
- Boudreau, Bernard P. *Diagenetic Models and Their Implementation - Modelling Transport and Reactions in Aquatic Sediments*. Springer Berlin / Heidelberg, 1997. (cited on pages 86, 101, and 117)
- Brenguier, F.; Campillo, M.; Hadziioannou, C.; Shapiro, N. M.; Nadeau, R. M. and Larose, E. Postseismic Relaxation Along the San Andreas Fault at Parkfield from Continuous Seismological Observations. *Science*, 321(5895):1478–1481, 2008a. ISSN 0036-8075. doi:10.1126/science.1160943. URL <http://science.sciencemag.org/content/321/5895/1478>. (cited on page 40)
- Brenguier, Florent; Shapiro, Nikolai M.; Campillo, Michel; Ferrazzini, Valerie; Duputel, Zacharie; Coutant, Olivier and Nercessian, Alexandre. Towards forecasting volcanic eruptions using seismic noise. *Nature Geoscience*, 1:126–130, 2008b. doi:10.1038/ngeo104. (cited on page 40)
- Brenguier, Florent; Clarke, Daniel; Aoki, Yosuke; Shapiro, Nikolai M.; Campillo, Michel and Ferrazzini, Valerie. Monitoring volcanoes using seismic noise correlations. *Comptes Rendus Geoscience*, 343(8):633–638, 2011. doi:10.1016/j.crte.2010.12.010. (cited on page 40)
- Briffa, Keith R.; Osborn, Timothy J.; Schweingruber, Fritz H.; Harris, Ian C.; Jones, Philip D.; Shiyatov, Stepan G. and Vaganov, Eugene A. Low-frequency temperature variations from a northern tree ring density network. *J. Geophys. Res.*, 106(D3):2929–2941, 2001. doi:10.1029/2000JD900617. (cited on page 133)
- Briffa, Keith R.; Shishov, Vladimir V.; Melvin, Thomas M.; Vaganov, Eugene A.; Grudd, Haken; Hantemirov, Rashit M.; Eronen, Matti and Naurzbaev, Muktar M. Trends in recent temperature and radial tree growth spanning 2000 years across northwest Eurasia. *Philosophical Transactions of the Royal Society B: Biological Sciences*, 363(1501):2271–2284, 2007. doi:10.1098/rstb.2007.2199. (cited on page 135)
- Brooks, Laura A. and Gerstoft, Peter. Ocean acoustic interferometry. *The Journal of the Acoustical Society of America*, 121(6):3377–3385, 2007. doi:10.1121/1.2723650. (cited on page 40)
- Brothers, Laura L.; Hart, Patrick E. and Ruppel, Carolyn D. Minimum distribution of sub-sea ice-bearing permafrost on the U.S. Beaufort Sea continental shelf. *Geophys. Res. Lett.*, 39(15):L15501, 2012. doi:10.1029/2012GL052222. (cited on pages 6, 23, 24, 27, and 80)
- Brothers, Laura L.; Herman, Bruce M.; Hart, Patrick E. and Ruppel, Carolyn D. Subsea ice-bearing permafrost on the U.S. Beaufort Margin: 1. Minimum seaward extent defined from multichannel seismic reflection data. *Geochemistry, Geophysics, Geosystems*, 17(11):4354–4365, 2016. doi:10.1002/2016GC006584. (cited on pages 6 and 23)
- Brown, J.; O.J. Ferrians, Jr.; Heginbottom, J.A. and E.S. Melnikov, eds. *Circum-Arctic map of permafrost and ground-ice conditions*. Circum-Pacific Map Series CP-45, scale 1:10,000,000. Washington, DC: U.S. Geological Survey in Cooperation with the Circum-Pacific Council for Energy and Mineral Resources, 1997. (cited on page 2)

- Brown, Ross D. and Brasnett, Bruce. Canadian Meteorological Centre (CMC) Daily Snow Depth Analysis Data. Environment Canada, 2010. Boulder, Colorado USA: National Snow and Ice Data Center, 2015, updated annually. URL https://nsidc.org/data/docs/daac/nsidc0447_CMC_snow_depth/. (cited on page 169)
- Budu, Paula. Stability results for convection in thawing subsea permafrost. *Continuum Mechanics and Thermodynamics*, 13(4):269–285, 2001. doi:10.1007/s001610100050. (cited on page 65)
- Bulygina, O. N. and Razuvaev, V. N. Daily Temperature and Precipitation Data for 518 Russian Meteorological Stations. Technical report, Carbon Dioxide Information Analysis Center, Oak Ridge National Laboratory, U.S. Department of Energy, Oak Ridge, Tennessee, 2012. (cited on page 165)
- Bussat, Sascha and Kugler, Simone. Offshore ambient-noise surface-wave tomography above 0.1 Hz and its applications. *The Leading Edge*, 30(5):514–524, 2011. doi:10.1190/1.3589107. (cited on page 52)
- Campbell, G. S.; Jungbauer Jr, J. D.; Bidlake, W. R. and Hungerford, R. D. Predicting the effect of temperature on soil thermal conductivity. *Soil Science*, 158(5):307–313, 1994. (cited on page 74)
- Campillo, Michel and Paul, Anne. Long-Range Correlations in the Diffuse Seismic Coda. *Science*, 299(5606):547–549, 2003. URL <http://www.sciencemag.org/content/299/5606/547.abstract>. (cited on pages 33 and 39)
- Carson, Chris J.; McLaren, Sandra; Roberts, Jason L.; Boger, Steven D. and Blankenship, Donald D. Hot rocks in a cold place: high sub-glacial heat flow in East Antarctica. *Journal of the Geological Society*, 171(1):9–12, 2014. doi:10.1144/jgs2013-030. (cited on page 168)
- CAVM Team. Circumpolar Arctic Vegetation Map (1:7,500,000 scale). Conservation of Arctic Flora and Fauna (CAFF) Map No. 1. U.S. Fish and Wildlife Service, Anchorage, Alaska, 2003. URL <http://www.geobotany.uaf.edu/cavm/finalcavm/index.html>. (cited on page 143)
- Chapman, David S.; Bartlett, Marshall G. and Harris, Robert N. Comment on "Ground vs. surface air temperature trends: Implications for borehole surface temperature reconstructions" by M. E. Mann and G. Schmidt. *Geophysical Research Letters*, 31(7):L07205, 2004. doi:10.1029/2003GL019054. (cited on pages 142 and 169)
- Charkin, A. N.; Rutgers van der Loeff, M.; Shakhova, N. E.; Gustafsson, Ö.; Dudarev, O. V.; Cherepnev, M. S.; Salyuk, A. N.; Koshurnikov, A. V.; Spivak, E. A.; Gunar, A. Y.; Ruban, A. S. and Semiletov, I. P. Discovery and characterization of submarine groundwater discharge in the Siberian Arctic seas: a case study in the Buor-Khaya Gulf, Laptev Sea. *The Cryosphere*, 11(5):2305–2327, 2017. doi:10.5194/tc-11-2305-2017. (cited on page 93)
- Chatelain, Jean-Luc; Guillier, Bertrand; Cara, Fabrizio; Duval, Anne-Marie; Atakan, Kuvvet; Bard, Pierre-Yves and The WP02 SESAME team. Evaluation of the influence of experimental conditions on H/V results from ambient noise recordings. *Bulletin of Earthquake Engineering*, 6(1):33–74, Feb 2008. doi:10.1007/s10518-007-9040-7. (cited on page 31)
- Claerbout, Jon F. Synthesis of a layered medium from its acoustic transmission response. *Geophysics*, 33(2):264–269, 1968. doi:10.1190/1.1439927. (cited on page 33)

- Clow, Gary D. The extent of temporal smearing in surface-temperature histories derived from borehole temperature measurements. *Global and Planetary Change*, 6:81–86, December 1992. doi:10.1016/0921-8181(92)90027-8. (cited on pages 140 and 151)
- Cohen, Judah. An observational analysis: Tropical relative to Arctic influence on midlatitude weather in the era of Arctic amplification. *Geophysical Research Letters*, 43(10): 5287–5294, 2016. doi:10.1002/2016GL069102. (cited on page 8)
- Collett, Timothy S.; Lee, Myung W.; Avena, Warren F.; Miller, John J.; Lewis, Kristen A.; Zyrianova, Margarita V.; Boswell, Ray and Inks, Tanya L. Permafrost-associated natural gas hydrate occurrences on the Alaska North Slope. *Marine and Petroleum Geology*, 28(2):279–294, 2011. doi:http://dx.doi.org/10.1016/j.marpetgeo.2009.12.001. (cited on page 9)
- Committee on Surface Temperature Reconstructions for the Last 2,000 Years, National Research Council. *Surface Temperature Reconstructions for the Last 2,000 Years*. The National Academies Press, Washington, DC, 2006. ISBN 978-0-309-10225-4. doi:10.17226/11676. (cited on page 140)
- Crowley, Thomas J. Causes of Climate Change Over the Past 1000 Years. *Science*, 289 (5477):270–277, 2000. doi:10.1126/science.289.5477.270. (cited on page 133)
- Cuffey, Kurt M. and Clow, Gary D. Temperature, accumulation, and ice sheet elevation in central Greenland through the last deglacial transition. *Journal of Geophysical Research: Oceans*, 102(C12):26383–26396, 1997. doi:10.1029/96JC03981. (cited on page 141)
- Cuffey, Kurt M.; Clow, Gary D.; Alley, Richard B.; Stuiver, Minze; Waddington, Edwin D. and Saltus, Richard W. Large Arctic Temperature Change at the Wisconsin-Holocene Glacial Transition. *Science*, 270(5235):455–458, 1995. doi:10.1126/science.270.5235.455. (cited on page 141)
- Curtis, Andrew; Gerstoft, Peter; Sato, Haruo; Snieder, Roel and Wapenaar, Kees. Seismic interferometry - turning noise into signal. *The Leading Edge*, 25(9):1082–1082, 2006. doi:10.1190/1.2349814. (cited on pages 33, 39, and 40)
- Dahl-Jensen, D.; Mosegaard, K.; Gundestrup, N.; Clow, G. D.; Johnsen, S. J.; Hansen, A. W. and Balling, N. Past Temperatures Directly from the Greenland Ice Sheet. *Science*, 282(5387):268–271, 1998. doi:10.1126/science.282.5387.268. (cited on page 141)
- Dahl-Jensen, Dorthe; Morgan, Vin I. and Elcheikh, Alan. Monte Carlo inverse modelling of the Law Dome (Antarctica) temperature profile. *Annals of Glaciology*, 29(1):145–150, 1999. doi:10.3189/172756499781821102. (cited on page 141)
- Davies, J. Huw. Global map of solid Earth surface heat flow. *Geochemistry, Geophysics, Geosystems*, 14(10):4608–4622, 2013. doi:10.1002/ggge.20271. (cited on page 168)
- de Vries, D. The thermal conductivity of granular materials. *Annexe Bul. Inst. Intern. du Froid*, 1992:115–131, 1952. (cited on page 74)
- de Vries, D.A. The thermal properties of soils. In: van Wijk, R.W.(ed.), *Physics of Plant Environment*, pages 210–235. North Holland, Amsterdam, 1963. (cited on pages 74, 90, and 148)
- Delisle, G. Temporal variability of subsea Permafrost and gas hydrate occurrences as function of climate change in the Laptev Sea, Siberia. *Polarforschung*, 68:221–225, 2000. (cited on pages 6 and 62)

- Demezhko, D. Y. and Gornostaeva, A. A. Late Pleistocene-Holocene ground surface heat flux changes reconstructed from borehole temperature data (the Urals, Russia). *Climate of the Past*, 11(4):647–652, 2015. doi:10.5194/cp-11-647-2015. (cited on pages 151 and 164)
- Demezhko, D. Yu. and Solomina, O. N. Ground surface temperature variations on Kunashir Island in the last 400 years inferred from borehole temperature data and tree-ring records. *Doklady Earth Sciences*, 426(1):628–631, 2009. doi:10.1134/S1028334X09040266. (cited on page 172)
- Demezhko, Dmitry Yu. and Shchapov, Vladislav A. 80,000 years ground surface temperature history inferred from the temperature-depth log measured in the superdeep hole SG-4 (the Urals, Russia). *Global and Planetary Change*, 29:219–230, 2001. doi:10.1016/S0921-8181(01)00091-1. (cited on pages 151 and 152)
- Dmitrenko, Igor A.; Kirillov, Sergey A.; Tremblay, L. Bruno; Kassens, Heidemarie; Anisimov, Oleg A.; Lavrov, Sergey A.; Razumov, Sergey O. and Grigoriev, Mikhail N. Recent changes in shelf hydrography in the Siberian Arctic: Potential for subsea permafrost instability. *Journal of Geophysical Research*, 116(C10):C10027, 2011. doi:10.1029/2011JC007218. (cited on pages 64 and 119)
- DOE. *Handbook of methods for the analysis of the various parameters of the carbon dioxide system in sea water, version 2*. ORNL/CDIAC-74, 1994. (cited on page 82)
- Dong, Hefeng and Hovem, Jens M. Interface waves. In: Vila, R. P.(ed.), *Waves in fluids and solids*, pages 153–176. InTech, 2011. (cited on pages 29, 51, and 55)
- Drachev, S. S.; Kaul, N. and Beliaev, V. N. Eurasia spreading basin to Laptev Shelf transition: structural pattern and heat flow. *Geophysical Journal International*, 152(3): 688–698, 2003. doi:10.1046/j.1365-246X.2003.01882.x. (cited on page 7)
- Drachev, Sergei S.; Savostin, Leonid A.; Groshev, Victor G. and Bruni, Inna E. Structure and geology of the continental shelf of the Laptev Sea, Eastern Russian Arctic. *Tectonophysics*, 298(4):357–393, 1998. doi:10.1016/S0040-1951(98)00159-0. (cited on page 45)
- Draganov, Deyan; Wapenaar, Kees; Mulder, Wim; Singer, Johannes and Verdel, Arie. Retrieval of reflections from seismic background-noise measurements. *Geophysical Research Letters*, 34(4):L04305, 2007. doi:10.1029/2006GL028735. (cited on page 33)
- Draganov, Deyan; Campman, Xander; Thorbecke, Jan; Verdel, Arie and Wapenaar, Kees. Reflection images from ambient seismic noise. *Geophysics*, 74(5):A63–A67, 2009. doi:10.1190/1.3193529. (cited on pages 33 and 40)
- Dravinski, M. and G. Ding, K.-L. Wen. Analysis of spectral ratios for estimating ground motion in deep basins. *Bulletin of the Seismological Society of America*, 86(3):646–654, 1996. URL <http://bssa.geoscienceworld.org/content/84/5/1350/article-info>. (cited on page 30)
- Ducellier, Ariane; Kawase, Hiroshi and Matsushima, Shinichi. Validation of a New Velocity Structure Inversion Method Based on Horizontal-to-Vertical (H/V) Spectral Ratios of Earthquake Motions in the Tohoku Area, Japan. *Bulletin of the Seismological Society of America*, 103(2A):958–970, 2013. doi:10.1785/0120120214. (cited on pages 31 and 33)
- Dullemond, C.P. and Springel, V. *Numerical Fluid Dynamics Lecture Notes*. Institute of Environmental Physics, Heidelberg University, 2012. URL http://www.ita.uni-heidelberg.de/~dullemond/lectures/num_fluid_2011/index.shtml. (cited on pages 85, 86, and 87)

- Dunaev, N.N. and Nikiforov, S.L. Shelf i berega arkticheskikh morei (Shelf and coasts of arctic seas). In: Aibulatov, N.A.(ed.), *Geoekologiya shelfa i beregov morei Rossii (Geoecology of shelf and coasts of Russian seas)*, chapter 2, pages 27–242. Noosphera, Moscow, 2001. (cited on page 71)
- Dziewonski, A.; Bloch, S. and Landisman, M. A technique for the analysis of transient seismic signals. *Bulletin of the Seismological Society of America*, 59(1):427–444, 1969. URL <https://pubs.geoscienceworld.org/ssa/bssa/article-abstract/59/1/427/101646/a-technique-for-the-analysis-of-transient-seismic>. (cited on page 49)
- Ebbesen, S.; Kiwitz, P. and Guzzella, L. A generic particle swarm optimization Matlab function. In *American Control Conference (ACC), 2012*, pages 1519–1524, 2012. (cited on page 153)
- Ehlers, Jürgen and Gibbard, Philip L. Extent and chronology of glaciations. *Quaternary Science Reviews*, 22(15–17):1561–1568, 2003. doi:10.1016/S0277-3791(03)00130-6. (cited on page 1)
- Endrun, Brigitte. Love wave contribution to the ambient vibration H/V amplitude peak observed with array measurements. *Journal of Seismology*, 15(3):443–472, 2011. doi:10.1007/s10950-010-9191-x. (cited on pages 28, 30, and 31)
- Eppelbaum, Lev; Kutasov, Izzy and Pilchin, Arkady. *Thermal Properties of Rocks and Density of Fluids*, pages 99–149. Springer Berlin Heidelberg, Berlin, Heidelberg, 2014. ISBN 978-3-642-34023-9. doi:10.1007/978-3-642-34023-9_2. (cited on page 148)
- Esper, Jan; Cook, Edward R. and Schweingruber, Fritz H. Low-Frequency Signals in Long Tree-Ring Chronologies for Reconstructing Past Temperature Variability. *Science*, 295(5563):2250–2253, 2002. doi:10.1126/science.1066208. (cited on page 133)
- Fäh, D.; Kind, F. and Giardini, D. Inversion of local S-wave velocity structures from average H/V ratios, and their use for the estimation of site-effects. *Journal of Seismology*, 7(4): 449–467, 2003. doi:10.1023/B:JOSE.0000005712.86058.42. (cited on pages 31 and 32)
- Fäh, Donat; Kind, Fortunat and Giardini, Domenico. A theoretical investigation of average H/V ratios. *Geophysical Journal International*, 145(2):535–549, 2001. doi:10.1046/j.0956-540x.2001.01406.x. (cited on page 30)
- Fleming, Kevin; Johnston, Paul; Zwartz, Dan; Yokoyama, Yusuke; Lambeck, Kurt and Chappell, John. Refining the eustatic sea-level curve since the Last Glacial Maximum using far- and intermediate-field sites. *Earth and Planetary Science Letters*, 163(1): 327–342, 1998. doi:10.1016/S0012-821X(98)00198-8. (cited on page 3)
- Forbes, D. L.; Manson, G. K.; Whalen, D. J. R.; Couture, N. J. and Hill, P. R. Coastal products of marine transgression in cold-temperate and high-latitude coastal-plain settings: Gulf of St Lawrence and Beaufort Sea. *Geological Society, London, Special Publications*, 388(1):131–163, 2014. doi:10.1144/SP388.18. (cited on page 128)
- Forghani, F. and Snieder, R. Underestimation of body waves and feasibility of surface-wave reconstruction by seismic interferometry. *The Leading Edge*, 29(7):790–794, 2010. doi:10.1190/1.3462779. (cited on page 39)
- Foti, Sebastiano; Parolai, Stefano; Albarello, Dario and Picozzi, Matteo. Application of Surface-Wave Methods for Seismic Site Characterization. *Surveys in Geophysics*, 32(6): 777–825, 2011. doi:10.1007/s10712-011-9134-2. (cited on page 31)

- Frederick, J. M. and Buffett, B. A. Taliks in relict submarine permafrost and methane hydrate deposits: Pathways for gas escape under present and future conditions. *Journal of Geophysical Research: Earth Surface*, 119(2):106–122, 2014. doi:10.1002/2013JF002987. (cited on page 6)
- Frederick, J. M. and Buffett, B. A. Effects of submarine groundwater discharge on the present-day extent of relict submarine permafrost and gas hydrate stability on the Beaufort Sea continental shelf. *Journal of Geophysical Research: Earth Surface*, 120(3): 417–432, 2015. doi:10.1002/2014JF003349. (cited on page 86)
- French, Hugh M. *The periglacial environment*. John Wiley & Sons, March 2007. (cited on page 4)
- Frenzel, B; Pecs, M and Velichko, A. *Atlas of Paleoclimates and Paleoenvironments of the Northern Hemisphere: Late Pleistocene–Holocene*. Gustav Fischer, Stuttgart, 1992. (cited on page 12)
- Frontera, Tanit; Ugalde, Arantza; Olivera, Carme; Jara, Jose Antonio and Goula, Xavier. Seismic Ambient Noise Characterization of a New Permanent Broadband Ocean Bottom Seismometer Site offshore Catalonia (Northeastern Iberian Peninsula). *Seismological Research Letters*, 81(5):740–749, 2010. doi:10.1785/gssrl.81.5.740. (cited on page 52)
- Fütterer, Dieter K and Niessen, Frank. Profile of sediment echo sounding during POLARSTERN cruise ARK-IX/4 with links to ParaSound data files, 2004. URL <https://doi.org/10.1594/PANGAEA.206530>. (cited on page 25)
- Galabala, R. O. New data on the structure of the Lena Delta (in Russian). In *Chetvertichnyi period Severo-Vostoka Azii*, pages 152–171. Magadan, SVKNII DVO AN SSSR, 1987. (cited on page 144)
- Galdi, G. P.; Payne, L. E.; Proctor, M. R. E. and Straughan, B. Convection in Thawing Subsea Permafrost. *Proceedings of the Royal Society of London. A. Mathematical and Physical Sciences*, 414(1846):83–102, 1987. doi:10.1098/rspa.1987.0134. (cited on page 65)
- Garcia-Garcia, A; Cuesta-Valero, F J; Beltrami, H and Smerdon, J E. Simulation of air and ground temperatures in PMIP3/CMIP5 last millennium simulations: implications for climate reconstructions from borehole temperature profiles. *Environmental Research Letters*, 11(4):044022, 2016. doi:10.1088/1748-9326/11/4/044022. (cited on page 142)
- Gebrande, H. and Miller, H. Refraktionsseismik. In: Bender, F.(ed.), *Angewandte Geowissenschaften Band II*, pages 226–260. Ferdinand Enke Verlag, Stuttgart, 1985. (cited on page 24)
- Golub, G. and Loan, C. V. *Matrix Computations*. The Johns Hopkins University Press, Baltimore, 2nd edition, 1990. (cited on page 163)
- Gonzalez-Rouco, J. F.; Beltrami, H.; Zorita, E. and von Storch, H. Simulation and inversion of borehole temperature profiles in surrogate climates: Spatial distribution and surface coupling. *Geophysical Research Letters*, 33(1):L01703, 2006. doi:10.1029/2005GL024693. (cited on page 142)
- Gosink, J. P. and Baker, G. C. Salt Fingering in Subsea Permafrost: Some Stability and Energy Considerations. *J. Geophys. Res.*, 95(C6):9575–9583, 1990. doi:10.1029/JC095iC06p09575. (cited on pages 65, 89, and 121)

- Grakhanov, S.A.; Prokopiev, A.V.; Grakhanov, O.S.; Tarabukin, V.P. and Soloviev, E.E. New data on the geology of the Lena River delta area and the diamond potential of the Arctic region (in Russian). *Fatherland Geologia*, 5:33–40, 2013. (cited on pages 144 and 145)
- Grigoriev, M. N. *Kriomorphogenez i litodinamika pribrezhno-shelfovoi zony morei Vostochnoi Sibiri (Cryomorphogenesis and Lithodynamics of the East Siberian Near-Shore Shelf Zone) [in Russian]*. Habilitation thesis, Russian Academy of Sciences, Siberian Branch, Permafrost Institute Yakutsk, 2008. (cited on page 70)
- Grigoriev, Mikhail N. and Rachold, Volker. The degradation of coastal permafrost and the organic carbon balance of the Laptev and East Siberian seas Permafrost. In *Proceedings of the 8th International Conference on Permafrost, 21-25 July 2003, Zurich, Switzerland*, pages 319–324. Balkema, Lisse, The Netherlands, 2003. (cited on page 70)
- Grigoriev, M.N. *Cryomorphogenesis of the Lena River mouth area (in Russian)*. Permafrost Institute Press SB RAS, Yakutsk, 1993. (cited on pages 71 and 144)
- Grigoriev, M.N.; Imaev, V.S.; Imaeva, L.P.; Kozmin, B.M.; Kunitsky, V.V.; Larionov, A.G.; Mikulenko, K.I.; Skryabin, R.M. and Timirshin, K.V. *Geology, seismicity, and cryogenic processes in the Arctic areas of western Yakutia (in Russian)*. Yakutian Scientific Center SD RAS, 1996. (cited on pages 68 and 145)
- Grigoriev, N. F. *Mnogoletnemerzlyye porodny primorskoy zony Yakutii (The permafrost of the coastal zone of Yakutia, in Russian)*. Nauka, Moscow, 1966. (cited on page 150)
- Grosse, Guido; Schirrmeister, Lutz and Malthus, Timothy J. Application of Landsat-7 satellite data and a DEM for the quantification of thermokarst-affected terrain types in the periglacial Lena-Anabar coastal lowland. *Polar Research*, 25(1):51–67, 2006. doi:<http://onlinelibrary.wiley.com/doi/10.1111/j.1751-8369.2006.tb00150.x/full>. (cited on pages 68 and 127)
- Grosse, Guido; Schirrmeister, Lutz; Siegert, Christine; Kunitsky, Viktor V.; Slagoda, Elena A.; Andreev, Andrei A. and Dereviagyn, Alexander Y. Geological and geomorphological evolution of a sedimentary periglacial landscape in Northeast Siberia during the Late Quaternary. *Geomorphology*, 86(1):25–51, 2007. doi:10.1016/j.geomorph.2006.08.005. (cited on page 71)
- Grosse, Guido; Romanovsky, Vladimir; Jorgenson, Torre; Anthony, Katey Walter; Brown, Jerry and Overduin, Pier Paul. Vulnerability and Feedbacks of Permafrost to Climate Change. *Eos, Transactions American Geophysical Union*, 92(9):73–74, 2011. doi:10.1029/2011EO090001. (cited on page 4)
- Guillier, Bertrand; Atakan, Kuvvet; Chatelain, Jean-Luc; Havskov, Jens; Ohrnberger, Matthias; Cara, Fabrizio; Duval, Anne-Marie; Zacharopoulos, Stratos and Teves-Costa, Paula. Influence of instruments on the H/V spectral ratios of ambient vibrations. *Bulletin of Earthquake Engineering*, 6(1):3–31, 2008. doi:10.1007/s10518-007-9039-0. (cited on page 45)
- Günther, F.; Overduin, P. P.; Sandakov, A. V.; Grosse, G. and Grigoriev, M. N. Thermo-erosion along the Yedoma Coast of the Buor Khaya Peninsula, Laptev Sea, East Siberia. In *Tenth Int. Conf. Permafr.*, volume 2, pages 137–142, 2012. (cited on page 71)

- Günther, F.; Overduin, P. P.; Sandakov, A. V.; Grosse, G. and Grigoriev, M. N. Short- and long-term thermo-erosion of ice-rich permafrost coasts in the Laptev Sea region. *Biogeosciences*, 10(6):4297–4318, 2013a. doi:10.5194/bg-10-4297-2013. (cited on pages 3, 8, 70, 71, 120, and 127)
- Günther, F.; Overduin, P. P.; Yakshina, I. A.; Opel, T.; Baranskaya, A. V. and Grigoriev, M. N. Observing Muostakh disappear: permafrost thaw subsidence and erosion of a ground-ice-rich island in response to arctic summer warming and sea ice reduction. *The Cryosphere*, 9(1):151–178, 2015. doi:10.5194/tc-9-151-2015. (cited on pages 44, 45, 56, 71, and 167)
- Günther, Frank. *Thermo-erosion of permafrost coasts in East Siberia*. PhD thesis, Universität Potsdam, 2013. URL <http://d-nb.info/1046028529>. (cited on pages 4 and 127)
- Günther, Frank; Overduin, Paul; Makarov, Aleksandr S. and Grigoriev, Mikhail N. Russian-German cooperation SYSTEM LAPTEV SEA: the expeditions Laptev Sea - Mamontov Klyk 2011 & Buor Khaya 2012. *Berichte zur Polar- und Meeresforschung = Reports on polar and marine research*, 664:75–86, 2013b. URL <http://hdl.handle.net/10013/epic.41834.d001>. ISSN 1866-3192. (cited on pages 7, 67, 70, and 71)
- Halliday, David F.; Curtis, Andrew; Vermeer, Peter; Strobbia, Claudio; Glushchenko, Anna; van Manen, Dirk-Jan and Robertsson, Johan O. Interferometric ground-roll removal: Attenuation of scattered surface waves in single-sensor data. *Geophysics*, 75(2): SA15–SA25, 2010. doi:10.1190/1.3360948. (cited on page 40)
- Hansen, J.; Ruedy, R.; Sato, M. and Lo, K. Global Surface Temperature Change. *Rev. Geophys.*, 48(4):RG4004, 2010. doi:10.1029/2010RG000345. (cited on pages 7, 134, and 166)
- Harris, I.; Jones, P.D.; Osborn, T.J. and Lister, D.H. Updated high-resolution grids of monthly climatic observations – the CRU TS3.10 Dataset. *International Journal of Climatology*, 34(3):623–642, 2014. doi:10.1002/joc.3711. (cited on page 165)
- Harris, Robert N. and Chapman, David S. Mid-latitude (30°–60°N) climatic warming inferred by combining borehole temperatures with surface air temperatures. *Geophysical Research Letters*, 28(5):747–750, 2001. doi:10.1029/2000GL012348. (cited on pages 142 and 169)
- Harrison, W. and Osterkamp, T. *Environmental Assessment of the Alaskan Continental Shelf - Annual Reports of Principal Investigators for the year ending March 1977*, volume XVII. Hazards, chapter Offshore Permafrost – drilling, boundary conditions, properties, processes and models, pages 424–466. U.S. Department of Commerce, U.S. Department of Interior, 1977. (cited on pages 93 and 118)
- Harrison, W. D. and Osterkamp, T. E. Heat and Mass Transport Processes in Subsea Permafrost 1. An Analysis of Molecular Diffusion and Its Consequences. *Journal of Geophysical Research*, 83:4707–4712, 1978. doi:10.1029/JC083iC09p04707. (cited on pages 62, 64, 74, 118, 121, and 124)
- Harrison, W. D.; Musgrave, D. and Reeburgh, W. S. A wave-induced transport process in marine sediments. *Journal of Geophysical Research: Oceans*, 88(C12):7617–7622, 1983. doi:10.1029/JC088iC12p07617. (cited on pages 89 and 120)

- Harrison, W.D. Formulation of a Model for Pore Water Convection in Thawing Subsea Permafrost (Mitteilungen der Versuchsanstalt für Wasserbau, Hydrologie und Glaziologie). *Zürich: Eidgenössische Technische Hochschule*, 57:3–24, 1982. (cited on pages 64, 117, and 121)
- Harrison, W.D. and Osterkamp, T.E. Measurements of the electrical conductivity of interstitial water in subsea permafrost. In *Proceedings of the Fourth Canadian Permafrost Conference*, pages 229–237, 1982. (cited on pages 64, 89, and 121)
- Hauck, C. and Kneisel, C. *Applied Geophysics in Periglacial Environments*. Cambridge University Press: Cambridge, 2008. URL www.cambridge.org/9780521889667. ISBN-13 978-0-521-88966-7. (cited on pages 20, 21, 22, and 23)
- Heim, B.; Abramova, E.; Doerffer, R.; Günther, F.; Hölemann, J.; Kraberg, A.; Lantuit, H.; Loginova, A.; Martynov, F.; Overduin, P. P. and Wegner, C. Ocean colour remote sensing in the southern Laptev Sea: evaluation and applications. *Biogeosciences*, 11(15): 4191–4210, 2014. doi:10.5194/bg-11-4191-2014. (cited on page 126)
- Hequette, Arnaud; Desrosiers, Marc and Barnes, Peter W. Sea ice scouring on the inner shelf of the southeastern Canadian Beaufort Sea. *Marine Geology*, 128(3):201–219, 1995. doi:10.1016/0025-3227(95)00095-G. (cited on page 127)
- Hillel, D. *Introduction to soil physics*. Academic Press, New York, USA, 1982. (cited on pages 91 and 148)
- Hinkel, K.M.; Paetzold, F.; Nelson, F.E. and Bockheim, J.G. Patterns of soil temperature and moisture in the active layer and upper permafrost at Barrow, Alaska: 1993–1999. *Global and Planetary Change*, 29(3–4):293–309, 2001. doi:10.1016/S0921-8181(01)00096-0. (cited on page 156)
- Hinz, K; Delisle, G and Block, M. Seismic evidence for the depth extent of permafrost in shelf sediments of the Laptev Sea, Russian Arctic. In *Proceedings of the 7th international conference on permafrost*, pages 453–458, 1998. (cited on pages 6 and 25)
- Hivon, E G and Segó, D C. Strength of frozen saline soils. *Canadian Geotechnical Journal*, 32(2):336–354, 1995. (cited on pages 77 and 80)
- Ho, Sze Ling and Laepple, Thomas. Flat meridional temperature gradient in the early Eocene in the subsurface rather than surface ocean. *Nature Geosci*, 9(8):606–610, 2016. doi:10.1038/ngeo2763. (cited on page 170)
- Hobiger, M.; Cornou, C.; Wathelet, M.; Giulio, G. Di; Knapmeyer-Endrun, B.; Renalier, F.; Bard, P.-Y.; Savvaidis, A.; Hailemichael, S.; Le, Bihan N.; Ohrnberger, M. and Theodoulidis, N. Ground structure imaging by inversions of Rayleigh wave ellipticity: sensitivity analysis and application to European strong-motion sites. *Geophysical Journal International*, 192(1):207–229, 2013. doi:10.1093/gji/ggs005. (cited on page 31)
- Hopcroft, Peter O.; Gallagher, Kerry and Pain, Chris C. Inference of past climate from borehole temperature data using Bayesian Reversible Jump Markov chain Monte Carlo. *Geophysical Journal International*, 171(3):1430–1439, 2007. doi:10.1111/j.1365-246X.2007.03596.x. (cited on page 141)
- Horike, Masanori. Inversion of phase velocity of long-period microtremors to the S-wave-velocity structure down to the basement in urbanized areas. *Journal of Physics of the Earth*, 33(2):59–96, 1985. doi:10.4294/jpe1952.33.59. (cited on page 28)

- Hu, K.; Issler, Z.; Chen, Z. and Brent, T. A. Permafrost investigation by well logs, and seismic velocity and repeated shallow temperature surveys, Beaufort-Mackenzie Basin. Technical report, Geological Survey of Canada, Open File Report 6956, 2013. (cited on page 6)
- Huang, S. P.; Pollack, H. N. and Shen, P.-Y. A late Quaternary climate reconstruction based on borehole heat flux data, borehole temperature data, and the instrumental record. *Geophys. Res. Lett.*, 35(13):L13703, 2008. doi:10.1029/2008GL034187. (cited on page 133)
- Huang, Shaopeng. Merging information from different resources for new insights into climate change in the past and future. *Geophys. Res. Lett.*, 31(13):L13205, 2004. doi:10.1029/2004GL019781. (cited on pages 133 and 166)
- Huang, Shaopeng; Shen, Po Yu and Pollack, Henry N. Deriving century-long trends of surface temperature change from borehole temperatures. *Geophysical Research Letters*, 23(3):257–260, 1996. doi:10.1029/96GL00020. (cited on page 141)
- Huang, Shaopeng; Pollack, Henry N. and Shen, Po-Yu. Temperature trends over the past five centuries reconstructed from borehole temperatures. *Nature*, 403(6771):756–758, 2000. doi:10.1038/35001556. (cited on pages 133, 134, 141, and 166)
- Hubberten, Hans W; Andreev, Andrei; Astakhov, Valery I; Demidov, Igor; Dowdeswell, Julian A; Henriksen, Mona; Hjort, Christian; Houmark-Nielsen, Michael; Jakobsson, Martin; Kuzmina, Svetlana; Larsen, Eiliv; Lunkka, Juha Pekka; Lysa, Astrid; Mangerud, Jan; Möller, Per; Saarnisto, Matti; Schirmer, Lutz; Sher, Andrei V; Siegert, Christine; Siegert, Martin J and Svendsen, John Inge. The periglacial climate and environment in northern Eurasia during the Last Glaciation. *Quaternary Science Reviews*, 23(11): 1333–1357, 2004. doi:10.1016/j.quascirev.2003.12.012. (cited on page 1)
- Hunter, J. A.; Neave, K. G.; MacAulay, H. A. and Hobson, G. D. Interpretation of Sub-Seabottom Permafrost in the Beaufort Sea by Seismic Methods; Part 1: seismic refraction methods. In *Proceedings of the Third International Permafrost Conference, V.1*, pages 514–520, 1978. (cited on pages 6 and 23)
- Hunter, S.J.; Goldobin, D.S.; Haywood, A.M.; Ridgwell, A. and Rees, J.G. Sensitivity of the global submarine hydrate inventory to scenarios of future climate change. *Earth and Planetary Science Letters*, 367:105–115, 2013. doi:10.1016/j.epsl.2013.02.017. (cited on page 9)
- Hutter, K. and Straughan, B. Penetrative convection in thawing subsea permafrost. *Continuum Mechanics and Thermodynamics*, 9(5):259–272, 1997. doi:10.1007/s001610050070. (cited on page 65)
- Hutter, Kolumban and Straughan, Brian. Models for convection in thawing porous media in support for the subsea permafrost equations. *Journal of Geophysical Research: Solid Earth*, 104(B12):29249–29260, 1999. doi:10.1029/1999JB900288. (cited on pages 57 and 65)
- Ibs-von Seht, Malte and Wohlenberg, Jürgen. Microtremor measurements used to map thickness of soft sediments. *Bulletin of the Seismological Society of America*, 89(1): 250–259, 1999. URL <https://pubs.geoscienceworld.org/bssa/article-abstract/89/1/250/120443/microtremor-measurements-used-to-map-thickness-of?redirectedFrom=fulltext>. (cited on page 32)

- Imaeva, L.P.; Kozmin, B.M.; Sergeyenko, A.I.; Belolyubskii, I.N and Siegert, C. Noveyshie struktury, stratigrafiya kvartera i sovremennaya geodinamika territorii Arkticheskogo sektora pribrezhno-shelfovoi zony Severnogo Verkhoyana (Severo-vostok Yakutii) - (Modern structures, quaternary stratigraphy and recent geodynamics in the Arctic sector of the Northern Verkhoyan coastal shelf zone (North of East Yakutia)). *Bulletin of the commission on studies of the quaternary period*, 67:6–19, 2007. (cited on page 70)
- Ingebritsen, Steven E.; Sanford, Ward E. and Neuzil, Christopher E. *Groundwater in geologic processes*. Cambridge Univ. Press, 2007. (cited on pages 64, 74, 84, 93, and 150)
- Intergovernmental Panel on Climate Change (IPCC). *Climate Change 2013: The Physical Science Basis. Contribution of Working Group I to the Fifth Assessment Report of the Intergovernmental Panel on Climate Change*. Cambridge Univ. Press, Cambridge, U.K., and New York, 2013. (cited on pages 7 and 9)
- International Heat Flow Commission (IHFC). The Global Heat Flow Database. Online, 2011. URL <http://www.heatflow.und.edu/>. (cited on pages 93 and 150)
- International Ocean Discovery Program (2013–2023). Illuminating Earth's Past, Present, and Future: The Science Plan for the IODP 2013–2023. URL <http://www.iodp.org>. (cited on page 8)
- Ippisch, O. *Coupled transport in natural porous media*. PhD thesis, University of Heidelberg, 2001. (cited on pages 73, 74, 90, and 148)
- Isaksen, K.; Benestad, R. E.; Harris, C. and Sollid, J. L. Recent extreme near-surface permafrost temperatures on Svalbard in relation to future climate scenarios. *Geophysical Research Letters*, 34(17):L17502, 2007. doi:10.1029/2007GL031002. (cited on page 167)
- James, Rachael H.; Bousquet, Philippe; Bussmann, Ingeborg; Haeckel, Matthias; Kipfer, Rolf; Leifer, Ira; Niemann, Helge; Ostrovsky, Ilia; Piskozub, Jacek; Rehder, Gregor; Treude, Tina; Vielstädte, Lisa and Greinert, Jens. Effects of climate change on methane emissions from seafloor sediments in the Arctic Ocean: A review. *Limnology and Oceanography*, 61(S1):S283–S299, 2016. doi:10.1002/lno.10307. (cited on pages 7 and 10)
- Jaume-Santero, F.; Pickler, C.; Beltrami, H. and Mareschal, J.-C. North American regional climate reconstruction from ground surface temperature histories. *Climate of the Past*, 12(12):2181–2194, 2016. doi:10.5194/cp-12-2181-2016. (cited on pages 136 and 141)
- Johansen, Tor Arne; Digranes, Per; van Schaack, Mark and Lønne, Ida. Seismic mapping and modeling of near-surface sediments in polar areas. *Geophysics*, 68(2):566–573, 2003. doi:10.1190/1.1567226. (cited on page 80)
- Johnsen, S. Stable isotope profiles compared with temperature profiles in firn with historical temperature records. In *Isotopes and impurities in snow and ice symposium*, number 118, pages 388–392. IAHS-AISH Publication, 1977. (cited on page 141)
- Johnsen, Sigfus J.; Dahl-Jensen, Dorthe; Dansgaard, Willi and Gundestrup, Niels. Greenland palaeotemperatures derived from GRIP bore hole temperature and ice core isotope profiles. *Tellus B: Chemical and Physical Meteorology*, 47(5):624–629, 1995. doi:10.3402/tellusb.v47i5.16077. (cited on page 141)
- Jones, P. D. and Mann, M. E. Climate over past millennia. *Rev. Geophys.*, 42(2):RG2002, 2004. doi:10.1029/2003RG000143. (cited on page 133)

- Jones, P. D.; Lister, D. H.; Osborn, T. J.; Harpham, C.; Salmon, M. and Morice, C. P. Hemispheric and large-scale land-surface air temperature variations: An extensive revision and an update to 2010. *J. Geophys. Res.*, 117(D5):D05127, 2012. doi:10.1029/2011JD017139. (cited on pages 164 and 165)
- Jouzel, J.; Masson-Delmotte, V.; Cattani, O.; Dreyfus, G.; Falourd, S.; Hoffmann, G.; Minster, B.; Nouet, J.; Barnola, J. M.; Chappellaz, J.; Fischer, H.; Gallet, J. C.; Johnsen, S.; Leuenberger, M.; Loulergue, L.; Luethi, D.; Oerter, H.; Parrenin, F.; Raisbeck, G.; Raynaud, D.; Schilt, A.; Schwander, J.; Selmo, E.; Souchez, R.; Spahni, R.; Stauffer, B.; Steffensen, J. P.; Stenni, B.; Stocker, T. F.; Tison, J. L.; Werner, M. and Wolff, E. W. Orbital and Millennial Antarctic Climate Variability over the Past 800,000 Years. *Science*, 317(5839):793–796, 2007. doi:10.1126/science.1141038. (cited on page 133)
- Junker, Ralf; Grigoriev, Mikhail N. and Kaul, Norbert. Non-contact infrared temperature measurements in dry permafrost boreholes. *Journal of Geophysical Research: Solid Earth*, 113:B04102, 2008. doi:10.1029/2007JB004946. (cited on page 115)
- Jury, W. and Horton, R. *Soil physics*. Wiley, 2004. (cited on page 72)
- Kassens, H; Bauch, HA; Dmitrenko, I; Drachev, S; Grikurov, G; Thiede, J and Tuschling, K. Transdrift VIII: drilling the Laptev Sea 2000. *The Nansen Icebreaker*, 12(1):8–9, 2001. (cited on page 7)
- Kaufman, Darrell S.; Schneider, David P.; McKay, Nicholas P.; Ammann, Caspar M.; Bradley, Raymond S.; Briffa, Keith R.; Miller, Gifford H.; Otto-Bliesner, Bette L.; Overpeck, Jonathan T. and Vinther, Bo M. Recent Warming Reverses Long-Term Arctic Cooling. *Science*, 325(5945):1236–1239, 2009. doi:10.1126/science.1173983. (cited on page 134)
- Kawase, Hiroshi; Sánchez-Sesma, Francisco J. and Matsushima, Shinichi. The Optimal Use of Horizontal-to-Vertical Spectral Ratios of Earthquake Motions for Velocity Inversions Based on Diffuse-Field Theory for Plane Waves. *Bulletin of the Seismological Society of America*, 101(5):2001–2014, 2011. doi:10.1785/0120100263. (cited on page 33)
- Kim, B.; Grikurov, G. and Soloviev, V. *Land-Ocean Systems in the Siberian Arctic*, chapter High Resolution Seismic Studies in the Laptev Sea Shelf: First Results and Future Needs, pages 683–692. Springer, Berlin, Heidelberg, 1999. ISBN 978-3-642-60134-7. doi:10.1007/978-3-642-60134-7_51. (cited on page 6)
- King, M. S. and Hunter, J. A. Some seismic, electrical and thermal properties of sub-seabottom permafrost samples from the Beaufort Sea. In *Proc. 4th Canadian Conference on Permafrost*. Natl. Res. Counc. of Can., Edmonton, Alberta, Canada, 1982. (cited on page 23)
- Knapmeyer-Endrun, Brigitte; Golombek, Matthew P. and Ohrnberger, Matthias. Rayleigh Wave Ellipticity Modeling and Inversion for Shallow Structure at the Proposed InSight Landing Site in Elysium Planitia, Mars. *Space Science Reviews*, 211(1):339–382, 2017. doi:10.1007/s11214-016-0300-1. (cited on page 30)
- Kneier, Fabian; Overduin, Pier Paul; Langer, Moritz; Boike, Julia and Grigoriev, Mikhail N. Borehole temperature reconstructions reveal differences in past surface temperature trends for the permafrost in the Laptev Sea region, Russian Arctic. *arktos*, 4(1):7, 2018. doi:10.1007/s41063-018-0041-3. (cited on pages 144, 149, 157, 158, 159, 161, 163, 165, and 169)

- Kneisel, Christof; Hauck, Christian; Fortier, Richard and Moorman, Brian. Advances in geophysical methods for permafrost investigations. *Permafrost and Periglacial Processes*, 19(2):157–178, 2008. ISSN 1099-1530. doi:10.1002/ppp.616. URL <http://dx.doi.org/10.1002/ppp.616>. (cited on pages 22 and 26)
- Kogan, A.D. The setting of seismic works using the method KMPV-GSZ from sea ice on the shelf of the Arctic Seas (in Russian). *Geophysical methods of exploration in the Arctic, L.:NIIGA*, 9:33–38, 1974. (cited on page 144)
- Köhler, Andreas; Ohrnberger, Matthias; Scherbaum, Frank; Wathelet, Marc and Cornou, Cecile. Assessing the reliability of the modified three-component spatial autocorrelation technique. *Geophysical Journal International*, 168(2):779–796, 2007. ISSN 1365-246X. doi:10.1111/j.1365-246X.2006.03253.x. (cited on page 31)
- Komarov, I. A. and Kiyashko, N. V. Method for Estimating Properties of Cryopegs from the Yamal Peninsula. In: Melnikov, V. P.(ed.), *Proceedings of the Tenth International Conference on Permafrost*, volume 2: Translations of Russian Contributions, pages 169–174. The Northern Publisher, Salekhard, June 2012. (cited on pages 82 and 83)
- Konno, Katsuaki and Ohmachi, Tatsuo. Ground-motion characteristics estimated from spectral ratio between horizontal and vertical components of microtremor. *Bulletin of the Seismological Society of America*, 88(1):228–241, 1998. URL <http://www.bssaonline.org/content/88/1/228.abstract>. (cited on pages 30 and 45)
- Koshurnikov, A. V.; Tumskoy, V. E.; Shakhova, N. E.; Sergienko, V. I.; Dudarev, O. V.; Gunar, A. Yu.; Pushkarev, P. Yu.; Semiletov, I. P. and Koshurnikov, A. A. The first ever application of electromagnetic sounding for mapping the submarine permafrost table on the Laptev Sea shelf. *Doklady Earth Sciences*, 469(2):860–863, 2016. doi:10.1134/S1028334X16080110. (cited on page 26)
- Kunitsky, V.V. *Kriolitologiya Nizovya Leny (Cryolithology of the Lower Lena)*. USSR Academy of Sciences, Siberian Branch, Permafrost Institute, Yakutsk, 1989. (cited on pages 7, 71, and 91)
- Kurek, Joshua; Cwynar, Les C.; Ager, Thomas A.; Abbott, Mark B. and Edwards, Mary E. Late Quaternary paleoclimate of western Alaska inferred from fossil chironomids and its relation to vegetation histories. *Quaternary Science Reviews*, 28(9):799–811, 2009. doi:10.1016/j.quascirev.2008.12.001. (cited on page 136)
- Lachenbruch, A.H. and Marshall, B.V. Changing Climate: Geothermal Evidence from Permafrost in the Alaskan Arctic. *Science*, 234(4777):689–696, 1986. doi:10.1126/science.234.4777.689. (cited on page 166)
- Lachenbruch, Arthur H. Thermal Effects of the Ocean on Permafrost. *Geological Society of America Bulletin*, 68(11):1515–1530, 1957. URL <http://gsabulletin.gsapubs.org/content/68/11/1515.abstract>. (cited on page 62)
- Lachet, Corinne and Bard, Pierre-Yves. Numerical and Theoretical Investigations on the Possibilities and Limitations of Nakamura's Technique. *Journal of Physics of the Earth*, 42(5):377–397, 1994. doi:10.4294/jpe1952.42.377. (cited on page 30)
- J.W.Lane, Jr.; White, E.A.; Steele, G.V. and Cannia, J.C. Estimation of bedrock depth using the horizontal-to-vertical (H/V) ambient-noise seismic method: Symposium on the Application of Geophysics to Engineering and Environmental Problems. In *Proceedings of the Environmental and Engineering Geophysical Society*, page 13, Philadelphia, Pennsylvania, 2008. (cited on page 32)

- Langer, M.; Westermann, S.; Muster, S.; Piel, K. and Boike, J. The surface energy balance of a polygonal tundra site in northern Siberia – Part 2: Winter. *The Cryosphere*, 5(2): 509–524, 2011. doi:10.5194/tc-5-509-2011. (cited on pages 78, 81, and 168)
- Langer, Moritz; Westermann, Sebastian; Heikenfeld, Max; Dorn, Wolfgang and Boike, Julia. Satellite-based modeling of permafrost temperatures in a tundra lowland landscape. *Remote Sensing of Environment*, 135(0):12–24, 2013. doi:10.1016/j.rse.2013.03.011. (cited on pages 78, 81, 90, and 169)
- Lawrence, David M.; Slater, Andrew G.; Tomas, Robert A.; Holland, Marika M. and Deser, Clara. Accelerated Arctic land warming and permafrost degradation during rapid sea ice loss. *Geophysical Research Letters*, 35(11):L11506, 2008. doi:10.1029/2008GL033985. (cited on page 167)
- Lawrimore, Jay H.; Menne, Matthew J.; Gleason, Byron E.; Williams, Claude N.; Wuertz, David B.; Vose, Russell S. and Rennie, Jared. An overview of the Global Historical Climatology Network monthly mean temperature data set, version 3. *Journal of Geophysical Research: Atmospheres*, 116(D19):D19121, 2011. doi:10.1029/2011JD016187. (cited on page 165)
- Lenz, Josefine; Jones, Benjamin M.; Wetterich, Sebastian; Tjallingii, Rik; Fritz, Michael; Arp, Christopher D.; Rudaya, Natalia and Grosse, Guido. Impacts of shore expansion and catchment characteristics on lacustrine thermokarst records in permafrost lowlands, Alaska Arctic Coastal Plain. *arktos*, 2(1):25, 2016. doi:10.1007/s41063-016-0025-0. (cited on page 115)
- Lermo, Javier and Chavez-Garcia, Francisco J. Are microtremors useful in site response evaluation? *Bulletin of the Seismological Society of America*, 84(5):1350–1364, 1994. URL <http://bssa.geoscienceworld.org/content/84/5/1350/article-info>. (cited on page 30)
- Lesperance, Marielle; Smerdon, Jason E. and Beltrami, Hugo. Propagation of linear surface air temperature trends into the terrestrial subsurface. *Journal of Geophysical Research: Atmospheres*, 115(D21):D21115, 2010. doi:10.1029/2010JD014377. (cited on page 142)
- Li, Todd M. C.; Ferguson, John F.; Herrin, Eugene and Durham, Howard B. High-frequency seismic noise at Lajitas, Texas. *Bulletin of the Seismological Society of America*, 74(5):2015–2033, 1984. URL <http://bssa.geoscienceworld.org/content/74/5/2015>. (cited on page 28)
- Li, Yuan-Hui and Gregory, Sandra. Diffusion of ions in sea water and in deep-sea sediments. *Geochimica et Cosmochimica Acta*, 38(5):703–714, 1974. doi:10.1016/0016-7037(74)90145-8. (cited on page 86)
- Lin, Fan-Chi; Ritzwoller, Michael H. and Snieder, Roel. Eikonal tomography: surface wave tomography by phase front tracking across a regional broad-band seismic array. *Geophysical Journal International*, 177(3):1091–1110, 2009. doi:10.1111/j.1365-246X.2009.04105.x. (cited on page 39)
- Ljungqvist, Fredrik Charpentier. A new reconstruction of temperature variability in the extra-tropical Northern Hemisphere during the last two millennia. *Geografiska Annaler. Series A, Physical Geography*, 92(3):339–351, 2010. URL <http://www.jstor.org/stable/40930999>. (cited on page 133)

- Lucas, T. Freezing of a porous medium in contact with a concentrated aqueous freezant: numerical modelling of coupled heat and mass transport. *International Journal of Heat and Mass Transfer*, 44:2093–2106, 2001. doi:10.1016/S0017-9310(00)00238-6. (cited on pages 63 and 86)
- Lunedei, Enrico and Albarello, Dario. On the seismic noise wavefield in a weakly dissipative layered Earth. *Geophysical Journal International*, 177(3):1001–1014, 2009. doi:10.1111/j.1365-246X.2008.04062.x. (cited on page 30)
- Lunedei, Enrico and Albarello, Dario. Theoretical HVSR curves from full wavefield modelling of ambient vibrations in a weakly dissipative layered Earth. *Geophysical Journal International*, 181(2):1093–1108, 2010. doi:10.1111/j.1365-246X.2010.04560.x. (cited on page 31)
- MacAulay, HA and Hunter, JA. Detailed seismic refraction analysis of ice-bonded permafrost layering in the Canadian Beaufort Sea. In *Proceedings, 4th Canadian Permafrost Conference: National Research Council Canada, The Roger JE Brown Memorial Volume*, pages 256–267, 1982. (cited on page 6)
- MacAyeal, Douglas R.; Firestone, John and Waddington, Edwin. Paleothermometry by control methods. *Journal of Glaciology*, 37(127):326–338, 1991. doi:10.3189/S0022143000005761. (cited on page 141)
- Majorowicz, Jacek; Safanda, Jan and Skinner, Walter. Past Surface Temperature Changes as Derived from Continental Temperature Logs—Canadian and Some Global Examples of Application of a New Tool in Climate Change Studies. In *Advances in Geophysics*, volume 47 of *Advances in Geophysics*, pages 113–174. Elsevier, 2004. doi:10.1016/S0065-2687(04)47003-4. (cited on pages 74, 138, 139, 140, 142, 145, 156, and 170)
- Malischewsky, Peter G. and Scherbaum, Frank. Love’s formula and H/V-ratio (ellipticity) of Rayleigh waves. *Wave Motion*, 40(1):57–67, 2004. doi:10.1016/j.wavemoti.2003.12.015. (cited on pages 30, 31, 52, and 55)
- Mann, Michael E. and Jones, Philip D. Global surface temperatures over the past two millennia. *Geophys. Res. Lett.*, 30(15):1820, 2003. doi:10.1029/2003GL017814. (cited on page 133)
- Mann, Michael E. and Schmidt, Gavin A. Ground vs. surface air temperature trends: Implications for borehole surface temperature reconstructions. *Geophysical Research Letters*, 30(12):1607, 2003. doi:10.1029/2003GL017170. (cited on page 142)
- Mann, Michael E.; Bradley, Raymond S. and Hughes, Malcolm K. Northern hemisphere temperatures during the past millennium: Inferences, uncertainties, and limitations. *Geophys. Res. Lett.*, 26(6):759–762, 1999. doi:10.1029/1999GL900070. (cited on page 133)
- Mann, Michael E.; Zhang, Zhihua; Hughes, Malcolm K.; Bradley, Raymond S.; Miller, Sonya K.; Rutherford, Scott and Ni, Fenbiao. Proxy-based reconstructions of hemispheric and global surface temperature variations over the past two millennia. *Proceedings of the National Academy of Sciences*, 105(36):13252–13257, 2008. doi:10.1073/pnas.0805721105. (cited on pages 133 and 153)
- Marcott, Shaun A.; Shakun, Jeremy D.; Clark, Peter U. and Mix, Alan C. A Reconstruction of Regional and Global Temperature for the Past 11,300 Years. *Science*, 339(6124):1198–1201, 2013. doi:10.1126/science.1228026. (cited on page 133)

- Mareschal, Jean-Claude and Beltrami, Hugo. Evidence for recent warming from perturbed geothermal gradients: examples from eastern Canada. *Climate Dynamics*, 6(3):135–143, 1992. doi:10.1007/BF00193525. (cited on page 141)
- Marion, G. M. Freeze-Thaw Processes and Soil Chemistry. Technical report, CRREL Special Report 95-12, 1995. (cited on page 81)
- Martins, Joaquim R. R. A.; Sturdza, Peter and Alonso, Juan J. The Complex-step Derivative Approximation. *ACM Trans. Math. Softw.*, 29(3):245–262, 2003. doi:10.1145/838250.838251. (cited on page 152)
- McDougall, T.J. and Barker, P.M. *Getting started with TEOS-10 and the Gibbs Seawater (GSW) Oceanographic Toolbox*. SCOR/IAPSO WG127, 2011. ISBN 978-0-646-55621-5. (cited on page 82)
- McGuire, A. David; Anderson, Leif G.; Christensen, Torben; Dallimore, Scott; Guo, Laodong; Hayes, Daniel J.; Heimann, Martin; Lorenson, Thomas D.; Macdonald, Robie W. and Roulet, Nigel. Sensitivity of the carbon cycle in the Arctic to climate change. In *Ecological Monographs*, volume 79, pages 523–555. Ecological Society of America (ESA), 2009. URL <http://lup.lub.lu.se/record/1506971>. (cited on pages 8, 9, and 134)
- McKay, Nicholas P. and Kaufman, Darrell S. An extended Arctic proxy temperature database for the past 2,000 years. *Scientific Data*, 1:140026, 2014. doi:10.1038/sdata.2014.26. (cited on pages 16, 134, 135, 153, and 166)
- Mehta, Kurang; Sheiman, Jon L.; Snieder, Roel and Calvert, Rodney. Strengthening the virtual-source method for time-lapse monitoring. *Geophysics*, 73(3):S73–S80, 2008. doi:10.1190/1.2894468. (cited on page 40)
- Meyer, Hanno; Opel, Thomas; Laepple, Thomas; Dereviagin, Alexander Yu; Hoffmann, Kirstin and Werner, Martin. Long-term winter warming trend in the Siberian Arctic during the mid- to late Holocene. *Nature Geosci*, 8(2):122–125, 2015. doi:10.1038/ngeo2349. (cited on pages 134, 136, and 172)
- Mitzscherling, Julia; Winkel, Matthias; Winterfeld, Maria; Horn, Fabian; Yang, Sizhong; Grigoriev, Mikhail N.; Wagner, Dirk; Overduin, Pier P. and Liebner, Susanne. The development of permafrost bacterial communities under submarine conditions. *Journal of Geophysical Research: Biogeosciences*, 122(7):1689–1704, 2017. doi:10.1002/2017JG003859. (cited on pages 10 and 70)
- Moberg, Anders; Sonechkin, Dmitry M.; Holmgren, Karin; Datsenko, Nina M. and Karlen, Wibjorn. Highly variable Northern Hemisphere temperatures reconstructed from low- and high-resolution proxy data. *Nature*, 433(7026):613–617, 2005. doi:10.1038/nature03265. (cited on page 133)
- Morack, J. L. and Rogers, J. C. Acoustic velocities of nearshore materials in the Alaskan Beaufort and Chukchi Seas. In: Barnes, P. W.; Schell, D. M. and Reimnitz, E.(eds.), *The Alaskan Beaufort Sea: Ecosystems and Environments*, pages 259–274. Academic, Orlando, Fla., 1984. (cited on page 23)
- Mueller, Klaus. Oberflächenstrukturen und Eigenschaften von Permafrostböden im nordsibirischen Lena-Delta (in German). *Z. Pflanzenernaehr. Bodenk.*, 160(4):497–503, 1997. doi:10.1002/jpln.19971600410. (cited on page 144)
- Musgrave, D. L. and Reeburgh, W. S. Density-driven interstitial water motion in sediments. *Nature*, 299:331–334, September 1982. doi:10.1038/299331a0. (cited on page 64)

- Muto, Atsuhiko; Scambos, Ted A.; Steffen, Konrad; Slater, Andrew G. and Clow, Gary D. Recent surface temperature trends in the interior of East Antarctica from borehole firn temperature measurements and geophysical inverse methods. *Geophysical Research Letters*, 38(15):L15502, 2011. doi:10.1029/2011GL048086. (cited on page 141)
- Nagornov, O. V.; Konovalov, Yu. V.; Zagorodnov, V. S. and Thompson, L. G. Reconstruction of the Surface Temperature of Arctic Glaciers from the Data of Temperature Measurements in Wells. *Journal of Engineering Physics and Thermophysics*, 74(2): 253–265, 2001. doi:10.1023/A:1016661616282. (cited on page 141)
- Nagornov, Oleg V.; Konovalov, Yuri V. and Tchijov, Vladimir. Temperature reconstruction for Arctic glaciers. *Palaeogeography, Palaeoclimatology, Palaeoecology*, 236(1):125–134, 2006. doi:10.1016/j.palaeo.2005.11.035. (cited on page 141)
- Nakamura, Y. A method for dynamic characteristics estimations of subsurface using microtremors on the ground surface. *Railw. Tech. Res. Inst. Quart. Rep.*, 30:25–33, 1989. (cited on page 30)
- Nakamura, Yutaka. Clear identification of fundamental idea of Nakamura's technique and its applications. In *Proceedings of the 12th World conference on earthquake engineering*, Auckland, 2000. (cited on page 30)
- National Climatic Data Center, NOAA. Climate Data Online, Station Tiksi, 2015. URL <https://www.ncdc.noaa.gov/cdo-web/datasets/GHCND/stations/GHCND:RSM00021824/detail>. Accessed 2015. (cited on page 165)
- Naurzbaev, M. M. and Vaganov, E. A. Variation of early summer and annual temperature in east Taymir and Putoran (Siberia) over the last two millennia inferred from tree rings. *Journal of Geophysical Research: Atmospheres*, 105(D6):7317–7326, 2000. doi:10.1029/1999JD901059. (cited on page 135)
- Neave, K. G. and Sellman, P. V. Subsea permafrost in Harrison Bay, Alaska, An interpretation from seismic data. Technical report, CRREL Report 82-24, 1982. (cited on page 23)
- Nicolsky, D and Shakhova, N. Modeling sub-sea permafrost in the East Siberian Arctic Shelf: the Dmitry Laptev Strait. *Environmental Research Letters*, 5(1):015006, 2010. doi:10.1088/1748-9326/5/1/015006. (cited on pages 6, 12, 63, and 131)
- Nicolsky, D. J.; Romanovsky, V. E.; Alexeev, V. A. and Lawrence, D. M. Improved modeling of permafrost dynamics in a GCM land-surface scheme. *Geophys. Res. Lett.*, 34(8):L08501, 2007. doi:10.1029/2007GL029525. (cited on pages 78, 91, and 93)
- Nicolsky, D. J.; Romanovsky, V. E.; Romanovskii, N. N.; Kholodov, A. L.; Shakhova, N. E. and Semiletov, I. P. Modeling sub-sea permafrost in the East Siberian Arctic Shelf: The Laptev Sea region. *Journal of Geophysical Research: Earth Surface*, 117:F03028, 2012. doi:10.1029/2012JF002358. (cited on pages 6, 7, 61, 63, 117, 118, 119, 128, 132, and 172)
- Niessen, Frank. Profile of sediment echo sounding during POLARSTERN cruise ARK-XI/1 with links to ParaSound data files, 2004. URL <https://doi.org/10.1594/PANGAEA.206531>. (cited on page 25)
- Nishimura, Takeshi; Tanaka, Satoru; Yamawaki, Teruo; Yamamoto, Hidekazu; Sano, Takashi; Sato, Minemori; Nakahara, Hisashi; Uchida, Naoki; Hori, Shuichiro and Sato, Haruo. Temporal changes in seismic velocity of the crust around Iwate volcano, Japan, as inferred from analyses of repeated active seismic experiment data from 1998

- to 2003. *Earth, Planets and Space*, 57(6):491–505, 2005. doi:10.1186/BF03352583. (cited on page 40)
- Nixon, J. F. Thermal simulation of subsea saline permafrost. *Can. J. Earth Sci.*, 23(12): 2039–2046, 1986. doi:10.1139/e86-188. (cited on pages 63 and 80)
- Nixon, J.F. and Halliwell, D.H. Practical applications of a versatile geothermal simulator. *Journal of Energy Resources Technology*, 105(4):442–447, 1983. (cited on pages 63 and 77)
- Nogoshi, M. and Igarashi, T. On the amplitude characteristics of microtremor (Part 2) [in Japanese with English abstract]. *J. Seismol. Soc. Jpn*, 24:26–40, 1971. (cited on page 30)
- Obermann, A.; Planes, T.; Larose, E. and Campillo, M. Imaging preruptive and coeruptive structural and mechanical changes of a volcano with ambient seismic noise. *Journal of Geophysical Research: Solid Earth*, 118(12):6285–6294, 2013. doi:10.1002/2013JB010399. (cited on page 40)
- O'Connor, Fiona M.; Boucher, O.; Gedney, N.; Jones, C. D.; Folberth, G. A.; Coppel, R.; Friedlingstein, P.; Collins, W. J.; Chappellaz, J.; Ridley, J. and Johnson, C. E. Possible role of wetlands, permafrost, and methane hydrates in the methane cycle under future climate change: A review. *Rev. Geophys.*, 48(4):RG4005, 2010. doi:10.1029/2010RG000326. (cited on page 8)
- Oerlemans, J. Extracting a Climate Signal from 169 Glacier Records. *Science*, 308(5722): 675–677, 2005. doi:10.1126/science.1107046. (cited on page 133)
- Ogorodov, S.; Arkhipov, V.; Kokin, O.; Marchenko, A.; Overduin, P. and Forbes, D. Ice effect on coast and seabed in Baydaratskaya Bay, Kara Sea. *Geography, Environment, Sustainability*, 6(3):21–37, 2013. doi:10.24057/2071-9388-2013-6-3-21-37. (cited on page 127)
- Opel, T.; Fritzsche, D. and Meyer, H. Eurasian Arctic climate over the past millennium as recorded in the Akademii Nauk ice core (Severnaya Zemlya). *Climate of the Past*, 9(5): 2379–2389, 2013. doi:10.5194/cp-9-2379-2013. (cited on pages 16, 134, and 135)
- Opel, Thomas; Laepple, Thomas; Meyer, Hanno; Dereviagin, Alexander Yu and Wetterich, Sebastian. Northeast Siberian ice wedges confirm Arctic winter warming over the past two millennia. *The Holocene*, 2017. doi:10.1177/0959683617702229. (cited on page 172)
- Orsi, Anais J.; Cornuelle, Bruce D. and Severinghaus, Jeffrey P. Little Ice Age cold interval in West Antarctica: Evidence from borehole temperature at the West Antarctic Ice Sheet (WAIS) Divide. *Geophysical Research Letters*, 39(9):L09710, 2012. doi:10.1029/2012GL051260. (cited on pages 141 and 151)
- Osterkamp, T. E. Freezing and thawing of soils and permafrost containing unfrozen water or brine. *Water Resour. Res.*, 23(12):2279–2285, 1987. doi:10.1029/WR023i012p02279. (cited on pages 62 and 83)
- Osterkamp, T. E.; Baker, G. C.; Harrison, W. D. and Matava, T. Characteristics of the active layer and shallow subsea permafrost. *Journal of Geophysical Research: Oceans*, 94(C11):16227–16236, 1989. doi:10.1029/JC094iC11p16227. (cited on pages 11, 64, 116, 118, and 125)
- Osterkamp, T.E. Sub-sea Permafrost. In: in Chief: John H. Steele, Editor(ed.), *Encyclopedia of Ocean Sciences*, pages 2902–2912. Academic Press, Oxford, 2001. ISBN 978-0-12-227430-5. doi:10.1006/rwos.2001.0008. (cited on pages 5, 11, 13, 14, 66, and 116)

- Osterkamp, T.E. and Harrison, W.D. Subsea permafrost: Probing, thermal regime and data analysis. *Environmental Assessment of the Alaskan Continental Shelf, Annual Reports*, 4:497–677, 1980. (cited on page 121)
- Overduin, P.; Grigoriev, M.; Junker, R.; Rachold, V.; Kunitsky, V.; Bolshiyarov, D. and Schirrmeister, L. The expedition COAST I: COAST drilling campaign 2005: subsea permafrost studies in the near-shore zone of the Laptev Sea. *Reports on Polar Research*, 550:1–40, 2007a. (cited on pages 7, 67, 68, 70, 91, 93, 124, and 125)
- Overduin, P. P.; Wetterich, S.; Günther, F.; Grigoriev, M. N.; Grosse, G.; Schirrmeister, L.; Hubberten, H.-W. and Makarov, A. Coastal dynamics and submarine permafrost in shallow water of the central Laptev Sea, East Siberia. *The Cryosphere*, 10(4):1449–1462, 2016. doi:10.5194/tc-10-1449-2016. (cited on pages 44, 54, 56, 71, 93, and 119)
- Overduin, Pier P.; Haberland, Christian; Ryberg, Trond; Kneier, Fabian; Jacobi, Tim; Grigoriev, Mikhail. N. and Ohrnberger, Matthias. Submarine permafrost depth from ambient seismic noise. *Geophysical Research Letters*, 42(18):7581–7588, 2015a. doi:10.1002/2015GL065409. (cited on pages 42, 44, 50, 51, 56, 183, and 184)
- Overduin, Pier Paul; Hubberten, Hans-W.; Rachold, Volker; Romanovskii, Nikolai; Grigoriev, Mikhail and Kasymkaya, Maria. The evolution and degradation of coastal and offshore permafrost in the Laptev and East Siberian Seas during the last climatic cycle. In *Special Paper 426: Coastline Changes: Interrelation of Climate and Geological Processes*, volume 426, pages 97–111. Geological Society of America, 2007b. doi:10.1130/2007.2426(07). (cited on pages 6, 12, 16, 57, and 66)
- Overduin, Pier Paul; Westermann, Sebastian; Yoshikawa, Kenji; Haberau, Thomas; Romanovsky, Vladimir and Wetterich, Sebastian. Geoelectric observations of the degradation of nearshore submarine permafrost at Barrow (Alaskan Beaufort Sea). *Journal of Geophysical Research: Earth Surface*, 117(F2):F02004, 2012. doi:10.1029/2011JF002088. (cited on pages 20, 21, 22, and 27)
- Overduin, Pier Paul; Liebner, Susanne; Knoblauch, Christian; Günther, Frank; Wetterich, Sebastian; Schirrmeister, Lutz; Hubberten, Hans-Wolfgang and Grigoriev, Mikhail N. Methane oxidation following submarine permafrost degradation: Measurements from a central Laptev Sea shelf borehole. *Journal of Geophysical Research: Biogeosciences*, 120(5):965–978, 2015b. doi:10.1002/2014JG002862. 2014JG002862. (cited on pages 7, 10, and 71)
- Overduin, Pier Paul; Liebner, Susanne; Knoblauch, Christian; Günther, Frank; Wetterich, Sebastian; Schirrmeister, Lutz; Hubberten, Hans-Wolfgang and Grigoriev, Mikhail N. Borehole temperature, submarine permafrost methane concentrations and pore water chemistry measured on borehole BK-2, central Laptev Sea shelf, 2015. URL <https://doi.org/10.1594/PANGAEA.846279>. Supplement to: Overduin, PP et al. (2015): Methane oxidation following submarine permafrost degradation: Measurements from a central Laptev Sea shelf borehole. *Journal of Geophysical Research-Biogeosciences*, 120(5), 965–978, doi: 10.1002/2014JG002862. (cited on page 124)
- PAGES 2k Consortium. Continental-scale temperature variability during the past two millennia. *Nature Geosci*, 6(5):339–346, 2013. doi:10.1038/ngeo1797. (cited on pages 133 and 165)
- Paige, Christopher C. and Saunders, Michael A. LSQR: An Algorithm for Sparse Linear Equations and Sparse Least Squares. *ACM Trans. Math. Softw.*, 8(1):43–71, 1982. doi:10.1145/355984.355989. (cited on page 151)

- Panning, Mark P.; Lognonné, Philippe; Bruce Banerdt, W.; Garcia, Raphaël; Golombek, Matthew; Kedar, Sharon; Knapmeyer-Endrun, Brigitte; Mocquet, Antoine; Teanby, Nick A.; Tromp, Jeroen; Weber, Renee; Beucler, Eric; Blanchette-Guertin, Jean-Francois; Bozdağ, Ebru; Drilleau, Mélanie; Gudkova, Tamara; Hempel, Stefanie; Khan, Amir; Lekić, Vedran; Murdoch, Naomi; Plesa, Ana-Catalina; Rivoldini, Atilio; Schmerr, Nicholas; Ruan, Youyi; Verhoeven, Olivier; Gao, Chao; Christensen, Ulrich; Clinton, John; Dehant, Veronique; Giardini, Domenico; Mimoun, David; Thomas Pike, W.; Smrekar, Sue; Wieczorek, Mark; Knapmeyer, Martin and Wookey, James. Planned Products of the Mars Structure Service for the InSight Mission to Mars. *Space Science Reviews*, 211(1):611–650, 2017. doi:10.1007/s11214-016-0317-5. (cited on page 30)
- Panou, A. A.; Theodulidis, N.P.; Hatzidimitriou, P.M.; Savvaidis, A.S. and Papazachos, C.B. Reliability of Ambient Noise Horizontal-to-Vertical Spectral Ratio in Urban Environments: The Case of Thessaloniki City (Northern Greece). *pure and applied geophysics*, 162(5):891–912, 2005. doi:10.1007/s00024-004-2647-6. (cited on page 31)
- Parolai, S.; Picozzi, M.; Richwalski, S. M. and Milkereit, C. Joint inversion of phase velocity dispersion and H/V ratio curves from seismic noise recordings using a genetic algorithm, considering higher modes. *Geophysical Research Letters*, 32(1):L01303, 2005. doi:10.1029/2004GL021115. (cited on pages 31 and 32)
- Patterson, D. E. and Smith, M. W. Unfrozen water content in saline soils: results using time-domain reflectometry. *Can. Geotech. J.*, 22(1):95–101, 1985. doi:10.1139/t85-009. (cited on page 80)
- Payne, L.E.; Song, J.C. and Straughan, B. Double diffusive porous penetrative convection: thawing subsea permafrost. *International Journal of Engineering Science*, 26(8):797–809, 1988. doi:10.1016/0020-7225(88)90031-6. (cited on page 65)
- Peterson, Bruce J.; Holmes, Robert M.; McClelland, James W.; Vörösmarty, Charles J.; Lammers, Richard B.; Shiklomanov, Alexander I.; Shiklomanov, Igor A. and Rahmstorf, Stefan. Increasing River Discharge to the Arctic Ocean. *Science*, 298(5601):2171–2173, 2002. doi:10.1126/science.1077445. (cited on page 168)
- Picozzi, M.; Parolai, S. and Richwalski, S. M. Joint inversion of H/V ratios and dispersion curves from seismic noise: Estimating the S-wave velocity of bedrock. *Geophysical Research Letters*, 32(11):L11308, 2005. doi:10.1029/2005GL022878. (cited on pages 31 and 32)
- Pilz, Marco; Parolai, Stefano and Bindi, Dino. Three-dimensional passive imaging of complex seismic fault systems: evidence of surface traces of the Issyk-Ata fault (Kyrgyzstan). *Geophysical Journal International*, 194(3):1955–1965, 2013. doi:10.1093/gji/ggt214. (cited on page 55)
- Pollack, Henry N. and Smerdon, Jason E. Borehole climate reconstructions: Spatial structure and hemispheric averages. *J. Geophys. Res.*, 109(D11):D11106, 2004. doi:10.1029/2003JD004163. (cited on pages 133, 142, and 166)
- Pollack, Henry N.; Hurter, Suzanne J. and Johnson, Jeffrey R. Heat flow from the Earth's interior: Analysis of the global data set. *Reviews of Geophysics*, 31(3):267–280, 1993. doi:10.1029/93RG01249. (cited on pages 93 and 150)
- Pollack, Henry N.; Huang, Shaopeng and Shen, Po-Yu. Climate Change Record in Subsurface Temperatures: A Global Perspective. *Science*, 282(5387):279–281, 1998. doi:10.1126/science.282.5387.279. (cited on page 141)

- Pollack, Henry N.; Demezhko, Dmitriy Y.; Duchkov, Albert D.; Golovanova, Inessa V.; Huang, Shaopeng; Shchapov, Vladislav A. and Smerdon, Jason E. Surface temperature trends in Russia over the past five centuries reconstructed from borehole temperatures. *J. Geophys. Res.*, 108(B4):2180, 2003. doi:10.1029/2002JB002154. (cited on pages 16 and 134)
- Pollack, Henry N.; Smerdon, Jason E. and van Keken, Peter E. Variable seasonal coupling between air and ground temperatures: A simple representation in terms of subsurface thermal diffusivity. *Geophysical Research Letters*, 32(15):L15405, 2005. doi:10.1029/2005GL023869. (cited on page 142)
- Ponomarev, V. On the history of the Kozhevnikov Bay in the Quaternary. *Sov. Geol.*, 11: 95–101, 1940. (cited on pages 89, 116, and 128)
- Portnov, Alexey; Smith, Andrew J.; Mienert, Jürgen; Cherkashov, Georgy; Rekant, Pavel; Semenov, Peter; Serov, Pavel and Vanshtein, Boris. Offshore permafrost decay and massive seabed methane escape in water depths >20 m at the South Kara Sea shelf. *Geophysical Research Letters*, 40(15):3962–3967, 2013. doi:10.1002/grl.50735. (cited on pages 6, 25, and 131)
- Rachold, Volker; Bolshiyarov, Dmitry Yu; Grigoriev, Mikhail N.; Hubberten, Hans-Wolfgang; Junker, Ralf; Kunitsky, Victor V.; Merker, Franziska; Overduin, Paul and Schneider, Waldemar. Nearshore arctic subsea permafrost in transition. *Eos Trans. AGU*, 88(13):149–156, 2007. doi:10.1029/2007EO130001. (cited on pages 6, 7, 11, 70, and 89)
- Rachor, Eike. Scientific Cruise Report of the Arctic Expedition ARK-XI/1 of RV ‘POLARSTERN’ in 1995. *Reports on Polar Research, Alfred Wegener Institute for Polar and Marine Research, Bremerhaven*, 226:173, 1997. ISSN 0176 - 5027. (cited on page 25)
- Rajeev, Pathmanathan and Kodikara, Jayantha. Estimating apparent thermal diffusivity of soil using field temperature time series. *Geomechanics and Geoengineering*, 11(1): 28–46, 2016. doi:10.1080/17486025.2015.1006266. (cited on page 148)
- Rekant, P.; Bauch, H. A.; Schwenk, T.; Portnov, A.; Gusev, E.; Spiess, V.; Cherkashov, G. and Kassens, H. Evolution of subsea permafrost landscapes in Arctic Siberia since the Late Pleistocene: a synoptic insight from acoustic data of the Laptev Sea. *arktos*, 1(1): 11, 2015. doi:10.1007/s41063-015-0011-y. (cited on pages 6, 25, and 131)
- Rekant, P.V. and Vasiliev, A.A. Offshore permafrost in the Kara Sea. *Earth Cryosphere*, XV(4):60–62, 2011. (cited on page 6)
- Reliable Prognostics. Weather archive on Stolb Island, 2017. URL https://rp5.ru/Weather_archive_on_Stolb_Island. Accessed 23 Feb 2017. (cited on page 165)
- Rickett, James and Claerbout, Jon. Acoustic daylight imaging via spectral factorization: Helioseismology and reservoir monitoring. *The Leading Edge*, 18(8):957–960, 1999. doi:10.1190/1.1438420. (cited on page 40)
- Rivera, Janiel; Karabanov, Eugene B.; Williams, Douglas F.; Buchinskyi, Valeryi and Kuzmin, Michael. Lena River discharge events in sediments of Laptev Sea, Russian Arctic. *Estuarine, Coastal and Shelf Science*, 66(1–2):185–196, 2006. doi:10.1016/j.ecss.2005.08.009. (cited on page 145)

- Roberts, J. L.; Moy, A. D.; van Ommen, T. D.; Curran, M. A. J.; Worby, A. P.; Goodwin, I. D. and Inoue, M. Borehole temperatures reveal a changed energy budget at Mill Island, East Antarctica, over recent decades. *The Cryosphere*, 7(1):263–273, 2013. doi:10.5194/tc-7-263-2013. (cited on pages 141, 147, 153, and 163)
- Rodgers, Peter W.; Martin, Aaron J.; Robertson, Michelle C.; Hsu, Mark M. and Harris, David B. Signal-coil calibration of electromagnetic seismometers. *Bulletin of the Seismological Society of America*, 85(3):845–850, 1995. URL <https://pubs.geoscienceworld.org/bssa/article-abstract/85/3/845/119992/signal-coil-calibration-of-electromagnetic?redirectedFrom=fulltext>. (cited on page 42)
- Roe, P. L. Characteristic-Based Schemes for the Euler Equations. *Annual Review of Fluid Mechanics*, 18(1):337–365, 1986. doi:10.1146/annurev.fl.18.010186.002005. (cited on page 87)
- Rogers, James C. and Morack, John L. Geophysical evidence of shallow nearshore permafrost, Prudhoe Bay, Alaska. *Journal of Geophysical Research: Solid Earth*, 85(B9): 4845–4853, 1980. doi:10.1029/JB085iB09p04845. (cited on pages 23 and 80)
- Romanovskii, N.; Hubberten, H.; Romanovsky, V. and Kholodov, A. Permafrost evolution under the influence of long-term climate fluctuations and glacio-eustatic sea-level variation: region of Laptev and East Siberian Seas, Russia. In: Phillips, Marcia; Springman, Sarah M. and Arenson, Lukas U.(eds.), *Permafrost: proceedings of the 8th International Conference on Permafrost, 21-25 July 2003, Zurich, Switzerland*, volume 2, pages 983–987. Balkema, 2003. (cited on pages 62, 132, and 172)
- Romanovskii, N.; Hubberten, H.; Gavrillov, A.V.; Tumskoy, V.E. and Kholodov, A.L. Permafrost of the east Siberian Arctic shelf and coastal lowlands. *Quaternary Science Reviews*, 23(11-13):1359–1369, 2004. doi:10.1016/j.quascirev.2003.12.014. (cited on pages 4, 5, 115, 119, 132, and 172)
- Romanovskii, N. N.; Hubberten, H. W.; Gavrillov, A. V.; Eliseeva, A. A. and Tipenko, G. S. Offshore permafrost and gas hydrate stability zone on the shelf of East Siberian Seas. *Geo-Marine Letters*, 25(2):167–182, 2005. doi:10.1007/s00367-004-0198-6. (cited on pages 6 and 7)
- Romanovskii, Nikolai N. and Hubberten, Hans-W. Results of permafrost modelling of the lowlands and shelf of the Laptev Sea Region, Russia. *Permafrost and Periglacial Processes*, 12(2):191–202, 2001. doi:10.1002/ppp.387. (cited on pages 5, 6, 12, and 62)
- Romanovsky, V. E. and Osterkamp, T. E. Effects of unfrozen water on heat and mass transport processes in the active layer and permafrost. *Permafrost and Periglacial Processes*, 11(3):219–239, 2000. doi:10.1002/1099-1530(200007/09)11:3<219::AID-PPP352>3.0.CO;2-7. (cited on page 78)
- Romanovsky, V. E.; Drozdov, D. S.; Oberman, N. G.; Malkova, G. V.; Kholodov, A. L.; Marchenko, S. S.; Moskalenko, N. G.; Sergeev, D. O.; Ukraintseva, N. G.; Abramov, A. A.; Gilichinsky, D. A. and Vasiliev, A. A. Thermal state of permafrost in Russia. *Permafrost and Periglacial Processes*, 21(2):136–155, 2010a. doi:10.1002/ppp.683. (cited on page 93)
- Romanovsky, Vladimir E.; Smith, Sharon L. and Christiansen, Hanne H. Permafrost thermal state in the polar Northern Hemisphere during the international polar year 2007–2009: a synthesis. *Permafrost and Periglacial Processes*, 21(2):106–116, 2010b. doi:10.1002/ppp.689. (cited on page 92)

- Roth, Kurt. *Soil Physics Lecture Notes, V2.2*. Institute of Environmental Physics, Heidelberg University, 2012. URL www.iup.uni-heidelberg.de/institut/forschung/groups/ts/students/sp. (cited on pages 84, 86, and 137)
- Roux, Philippe and Fink, Mathias. Green's function estimation using secondary sources in a shallow water environment. *The Journal of the Acoustical Society of America*, 113(3): 1406–1416, 2003. doi:10.1121/1.1542645. (cited on page 40)
- Ruddiman, W. F.; Fuller, D. Q.; Kutzbach, J. E.; Tzedakis, P. C.; Kaplan, J. O.; Ellis, E. C.; Vavrus, S. J.; Roberts, C. N.; Fyfe, R.; He, F.; Lemmen, C. and Woodbridge, J. Late Holocene climate: Natural or anthropogenic? *Rev. Geophys.*, 54(1):93–118, 2016. doi:10.1002/2015RG000503. (cited on page 133)
- Ruppel, C. Methane hydrates and contemporary climate change. *Nature Education Knowledge*, 3(10):29, 2011. URL <http://www.nature.com/scitable/knowledge/library/methane-hydrates-and-contemporary-climate-change-24314790>. (cited on page 9)
- Ruppel, Carolyn D. and Kessler, John D. The interaction of climate change and methane hydrates. *Reviews of Geophysics*, 55(1):126–168, 2017. doi:10.1002/2016RG000534. 2016RG000534. (cited on pages 6, 9, and 10)
- Ruppel, Carolyn D.; Herman, Bruce M.; Brothers, Laura L. and Hart, Patrick E. Subsea ice-bearing permafrost on the U.S. Beaufort Margin: 2. Borehole constraints. *Geochemistry, Geophysics, Geosystems*, 17(11):4333–4353, 2016. doi:10.1002/2016GC006582. (cited on page 6)
- Sabra, Karim G.; Gerstoft, Peter; Roux, Philippe; Kuperman, W. A. and Fehler, Michael C. Extracting time-domain Green's function estimates from ambient seismic noise. *Geophys. Res. Lett.*, 32(3):L03310, 2005a. doi:10.1029/2004GL021862. (cited on pages 33 and 39)
- Sabra, Karim G.; Gerstoft, Peter; Roux, Philippe; Kuperman, W. A. and Fehler, Michael C. Surface wave tomography from microseisms in Southern California. *Geophys. Res. Lett.*, 32(14):L14311, 2005b. doi:10.1029/2005GL023155. (cited on page 39)
- Sanchez-Sesma, Francisco J.; Rodriguez, Miguel; Iturraran-Viveros, Ursula; Luzon, Francisco; Campillo, Michel; Margerin, Ludovic; Garcia-Jerez, Antonio; Suarez, Martha; Santoyo, Miguel A. and Rodriguez-Castellanos, Alejandro. A theory for microtremor H/V spectral ratio: application for a layered medium. *Geophysical Journal International*, 186(1):221–225, 2011. doi:10.1111/j.1365-246X.2011.05064.x. (cited on pages 31, 32, and 55)
- Scherbaum, Frank. Seismic imaging of the site response using microearthquake recordings. Part II. Application to the Swabian Jura, southwest Germany, Seismic network. *Bulletin of the Seismological Society of America*, 77(6):1924–1944, 1987. URL <https://pubs.geoscienceworld.org/bssa/article-abstract/77/6/1924/118994/seismic-imaging-of-the-site-response-using?redirectedFrom=fulltext>. (cited on page 33)
- Scherbaum, Frank. *Of poles and zeros: Fundamentals of digital seismology*. Kluwer Academic Publishers, Dordrecht, The Netherlands, 1996. (cited on page 42)
- Scherbaum, Frank; Hinzen, Klaus-G. and Ohrnberger, Matthias. Determination of shallow shear wave velocity profiles in the Cologne, Germany area using ambient vibrations. *Geophysical Journal International*, 152(3):597–612, 2003. doi:10.1046/j.1365-246X.2003.01856.x. (cited on page 31)

- Schirrmeister, L.; Kunitsky, V.; Grosse, G.; Wetterich, S.; Meyer, H.; Schwamborn, G.; Babiy, O.; Derevyagin, A. and Siegert, C. Sedimentary characteristics and origin of the Late Pleistocene Ice Complex on north-east Siberian Arctic coastal lowlands and islands - A review. *Quaternary International*, 241(1-2):3–25, 2011a. doi:10.1016/j.quaint.2010.04.004. (cited on page 2)
- Schirrmeister, L.; Froese, D.; Tumskey, V.; Grosse, G. and Wetterich, S. Yedoma: Late Pleistocene Ice-Rich Syngenetic Permafrost of Beringia. In: Elias, S.A.(ed.), *The Encyclopedia of Quaternary Science*, volume 3, pages 542–552. Amsterdam: Elsevier, 2013. (cited on pages 1 and 2)
- Schirrmeister, L.; Schwamborn, G.; Overduin, P. P.; Strauss, J.; Fuchs, M. C.; Grigoriev, M.; Yakshina, I.; Rethemeyer, J.; Dietze, E. and Wetterich, S. Yedoma Ice Complex of the Buor Khaya Peninsula (southern Laptev Sea). *Biogeosciences*, 14(5):1261–1283, 2017. doi:10.5194/bg-14-1261-2017. (cited on page 71)
- Schirrmeister, Lutz; Grosse, Guido; Kunitsky, Viktor; Magens, Diana; Meyer, Hanno; Dereviagin, Alexander; Kuznetsova, Tatyana; Andreev, Andrei; Babiy, Olga; Kienast, Frank; Grigoriev, Mikhael; Overduin, Pier Paul and Preusser, Frank. Periglacial landscape evolution and environmental changes of Arctic lowland areas for the last 60 000 years (western Laptev Sea coast, Cape Mamontov Klyk). *Polar Research*, 27(2): 249–272, 2008. doi:10.1111/j.1751-8369.2008.00067.x. (cited on page 68)
- Schirrmeister, Lutz; Grosse, Guido; Wetterich, Sebastian; Overduin, Pier Paul; Strauss, Jens; Schuur, Edward A. G. and Hubberten, Hans-Wolfgang. Fossil organic matter characteristics in permafrost deposits of the northeast Siberian Arctic. *Journal of Geophysical Research: Biogeosciences*, 116:G00M02, 2011b. doi:10.1029/2011JG001647. (cited on page 91)
- Schuster, G. T. Theory of daylight/interferometric imaging: Tutorial. In *63rd EAGE Conference & Exhibition*, 2001. (cited on page 33)
- Schuster, Gerard T. *Seismic Interferometry*, chapter 5, pages Q1–1–Q1–41. 2016. doi:10.1190/1.9781560803027.entry5. (cited on page 33)
- Schuster, Gerard Thomas. *Seismic Interferometry*. Cambridge University Press, 2009. doi:10.1017/CBO9780511581557. (cited on page 33)
- Schuur, Edward A. G.; Vogel, Jason G.; Crummer, Kathryn G.; Lee, Hanna; Sickman, James O. and Osterkamp, T. E. The effect of permafrost thaw on old carbon release and net carbon exchange from tundra. *Nature*, 459(7246):556–559, 2009. doi:10.1038/nature08031. (cited on page 134)
- Schwamborn, Georg; Rachold, Volker and Grigoriev, Mikhail N. Late Quaternary sedimentation history of the Lena Delta. *Quaternary International*, 89(1):119–134, 2002. doi:10.1016/S1040-6182(01)00084-2. (cited on pages 22 and 144)
- Schwamborn, Georg Johannes. *Late quaternary sedimentation history of the Lena delta = Spätquartäre Sedimentationsgeschichte im Lena-Delta*, volume 471 of *Berichte zur Polar- und Meeresforschung (Reports on Polar and Marine Research)*. Alfred Wegener Institute for Polar and Marine Research, Bremerhaven, Germany, 2004. (cited on page 68)
- Sens-Schönfelder, C. and Wegler, U. Passive image interferometry and seasonal variations of seismic velocities at Merapi Volcano, Indonesia. *Geophysical Research Letters*, 33(21): L21302, 2006. doi:10.1029/2006GL027797. (cited on page 40)

- SESAME. Guidelines for the implementation of the H/V spectral ratio technique on ambient vibrations measurements, processing and interpretation. *SESAME EVG1-CT-2000-00026, WP12, Deliverable D23.12*, page 62, 2004. (cited on page 45)
- Shakhova, N.; Semiletov, I.; Leifer, I.; Salyuk, A.; Rekant, P. and Kosmach, D. Geochemical and geophysical evidence of methane release over the East Siberian Arctic Shelf. *Journal of Geophysical Research: Oceans*, 115(C8):C08007, 2010. doi:10.1029/2009JC005602. (cited on pages 6, 7, and 9)
- Shakhova, Natalia; Semiletov, Igor; Gustafsson, Orjan; Sergienko, Valentin; Lobkovsky, Leopold; Dudarev, Oleg; Tumskey, Vladimir; Grigoriev, Michael; Mazurov, Alexey; Salyuk, Anatoly; Ananiev, Roman; Koshurnikov, Andrey; Kosmach, Denis; Charkin, Alexander; Dmitrevsky, Nicolay; Karnaukh, Victor; Gunar, Alexey; Meluzov, Alexander and Chernykh, Denis. Current rates and mechanisms of subsea permafrost degradation in the East Siberian Arctic Shelf. *Nature Communications*, 8:15872, 2017. doi:10.1038/ncomms15872. (cited on pages 10 and 131)
- Shapiro, N. M. and Campillo, M. Emergence of broadband Rayleigh waves from correlations of the ambient seismic noise. *Geophys. Res. Lett.*, 31(7):L07614, 2004. doi:10.1029/2004GL019491. (cited on pages 33 and 39)
- Shapiro, Nikolai M.; Campillo, Michel; Stehly, Laurent and Ritzwoller, Michael H. High-Resolution Surface-Wave Tomography from Ambient Seismic Noise. *Science*, 307(5715): 1615–1618, 2005. doi:10.1126/science.1108339. (cited on pages 33 and 39)
- Shen, P. Y. and Beck, A. E. Least squares inversion of borehole temperature measurements in functional space. *Journal of Geophysical Research: Solid Earth*, 96(B12):19965–19979, 1991. doi:10.1029/91JB01883. (cited on page 141)
- Shen, P.Y. and Beck, A.E. Paleoclimate change and heat flow density inferred from temperature data in the Superior Province of the Canadian shield. *Global and Planetary Change*, 6:143–165, 1992. (cited on page 141)
- Shen, P.Y.; Wang, K.; Beltrami, H. and Mareschal, J.-C. Climatic Change Inferred from Underground Temperatures: A comparative study of inverse methods for estimating climatic history from borehole temperature data. *Palaeogeography, Palaeoclimatology, Palaeoecology*, 98(2):113–127, 1992. doi:10.1016/0031-0182(92)90192-8. (cited on pages 140 and 162)
- Sheriff, R.E. and Geldart, L.P. *Exploration Seismology*. Cambridge University Press, 1995. (cited on page 23)
- Shi, Feng; Yang, Bao; Mairesse, Aurélien; von Gunten, Lucien; Li, Jianping; Bräuning, Achim; Yang, Fengmei and Xiao, Xia. Northern Hemisphere temperature reconstruction during the last millennium using multiple annual proxies. *Clim Res*, 56(3):231–244, 2013. doi:10.3354/cr01156. (cited on page 133)
- Slagoda, E. A. *Genesis i mikrostroenie kriolitogennykh otlozhenii Bykovskogo polystrova i ostrova Muostakh [Genesis and microstructure of cryolithogenic deposits at the Bykovsky Peninsula and the Muostakh Island] [in Russian]*. PhD thesis, Russian Academy of Science, Siberian Branch, Mel'nikov Permafrost Institute, Yakutsk, 1993. (cited on pages 7, 43, 54, and 56)

- Slagoda, E.A. *Kriolitogennye otlozheniya primorskoi ravniny morya Laptevykh: litologiya i mikromorfologiya (poluostrov Bykovskiy i ostrov Muostakh) - Cryolitic sediments of the Laptev Sea coastal lowland: lithology and micromorphology (Bykovsky Peninsula and Muostakh Island)*. Ekspress, Tyumen, 2004. ISBN 5-98100-025-2. (cited on page 71)
- Smalls, P. T.; Paull, C. K. and Dallimore, S. Benthic Gouge Marks in the Canadian Beaufort Sea: Associations Between Whales and Methane Seeps? In *American Geophysical Union, Fall Meeting 2015, abstract id. OS33A-2007*, 2015. (cited on page 127)
- Smerdon, Jason E. and Stieglitz, Marc. Simulating heat transport of harmonic temperature signals in the Earth's shallow subsurface: Lower-boundary sensitivities. *Geophysical Research Letters*, 33(14):L14402, 2006. doi:10.1029/2006GL026816. (cited on pages 93 and 150)
- Smerdon, Jason E.; Pollack, Henry N.; Cermak, Vladimir; Enz, John W.; Kresl, Milan; Safanda, Jan and Wehmiller, John F. Air-ground temperature coupling and subsurface propagation of annual temperature signals. *Journal of Geophysical Research: Atmospheres*, 109(D21):D21107, 2004. doi:10.1029/2004JD005056. (cited on pages 142 and 156)
- Snieder, Roel. Extracting the Green's function from the correlation of coda waves: A derivation based on stationary phase. *Phys. Rev. E*, 69(4):046610, 2004. doi:10.1103/PhysRevE.69.046610. (cited on page 37)
- Snieder, Roel and Safak, Erdal. Extracting the Building Response Using Seismic Interferometry: Theory and Application to the Millikan Library in Pasadena, California. *Bulletin of the Seismological Society of America*, 96(2):586–598, 2006. doi:10.1785/0120050109. (cited on page 40)
- Solomon, S. M.; Taylor, A. E. and Stevens, C. W. Nearshore ground temperatures, seasonal ice bonding, and permafrost formation within the bottom-fast ice zone, Mackenzie Delta, NWT. In: Kane, D.L. and Hinkel, K.M.(eds.), *Proceedings of the Ninth International Conference on Permafrost*, volume 1, pages 1675–1680. Inst. of North. Eng., Univ. of Alaska Fairbanks, Fairbanks, 2008. (cited on page 124)
- Soloviev, V.A.; Ginsburg, G.D.; Telepnev, Eu.V. and Mikhalyuk, Yu.N. Cryogeothermal parameters and hydrates of near-bottom gases in the Arctic Ocean (in Russian). *PGO "Sevmorgeologia", Leningrad*, page 150, 1987. (cited on pages 6 and 128)
- Stevens, M. Bruce; Smerdon, Jason E.; Gonzalez-Rouco, J. Fidel; Stieglitz, Marc and Beltrami, Hugo. Effects of bottom boundary placement on subsurface heat storage: Implications for climate model simulations. *Geophys. Res. Lett.*, 34(2):L02702, 2007. doi:10.1029/2006GL028546. (cited on pages 93 and 150)
- Stieglitz, Marc; Dery, S. J.; Romanovsky, V. E. and Osterkamp, T. E. The role of snow cover in the warming of arctic permafrost. *Geophysical Research Letters*, 30(13):1721, 2003. doi:10.1029/2003GL017337. (cited on page 142)
- Stoll, Robert D. Acoustic waves in ocean sediments. *Geophysics*, 42(4):715–725, 1977. doi:10.1190/1.1440741. (cited on pages 51, 55, and 183)
- Strauß, Jens. *Organic carbon in ice-rich permafrost: Characteristics, quantity, and availability*. PhD thesis, Universität Potsdam, 2014. URL <http://d-nb.info/1070693308>. (cited on page 4)

- Strauss, Jens; Schirrmeister, Lutz; Grosse, Guido; Fortier, Daniel; Hugelius, Gustaf; Knoblauch, Christian; Romanovsky, Vladimir; Schädel, Christina; von Deimling, Thomas Schneider; Schuur, Edward A.G.; Shmelev, Denis; Ulrich, Mathias and Veremeeva, Alexandra. Deep Yedoma permafrost: A synthesis of depositional characteristics and carbon vulnerability. *Earth-Science Reviews*, 172:75–86, 2017. doi:10.1016/j.earscirev.2017.07.007. (cited on pages 71 and 91)
- Strollo, A.; Bindi, D.; Parolai, S. and Jäckel, K.-H. On the suitability of 1 s geophone for ambient noise measurements in the 0.1–20 Hz frequency range: experimental outcomes. *Bulletin of Earthquake Engineering*, 6(1):141–147, 2008a. doi:10.1007/s10518-008-9061-x. (cited on page 45)
- Strollo, A.; Parolai, S.; Jäckel, K.-H.; Marzorati, S. and Bindi, D. Suitability of Short-Period Sensors for Retrieving Reliable H/V Peaks for Frequencies Less Than 1 Hz. *Bulletin of the Seismological Society of America*, 98(2):671–681, 2008b. doi:10.1785/0120070055. (cited on page 45)
- Subcommittee Permafrost. Glossary of permafrost and related ground-ice terms. *Associate Committee on Geotechnical Research, National Research Council of Canada, Technical Memorandum*, 142:156, 1988. (cited on page 1)
- Swift, Daniel W. and Harrison, William D. Convective transport of brine and thaw of subsea permafrost: Results of numerical simulations. *Journal of Geophysical Research: Oceans*, 89(C2):2080–2086, 1984. doi:10.1029/JC089iC02p02080. (cited on pages 13, 65, 66, 89, 121, and 129)
- Swift, D.W.; Harrison, W. D. and Osterkamp, T.E. Heat and salt transport transport processes in thawing subsea permafrost at Prudhoe Bay, Alaska. In *Permafrost: Fourth Intern. Conf., Proceedings*, pages 1221–1226. Nat. Acad. Press, 1983. (cited on pages 64, 89, and 121)
- Taylor, Alan E.; Dallimore, Scott R. and Outcalt, S. I. Late Quaternary history of the Mackenzie-Beaufort region, Arctic Canada, from modelling of permafrost temperatures. 1. The onshore-offshore transition. *Canadian Journal of Earth Sciences*, 33(1):52–61, 1996. doi:10.1139/e96-006. (cited on page 63)
- Taylor, Alan E.; Dallimore, S. R.; Hill, P. R.; Issler, D. R.; Blasco, S. and Wright, F. Numerical model of the geothermal regime on the Beaufort Shelf, arctic Canada since the Last Interglacial. *Journal of Geophysical Research: Earth Surface*, 118(4):2365–2379, 2013. doi:10.1002/2013JF002859. (cited on page 63)
- Tikhonov, A. N. and Samarskii, A. A. *Equations of Mathematical Physics*. Dover Publications, 1990. (cited on page 141)
- Timokhov, L.A. Regional characteristics of the Laptev and the East Siberian Seas: Climate, topography, ice phases, thermohaline regime, circulation. In: Kassens, Heidemarie; Hubberten, Hans-Wolfgang; Pryamikov, Sergey M. and Stein, Rüdiger (eds.), *Russian-German Cooperation in the Siberian Shelf Seas: Geo-System Laptev-Sea*. Ber. Polarforsch. 144, 1994. (cited on page 143)
- Timur, A. Velocity of compressional waves in porous media at permafrost temperatures. *Geophysics*, 33(4):584–595, 1968. (cited on page 23)

- Toohey, R. C.; Herman-Mercer, N. M.; Schuster, P. F.; Mutter, E. A. and Koch, J. C. Multidecadal increases in the Yukon River Basin of chemical fluxes as indicators of changing flowpaths, groundwater, and permafrost. *Geophysical Research Letters*, 43(23): 12,120–12,130, 2016. doi:10.1002/2016GL070817. (cited on page 8)
- Tuan, Tran Thanh; Malischewsky, Peter G.; Scherbaum, Frank and Ohrnberger, Matthias. Dispersion of zero-frequency Rayleigh waves in an isotropic model 'Layer over half-space'. *Geophysical Journal International*, 175(2):537–540, 2008. doi:10.1111/j.1365-246X.2008.03917.x. (cited on page 31)
- Tuan, Tran Thanh; Scherbaum, Frank and Malischewsky, Peter G. On the relationship of peaks and troughs of the ellipticity (H/V) of Rayleigh waves and the transmission response of single layer over half-space models. *Geophysical Journal International*, 184(2):793–800, 2011. doi:10.1111/j.1365-246X.2010.04863.x. (cited on page 31)
- van Manen, Dirk-Jan; Curtis, Andrew and Robertsson, Johan A. O. Interferometric modeling of wave propagation in inhomogeneous elastic media using time reversal and reciprocity. *Geophysics*, 71(4):SI47–SI60, 2006. doi:10.1190/1.2213218. (cited on page 40)
- Vanneste, Maarten; Madshus, Christian; Socco, Valentina L.; Maraschini, Margherita; Sparrevik, Per M.; Westerdahl, Harald; Duffaut, Kenneth; Skomedal, Eiliv and Bjornara, Tore I. On the use of the Norwegian Geotechnical Institute's prototype seabed-coupled shear wave vibrator for shallow soil characterization – I. Acquisition and processing of multimodal surface waves. *Geophysical Journal International*, 185(1):221–236, 2011. doi:10.1111/j.1365-246X.2011.04960.x. (cited on pages 51 and 55)
- Vasil'ev, V. I.; Maksimov, A. M.; Petrov, E. E. and Tsyppkin, G. G. Mathematical model of the freezing-thawing of saline frozen soil. *Journal of Applied Mechanics and Technical Physics*, 36:689–696, 1995. doi:10.1007/BF02369282. (cited on page 63)
- Vavrus, Steve; Holland, Marika M. and Bailey, David A. Changes in Arctic clouds during intervals of rapid sea ice loss. *Climate Dynamics*, 36(7):1475–1489, 2011. doi:10.1007/s00382-010-0816-0. (cited on page 168)
- Wagner, D.; Kobabe, S.; Pfeiffer, E.-M. and Hubberten, H.-W. Microbial controls on methane fluxes from a polygonal tundra of the Lena Delta, Siberia. *Permafrost Periglac. Process.*, 14(2):173–185, 2003. doi:10.1002/ppp.443. (cited on pages 92, 144, and 145)
- Walter Anthony, Katey M.; Anthony, Peter; Grosse, Guido and Chanton, Jeffrey. Geologic methane seeps along boundaries of Arctic permafrost thaw and melting glaciers. *Nature Geoscience*, advance online publication:419–426, 2012. doi:10.1038/ngeo1480. (cited on page 10)
- Wang, Kelin. Estimation of ground surface temperatures from borehole temperature data. *Journal of Geophysical Research: Solid Earth*, 97(B2):2095–2106, 1992. doi:10.1029/91JB02716. (cited on page 141)
- Wang, Rongjiang. A simple orthonormalization method for stable and efficient computation of Green's functions. *Bulletin of the Seismological Society of America*, 89(3):733–741, 1999. URL <https://pubs.geoscienceworld.org/ssa/bssa/article-abstract/89/3/733/120414/a-simple-orthonormalization-method-for-stable-and>. (cited on page 183)
- Wapenaar, Kees. Synthesis of an inhomogeneous medium from its acoustic transmission response. *Geophysics*, 68(5):1756–1759, 2003. doi:10.1190/1.1620649. (cited on page 33)

- Wapenaar, Kees. Retrieving the Elastodynamic Green's Function of an Arbitrary Inhomogeneous Medium by Cross Correlation. *Phys. Rev. Lett.*, 93(25):254301, 2004. doi:10.1103/PhysRevLett.93.254301. (cited on page 39)
- Wapenaar, Kees; Draganov, Deyan; Snieder, Roel; Campman, Xander and Verdel, Arie. Tutorial on seismic interferometry: Part 1 - Basic principles and applications. *Geophysics*, 75(5):75A195–75A209, 2010a. doi:10.1190/1.3457445. (cited on pages 33, 35, 38, and 39)
- Wapenaar, Kees; Slob, Evert; Snieder, Roel and Curtis, Andrew. Tutorial on seismic interferometry: Part 2 - Underlying theory and new advances. *Geophysics*, 75(5):75A211–75A227, 2010b. doi:10.1190/1.3463440. (cited on page 33)
- Weismüller, J.; Wollschläger, U.; Boike, J.; Pan, X.; Yu, Q. and Roth, K. Modeling the thermal dynamics of the active layer at two contrasting permafrost sites on Svalbard and on the Tibetan Plateau. *The Cryosphere*, 5(3):741–757, 2011. doi:10.5194/tc-5-741-2011. (cited on pages 156 and 170)
- Westermann, S. *Sensitivity of permafrost*. PhD thesis, Ruperto-Carola University of Heidelberg, Germany, 2010. (cited on page 72)
- Westermann, S.; Boike, J.; Langer, M.; Schuler, T. V. and Etzelmüller, B. Modeling the impact of wintertime rain events on the thermal regime of permafrost. *The Cryosphere*, 5(4):945–959, 2011. doi:10.5194/tc-5-945-2011. (cited on page 90)
- Westermann, S.; Schuler, T. V.; Gislås, K. and Etzelmüller, B. Transient thermal modeling of permafrost conditions in Southern Norway. *The Cryosphere*, 7(2):719–739, 2013. doi:10.5194/tc-7-719-2013. (cited on page 90)
- Whitehouse, Pippa L.; Allen, Mark B. and Milne, Glenn A. Glacial isostatic adjustment as a control on coastal processes: An example from the Siberian Arctic. *Geology*, 35(8):747–750, 2007. doi:10.1130/G23437A.1. (cited on page 3)
- Winterfeld, Maria; Schirrmeister, Lutz; Grigoriev, Mikhail N.; Kunitsky, Viktor V.; Andreev, Andrei; Murray, Andrew and Overduin, Pier Paul. Coastal permafrost landscape development since the Late Pleistocene in the western Laptev Sea, Siberia. *Boreas*, 40(4):697–713, 2011. doi:10.1111/j.1502-3885.2011.00203.x. (cited on pages 70, 89, 91, 128, and 148)
- Wood, W. T.; Gettrust, J. F.; Chapman, N. R.; Spence, G. D. and Hyndman, R. D. Decreased stability of methane hydrates in marine sediments owing to phase-boundary roughness. *Nature*, 420(6916):656–660, 2002. doi:10.1038/nature01263. (cited on page 25)
- Yamanaka, Hiroaki; Takemura, Masayuki; Ishida, Hiroshi and Niwa, Masanori. Characteristics of long-period microtremors and their applicability in exploration of deep sedimentary layers. *Bulletin of the Seismological Society of America*, 84(6):1831–1841, 1994. URL <https://pubs.geoscienceworld.org/bssa/article-abstract/84/6/1831/119826/characteristics-of-long-period-microtremors-and?redirectedFrom=fulltext>. (cited on pages 28 and 30)
- Yang, Daqing; Liu, Baozhong and Ye, Baisheng. Stream temperature changes over Lena River Basin in Siberia. *Geophys. Res. Lett.*, 32(5):L05401, 2005. doi:10.1029/2004GL021568. (cited on page 168)
- Yun, T. S.; Santamarina, J. C. and Ruppel, C. Mechanical properties of sand, silt, and clay containing tetrahydrofuran hydrate. *Journal of Geophysical Research: Solid Earth*, 112:B04106, 2007. doi:10.1029/2006JB004484. (cited on page 80)

- Zagorodnov, V.; Nagornov, O.; Scambos, T. A.; Muto, A.; Mosley-Thompson, E.; Pettit, E. C. and Tyuffin, S. Borehole temperatures reveal details of 20th century warming at Bruce Plateau, Antarctic Peninsula. *The Cryosphere*, 6(3):675–686, 2012. doi:10.5194/tc-6-675-2012. (cited on page 141)
- Zhang, T.; Barry, R. G.; Knowles, K.; Heginbottom, J. A. and Brown, J. Statistics and characteristics of permafrost and ground-ice distribution in the Northern Hemisphere. *Polar Geography*, 23(2):132–154, 1999. doi:10.1080/10889379909377670. (cited on page 1)
- Zhigarev, L.A. *Submarine cryolithozone (Okeanicheskaya kriolitozona) (in Russian)*. MSU Publishing, Moscow, 1997. (cited on page 7)
- Zimmerman, R. W. and King, M. S. The effect of the extent of freezing on seismic velocities in unconsolidated permafrost. *Geophysics*, 51(6):1285–1290, 1986. doi:10.1190/1.1442181. (cited on pages 23, 51, and 80)

Acknowledgements

This work would not have been possible without the support and help of a multitude of people. First of all, I would like to thank my PhD committee.

My special and warm thanks goes to Dr. Paul Overduin for being the best supervisor I could have wished for – scientifically but also personally. Thank you for providing excellent guidance, help, motivation, advice and all the support throughout my time at the Alfred Wegener Institute in Potsdam. I will always be thankful.

I would also like to thank Prof. Hans-Wolfgang Hubberten for the opportunity to work at AWI and especially in the Arctic, for his supervision, and ensuring financial support when I really needed it.

I am additionally indebted to Dr. Trond Ryberg (German Research Centre for Geoscience, GFZ) and Dr. Moritz Langer for their fruitful discussions, invaluable support, initial learning and continued advice regarding all geophysical (fieldwork and processing) and permafrost modelling aspects.

My Arctic expedition and the field work was only possible due to the row of people on the 2013 Lena-Delta crew. A great thanks to Dr. Birgit Heim, Antje Eulenburg, Dr. Mischa Grigoriev for giving me such a warm welcome on Samoylov. I am grateful to Waldemar Schneider for making all logistics possible. And a great thanks to Steffen Frey for enabling me to finish all the work on that last boat trip to Muostakh under the worst conditions! Thanks to Dr. Maria Winterfeld and all the other participants of the cruise that got delayed and that were invaluable company during my long lone days in Tiksi.

This work was partially funded by a Helmholtz Association Joint Russian-German Research Group (HGF JRG-100).

I am also grateful to the Graduate School for Polar and Marine Research (Dr. Claudia Hanfland and Dr. Claudia Sprengel) and the Potsdam Graduate School for providing possibilities for my career development including advanced research

training and financial support for my travels to conferences and meetings with project collaborators.

This work would also not have been possible without the IT help of Heiko Gericke and Tobias Schmidt. Thank you for enabling my use of the modelling capacities in Potsdam and the supercomputer in Bremerhaven. Thank you to Sigrun Gräning and Christine Litz for always finding a way in all administrative challenges.

I also want to acknowledge the help of Dr. Jens Strauss for synthetic core creation, and to thank Frank Günther, Stefan Kruse, and Dr. Heidrun Matthes for assisting in data compilation, and Dr. Tomas Opel and Dr. Volker Rath for helpful comments regarding the temperature reconstruction.

A special thanks to my office roomies at AWI: Dr. Frank Günther, Dr. Mathias Ulrich, and Michael Angelopoulos for the fun and great mood in the office. Thanks so much to all my PhD colleagues and friends, who supported me on this way, thanks to the AWI family for discussions scientific and otherwise, great times at conferences and the welcome in Potsdam: Dr. Josefine Lenz, Boris Radosavljevic, Dr. Lukas Schmidt, Dr. Franziska Hanf, Dr. Anja Sommerfeld, Dr. Paloma Serrano, Dr. Daniel Kreyling, Dr. Mareike Wiczorek, Dr. Heike Zimmermann, Dr. Romy Zibulski, Dr. Arne Ramisch, Stefan Schimpf, Dr. Julia Boike, Dr. Lutz Schirrmeister, Dr. Hugues Lantuit, Dr. Anne Morgenstern, Dr. Hanno Meyer, Dr. George Tanski, Samuel Stettner, Alison Beamish, Dr. Juliane Wolter, Dr. Anna Irrgang, Dr. Boris Biskaborn, Dr. Justine Ramage, Dr. Stefan Kruse, Dr. Roman Osudar, Dr. Frederieke Miesner, Bennet Juhls, Sofya Antonova, Dr. Sina Muster, Alex Runge. Especially for taking me in in Chamonix, Matthias Fuchs and Dr. Ingmar Nietzsche. The most heartfelt thanks go especially to Dr. Liv Heinecke, Dr. Stefanie Weege and Caroline Coch for being there, encouraging words, energizing walks, and the greatest ice cream sessions in the world.

In addition, I would like to thank Doris Piotrowski, and Peter Linzenich.

Over the last years many people from both work and personal life helped me to finalize this dissertation. To all of you who are not being mentioned by name my warmest thanks!

Mein ganz besonderer und größter Dank geht an Franziska, die unglaublich viel ausgehalten hat, meine Schwester Kirsten und meine Eltern Gerti und Jürgen! Danke für all die unglaubliche Unterstützung, welche nicht in Worte zu fassen ist. Ihr wart immer da, habt mich aufgebaut und mir den Glauben gegeben, dass alles wird. Ohne euch hätte ich es nicht geschafft!

Eidesstattliche Erklärung

Hiermit versichere ich an Eides statt, dass ich die vorliegende Arbeit selbständig verfasst und keine anderen als die angegebenen Quellen und Hilfsmittel verwendet habe.

Ich habe diese Dissertation am Alfred-Wegener-Institut Helmholtz Zentrum für Polar- und Meeresforschung in Potsdam erarbeitet und in englischer Sprache verfasst. Diese Dissertation wird erstmalig und ausschließlich an der Universität Potsdam eingereicht.

Die dem Verfahren zu Grunde liegende Promotionsordnung ist mir bekannt.

Fabian Kneier

Potsdam, 16. November 2018